

Air Force Institute of Technology

AFIT Scholar

Theses and Dissertations

Student Graduate Works

12-1996

Performance Analysis of a Hartman Wavefront Sensor Used for Sensing Atmospheric Turbulence Statistics

Toby D. Reeves

Follow this and additional works at: <https://scholar.afit.edu/etd>



Part of the [Atmospheric Sciences Commons](#), and the [Signal Processing Commons](#)

Recommended Citation

Reeves, Toby D., "Performance Analysis of a Hartman Wavefront Sensor Used for Sensing Atmospheric Turbulence Statistics" (1996). *Theses and Dissertations*. 5930.

<https://scholar.afit.edu/etd/5930>

This Thesis is brought to you for free and open access by the Student Graduate Works at AFIT Scholar. It has been accepted for inclusion in Theses and Dissertations by an authorized administrator of AFIT Scholar. For more information, please contact AFIT.ENWL.Repository@us.af.mil.

AFIT/GEO/ENG/96D-17

PERFORMANCE ANALYSIS
OF A
HARTMANN WAVEFRONT SENSOR
USED FOR SENSING
ATMOSPHERIC TURBULENCE STATISTICS

THESIS
Toby D. Reeves
Captain, USAF

AFIT/GEO/ENG/96D-17

Approved for public release; distribution unlimited

The views expressed in this thesis are those of the author and do not reflect the official policy or position of the Department of Defense or the U. S. Government.

AFIT/GEO/ENG/96D-17

PERFORMANCE ANALYSIS
OF A
HARTMANN WAVEFRONT SENSOR
USED FOR SENSING
ATMOSPHERIC TURBULENCE STATISTICS

THESIS

Presented to the Faculty of the Graduate School of Engineering
of the Air Force Institute of Technology
Air University
In Partial Fulfillment of the
Requirements for the Degree of
Master of Science in Electro-Optical Engineering

Toby D. Reeves, B.S.E.E
Captain, USAF

December, 1996

Approved for public release; distribution unlimited

Acknowledgements

In the past eighteen months, many people contributed to my successful AFIT experience. I thank Dr. Byron Welsh for his effort and patience as my thesis advisor. I thank Dr. Michael Roggemann and Dr. Theodore Luke for their effort and dedication as educators. I thank Capt Eddie Ochoa—we survived the fire hose. I thank Maj. Mark A. Zelkovic, MD, for figuring out what was wrong before it was too late. But most of all, I thank my wonderful, loving family: Anita, my best friend and wife, for keeping me ever aware of what is truly important and for her unwavering encouragement; Renée, my beautiful, wonderful little daughter, for the hugs, kisses, and encouragement only she could give.

Toby D. Reeves

Table of Contents

	Page
Acknowledgements	ii
List of Figures	v
List of Tables	xvii
Abstract	xix
I. Introduction	1-1
1.1 Background	1-1
1.2 Atmospheric Turbulence	1-2
1.3 Hartman Wavefront Sensor as Turbulence Monitor	1-4
1.4 Problem Description and Scope	1-8
1.5 Organization	1-8
II. Slope Correlation Function and Slope Structure Function (SSF)	2-1
2.1 Zernike Polynomials	2-1
2.2 Zernike Expansion Coefficient Spatial Covariance for Turbulence Induced Phase	2-4
2.3 Slope Correlation Function and Slope Structure Function Evaluation	2-8
III. SSF Estimator Signal-to-Noise Ratio	3-1
3.1 H-WFS Specification	3-1
3.2 Slope Measurement Model	3-2
3.3 Slope Measurement Correlation	3-2
3.4 SSF Estimate SNR Definition	3-3
3.5 First Moment of the SSF Estimator	3-3

	Page	
3.6	Second Moment of SSF Estimator	3-4
3.6.1	Expectation Simplification	3-4
3.6.2	Four Dimensional Summation Simplification	3-9
3.7	Final SSF Estimator SNR Expression	3-11
3.8	Extension to a Multi-layer Atmospheric Model	3-11
IV.	SSF Estimator SNR Numerical Results	4-1
4.1	SSF Estimator SNR Numerical Results for the DIMM Geometry	4-1
4.2	SSF Estimator SNR Numerical Results for non-DIMM Geom- etry	4-8
V.	Results, Conclusions and Recommendations	5-1
5.1	Summary of Theoretical Development	5-1
5.2	Summary of Numerical Results	5-1
5.3	Recommendation for Future Research	5-2
Appendix A.	Zernike Expansion Coefficient Covariance Plots	A-1
Appendix B.	Zernike Expansion Coefficient Covariance Tables	B-1
Appendix C.	SSF Estimator Second Moment Simplification	C-1
Appendix D.	SSF SNR Results for DIMM Geometry H-WFS	D-1
Bibliography	BIB-1
Vita	VITA-1

List of Figures

Figure		Page
1.1.	Typical H-WFS subaperture arrangements	1-5
1.2.	Typical H-WFS subaperture element	1-6
2.1.	Zernike expansion coefficient correlation calculation geometry . . .	2-5
2.2.	$\Gamma_s(0) \left(\frac{D}{\rho_0}\right)^{2-\alpha}$ vs. mode count for $L_0/D = \infty$ and various α	2-12
2.3.	$\Gamma_s(0) \left(\frac{D}{\rho_0}\right)^{2-\alpha}$ vs. mode count for $\alpha = 11/3$ and various L_0/D . . .	2-13
2.4.	$\Gamma_s(\vec{u}) \left(\frac{D}{\rho_0}\right)^{2-\alpha}$ as a function of $ \vec{u} $ for various mode counts, with $\alpha = 3.6667$, $\frac{L_0}{D} = \infty$, and $\theta_0 = 0$	2-13
2.5.	$\Gamma_s(\vec{u}) \left(\frac{D}{\rho_0}\right)^{2-\alpha}$ as a function of $ \vec{u} $ for various mode counts, with $\alpha = 3.6667$, $\frac{L_0}{D} = 100.00$, and $\theta_0 = 0$	2-14
2.6.	$\Gamma_s(\vec{u}) \left(\frac{D}{\rho_0}\right)^{2-\alpha}$ as a function of $ \vec{u} $ for various mode counts, with $\alpha = 3.6667$, $\frac{L_0}{D} = 10.00$, and $\theta_0 = 0$	2-14
2.7.	$\Gamma_s(\vec{u}) \left(\frac{D}{\rho_0}\right)^{2-\alpha}$ as a function of $ \vec{u} $ for various mode counts, with $\alpha = 3.6667$, $\frac{L_0}{D} = 1.00$, and $\theta_0 = 0$	2-15
2.8.	$\Gamma_s(\vec{u}) \left(\frac{D}{\rho_0}\right)^{2-\alpha}$ vs. $ u $ for various L_0/D	2-15
2.9.	$\Gamma_s(\vec{u})$ for plane wave as a function of $ \vec{u} $ for various $\frac{D}{\rho_0}$, with $\alpha = 3.6667$, $\frac{L_0}{D} = \infty$, and $\theta_0 = 0$	2-16
2.10.	$D_s(\vec{u}) \left(\frac{D}{\rho_0}\right)^{2-\alpha}$ as a function of $ \vec{u} $ for various mode counts, with $\alpha = 3.6667$, $\frac{L_0}{D} = \infty$, and $\theta_0 = 0$	2-16
2.11.	$D_s(\vec{u}) \left(\frac{D}{\rho_0}\right)^{2-\alpha}$ as a function of $ \vec{u} $ for various mode counts, with $\alpha = 3.6667$, $\frac{L_0}{D} = 100.00$, and $\theta_0 = 0$	2-17
2.12.	$D_s(\vec{u}) \left(\frac{D}{\rho_0}\right)^{2-\alpha}$ as a function of $ \vec{u} $ for various mode counts, with $\alpha = 3.6667$, $\frac{L_0}{D} = 10.00$, and $\theta_0 = 0$	2-17
2.13.	$D_s(\vec{u}) \left(\frac{D}{\rho_0}\right)^{2-\alpha}$ as a function of $ \vec{u} $ for various mode counts, with $\alpha = 3.6667$, $\frac{L_0}{D} = 1.00$, and $\theta_0 = 0$	2-18
2.14.	$D_s(\vec{u})$ as a function of $ \vec{u} $ for various D/ρ_0 with $\alpha = 3.6667$, $\frac{L_0}{D} = \infty$, $\theta_0 = 0$, and mode count of 6.	2-18

Figure		Page
2.15.	$D_s(\vec{u}) \left(\frac{D}{\rho_0}\right)^{2-\alpha}$ vs. $ u $ for various L_0/D with $\alpha = 3.6667$, $\theta_0 = 0$, and mode count of 6.	2-19
3.1.	Geometry used in calculating second moment of SSF estimator . . .	3-6
3.2.	Four cases within SSF estimator second moment calculation	3-7
3.3.	Duplication of $F_{sm}(\vec{\rho}, \sigma_n, \vec{v}\tau i, \vec{p}_m^{(j)}, \vec{q}_m^{(j)}, \vec{p}_\mu^{(j)}, \vec{q}_\mu^{(j)})$ for a 2 by 3 H-WFS	3-13
4.1.	SNR vs. N , DIMM with $\vec{\rho} = (1.00D, 0.00^\circ)$, various L_0/D , $\alpha = 3.6667$, $\vec{v}\tau = (0.10D, 90.00^\circ)$, $\sigma_n^2 = 0\%$	4-2
4.2.	SNR vs. N , DIMM with $\vec{\rho} = (1.00D, 0.00^\circ)$, various L_0/D , $\alpha = 3.6667$, $\vec{v}\tau = (0.50D, 90.00^\circ)$, $\sigma_n^2 = 0\%$	4-3
4.3.	SNR vs. N , DIMM with $\vec{\rho} = (1.00D, 0.00^\circ)$, various L_0/D , $\alpha = 3.6667$, $\vec{v}\tau = (2.50D, 90.00^\circ)$, $\sigma_n^2 = 0\%$	4-3
4.4.	SNR vs. N , DIMM with $\vec{\rho} = (4.00D, 0.00^\circ)$, various L_0/D , $\alpha = 3.6667$, $\vec{v}\tau = (0.10D, 90.00^\circ)$, $\sigma_n^2 = 0\%$	4-4
4.5.	SNR vs. N , DIMM with $\vec{\rho} = (4.00D, 0.00^\circ)$, various L_0/D , $\alpha = 3.6667$, $\vec{v}\tau = (0.50D, 90.00^\circ)$, $\sigma_n^2 = 0\%$	4-5
4.6.	SNR vs. N , DIMM with $\vec{\rho} = (4.00D, 0.00^\circ)$, various L_0/D , $\alpha = 3.6667$, $\vec{v}\tau = (2.50D, 90.00^\circ)$, $\sigma_n^2 = 0\%$	4-5
4.7.	SNR vs. N , DIMM with $\vec{\rho} = (4.00D, 0.00^\circ)$, various $\sigma_n^2/\Gamma_s(0)$, $\alpha = 3.6667$, $\vec{v}\tau = (2.50D, 90.00^\circ)$, $L_0/D = \infty$	4-6
4.8.	SNR vs. N , DIMM with $\vec{\rho} = (4.00D, 0.00^\circ)$, various $\vec{v}\tau/D$, $\alpha = 3.6667$, $\arg(\vec{v}) = 90.00^\circ$, $L_0/D = \infty$	4-7
4.9.	SNR vs. N , DIMM with $\vec{\rho} = (4.00D, 0.00^\circ)$, various $\arg(\vec{v})$, $\alpha = 3.6667$, $ \vec{v} = 1.00D$, $L_0/D = \infty$	4-8
4.10.	SSF estimator SNR vs. sensor subaperture array size for various $\frac{\sigma_n^2}{\Gamma_s(0)}$	4-9
4.11.	SSF estimator SNR vs. σ_n^2 for various sensor arrays	4-9
A.1.	$\mathcal{E}\{a_2 a_2(\vec{u})\} / \mathcal{E}\{a_2 a_2(0)\}$, Takato and Yamaguchi's Fig.3	A-4
A.2.	$\mathcal{E}\{a_3 a_3(\vec{u})\} / \mathcal{E}\{a_3 a_3(0)\}$, Takato and Yamaguchi's Fig.4	A-5
A.3.	$\mathcal{E}\{a_3 a_3(\vec{u})\} / \mathcal{E}\{a_3 a_3(0)\}$, Takato and Yamaguchi's Fig.5	A-6

Figure		Page
A.4.	$\mathcal{E} \left\{ a_j a_{j'}(\bar{u}) \right\} \left(\frac{D}{\rho_0} \right)^{(2-\alpha)}$, odd modes, $\theta_0 = 0^\circ$, $L_0/D = 10.00$, $\alpha = 3.3000$	A-7
A.5.	$\mathcal{E} \left\{ a_j a_{j'}(\bar{u}) \right\} \left(\frac{D}{\rho_0} \right)^{(2-\alpha)}$, odd modes, $\theta_0 = 0^\circ$, $L_0/D = 100.00$, $\alpha = 3.3000$	A-8
A.6.	$\mathcal{E} \left\{ a_j a_{j'}(\bar{u}) \right\} \left(\frac{D}{\rho_0} \right)^{(2-\alpha)}$, odd modes, $\theta_0 = 0^\circ$, $L_0/D = \infty$, $\alpha = 3.3000$	A-9
A.7.	$\mathcal{E} \left\{ a_j a_{j'}(\bar{u}) \right\} \left(\frac{D}{\rho_0} \right)^{(2-\alpha)}$, odd modes, $\theta_0 = 0^\circ$, $L_0/D = 10.00$, $\alpha = 3.6667$	A-10
A.8.	$\mathcal{E} \left\{ a_j a_{j'}(\bar{u}) \right\} \left(\frac{D}{\rho_0} \right)^{(2-\alpha)}$, odd modes, $\theta_0 = 0^\circ$, $L_0/D = 100.00$, $\alpha = 3.6667$	A-11
A.9.	$\mathcal{E} \left\{ a_j a_{j'}(\bar{u}) \right\} \left(\frac{D}{\rho_0} \right)^{(2-\alpha)}$, odd modes, $\theta_0 = 0^\circ$, $L_0/D = \infty$, $\alpha = 3.6667$	A-12
A.10.	$\mathcal{E} \left\{ a_j a_{j'}(\bar{u}) \right\} \left(\frac{D}{\rho_0} \right)^{(2-\alpha)}$, odd modes, $\theta_0 = 0^\circ$, $L_0/D = 10.00$, $\alpha = 3.8000$	A-13
A.11.	$\mathcal{E} \left\{ a_j a_{j'}(\bar{u}) \right\} \left(\frac{D}{\rho_0} \right)^{(2-\alpha)}$, odd modes, $\theta_0 = 0^\circ$, $L_0/D = 100.00$, $\alpha = 3.8000$	A-14
A.12.	$\mathcal{E} \left\{ a_j a_{j'}(\bar{u}) \right\} \left(\frac{D}{\rho_0} \right)^{(2-\alpha)}$, odd modes, $\theta_0 = 0^\circ$, $L_0/D = \infty$, $\alpha = 3.8000$	A-15
A.13.	$\mathcal{E} \left\{ a_j a_{j'}(\bar{u}) \right\} \left(\frac{D}{\rho_0} \right)^{(2-\alpha)}$, odd modes, $\theta_0 = 90^\circ$, $L_0/D = 10.00$, $\alpha = 3.3000$	A-16
A.14.	$\mathcal{E} \left\{ a_j a_{j'}(\bar{u}) \right\} \left(\frac{D}{\rho_0} \right)^{(2-\alpha)}$, odd modes, $\theta_0 = 90^\circ$, $L_0/D = 100.00$, $\alpha = 3.3000$	A-17
A.15.	$\mathcal{E} \left\{ a_j a_{j'}(\bar{u}) \right\} \left(\frac{D}{\rho_0} \right)^{(2-\alpha)}$, odd modes, $\theta_0 = 90^\circ$, $L_0/D = \infty$, $\alpha = 3.3000$	A-18
A.16.	$\mathcal{E} \left\{ a_j a_{j'}(\bar{u}) \right\} \left(\frac{D}{\rho_0} \right)^{(2-\alpha)}$, odd modes, $\theta_0 = 90^\circ$, $L_0/D = 10.00$, $\alpha = 3.6667$	A-19
A.17.	$\mathcal{E} \left\{ a_j a_{j'}(\bar{u}) \right\} \left(\frac{D}{\rho_0} \right)^{(2-\alpha)}$, odd modes, $\theta_0 = 90^\circ$, $L_0/D = 100.00$, $\alpha = 3.6667$	A-20
A.18.	$\mathcal{E} \left\{ a_j a_{j'}(\bar{u}) \right\} \left(\frac{D}{\rho_0} \right)^{(2-\alpha)}$, odd modes, $\theta_0 = 90^\circ$, $L_0/D = \infty$, $\alpha = 3.6667$	A-21
A.19.	$\mathcal{E} \left\{ a_j a_{j'}(\bar{u}) \right\} \left(\frac{D}{\rho_0} \right)^{(2-\alpha)}$, odd modes, $\theta_0 = 90^\circ$, $L_0/D = 10.00$, $\alpha = 3.8000$	A-22
A.20.	$\mathcal{E} \left\{ a_j a_{j'}(\bar{u}) \right\} \left(\frac{D}{\rho_0} \right)^{(2-\alpha)}$, odd modes, $\theta_0 = 90^\circ$, $L_0/D = 100.00$, $\alpha = 3.8000$	A-23
A.21.	$\mathcal{E} \left\{ a_j a_{j'}(\bar{u}) \right\} \left(\frac{D}{\rho_0} \right)^{(2-\alpha)}$, odd modes, $\theta_0 = 90^\circ$, $L_0/D = \infty$, $\alpha = 3.8000$	A-24
A.22.	$\mathcal{E} \left\{ a_j a_{j'}(\bar{u}) \right\} \left(\frac{D}{\rho_0} \right)^{(2-\alpha)}$, even modes, $\theta_0 = 0^\circ$, $L_0/D = 10.00$, $\alpha = 3.3000$	A-25

Figure		Page
A.23.	$\mathcal{E} \left\{ a_j a_{j'}(\bar{u}) \right\} \left(\frac{D}{\rho_0} \right)^{(2-\alpha)}$, even modes, $\theta_0 = 0^\circ$, $L_0/D = 100.00$, $\alpha = 3.3000$	A-26
A.24.	$\mathcal{E} \left\{ a_j a_{j'}(\bar{u}) \right\} \left(\frac{D}{\rho_0} \right)^{(2-\alpha)}$, even modes, $\theta_0 = 0^\circ$, $L_0/D = \infty$, $\alpha = 3.3000$	A-27
A.25.	$\mathcal{E} \left\{ a_j a_{j'}(\bar{u}) \right\} \left(\frac{D}{\rho_0} \right)^{(2-\alpha)}$, even modes, $\theta_0 = 0^\circ$, $L_0/D = 10.00$, $\alpha = 3.6667$	A-28
A.26.	$\mathcal{E} \left\{ a_j a_{j'}(\bar{u}) \right\} \left(\frac{D}{\rho_0} \right)^{(2-\alpha)}$, even modes, $\theta_0 = 0^\circ$, $L_0/D = 100.00$, $\alpha = 3.6667$	A-29
A.27.	$\mathcal{E} \left\{ a_j a_{j'}(\bar{u}) \right\} \left(\frac{D}{\rho_0} \right)^{(2-\alpha)}$, even modes, $\theta_0 = 90^\circ$, $L_0/D = \infty$, $\alpha = 3.6667$	A-30
A.28.	$\mathcal{E} \left\{ a_j a_{j'}(\bar{u}) \right\} \left(\frac{D}{\rho_0} \right)^{(2-\alpha)}$, even modes, $\theta_0 = 0^\circ$, $L_0/D = 10.00$, $\alpha = 3.8000$	A-31
A.29.	$\mathcal{E} \left\{ a_j a_{j'}(\bar{u}) \right\} \left(\frac{D}{\rho_0} \right)^{(2-\alpha)}$, even modes, $\theta_0 = 0^\circ$, $L_0/D = 100.00$, $\alpha = 3.8000$	A-32
A.30.	$\mathcal{E} \left\{ a_j a_{j'}(\bar{u}) \right\} \left(\frac{D}{\rho_0} \right)^{(2-\alpha)}$, even modes, $\theta_0 = 0^\circ$, $L_0/D = \infty$, $\alpha = 3.8000$	A-33
A.31.	$\mathcal{E} \left\{ a_j a_{j'}(\bar{u}) \right\} \left(\frac{D}{\rho_0} \right)^{(2-\alpha)}$, even modes, $\theta_0 = 90^\circ$, $L_0/D = 10.00$, $\alpha = 3.3000$	A-34
A.32.	$\mathcal{E} \left\{ a_j a_{j'}(\bar{u}) \right\} \left(\frac{D}{\rho_0} \right)^{(2-\alpha)}$, even modes, $\theta_0 = 90^\circ$, $L_0/D = 100.00$, $\alpha = 3.3000$	A-35
A.33.	$\mathcal{E} \left\{ a_j a_{j'}(\bar{u}) \right\} \left(\frac{D}{\rho_0} \right)^{(2-\alpha)}$, even modes, $\theta_0 = 90^\circ$, $L_0/D = \infty$, $\alpha = 3.3000$	A-36
A.34.	$\mathcal{E} \left\{ a_j a_{j'}(\bar{u}) \right\} \left(\frac{D}{\rho_0} \right)^{(2-\alpha)}$, even modes, $\theta_0 = 90^\circ$, $L_0/D = 10.00$, $\alpha = 3.6667$	A-37
A.35.	$\mathcal{E} \left\{ a_j a_{j'}(\bar{u}) \right\} \left(\frac{D}{\rho_0} \right)^{(2-\alpha)}$, even modes, $\theta_0 = 90^\circ$, $L_0/D = 100.00$, $\alpha = 3.6667$	A-38
A.36.	$\mathcal{E} \left\{ a_j a_{j'}(\bar{u}) \right\} \left(\frac{D}{\rho_0} \right)^{(2-\alpha)}$, even modes, $\theta_0 = 90^\circ$, $L_0/D = \infty$, $\alpha = 3.6667$	A-39
A.37.	$\mathcal{E} \left\{ a_j a_{j'}(\bar{u}) \right\} \left(\frac{D}{\rho_0} \right)^{(2-\alpha)}$, even modes, $\theta_0 = 90^\circ$, $L_0/D = 10.00$, $\alpha = 3.8000$	A-40
A.38.	$\mathcal{E} \left\{ a_j a_{j'}(\bar{u}) \right\} \left(\frac{D}{\rho_0} \right)^{(2-\alpha)}$, even modes, $\theta_0 = 90^\circ$, $L_0/D = 100.00$, $\alpha = 3.8000$	A-41
A.39.	$\mathcal{E} \left\{ a_j a_{j'}(\bar{u}) \right\} \left(\frac{D}{\rho_0} \right)^{(2-\alpha)}$, even modes, $\theta_0 = 90^\circ$, $L_0/D = \infty$, $\alpha = 3.8000$	A-42
D.1.	SNR vs. N , DIMM with $\vec{\rho} = (1.00D, 0.00^\circ)$, various L_0/D , $\alpha = 3.6667$, $\vec{v}\tau = (0.10D, 90.00^\circ)$, $\sigma_n^2/\Gamma_s(0) = 0\%$	D-3

Figure		Page
D.2.	SNR vs. N , DIMM with $\vec{\rho} = (1.00D, 0.00^\circ)$, various L_0/D , $\alpha = 3.6667$, $\vec{\nu}\tau = (0.50D, 90.00^\circ)$, $\sigma_n^2/\Gamma_s(0) = 0\%$	D-3
D.3.	SNR vs. N , DIMM with $\vec{\rho} = (1.00D, 0.00^\circ)$, various L_0/D , $\alpha = 3.6667$, $\vec{\nu}\tau = (1.00D, 90.00^\circ)$, $\sigma_n^2/\Gamma_s(0) = 0\%$	D-4
D.4.	SNR vs. N , DIMM with $\vec{\rho} = (1.00D, 0.00^\circ)$, various L_0/D , $\alpha = 3.6667$, $\vec{\nu}\tau = (2.50D, 90.00^\circ)$, $\sigma_n^2/\Gamma_s(0) = 0\%$	D-4
D.5.	SNR vs. N , DIMM with $\vec{\rho} = (1.00D, 0.00^\circ)$, various L_0/D , $\alpha = 3.6667$, $\vec{\nu}\tau = (5.00D, 90.00^\circ)$, $\sigma_n^2/\Gamma_s(0) = 0\%$	D-5
D.6.	SNR vs. N , DIMM with $\vec{\rho} = (1.00D, 0.00^\circ)$, various L_0/D , $\alpha = 3.6667$, $\vec{\nu}\tau = (10.00D, 90.00^\circ)$, $\sigma_n^2/\Gamma_s(0) = 0\%$	D-5
D.7.	SNR vs. N , DIMM with $\vec{\rho} = (1.00D, 0.00^\circ)$, various L_0/D , $\alpha = 3.6667$, $\vec{\nu}\tau = (0.10D, 90.00^\circ)$, $\sigma_n^2/\Gamma_s(0) = 10\%$	D-6
D.8.	SNR vs. N , DIMM with $\vec{\rho} = (1.00D, 0.00^\circ)$, various L_0/D , $\alpha = 3.6667$, $\vec{\nu}\tau = (0.50D, 90.00^\circ)$, $\sigma_n^2/\Gamma_s(0) = 10\%$	D-6
D.9.	SNR vs. N , DIMM with $\vec{\rho} = (1.00D, 0.00^\circ)$, various L_0/D , $\alpha = 3.6667$, $\vec{\nu}\tau = (1.00D, 90.00^\circ)$, $\sigma_n^2/\Gamma_s(0) = 10\%$	D-7
D.10.	SNR vs. N , DIMM with $\vec{\rho} = (1.00D, 0.00^\circ)$, various L_0/D , $\alpha = 3.6667$, $\vec{\nu}\tau = (2.50D, 90.00^\circ)$, $\sigma_n^2/\Gamma_s(0) = 10\%$	D-7
D.11.	SNR vs. N , DIMM with $\vec{\rho} = (1.00D, 0.00^\circ)$, various L_0/D , $\alpha = 3.6667$, $\vec{\nu}\tau = (5.00D, 90.00^\circ)$, $\sigma_n^2/\Gamma_s(0) = 10\%$	D-8
D.12.	SNR vs. N , DIMM with $\vec{\rho} = (1.00D, 0.00^\circ)$, various L_0/D , $\alpha = 3.6667$, $\vec{\nu}\tau = (10.00D, 90.00^\circ)$, $\sigma_n^2/\Gamma_s(0) = 10\%$	D-8
D.13.	SNR vs. N , DIMM with $\vec{\rho} = (1.00D, 0.00^\circ)$, various L_0/D , $\alpha = 3.6667$, $\vec{\nu}\tau = (0.10D, 90.00^\circ)$, $\sigma_n^2/\Gamma_s(0) = 20\%$	D-9
D.14.	SNR vs. N , DIMM with $\vec{\rho} = (1.00D, 0.00^\circ)$, various L_0/D , $\alpha = 3.6667$, $\vec{\nu}\tau = (0.50D, 90.00^\circ)$, $\sigma_n^2/\Gamma_s(0) = 20\%$	D-9
D.15.	SNR vs. N , DIMM with $\vec{\rho} = (1.00D, 0.00^\circ)$, various L_0/D , $\alpha = 3.6667$, $\vec{\nu}\tau = (1.00D, 90.00^\circ)$, $\sigma_n^2/\Gamma_s(0) = 20\%$	D-10
D.16.	SNR vs. N , DIMM with $\vec{\rho} = (1.00D, 0.00^\circ)$, various L_0/D , $\alpha = 3.6667$, $\vec{\nu}\tau = (2.50D, 90.00^\circ)$, $\sigma_n^2/\Gamma_s(0) = 20\%$	D-10

Figure		Page
D.17.	SNR vs. N , DIMM with $\vec{\rho} = (1.00D, 0.00^\circ)$, various L_0/D , $\alpha = 3.6667$, $\vec{\nu}\tau = (5.00D, 90.00^\circ)$, $\sigma_n^2/\Gamma_s(0) = 20\%$	D-11
D.18.	SNR vs. N , DIMM with $\vec{\rho} = (1.00D, 0.00^\circ)$, various L_0/D , $\alpha = 3.6667$, $\vec{\nu}\tau = (10.00D, 90.00^\circ)$, $\sigma_n^2/\Gamma_s(0) = 20\%$	D-11
D.19.	SNR vs. N , DIMM with $\vec{\rho} = (1.00D, 0.00^\circ)$, various L_0/D , $\alpha = 3.6667$, $\vec{\nu}\tau = (0.10D, 90.00^\circ)$, $\sigma_n^2/\Gamma_s(0) = 50\%$	D-12
D.20.	SNR vs. N , DIMM with $\vec{\rho} = (1.00D, 0.00^\circ)$, various L_0/D , $\alpha = 3.6667$, $\vec{\nu}\tau = (0.50D, 90.00^\circ)$, $\sigma_n^2/\Gamma_s(0) = 50\%$	D-12
D.21.	SNR vs. N , DIMM with $\vec{\rho} = (1.00D, 0.00^\circ)$, various L_0/D , $\alpha = 3.6667$, $\vec{\nu}\tau = (1.00D, 90.00^\circ)$, $\sigma_n^2/\Gamma_s(0) = 50\%$	D-13
D.22.	SNR vs. N , DIMM with $\vec{\rho} = (1.00D, 0.00^\circ)$, various L_0/D , $\alpha = 3.6667$, $\vec{\nu}\tau = (2.50D, 90.00^\circ)$, $\sigma_n^2/\Gamma_s(0) = 50\%$	D-13
D.23.	SNR vs. N , DIMM with $\vec{\rho} = (1.00D, 0.00^\circ)$, various L_0/D , $\alpha = 3.6667$, $\vec{\nu}\tau = (5.00D, 90.00^\circ)$, $\sigma_n^2/\Gamma_s(0) = 50\%$	D-14
D.24.	SNR vs. N , DIMM with $\vec{\rho} = (1.00D, 0.00^\circ)$, various L_0/D , $\alpha = 3.6667$, $\vec{\nu}\tau = (10.00D, 90.00^\circ)$, $\sigma_n^2/\Gamma_s(0) = 50\%$	D-14
D.25.	SNR vs. N , DIMM with $\vec{\rho} = (4.00D, 0.00^\circ)$, various L_0/D , $\alpha = 3.6667$, $\vec{\nu}\tau = (0.10D, 90.00^\circ)$, $\sigma_n^2/\Gamma_s(0) = 0\%$	D-15
D.26.	SNR vs. N , DIMM with $\vec{\rho} = (4.00D, 0.00^\circ)$, various L_0/D , $\alpha = 3.6667$, $\vec{\nu}\tau = (0.50D, 90.00^\circ)$, $\sigma_n^2/\Gamma_s(0) = 0\%$	D-15
D.27.	SNR vs. N , DIMM with $\vec{\rho} = (4.00D, 0.00^\circ)$, various L_0/D , $\alpha = 3.6667$, $\vec{\nu}\tau = (1.00D, 90.00^\circ)$, $\sigma_n^2/\Gamma_s(0) = 0\%$	D-16
D.28.	SNR vs. N , DIMM with $\vec{\rho} = (4.00D, 0.00^\circ)$, various L_0/D , $\alpha = 3.6667$, $\vec{\nu}\tau = (2.50D, 90.00^\circ)$, $\sigma_n^2/\Gamma_s(0) = 0\%$	D-16
D.29.	SNR vs. N , DIMM with $\vec{\rho} = (4.00D, 0.00^\circ)$, various L_0/D , $\alpha = 3.6667$, $\vec{\nu}\tau = (5.00D, 90.00^\circ)$, $\sigma_n^2/\Gamma_s(0) = 0\%$	D-17
D.30.	SNR vs. N , DIMM with $\vec{\rho} = (4.00D, 0.00^\circ)$, various L_0/D , $\alpha = 3.6667$, $\vec{\nu}\tau = (10.00D, 90.00^\circ)$, $\sigma_n^2/\Gamma_s(0) = 0\%$	D-17
D.31.	SNR vs. N , DIMM with $\vec{\rho} = (4.00D, 0.00^\circ)$, various L_0/D , $\alpha = 3.6667$, $\vec{\nu}\tau = (0.10D, 90.00^\circ)$, $\sigma_n^2/\Gamma_s(0) = 10\%$	D-18

Figure		Page
D.32.	SNR vs. N , DIMM with $\vec{\rho} = (4.00D, 0.00^\circ)$, various L_0/D , $\alpha = 3.6667$, $\vec{\nu}\tau = (0.50D, 90.00^\circ)$, $\sigma_n^2/\Gamma_s(0) = 10\%$	D-18
D.33.	SNR vs. N , DIMM with $\vec{\rho} = (4.00D, 0.00^\circ)$, various L_0/D , $\alpha = 3.6667$, $\vec{\nu}\tau = (1.00D, 90.00^\circ)$, $\sigma_n^2/\Gamma_s(0) = 10\%$	D-19
D.34.	SNR vs. N , DIMM with $\vec{\rho} = (4.00D, 0.00^\circ)$, various L_0/D , $\alpha = 3.6667$, $\vec{\nu}\tau = (2.50D, 90.00^\circ)$, $\sigma_n^2/\Gamma_s(0) = 10\%$	D-19
D.35.	SNR vs. N , DIMM with $\vec{\rho} = (4.00D, 0.00^\circ)$, various L_0/D , $\alpha = 3.6667$, $\vec{\nu}\tau = (5.00D, 90.00^\circ)$, $\sigma_n^2/\Gamma_s(0) = 10\%$	D-20
D.36.	SNR vs. N , DIMM with $\vec{\rho} = (4.00D, 0.00^\circ)$, various L_0/D , $\alpha = 3.6667$, $\vec{\nu}\tau = (10.00D, 90.00^\circ)$, $\sigma_n^2/\Gamma_s(0) = 10\%$	D-20
D.37.	SNR vs. N , DIMM with $\vec{\rho} = (4.00D, 0.00^\circ)$, various L_0/D , $\alpha = 3.6667$, $\vec{\nu}\tau = (0.10D, 90.00^\circ)$, $\sigma_n^2/\Gamma_s(0) = 20\%$	D-21
D.38.	SNR vs. N , DIMM with $\vec{\rho} = (4.00D, 0.00^\circ)$, various L_0/D , $\alpha = 3.6667$, $\vec{\nu}\tau = (0.50D, 90.00^\circ)$, $\sigma_n^2/\Gamma_s(0) = 20\%$	D-21
D.39.	SNR vs. N , DIMM with $\vec{\rho} = (4.00D, 0.00^\circ)$, various L_0/D , $\alpha = 3.6667$, $\vec{\nu}\tau = (1.00D, 90.00^\circ)$, $\sigma_n^2/\Gamma_s(0) = 20\%$	D-22
D.40.	SNR vs. N , DIMM with $\vec{\rho} = (4.00D, 0.00^\circ)$, various L_0/D , $\alpha = 3.6667$, $\vec{\nu}\tau = (2.50D, 90.00^\circ)$, $\sigma_n^2/\Gamma_s(0) = 20\%$	D-22
D.41.	SNR vs. N , DIMM with $\vec{\rho} = (4.00D, 0.00^\circ)$, various L_0/D , $\alpha = 3.6667$, $\vec{\nu}\tau = (5.00D, 90.00^\circ)$, $\sigma_n^2/\Gamma_s(0) = 20\%$	D-23
D.42.	SNR vs. N , DIMM with $\vec{\rho} = (4.00D, 0.00^\circ)$, various L_0/D , $\alpha = 3.6667$, $\vec{\nu}\tau = (10.00D, 90.00^\circ)$, $\sigma_n^2/\Gamma_s(0) = 20\%$	D-23
D.43.	SNR vs. N , DIMM with $\vec{\rho} = (4.00D, 0.00^\circ)$, various L_0/D , $\alpha = 3.6667$, $\vec{\nu}\tau = (0.10D, 90.00^\circ)$, $\sigma_n^2/\Gamma_s(0) = 50\%$	D-24
D.44.	SNR vs. N , DIMM with $\vec{\rho} = (4.00D, 0.00^\circ)$, various L_0/D , $\alpha = 3.6667$, $\vec{\nu}\tau = (0.50D, 90.00^\circ)$, $\sigma_n^2/\Gamma_s(0) = 50\%$	D-24
D.45.	SNR vs. N , DIMM with $\vec{\rho} = (4.00D, 0.00^\circ)$, various L_0/D , $\alpha = 3.6667$, $\vec{\nu}\tau = (1.00D, 90.00^\circ)$, $\sigma_n^2/\Gamma_s(0) = 50\%$	D-25
D.46.	SNR vs. N , DIMM with $\vec{\rho} = (4.00D, 0.00^\circ)$, various L_0/D , $\alpha = 3.6667$, $\vec{\nu}\tau = (2.50D, 90.00^\circ)$, $\sigma_n^2/\Gamma_s(0) = 50\%$	D-25

Figure	Page
D.47. SNR vs. N , DIMM with $\vec{\rho} = (4.00D, 0.00^\circ)$, various L_0/D , $\alpha = 3.6667$, $\vec{\nu}\tau = (5.00D, 90.00^\circ)$, $\sigma_n^2/\Gamma_s(0) = 50\%$	D-26
D.48. SNR vs. N , DIMM with $\vec{\rho} = (4.00D, 0.00^\circ)$, various L_0/D , $\alpha = 3.6667$, $\vec{\nu}\tau = (10.00D, 90.00^\circ)$, $\sigma_n^2/\Gamma_s(0) = 50\%$	D-26
D.49. SNR vs. N , DIMM with $\vec{\rho} = (4.00D, 0.00^\circ)$, various $\sigma_n^2/\Gamma_s(0)$, $\alpha = 3.6667$, $\vec{\nu}\tau = (0.10D, 90.00^\circ)$, $L_0/D = 1.00$	D-27
D.50. SNR vs. N , DIMM with $\vec{\rho} = (4.00D, 0.00^\circ)$, various $\sigma_n^2/\Gamma_s(0)$, $\alpha = 3.6667$, $\vec{\nu}\tau = (0.50D, 90.00^\circ)$, $L_0/D = 1.00$	D-27
D.51. SNR vs. N , DIMM with $\vec{\rho} = (4.00D, 0.00^\circ)$, various $\sigma_n^2/\Gamma_s(0)$, $\alpha = 3.6667$, $\vec{\nu}\tau = (1.00D, 90.00^\circ)$, $L_0/D = 1.00$	D-28
D.52. SNR vs. N , DIMM with $\vec{\rho} = (4.00D, 0.00^\circ)$, various $\sigma_n^2/\Gamma_s(0)$, $\alpha = 3.6667$, $\vec{\nu}\tau = (2.50D, 90.00^\circ)$, $L_0/D = 1.00$	D-28
D.53. SNR vs. N , DIMM with $\vec{\rho} = (4.00D, 0.00^\circ)$, various $\sigma_n^2/\Gamma_s(0)$, $\alpha = 3.6667$, $\vec{\nu}\tau = (5.00D, 90.00^\circ)$, $L_0/D = 1.00$	D-29
D.54. SNR vs. N , DIMM with $\vec{\rho} = (4.00D, 0.00^\circ)$, various $\sigma_n^2/\Gamma_s(0)$, $\alpha = 3.6667$, $\vec{\nu}\tau = (10.00D, 90.00^\circ)$, $L_0/D = 1.00$	D-29
D.55. SNR vs. N , DIMM with $\vec{\rho} = (4.00D, 0.00^\circ)$, various $\sigma_n^2/\Gamma_s(0)$, $\alpha = 3.6667$, $\vec{\nu}\tau = (0.10D, 90.00^\circ)$, $L_0/D = 5.00$	D-30
D.56. SNR vs. N , DIMM with $\vec{\rho} = (4.00D, 0.00^\circ)$, various $\sigma_n^2/\Gamma_s(0)$, $\alpha = 3.6667$, $\vec{\nu}\tau = (0.50D, 90.00^\circ)$, $L_0/D = 5.00$	D-30
D.57. SNR vs. N , DIMM with $\vec{\rho} = (4.00D, 0.00^\circ)$, various $\sigma_n^2/\Gamma_s(0)$, $\alpha = 3.6667$, $\vec{\nu}\tau = (1.00D, 90.00^\circ)$, $L_0/D = 5.00$	D-31
D.58. SNR vs. N , DIMM with $\vec{\rho} = (4.00D, 0.00^\circ)$, various $\sigma_n^2/\Gamma_s(0)$, $\alpha = 3.6667$, $\vec{\nu}\tau = (2.50D, 90.00^\circ)$, $L_0/D = 5.00$	D-31
D.59. SNR vs. N , DIMM with $\vec{\rho} = (4.00D, 0.00^\circ)$, various $\sigma_n^2/\Gamma_s(0)$, $\alpha = 3.6667$, $\vec{\nu}\tau = (5.00D, 90.00^\circ)$, $L_0/D = 5.00$	D-32
D.60. SNR vs. N , DIMM with $\vec{\rho} = (4.00D, 0.00^\circ)$, various $\sigma_n^2/\Gamma_s(0)$, $\alpha = 3.6667$, $\vec{\nu}\tau = (10.00D, 90.00^\circ)$, $L_0/D = 5.00$	D-32
D.61. SNR vs. N , DIMM with $\vec{\rho} = (4.00D, 0.00^\circ)$, various $\sigma_n^2/\Gamma_s(0)$, $\alpha = 3.6667$, $\vec{\nu}\tau = (0.10D, 90.00^\circ)$, $L_0/D = 10.00$	D-33

Figure		Page
D.62.	SNR vs. N , DIMM with $\vec{\rho} = (4.00D, 0.00^\circ)$, various $\sigma_n^2/\Gamma_s(0)$, $\alpha = 3.6667$, $\vec{\nu}\tau = (0.50D, 90.00^\circ)$, $L_0/D = 10.00$	D-33
D.63.	SNR vs. N , DIMM with $\vec{\rho} = (4.00D, 0.00^\circ)$, various $\sigma_n^2/\Gamma_s(0)$, $\alpha = 3.6667$, $\vec{\nu}\tau = (1.00D, 90.00^\circ)$, $L_0/D = 10.00$	D-34
D.64.	SNR vs. N , DIMM with $\vec{\rho} = (4.00D, 0.00^\circ)$, various $\sigma_n^2/\Gamma_s(0)$, $\alpha = 3.6667$, $\vec{\nu}\tau = (2.50D, 90.00^\circ)$, $L_0/D = 10.00$	D-34
D.65.	SNR vs. N , DIMM with $\vec{\rho} = (4.00D, 0.00^\circ)$, various $\sigma_n^2/\Gamma_s(0)$, $\alpha = 3.6667$, $\vec{\nu}\tau = (5.00D, 90.00^\circ)$, $L_0/D = 10.00$	D-35
D.66.	SNR vs. N , DIMM with $\vec{\rho} = (4.00D, 0.00^\circ)$, various $\sigma_n^2/\Gamma_s(0)$, $\alpha = 3.6667$, $\vec{\nu}\tau = (10.00D, 90.00^\circ)$, $L_0/D = 10.00$	D-35
D.67.	SNR vs. N , DIMM with $\vec{\rho} = (4.00D, 0.00^\circ)$, various $\sigma_n^2/\Gamma_s(0)$, $\alpha = 3.6667$, $\vec{\nu}\tau = (0.10D, 90.00^\circ)$, $L_0/D = 100.00$	D-36
D.68.	SNR vs. N , DIMM with $\vec{\rho} = (4.00D, 0.00^\circ)$, various $\sigma_n^2/\Gamma_s(0)$, $\alpha = 3.6667$, $\vec{\nu}\tau = (0.50D, 90.00^\circ)$, $L_0/D = 100.00$	D-36
D.69.	SNR vs. N , DIMM with $\vec{\rho} = (4.00D, 0.00^\circ)$, various $\sigma_n^2/\Gamma_s(0)$, $\alpha = 3.6667$, $\vec{\nu}\tau = (1.00D, 90.00^\circ)$, $L_0/D = 100.00$	D-37
D.70.	SNR vs. N , DIMM with $\vec{\rho} = (4.00D, 0.00^\circ)$, various $\sigma_n^2/\Gamma_s(0)$, $\alpha = 3.6667$, $\vec{\nu}\tau = (2.50D, 90.00^\circ)$, $L_0/D = 100.00$	D-37
D.71.	SNR vs. N , DIMM with $\vec{\rho} = (4.00D, 0.00^\circ)$, various $\sigma_n^2/\Gamma_s(0)$, $\alpha = 3.6667$, $\vec{\nu}\tau = (5.00D, 90.00^\circ)$, $L_0/D = 100.00$	D-38
D.72.	SNR vs. N , DIMM with $\vec{\rho} = (4.00D, 0.00^\circ)$, various $\sigma_n^2/\Gamma_s(0)$, $\alpha = 3.6667$, $\vec{\nu}\tau = (10.00D, 90.00^\circ)$, $L_0/D = 100.00$	D-38
D.73.	SNR vs. N , DIMM with $\vec{\rho} = (4.00D, 0.00^\circ)$, various $\sigma_n^2/\Gamma_s(0)$, $\alpha = 3.6667$, $\vec{\nu}\tau = (0.10D, 90.00^\circ)$, $L_0/D = \infty$	D-39
D.74.	SNR vs. N , DIMM with $\vec{\rho} = (4.00D, 0.00^\circ)$, various $\sigma_n^2/\Gamma_s(0)$, $\alpha = 3.6667$, $\vec{\nu}\tau = (0.50D, 90.00^\circ)$, $L_0/D = \infty$	D-39
D.75.	SNR vs. N , DIMM with $\vec{\rho} = (4.00D, 0.00^\circ)$, various $\sigma_n^2/\Gamma_s(0)$, $\alpha = 3.6667$, $\vec{\nu}\tau = (1.00D, 90.00^\circ)$, $L_0/D = \infty$	D-40
D.76.	SNR vs. N , DIMM with $\vec{\rho} = (4.00D, 0.00^\circ)$, various $\sigma_n^2/\Gamma_s(0)$, $\alpha = 3.6667$, $\vec{\nu}\tau = (2.50D, 90.00^\circ)$, $L_0/D = \infty$	D-40

Figure		Page
D.77.	SNR vs. N , DIMM with $\vec{\rho} = (4.00D, 0.00^\circ)$, various $\sigma_n^2/\Gamma_s(0)$, $\alpha = 3.6667$, $\vec{v}\tau = (5.00D, 90.00^\circ)$, $L_0/D = \infty$	D-41
D.78.	SNR vs. N , DIMM with $\vec{\rho} = (4.00D, 0.00^\circ)$, various $\sigma_n^2/\Gamma_s(0)$, $\alpha = 3.6667$, $\vec{v}\tau = (10.00D, 90.00^\circ)$, $L_0/D = \infty$	D-41
D.79.	SNR vs. N , DIMM with $\vec{\rho} = (4.00D, 0.00^\circ)$, various $\vec{v}\tau/D$, $\alpha = 3.6667$, $\arg(\vec{v}) = 90.00^\circ$, $L_0/D = 1.00$	D-42
D.80.	SNR vs. N , DIMM with $\vec{\rho} = (4.00D, 0.00^\circ)$, various $\vec{v}\tau/D$, $\alpha = 3.6667$, $\arg(\vec{v}) = 90.00^\circ$, $L_0/D = 1.00$	D-42
D.81.	SNR vs. N , DIMM with $\vec{\rho} = (4.00D, 0.00^\circ)$, various $\vec{v}\tau/D$, $\alpha = 3.6667$, $\arg(\vec{v}) = 90.00^\circ$, $L_0/D = 1.00$	D-43
D.82.	SNR vs. N , DIMM with $\vec{\rho} = (4.00D, 0.00^\circ)$, various $\vec{v}\tau/D$, $\alpha = 3.6667$, $\arg(\vec{v}) = 90.00^\circ$, $L_0/D = 1.00$	D-43
D.83.	SNR vs. N , DIMM with $\vec{\rho} = (4.00D, 0.00^\circ)$, various $\vec{v}\tau/D$, $\alpha = 3.6667$, $\arg(\vec{v}) = 90.00^\circ$, $L_0/D = 5.00$	D-44
D.84.	SNR vs. N , DIMM with $\vec{\rho} = (4.00D, 0.00^\circ)$, various $\vec{v}\tau/D$, $\alpha = 3.6667$, $\arg(\vec{v}) = 90.00^\circ$, $L_0/D = 5.00$	D-44
D.85.	SNR vs. N , DIMM with $\vec{\rho} = (4.00D, 0.00^\circ)$, various $\vec{v}\tau/D$, $\alpha = 3.6667$, $\arg(\vec{v}) = 90.00^\circ$, $L_0/D = 5.00$	D-45
D.86.	SNR vs. N , DIMM with $\vec{\rho} = (4.00D, 0.00^\circ)$, various $\vec{v}\tau/D$, $\alpha = 3.6667$, $\arg(\vec{v}) = 90.00^\circ$, $L_0/D = 5.00$	D-45
D.87.	SNR vs. N , DIMM with $\vec{\rho} = (4.00D, 0.00^\circ)$, various $\vec{v}\tau/D$, $\alpha = 3.6667$, $\arg(\vec{v}) = 90.00^\circ$, $L_0/D = 10.00$	D-46
D.88.	SNR vs. N , DIMM with $\vec{\rho} = (4.00D, 0.00^\circ)$, various $\vec{v}\tau/D$, $\alpha = 3.6667$, $\arg(\vec{v}) = 90.00^\circ$, $L_0/D = 10.00$	D-46
D.89.	SNR vs. N , DIMM with $\vec{\rho} = (4.00D, 0.00^\circ)$, various $\vec{v}\tau/D$, $\alpha = 3.6667$, $\arg(\vec{v}) = 90.00^\circ$, $L_0/D = 10.00$	D-47
D.90.	SNR vs. N , DIMM with $\vec{\rho} = (4.00D, 0.00^\circ)$, various $\vec{v}\tau/D$, $\alpha = 3.6667$, $\arg(\vec{v}) = 90.00^\circ$, $L_0/D = 10.00$	D-47
D.91.	SNR vs. N , DIMM with $\vec{\rho} = (4.00D, 0.00^\circ)$, various $\vec{v}\tau/D$, $\alpha = 3.6667$, $\arg(\vec{v}) = 90.00^\circ$, $L_0/D = 100.00$	D-48

Figure		Page
D.92.	SNR vs. N , DIMM with $\vec{\rho} = (4.00D, 0.00^\circ)$, various $\vec{v}\tau/D$, $\alpha = 3.6667$, $\arg(\vec{v}) = 90.00^\circ$, $L_0/D = 100.00$	D-48
D.93.	SNR vs. N , DIMM with $\vec{\rho} = (4.00D, 0.00^\circ)$, various $\vec{v}\tau/D$, $\alpha = 3.6667$, $\arg(\vec{v}) = 90.00^\circ$, $L_0/D = 100.00$	D-49
D.94.	SNR vs. N , DIMM with $\vec{\rho} = (4.00D, 0.00^\circ)$, various $\vec{v}\tau/D$, $\alpha = 3.6667$, $\arg(\vec{v}) = 90.00^\circ$, $L_0/D = 100.00$	D-49
D.95.	SNR vs. N , DIMM with $\vec{\rho} = (4.00D, 0.00^\circ)$, various $\vec{v}\tau/D$, $\alpha = 3.6667$, $\arg(\vec{v}) = 90.00^\circ$, $L_0/D = \infty$	D-50
D.96.	SNR vs. N , DIMM with $\vec{\rho} = (4.00D, 0.00^\circ)$, various $\vec{v}\tau/D$, $\alpha = 3.6667$, $\arg(\vec{v}) = 90.00^\circ$, $L_0/D = \infty$	D-50
D.97.	SNR vs. N , DIMM with $\vec{\rho} = (4.00D, 0.00^\circ)$, various $\vec{v}\tau/D$, $\alpha = 3.6667$, $\arg(\vec{v}) = 90.00^\circ$, $L_0/D = \infty$	D-51
D.98.	SNR vs. N , DIMM with $\vec{\rho} = (4.00D, 0.00^\circ)$, various $\vec{v}\tau/D$, $\alpha = 3.6667$, $\arg(\vec{v}) = 90.00^\circ$, $L_0/D = \infty$	D-51
D.99.	SNR vs. N , DIMM with $\vec{\rho} = (4.00D, 0.00^\circ)$, various $\arg(\vec{v})$, $\alpha = 3.6667$, $ \vec{v} = 1.00D$, $L_0/D = \infty$	D-52
D.100.	SNR vs. N , DIMM with $\vec{\rho} = (4.00D, 0.00^\circ)$, various $\arg(\vec{v})$, $\alpha = 3.6667$, $ \vec{v} = 1.00D$, $L_0/D = \infty$	D-52
D.101.	SNR vs. N , DIMM with $\vec{\rho} = (4.00D, 0.00^\circ)$, various $\arg(\vec{v})$, $\alpha = 3.6667$, $ \vec{v} = 1.00D$, $L_0/D = \infty$	D-53
D.102.	SNR vs. N , DIMM with $\vec{\rho} = (4.00D, 0.00^\circ)$, various $\arg(\vec{v})$, $\alpha = 3.6667$, $ \vec{v} = 1.00D$, $L_0/D = \infty$	D-53
D.103.	SNR vs. N , DIMM with $\vec{\rho} = (4.00D, 0.00^\circ)$, various $\arg(\vec{v})$, $\alpha = 3.6667$, $ \vec{v} = 1.00D$, $L_0/D = \infty$	D-54
D.104.	SNR vs. N , DIMM with $\vec{\rho} = (4.00D, 0.00^\circ)$, various $\arg(\vec{v})$, $\alpha = 3.6667$, $ \vec{v} = 1.00D$, $L_0/D = \infty$	D-54
D.105.	SNR vs. N , DIMM with $\vec{\rho} = (4.00D, 0.00^\circ)$, various $\arg(\vec{v})$, $\alpha = 3.6667$, $ \vec{v} = 1.00D$, $L_0/D = \infty$	D-55
D.106.	SNR vs. N , DIMM with $\vec{\rho} = (4.00D, 0.00^\circ)$, various $\arg(\vec{v})$, $\alpha = 3.6667$, $ \vec{v} = 1.00D$, $L_0/D = \infty$	D-55

Figure		Page
D.107.	SNR vs. N , DIMM with $\vec{\rho} = (4.00D, 0.00^\circ)$, various $\arg(\vec{v})$, $\alpha = 3.6667$, $ \vec{v} = 1.00D$, $L_0/D = \infty$	D-56
D.108.	SNR vs. N , DIMM with $\vec{\rho} = (4.00D, 0.00^\circ)$, various $\arg(\vec{v})$, $\alpha = 3.6667$, $ \vec{v} = 1.00D$, $L_0/D = \infty$	D-56
D.109.	SNR vs. N , DIMM with $\vec{\rho} = (4.00D, 0.00^\circ)$, various $\arg(\vec{v})$, $\alpha = 3.6667$, $ \vec{v} = 1.00D$, $L_0/D = \infty$	D-57
D.110.	SNR vs. N , DIMM with $\vec{\rho} = (4.00D, 0.00^\circ)$, various $\arg(\vec{v})$, $\alpha = 3.6667$, $ \vec{v} = 1.00D$, $L_0/D = \infty$	D-57
D.111.	SNR vs. N , DIMM with $\vec{\rho} = (4.00D, 0.00^\circ)$, various $\arg(\vec{v})$, $\alpha = 3.6667$, $ \vec{v} = 1.00D$, $L_0/D = \infty$	D-58
D.112.	SNR vs. N , DIMM with $\vec{\rho} = (4.00D, 0.00^\circ)$, various $\arg(\vec{v})$, $\alpha = 3.6667$, $ \vec{v} = 1.00D$, $L_0/D = \infty$	D-58
D.113.	SNR vs. N , DIMM with $\vec{\rho} = (4.00D, 0.00^\circ)$, various $\arg(\vec{v})$, $\alpha = 3.6667$, $ \vec{v} = 1.00D$, $L_0/D = \infty$	D-59
D.114.	SNR vs. N , DIMM with $\vec{\rho} = (4.00D, 0.00^\circ)$, various $\arg(\vec{v})$, $\alpha = 3.6667$, $ \vec{v} = 1.00D$, $L_0/D = \infty$	D-59
D.115.	SNR vs. N , DIMM with $\vec{\rho} = (4.00D, 0.00^\circ)$, various $\arg(\vec{v})$, $\alpha = 3.6667$, $ \vec{v} = 1.00D$, $L_0/D = \infty$	D-60
D.116.	SNR vs. N , DIMM with $\vec{\rho} = (4.00D, 0.00^\circ)$, various $\arg(\vec{v})$, $\alpha = 3.6667$, $ \vec{v} = 1.00D$, $L_0/D = \infty$	D-60
D.117.	SNR vs. N , DIMM with $\vec{\rho} = (4.00D, 0.00^\circ)$, various $\arg(\vec{v})$, $\alpha = 3.6667$, $ \vec{v} = 1.00D$, $L_0/D = \infty$	D-61
D.118.	SNR vs. N , DIMM with $\vec{\rho} = (4.00D, 0.00^\circ)$, various $\arg(\vec{v})$, $\alpha = 3.6667$, $ \vec{v} = 1.00D$, $L_0/D = \infty$	D-61

List of Tables

Table		Page
2.1.	The first 35 Zernike polynomials	2-3
2.2.	$Z_j(1, 0)$ and $Z_j(1, \frac{\pi}{2})$ for $j \leq 500$ and $m = 1$	2-11
3.1.	Computational savings realized by identifying like-oriented sets of sub-aperture pairs	3-12
A.1.	Summarization of Figures A.4 through A.39 showing Zernike coefficient correlations	A-2
B.1.	Summarization of Tables B.2 through B.31	B-1
B.2.	$\mathcal{E} \{a_j a_{j'}\} \left(\frac{D}{\rho_0}\right)^{2-\alpha}$, $\alpha = 3.100$, $\frac{L_0}{D} = 1.00$	B-2
B.3.	$\mathcal{E} \{a_j a_{j'}\} \left(\frac{D}{\rho_0}\right)^{2-\alpha}$, $\alpha = 3.100$, $\frac{L_0}{D} = 5.00$	B-3
B.4.	$\mathcal{E} \{a_j a_{j'}\} \left(\frac{D}{\rho_0}\right)^{2-\alpha}$, $\alpha = 3.100$, $\frac{L_0}{D} = 10.00$	B-4
B.5.	$\mathcal{E} \{a_j a_{j'}\} \left(\frac{D}{\rho_0}\right)^{2-\alpha}$, $\alpha = 3.100$, $\frac{L_0}{D} = 100.00$	B-5
B.6.	$\mathcal{E} \{a_j a_{j'}\} \left(\frac{D}{\rho_0}\right)^{2-\alpha}$, $\alpha = 3.100$, $\frac{L_0}{D} = \infty$	B-6
B.7.	$\mathcal{E} \{a_j a_{j'}\} \left(\frac{D}{\rho_0}\right)^{2-\alpha}$, $\alpha = 3.200$, $\frac{L_0}{D} = 1.00$	B-7
B.8.	$\mathcal{E} \{a_j a_{j'}\} \left(\frac{D}{\rho_0}\right)^{2-\alpha}$, $\alpha = 3.200$, $\frac{L_0}{D} = 5.00$	B-8
B.9.	$\mathcal{E} \{a_j a_{j'}\} \left(\frac{D}{\rho_0}\right)^{2-\alpha}$, $\alpha = 3.200$, $\frac{L_0}{D} = 10.00$	B-9
B.10.	$\mathcal{E} \{a_j a_{j'}\} \left(\frac{D}{\rho_0}\right)^{2-\alpha}$, $\alpha = 3.200$, $\frac{L_0}{D} = 100.00$	B-10
B.11.	$\mathcal{E} \{a_j a_{j'}\} \left(\frac{D}{\rho_0}\right)^{2-\alpha}$, $\alpha = 3.200$, $\frac{L_0}{D} = \infty$	B-11
B.12.	$\mathcal{E} \{a_j a_{j'}\} \left(\frac{D}{\rho_0}\right)^{2-\alpha}$, $\alpha = 3.400$, $\frac{L_0}{D} = 1.00$	B-12
B.13.	$\mathcal{E} \{a_j a_{j'}\} \left(\frac{D}{\rho_0}\right)^{2-\alpha}$, $\alpha = 3.400$, $\frac{L_0}{D} = 5.00$	B-13
B.14.	$\mathcal{E} \{a_j a_{j'}\} \left(\frac{D}{\rho_0}\right)^{2-\alpha}$, $\alpha = 3.400$, $\frac{L_0}{D} = 10.00$	B-14
B.15.	$\mathcal{E} \{a_j a_{j'}\} \left(\frac{D}{\rho_0}\right)^{2-\alpha}$, $\alpha = 3.400$, $\frac{L_0}{D} = 100.00$	B-15
B.16.	$\mathcal{E} \{a_j a_{j'}\} \left(\frac{D}{\rho_0}\right)^{2-\alpha}$, $\alpha = 3.400$, $\frac{L_0}{D} = \infty$	B-16

Table		Page
B.17.	$\mathcal{E} \{a_j a_{j'}\} \left(\frac{D}{\rho_0}\right)^{2-\alpha}, \alpha = \frac{11}{3}, \frac{L_0}{D} = 1.00$	B-17
B.18.	$\mathcal{E} \{a_j a_{j'}\} \left(\frac{D}{\rho_0}\right)^{2-\alpha}, \alpha = \frac{11}{3}, \frac{L_0}{D} = 5.00$	B-18
B.19.	$\mathcal{E} \{a_j a_{j'}\} \left(\frac{D}{\rho_0}\right)^{2-\alpha}, \alpha = \frac{11}{3}, \frac{L_0}{D} = 10.00$	B-19
B.20.	$\mathcal{E} \{a_j a_{j'}\} \left(\frac{D}{\rho_0}\right)^{2-\alpha}, \alpha = \frac{11}{3}, \frac{L_0}{D} = 100.00$	B-20
B.21.	$\mathcal{E} \{a_j a_{j'}\} \left(\frac{D}{\rho_0}\right)^{2-\alpha}, \alpha = \frac{11}{3}, \frac{L_0}{D} = \infty$	B-21
B.22.	$\mathcal{E} \{a_j a_{j'}\} \left(\frac{D}{\rho_0}\right)^{2-\alpha}, \alpha = 3.800, \frac{L_0}{D} = 1.00$	B-22
B.23.	$\mathcal{E} \{a_j a_{j'}\} \left(\frac{D}{\rho_0}\right)^{2-\alpha}, \alpha = 3.800, \frac{L_0}{D} = 5.00$	B-23
B.24.	$\mathcal{E} \{a_j a_{j'}\} \left(\frac{D}{\rho_0}\right)^{2-\alpha}, \alpha = 3.800, \frac{L_0}{D} = 10.00$	B-24
B.25.	$\mathcal{E} \{a_j a_{j'}\} \left(\frac{D}{\rho_0}\right)^{2-\alpha}, \alpha = 3.800, \frac{L_0}{D} = 100.00$	B-25
B.26.	$\mathcal{E} \{a_j a_{j'}\} \left(\frac{D}{\rho_0}\right)^{2-\alpha}, \alpha = 3.800, \frac{L_0}{D} = \infty$	B-26
B.27.	$\mathcal{E} \{a_j a_{j'}\} \left(\frac{D}{\rho_0}\right)^{2-\alpha}, \alpha = 3.900, \frac{L_0}{D} = 1.00$	B-27
B.28.	$\mathcal{E} \{a_j a_{j'}\} \left(\frac{D}{\rho_0}\right)^{2-\alpha}, \alpha = 3.900, \frac{L_0}{D} = 5.00$	B-28
B.29.	$\mathcal{E} \{a_j a_{j'}\} \left(\frac{D}{\rho_0}\right)^{2-\alpha}, \alpha = 3.900, \frac{L_0}{D} = 10.00$	B-29
B.30.	$\mathcal{E} \{a_j a_{j'}\} \left(\frac{D}{\rho_0}\right)^{2-\alpha}, \alpha = 3.900, \frac{L_0}{D} = 100.00$	B-30
B.31.	$\mathcal{E} \{a_j a_{j'}\} \left(\frac{D}{\rho_0}\right)^{2-\alpha}, \alpha = 3.900, \frac{L_0}{D} = \infty$	B-31
D.1.	DIMM SSF estimator SNR plot summary	D-2

Abstract

Atmospheric turbulence parameters, such as Fried's coherence diameter, the outer scale of turbulence, and the turbulence power law, are related to the wavefront slope structure function (SSF). The SSF is defined as the second moment of the wavefront slope difference as a function of both time and position. Knowledge of the SSF allows turbulence parameters to be estimated. Hartmann wavefront sensor (H-WFS) slope measurements, composed of both signal and noise, allow the SSF to be estimated by computing a mean square difference of H-WFS slope measurements. Wavefront slope measurements within a single temporal frame are correlated as are the wavefront slope measurements in temporally spaced frames. This correlation is a function of the space-time separation between measurements, the outer scale, the power law, and the temporal properties of the turbulence.

The quality of the SSF estimate is quantified by the signal-to-noise ratio (SNR) of the estimator. This thesis develops a theoretical SNR expression for the SSF estimator. This SNR is a function of H-WFS geometry, the number of temporal frames included in the estimate, the outer scale, power law, and temporal properties of the turbulence. Spatial slope correlations are incorporated. Temporal slope correlations are incorporated using Taylor's frozen flow hypothesis. Results are presented for various H-WFS configurations and atmospheric turbulence properties.

PERFORMANCE ANALYSIS
OF A
HARTMANN WAVEFRONT SENSOR
USED FOR SENSING
ATMOSPHERIC TURBULENCE STATISTICS

I. Introduction

1.1 Background

Images taken from ground-based telescopes suffer degradation induced by atmospheric turbulence. This degradation is widely described in the literature [11]. The degree of degradation is characterized by the *seeing* condition and is commonly quantified by Fried's parameter, r_0 [11]. With the development of modern adaptive optics systems [20, 21], understanding real-time seeing conditions may allow increased system performance.

A *seeing monitor* is a device for determining seeing conditions and several such devices are described in the literature [17, 2, 6, 18]. These devices generally image a bright point source, such as a distant star. As the light travels through the atmosphere, both phase and amplitude wavefront aberrations are induced. The seeing monitor senses the perturbed wavefronts to infer turbulence properties. A simple method involves characterizing the variance of the image motion as seen by a single aperture [18]. A second method involves measuring the mean-square difference in angle-of-arrival of the light as seen through two small apertures [4]. This method is commonly referred to as the Dual Image Motion Monitor (DIMM) and is widely used [3, 2, 6, 17, 12]. Yet another, the generalization of the DIMM idea, uses a Hartmann wavefront sensor (H-WFS) array to make multiple wavefront slope measurements [13, 7].

Wavefront slope sensing devices make a sequence of measurements over a period time. From these slope measurements, atmospheric parameters, such as Fried's r_0 , may

be inferred by relating the estimated slope statistics to a theoretical model for turbulence induced phase. The quality of the estimation must be addressed. The number of measurements taken, the time between measurements, and the noise induced through the measurement process are factors that must be considered. A standard measure for estimation quality is the signal-to-noise ratio (SNR) defined as the estimator's unbiased mean divided by the estimator's standard deviation.

This thesis focuses on using a H-WFS array for turbulence sensing. H-WFS measurements allow the slope structure function (SSF) to be estimated. The SSF is related to a theoretical model for atmospheric turbulence and thus may be used in determining turbulence parameters. The theoretical SSF estimator SNR is developed and examined.

1.2 Atmospheric Turbulence

We begin by summarizing the properties of atmospheric turbulence. Turbulence-induced index of refraction fluctuations are most often modeled by the Kolmogorov or von Kármán power spectral density with a 11/3 power law [10, 11]. Stribling [14] generalized the Kolmogorov power spectral density to an arbitrary power law ranging between 3 and 4. Stribling's expressions can be modified to obtain an equivalent arbitrary power law expression for the von Kármán power spectrum. Assuming that diffraction effects can be ignored, the turbulence-induced index-of-refraction fluctuation power spectral density can be related to the turbulence-induced phase fluctuation power spectral density, $\Phi_\phi(k)$, for a plane wave propagating through the atmosphere [22, 1, 15]. The phase power spectral density is

$$\Phi_\phi(k) = (2\pi)^{(3-\alpha)} \left[\left(\frac{1}{\rho_0^{\alpha-2}} \right) \frac{c_1 \Gamma\left(\frac{\alpha}{2}\right)}{-(2)^{(4-\alpha)} \pi^2 \Gamma\left(\frac{2-\alpha}{2}\right)} \right] (k^2 + k_0^2)^{-\frac{\alpha}{2}}, \quad (1.1)$$

where

$$c_1 = 2 \left(\frac{8}{\alpha-2} \Gamma\left[\frac{2}{\alpha-2}\right] \right)^{\frac{\alpha-2}{2}}, \quad (1.2)$$

$$\rho_0 = \left[\frac{c_1 \Gamma\left(\frac{\alpha}{2}\right)}{-(2)^{(4-\alpha)} \pi^2 k^2 a(\alpha) \Gamma\left(\frac{2-\alpha}{2}\right) \int_0^L C_n^2(z) dz} \right]^{\frac{1}{\alpha-2}}, \quad (1.3)$$

$$a(\alpha) = -(2)^{(\alpha-4)} \pi^{-3/2} \frac{\Gamma\left(\frac{\alpha}{2}\right)}{\Gamma\left(\frac{3-\alpha}{2}\right)}, \quad (1.4)$$

and Γ is Euler's Gamma function, k is the wavenumber for the propagating light, α is the power law, ρ_0 is a generalized coherence diameter analogous to Fried's r_0 , C_n^2 is the index of refraction structure constant, and

$$k_0 = 1/L_0, \quad (1.5)$$

where L_0 is the outer scale of turbulence.

Equation (1.1) does not model the temporal evolution of turbulence. Temporal effects are included using Taylor's frozen flow hypothesis [11:65]. This hypothesis states during short time intervals and a single layer of turbulence, phase fluctuations remain fixed except for a uniform transverse translation at a velocity \vec{v} . Thus, if \vec{r} is a point in space, then the phase at time t_2 , $\phi(\vec{r}, t_2)$, is related to the phase at time $t_1 < t_2$, $\phi(\vec{r}, t_1)$, by

$$\phi(\vec{r}, t_2) = \phi(\vec{r} + \vec{v}(t_2 - t_1), t_1). \quad (1.6)$$

Equation (1.6) states that time differences may be represented by spatial shifts.

Equation (1.1) also assumes a single turbulent layer. A common model for layered turbulence assumes the atmosphere is composed of a finite number of layers [11:66]. The turbulence in each layer is assumed statistically independent to turbulence in any other layer. Each layer is described by a ρ_{0_i} , defined in Eqn. (1.3), and a layer velocity vector \vec{v}_i . If there are Q layers, and the power law is assumed equal in all layers, the overall $\rho_{0_{tot}}$ is related to the individual ρ_{0_i} by [11:72]

$$\rho_{0_{tot}}^{2-\alpha} = \sum_{i=1}^Q \rho_{0_i}^{2-\alpha}. \quad (1.7)$$

1.3 Hartman Wavefront Sensor as Turbulence Monitor

A H-WFS is a device which produces wavefront slope measurements spatially separated over an arbitrary arrangement of arbitrarily shaped subapertures. Typical arrangements are shown in Fig. 1.1 and include the DIMM as a special case.

A lens over each subaperture focuses the wavefront onto a detector array. The irradiance centroid provides information as to the average wavefront slope over the subaperture. Figure 1.2 shows a cross section for a representative subaperture.

We can define a slope structure function (SSF) as

$$D_s(\vec{p}, \vec{q}, t_1, t_2) = \mathcal{E} \left\{ [s_{\hat{a}}(\vec{p}, t_1) - s_{\hat{b}}(\vec{q}, t_2)]^2 \right\} \quad (1.8)$$

where $\mathcal{E} \{ \dots \}$ is the statistical expectation operator; $s_{\hat{a}}(\vec{p}, t_1)$ is the slope at time t_1 over a subaperture centered at the point \vec{p} and in the direction of the unit vector \hat{a} ; $s_{\hat{b}}(\vec{q}, t_2)$ is the slope at time t_2 over a subaperture centered at \vec{q} and in the direction of the unit vector \hat{b} . Expanding Eqn. (1.8), assuming isotropic turbulence and Taylor's frozen flow hypothesis, we write

$$\begin{aligned} D_{s_{\hat{a}\hat{b}}}(\vec{p}, \vec{q}, t_1, t_2) &= \mathcal{E} \left\{ s_{\hat{a}}^2(\vec{p}, t_1) + s_{\hat{b}}^2(\vec{q}, t_2) - 2s_{\hat{a}}(\vec{p}, t_1)s_{\hat{b}}(\vec{q}, t_2) \right\} \\ &= 2\Gamma_{s_{\hat{a}\hat{b}}}(\vec{q} - \vec{p} + \vec{v}(t_2 - t_1)), \end{aligned} \quad (1.9)$$

where \vec{v} is the velocity of a single turbulent layer, and Γ_s is the space-time slope correlation function defined as

$$\Gamma_{s_{\hat{a}\hat{b}}}(\vec{q} - \vec{p} + \vec{v}(t_2 - t_1)) = \mathcal{E} \{ s_{\hat{a}}(\vec{p}, t_1)s_{\hat{b}}(\vec{q}, t_2) \}. \quad (1.10)$$

When \hat{a} and \hat{b} are in the same direction, the SSF is said to be a *self slope structure function* whereas if \hat{a} and \hat{b} are in different directions, the SSF is termed a *cross slope structure function*. To simplify the analysis, only self slope structure functions are considered. Additionally, our interest is limited to slopes in either of two orthogonal directions. We thus

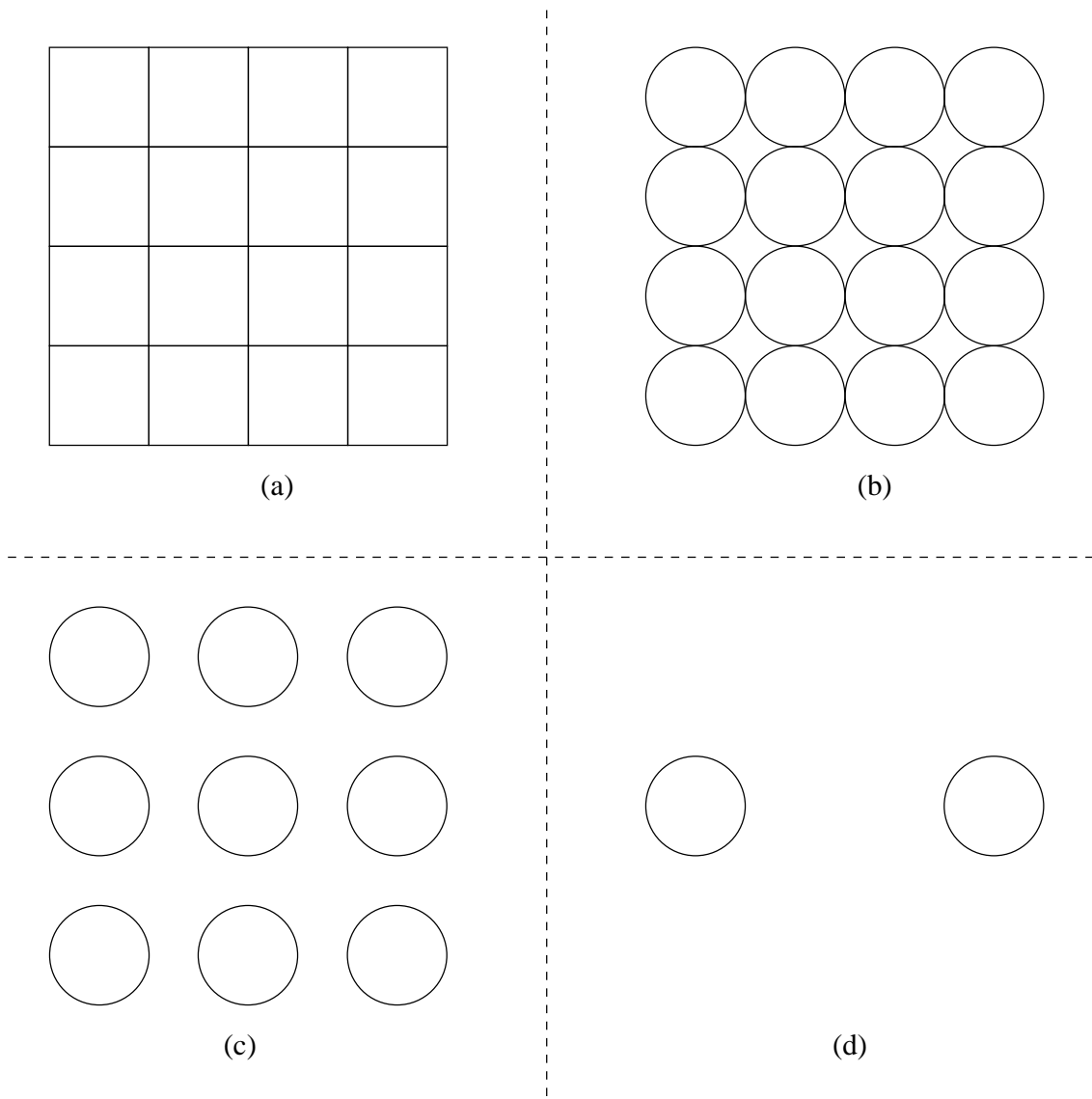


Figure 1.1 Typical H-WFS subaperture arrangements: (a) dense grid of square subapertures (b) dense grid of circular subapertures (c) non-dense grid of circular subapertures (d) two circular subapertures separated by several diameters, a Dual Image Motion Monitor (DIMM).

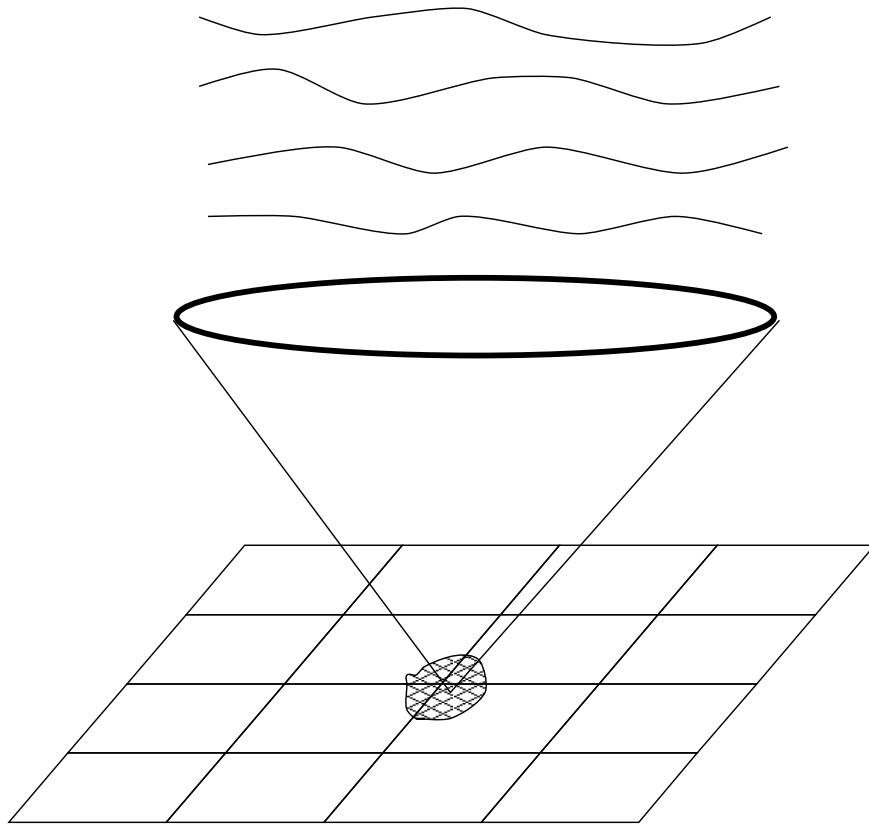


Figure 1.2 Typical H-WFS subaperture element is a lens that images energy onto a charge-coupled device (CCD) array. The location of the image centroid is related to the average wavefront gradient over the lens.

drop the \hat{a} and \hat{b} notation and require the slopes within our SSF to be in the same direction and write

$$\Gamma_s(\vec{q} - \vec{p} + \vec{v}(t_2 - t_1)) = \mathcal{E} \{s(\vec{p}, t_1)s(\vec{q}, t_2)\}. \quad (1.11)$$

The slope structure function of Eqn. (1.8) may be estimated for a particular vector separation, $\vec{\rho} = \vec{p} - \vec{q}$, by computing the average mean square difference of H-WFS slope measurements for all subapertures separated by $\vec{\rho}$. Assume a particular time realization of H-WFS slope measurements contains M different slope measurements having the same vector separation $\vec{\rho}$. Thus, a set of N time realizations contains MN measurements at a vector separation $\vec{\rho}$. The SSF estimate can be written as

$$\hat{D}_s(\vec{\rho}) = \frac{1}{NM} \sum_{m=1}^M \sum_{n=1}^N [\hat{s}(\vec{q}_m, t_n) - \hat{s}(\vec{p}_m, t_n)]^2, \quad (1.12)$$

where $\hat{D}_s(\vec{\rho})$ is the SSF estimate for a vector separation $\vec{\rho} = \vec{q}_m - \vec{p}_m$, m is the index to pairs of subapertures separated by $\vec{\rho} = \vec{q}_m - \vec{p}_m$, and $\hat{s}(\vec{p}_m, t_n)$ is the slope measurement taken at time t_n for a subaperture centered at \vec{p}_m .

Knowledge of the SSF as provided by the SSF estimator allows atmospheric turbulence statistics to be estimated if a theoretical expression for Γ_s is known. The quality of this estimation can be quantitatively considered if the SNR for the SSF estimator is known. This SNR is defined as the estimator's unbiased mean divided by the estimator's standard deviation,

$$SNR(\hat{D}_s(\vec{\rho})) = \frac{\mathcal{E} \{ \hat{D}_s(\vec{\rho}) \} - \text{bias}}{\left[\mathcal{E} \left\{ \left(\hat{D}_s(\vec{\rho}) \right)^2 \right\} - \mathcal{E} \{ \hat{D}_s(\vec{\rho}) \}^2 \right]^{1/2}}, \quad (1.13)$$

where D_s is the SSF estimator.

1.4 *Problem Description and Scope*

The goal of this thesis is to develop and analyze the signal-to-noise ratio (SNR) of the SSF estimator for an arbitrary H-WFS arrangement when used for sensing atmospheric turbulence statistics.

The analysis steps used in this thesis are:

- Model atmospheric induced phase fluctuations with the spectral density given in Eqn. (1.1).
- Include temporal effects with the Taylor frozen flow hypothesis.
- Derive the theoretical expression for the slope correlation function, Γ_s , as defined in Eqn. (1.11).
- Develop a theoretical SNR expression for the SSF estimator.
- Extend the SNR expression to a multi-layer atmospheric model.
- Develop a computer program to evaluate the SNR expression for an arbitrary H-WFS arrangement.
- Use the computer program to present SNR results for various atmospheric conditions and H-WFS configurations.

1.5 *Organization*

In Chapter II, a theoretical expression for the wavefront slope correlation function, Γ_s , is developed based on a Zernike polynomial expansion of the atmospheric induced phase. With this expression, the theoretical SSF, Eqn. (1.8), is evaluated for various atmospheric conditions.

In Chapter III, the H-WFS model is discussed and the slope measurement model is defined. Next, the first and second moments of the SSF estimator, Eqn. (1.12), are developed and combined to obtain the theoretical SNR expression. Finally, these results are extended to a multi-layered atmospheric model.

In Chapter IV, selected numerical results for the SSF estimator SNR expression are presented and discussed.

Chapter V summarizes the major findings of this research and recommends areas for further research.

II. Slope Correlation Function and Slope Structure Function (SSF)

This chapter develops a method to evaluate the theoretical expression for the space-time SSF defined in Eqn. (1.8) for turbulence induced phase fluctuations modeled with arbitrary power law and finite outer scale. Taylor's frozen flow hypothesis allows the temporal evolution of turbulence to be included. The analysis is based on a Zernike polynomial expansion of phase and we begin by summarizing this expansion. Next, a covariance expression between expansion coefficients for two spatially separated circular apertures is presented. Then, an expression for the space-time slope correlation function, Γ_s , is derived and examined. Last, the space-time SSF is evaluated for various values of turbulence power law and outer scale.

2.1 Zernike Polynomials

The analysis in this thesis is based on a modal decomposition of the wavefront phase using the Zernike polynomials as defined by Noll [8]. The defining equations and properties required for our analysis are summarized.

The Zernike polynomials are the set of polynomials defined on a unit circle in polar coordinates by

$$\left. \begin{aligned} Z_{\text{even } j}(r, \theta) &= \sqrt{n+1} R_n^m(r) \sqrt{2} \cos(m\theta) \\ Z_{\text{odd } j}(r, \theta) &= \sqrt{n+1} R_n^m(r) \sqrt{2} \sin(m\theta) \\ Z_j(r, \theta) &= \sqrt{n+1} R_n^0(r) \end{aligned} \right\} \begin{array}{l} m \neq 0 \\ \\ m = 0 \end{array}, \quad (2.1)$$

where

$$R_n^m(r) = \sum_{s=0}^{(n-m)/2} \frac{(-1)^s (n-s)!}{s! [(n+m)/2 - s]! [(n-m)/2 - s]!} r^{n-2s}. \quad (2.2)$$

The value j is a mode ordering number and is a function of n and m . The values n and m are integers and satisfy

$$\left. \begin{aligned} m &\leq n \\ n - |m| &= \text{even} \end{aligned} \right\}. \quad (2.3)$$

These polynomials satisfy the orthogonality relation

$$\int_{-\infty}^{\infty} dr d\theta W(r) Z_j(r, \theta) Z_{j'}(r, \theta) = \delta_{jj'}, \quad (2.4)$$

where

$$W(r) = \begin{cases} 1/\pi & r \leq 1 \\ 0 & r > 1 \end{cases}, \quad (2.5)$$

and

$$\delta_{jj'} = \begin{cases} 1 & j = j' \\ 0 & \text{otherwise} \end{cases}. \quad (2.6)$$

The Zernike expansion of an arbitrary function, $\phi(r, \theta)$, over a circular aperture of arbitrary radius, R , is given by

$$\phi(R\rho, \theta) = \sum_j a_j Z_j(\rho, \theta), \quad (2.7)$$

with

$$\rho = r/R, \quad (2.8)$$

and

$$a_j = \frac{1}{R^2} \int_{-\infty}^{\infty} dr d\theta W\left(\frac{r}{R}\right) \phi\left(r, \theta\right) Z_j\left(\frac{r}{R}, \theta\right). \quad (2.9)$$

The first 35 Zernike polynomials are listed in Tab. 2.1.

The development that follows requires the Fourier transform of the Zernike polynomials. If $Q_j(k, \phi)$ is the Fourier transform of $Z_j(\rho, \theta)$, then [8]

$$W(\rho) Z_j(\rho, \theta) = \int_{-\infty}^{\infty} d^2\vec{k} Q_j(k, \phi) \exp(-2\pi i \vec{k} \cdot \vec{\rho}), \quad (2.10)$$

where $i = \sqrt{-1}$, and with

$$\begin{aligned} Q_{\text{even } j}(k, \phi) &= \\ Q_{\text{even } j}(k, \phi) &= \\ Q_j(k, \phi) &= \end{aligned} \left\{ \sqrt{n+1} \frac{J_{n+1}(2\pi k)}{\pi} k \begin{cases} (-1)^{(n-m)/2} i^m \sqrt{2} \cos(m\phi) \\ (-1)^{(n-m)/2} i^m \sqrt{2} \sin(m\phi) \\ (-1)^{n/2}, \text{ if } m = 0 \end{cases} \right. . \quad (2.11)$$

j	m	n	$Z_j(r, \theta)$
1	0	0	1
2	1	1	$2r \cos(\theta)$
3	1	1	$2r \sin(\theta)$
4	0	2	$\sqrt{3}(-1 + 2r^2)$
5	2	2	$\sqrt{6}r^2 \sin(2\theta)$
6	2	2	$\sqrt{6}r^2 \cos(2\theta)$
7	1	3	$2^{\frac{3}{2}}(-2r + 3r^3) \sin(\theta)$
8	1	3	$2^{\frac{3}{2}}(-2r + 3r^3) \cos(\theta)$
9	3	3	$2^{\frac{3}{2}}r^3 \sin(3\theta)$
10	3	3	$2^{\frac{3}{2}}r^3 \cos(3\theta)$
11	0	4	$\sqrt{5}(1 - 6r^2 + 6r^4)$
12	2	4	$\sqrt{10}(-3r^2 + 4r^4) \cos(2\theta)$
13	2	4	$\sqrt{10}(-3r^2 + 4r^4) \sin(2\theta)$
14	4	4	$\sqrt{10}r^4 \cos(4\theta)$
15	4	4	$\sqrt{10}r^4 \sin(4\theta)$
16	1	5	$2\sqrt{3}(3r - 12r^3 + 10r^5) \cos(\theta)$
17	1	5	$2\sqrt{3}(3r - 12r^3 + 10r^5) \sin(\theta)$
18	3	5	$2\sqrt{3}(-4r^3 + 5r^5) \cos(3\theta)$
19	3	5	$2\sqrt{3}(-4r^3 + 5r^5) \sin(3\theta)$
20	5	5	$2\sqrt{3}r^5 \cos(5\theta)$
21	5	5	$2\sqrt{3}r^5 \sin(5\theta)$
22	0	6	$\sqrt{7}(-1 + 12r^2 - 30r^4 + 20r^6)$
23	2	6	$\sqrt{14}(6r^2 - 20r^4 + 15r^6) \sin(2\theta)$
24	2	6	$\sqrt{14}(6r^2 - 20r^4 + 15r^6) \cos(2\theta)$
25	4	6	$\sqrt{14}(-5r^4 + 6r^6) \sin(4\theta)$
26	4	6	$\sqrt{14}(-5r^4 + 6r^6) \cos(4\theta)$
27	6	6	$\sqrt{14}r^6 \sin(6\theta)$
28	6	6	$\sqrt{14}r^6 \cos(6\theta)$
29	1	7	$4(-4r + 30r^3 - 60r^5 + 35r^7) \sin(\theta)$
30	1	7	$4(-4r + 30r^3 - 60r^5 + 35r^7) \cos(\theta)$
31	3	7	$4(10r^3 - 30r^5 + 21r^7) \sin(3\theta)$
32	3	7	$4(10r^3 - 30r^5 + 21r^7) \cos(3\theta)$
33	5	7	$4(-6r^5 + 7r^7) \sin(5\theta)$
34	5	7	$4(-6r^5 + 7r^7) \cos(5\theta)$
35	7	7	$4r^7 \sin(7\theta)$

Table 2.1 The first 35 Zernike polynomials defined as Noll [8] where j is the mode ordering index, m is the azimuthal frequency, and n is the radial frequency.

2.2 Zernike Expansion Coefficient Spatial Covariance for Turbulence Induced Phase

We now use the Zernike polynomial expansion as summarized in the previous section to derive an expression quantifying the correlation of phase between two H-WFS subapertures with arbitrary spatial separation.

Consider two circular apertures of equal diameter D , with $D = 2R$, as shown in Fig. 2.1. One is located with its center at the origin of the xy coordinate system; the other is centered at the vertex of the vector \vec{u} . Let the magnitude of \vec{u} , u , be measured in units of diameter, and let θ_0 be the angle between \vec{u} and the x axis. The Zernike expansion of the atmospheric induced phase over these apertures can be written as

$$\phi(R\vec{\rho}) = \sum_{j=1}^{\infty} a_j Z_j(\vec{\rho}), \quad (2.12)$$

and

$$\phi(R(\vec{\rho}' + 2\vec{u})) = \sum_{j'=1}^{\infty} a_{j'}(\vec{u}) Z_{j'}(\vec{\rho}'). \quad (2.13)$$

The function ϕ is a random process whose spectral density, Φ_ϕ , is given in Eqn. (1.1). Using Eqn. (2.9), the expansion coefficients may be written as

$$a_j = \int_{-\infty}^{\infty} \phi(R\vec{\rho}) Z_j(\vec{\rho}) W(\vec{\rho}) d\vec{\rho}, \quad (2.14)$$

and

$$a_{j'}(\vec{u}) = \int_{-\infty}^{\infty} \phi(R(\vec{\rho}' + 2\vec{u})) Z_{j'}(\vec{\rho}') W(\vec{\rho}') d\vec{\rho}', \quad (2.15)$$

where $W(\vec{\rho})$ is given by Eqn. (2.5). The correlation of Eqns. (2.14) and (2.15) is by definition

$$\mathcal{E} \{ a_j a_{j'}^*(\vec{u}) \} = \int_{-\infty}^{\infty} d\vec{\rho} \int_{-\infty}^{\infty} d\vec{\rho}' \mathcal{E} \{ \phi(R\vec{\rho}) \phi^*(R(\vec{\rho}' + 2\vec{u})) \} Z_j(\vec{\rho}) Z_{j'}^*(\vec{\rho}') W(\vec{\rho}) W(\vec{\rho}'), \quad (2.16)$$

where $\mathcal{E} \{ \dots \}$ is the statistical expectation operator.

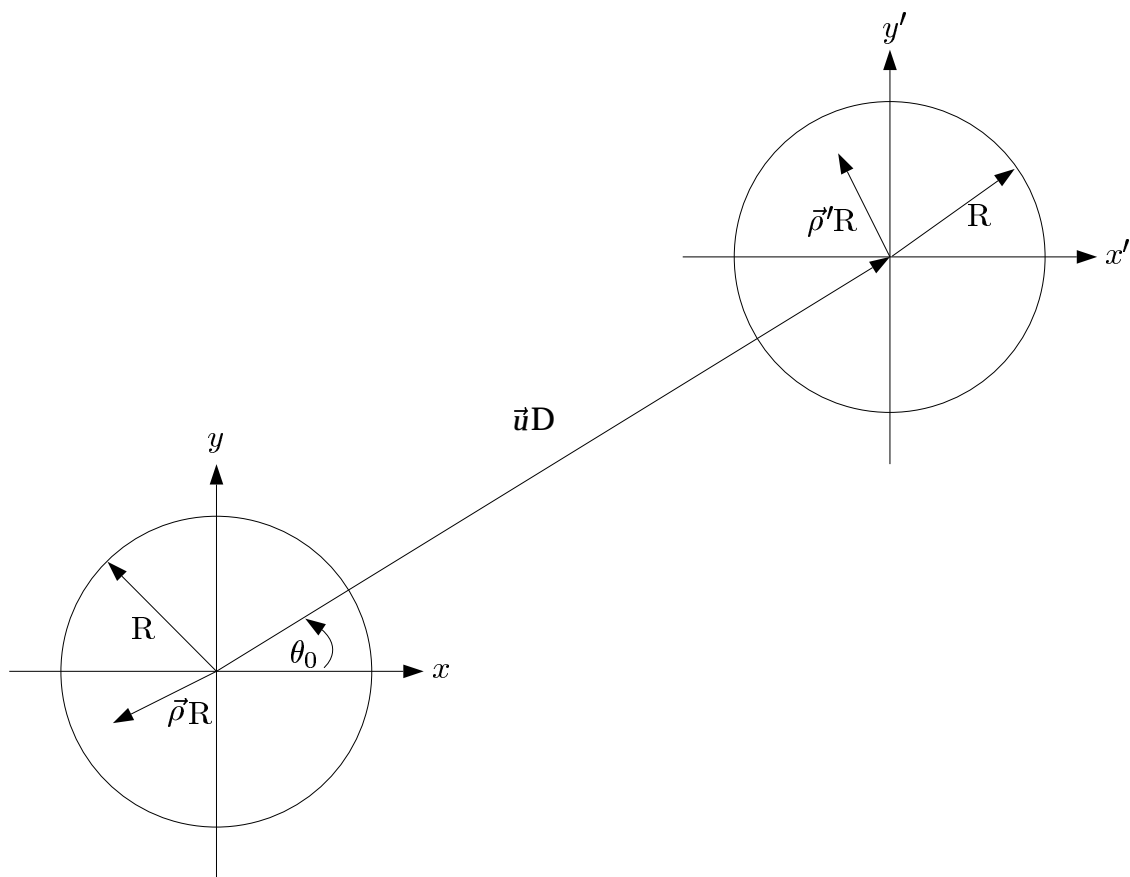


Figure 2.1 Zernike coefficient correlation calculation geometry: two circular apertures of equal radius, $R = D/2$; one is centered at the origin of the xy plane; the other is centered at the vertex of the vector $\vec{u}D$ with respect to the origin of the xy plane and is centered at the origin of the $x'y'$ plane; the magnitude of the vector \vec{u} , $|\vec{u}|$, is measured in units of diameter, D ; θ_0 is the angle between \vec{u} and the x axis.

Takato and Yamaguchi [15] present the solution of Eqn. (2.16) for a 11/3 power law phase spectral density. Applying Parseval's theorem, the Wiener-Kinchine theorem, the Fourier shift theorem, and the Fourier scaling theorem, Eqn. (2.16) transforms to

$$\mathcal{E} \{ a_j a_{j'}^* (\vec{u}) \} = \frac{1}{R^2} \int_0^\infty dk \int_0^{2\pi} d\theta \exp^{-i 2\pi 2uk \cos(\theta - \theta_0)} \Phi_\phi(k/R) Q_j(k, \theta) Q_{j'}^*(k, \theta), \quad (2.17)$$

where $Q_j(k, \theta)$ is the Fourier transform of the Zernike polynomials as given in Eqn. (2.11), and k is the wavenumber of the propagating light. The integration over θ is analytically performed to arrive at a complicated expression given in Eqn. (12) of Ref. [15].

We modify Takato and Yamaguchi's results for the arbitrary power law spectral density given in Eqn. (1.1) and absorb the index-of-refraction structure constant $C_n^2(z)$ into the convenient ρ_0 definition given in Eqn. (1.3). The integration over θ is unchanged from Takato and Yamaguchi's result; only the correct scaling factor must be determined. We find the coefficient correlation is

$$\mathcal{E} \{ a_j a_{j'}^* (\vec{u}) \} = 4c_1 \left(\frac{D}{\rho_0} \right)^{(\alpha-2)} \left[\frac{\Gamma(\frac{\alpha}{2})}{-\Gamma(\frac{2-\alpha}{2})} \right] [(n+1)(n'+1)]^{1/2} f_{jj'}(u, \theta_0, k_0), \quad (2.18)$$

where

$$\begin{aligned}
f_{jj'}(u, \theta_0, k_0) = & \\
\left\{ \begin{array}{l}
\text{if } m, n' \neq 0; j, j' \text{ are both even:} \\
+(-1)^{(n+n'-m+m')/2} \cos((m+m')\theta_0) I_{m+m', n+1, n'+1}(2u, k_0) \\
+(-1)^{(n+n'+2m+|m-m'|)/2} \cos((m-m')\theta_0) I_{|m-m'|, n+1, n'+1}(2u, k_0) \\
\\
\text{if } m, n' \neq 0; j, j' \text{ are both odd:} \\
-(-1)^{(n+n'-m+m')/2} \cos((m+m')\theta_0) I_{m+m', n+1, n'+1}(2u, k_0) \\
+(-1)^{(n+n'+2m+|m-m'|)/2} \cos((m-m')\theta_0) I_{|m-m'|, n+1, n'+1}(2u, k_0) \\
\\
\text{if } m, n' \neq 0; j \text{ even, } j' \text{ odd:} \\
(-1)^{(n+n'-m+m')/2} \sin((m+m')\theta_0) I_{m+m', n+1, n'+1}(2u, k_0) \\
-(-1)^{(n+n'+2m+|m-m'|)/2} \sin((m-m')\theta_0) I_{|m-m'|, n+1, n'+1}(2u, k_0) \\
\\
\text{if } m, n' \neq 0; j \text{ odd, } j' \text{ even:} \\
(-1)^{(n+n'-m+m')/2} \sin((m+m')(\theta_0 + \pi)) I_{m+m', n+1, n'+1}(2u, k_0) \\
-(-1)^{(n+n'+2m+|m-m'|)/2} \sin((m-m')(\theta_0 + \pi)) I_{|m-m'|, n+1, n'+1}(2u, k_0) \quad , \quad (2.19) \\
\\
\text{if } m' = 0, j \text{ even:} \\
(-1)^{(n+n'-m)/2} \sqrt{2} \cos(m\theta_0) I_{m, n+1, n'+1}(2u, k_0) \\
\\
\text{if } m = 0, j' \text{ even:} \\
(-1)^{(n+n'-m)/2} \sqrt{2} \cos(m(\theta_0 + \pi)) I_{m, n+1, n'+1}(2u, k_0) \\
\\
m' = 0, j \text{ odd:} \\
(-1)^{(n+n'-m)/2} \sqrt{2} \sin(m\theta_0) I_{m, n+1, n'+1}(2u, k_0) \\
\\
\text{if } m = 0, j' \text{ odd:} \\
(-1)^{(n+n'-m)/2} \sqrt{2} \sin(m(\theta_0 + \pi)) I_{m, n+1, n'+1}(2u, k_0) \\
\\
\text{if } m = m' = 0: \\
(-1)^{(n+n')/2} I_{0, n+1, n'+1}(2u, k_0)
\end{array} \right.
\end{aligned}$$

$$k_0 = \pi \frac{D}{L_0}, \quad (2.20)$$

$$I_{\kappa, \mu, \nu}(a, x_0) = \int_0^\infty \frac{x^{-1} J_\kappa(ax) J_\mu(x) J_\nu(x)}{(x^2 + x_0^2)^{\alpha/2}} dx, \quad (2.21)$$

and c_1 is given by Eqn. (1.2), D is the aperture diameter, L_0 is the outer scale size, u and θ_0 are as shown in Fig. 2.1, and the functions $J_\kappa(x)$, $J_\mu(x)$, $J_\nu(x)$ are Bessel functions of the first kind and order κ , μ , and ν respectively ¹.

Equation (2.18) allows the theoretical correlation of the Zernike expansion coefficients for any two modes, j and j' , to be calculated under very general conditions. The evaluation of Eqn. (2.18) is central to this thesis. Plots of Eqn. (2.18) for various parameter values are provided in Appendix A. Appendix B lists tables of Eqn. (2.18) evaluated with zero vector separation and various parameter values: $\mathcal{E} \{a_j a_{j'}\}$.

2.3 Slope Correlation Function and Slope Structure Function Evaluation

We now consider how to evaluate the self-slope correlation function, Γ_s , as defined in Eqn. (1.11) and the SSF, D_s , as defined in Eqn. (1.8). A common mathematical model for slope is given by the average gradient of wavefront phase over a subaperture,

$$s_{\hat{a}}(\vec{x}, t) = \int d\vec{r} W(\vec{r} - \vec{x}) (\nabla \phi(\vec{r}, t) \cdot \hat{a}), \quad (2.22)$$

where $s_{\hat{a}}(\vec{x}, t)$ is the wavefront phase slope at time t in the direction of the unit vector \hat{a} and for the subaperture centered at position \vec{x} , $W(\vec{r})$ limits the integration to within the subaperture and has unit area, $\phi(\vec{r}, t)$ is the wavefront phase, ∇ is the vector gradient operator, and \cdot is the vector dot product [13]. If $W(\vec{r})$ is taken as a circular weighting function, the average phase gradient, $s(\vec{x}, t)$, over the aperture centered at \vec{x} and in a particular direction is often approximated as a linear combination of the second and third modes of the Zernike decomposition for the phase [4]. This assumption is made to simplify the mathematical analysis.

Noll [8] shows that the derivatives of the Zernike polynomials can always be stated as a linear combination of Zernike polynomials. Using this fact, Primot *et. al.* [9] develop an expression for Eqn. (2.22) as a function of Zernike polynomial. Our approach starts

¹Evaluating Eqn. (2.21) is computational expensive and ultimately limits which problems can realistically be solved. Reference [15] presents a closed form solution for Eqn. (2.21), where $\bar{u} \geq 2$, consisting of infinite sums of hypergeometric functions of type ${}_4F_3$. They also state it is easier to numerically integrate Eqn. (2.21) than to use the closed form. This author has explored both approaches and agrees.

with Brummelaar's [16] expression for the average gradient of $Z_j(\rho, \theta)$ over the aperture $W(\rho)$,

$$\int d\bar{\rho} W(\rho) \frac{\partial Z_j(\rho, \theta)}{\partial X} = \begin{cases} Z_j(1, \epsilon), & m = 1 \\ 0, & m \neq 1 \end{cases}, \quad (2.23)$$

where X is an axis at an angle ϵ to the x axis such that

$$X = \rho \cos(\theta - \epsilon). \quad (2.24)$$

We begin by writing each wavefront slope as an average wavefront gradient over a sub-aperture as given by Eqn. (2.22). Thus, the self slope correlation function can be written in polar coordinates on the unit circle as,

$$\begin{aligned} \Gamma_s(\vec{x}_2 - \vec{x}_1) &= \mathcal{E} \{s(\vec{x}_1)s(\vec{x}_2)\} \\ &= \mathcal{E} \left\{ \left(\int d\bar{\rho} W(\rho) \frac{\partial \phi(R\bar{\rho})}{\partial X} \right) \left(\int d\bar{\rho}' W(\rho') \frac{\partial \phi(R(\bar{\rho}' + 2\vec{u}))}{\partial X'} \right) \right\}, \end{aligned} \quad (2.25)$$

where X and X' are as defined in Eqn. (2.24), $0 \leq \rho \leq 1$, R is the aperture radius, and

$$\vec{u} = \frac{1}{2R}(\vec{x}_2 - \vec{x}_1). \quad (2.26)$$

Applying Eqns. (2.12) and (2.13) to Eqn. (2.25), we write

$$\Gamma_s(\vec{x}_2 - \vec{x}_1) = \mathcal{E} \left\{ \left(\int d\bar{\rho} W(\rho) \frac{\partial \sum_{j=1}^{\infty} a_j Z_j(\bar{\rho})}{\partial X} \right) \left(\int d\bar{\rho}' W(\rho') \frac{\partial \sum_{j'=1}^{\infty} a_{j'}(\vec{u}) Z_{j'}(\bar{\rho}')}{\partial X'} \right) \right\}. \quad (2.27)$$

Exchanging the order of summation and integration and applying Eqn. (2.23) twice, Eqn. (2.27) is written as

$$\begin{aligned} \Gamma_s(\vec{x}_2 - \vec{x}_1) &= \mathcal{E} \left\{ \left(\sum_{j,m=1} a_j Z_j(1, \epsilon) \right) \left(\sum_{j',m'=1} a_{j'}(\vec{u}) Z_{j'}(1, \epsilon) \right) \right\} \\ &= \sum_{j,m=1} \sum_{j',m'=1} \mathcal{E} \{a_j a_{j'}(\vec{u})\} Z_j(1, \epsilon) Z_{j'}(1, \epsilon). \end{aligned} \quad (2.28)$$

As discussed in Sec. (1.3), only SSF's for slopes in the orthogonal \hat{x} and \hat{y} directions, or $\epsilon = 0$ and $\epsilon = \pi/2$ respectfully, are of interest. Numerical evaluations for $Z_j(1, 0)$ and $Z_j(1, \pi/2)$ satisfying $m = 1$ are listed in Tab. 2.3 for all $j \leq 500$. Examining the definition of Z_j given in Eqn. (2.1) or looking at Tab. 2.3, we see only terms such that j and j' are *both even* or are *both odd* contribute to the double summation within Eqn. (2.28). Simplifying Eqn. (2.18) for this special case we find

$$\mathcal{E} \left\{ a_j a_{j'}^*(\vec{u}) \right\} = 4c_1 \left(\frac{D}{\rho_0} \right)^{(\alpha-2)} \left[\frac{\Gamma(\frac{\alpha}{2})}{-\Gamma(\frac{2-\alpha}{2})} \right] [(n+1)(n'+1)]^{1/2} f_{jj'}(u, \theta_0, k_0), \quad (2.29)$$

where

$$f_{jj'}(u, \theta_0, k_0) = \begin{cases} +(-1)^{(n+n')/2} \cos(2\theta_0) I_{2,n+1,n'+1}(2u, k_0) & \text{if } j, j' \text{ are both even} \\ +(-1)^{(n+n'+2)/2} I_{0,n+1,n'+1}(2u, k_0) & \\ -(-1)^{(n+n')/2} \cos(2\theta_0) I_{2,n+1,n'+1}(2u, k_0) & \text{if } j, j' \text{ are both odd} \\ +(-1)^{(n+n'+2)/2} I_{0,n+1,n'+1}(2u, k_0) & \end{cases}, \quad (2.30)$$

with all symbols as previously defined. Since the cosine function in Eqn. (2.30) is an even function, Eqn. (2.28) has the property

$$\Gamma_s(\vec{x}_2 - \vec{x}_1) = \Gamma_s(\vec{x}_1 - \vec{x}_2). \quad (2.31)$$

Figures 2.2 through 2.9 show Γ_s evaluated for various scenarios. Mode count refers to how many contributing Zernike polynomials, as listed Tab. 2.3, are included in the summation within Eqn. (2.28). Figures 2.10 through 2.15 show examples for the theoretical SSF, Eqn. (1.9). For additional insight as to the behavior of Γ_s and D_s , consult Appendix A where the contributions to the wavefront slope for first six non-zero terms of Eqn. (2.28) are plotted.

mode count	j	m	n	$Z_j(1, 0)$	$Z_j(1, \frac{\pi}{2})$
1	2	1	1	2	0
2	3	1	1	0	2
3	7	1	3	0	$2^{\frac{3}{2}}$
4	8	1	3	$2^{\frac{3}{2}}$	0
5	16	1	5	$2\sqrt{3}$	0
6	17	1	5	0	$2\sqrt{3}$
7	29	1	7	0	4
8	30	1	7	4	0
9	46	1	9	$2\sqrt{5}$	0
10	47	1	9	0	$2\sqrt{5}$
11	67	1	11	0	$\sqrt{24}$
12	68	1	11	$\sqrt{24}$	0
13	92	1	13	$2\sqrt{7}$	0
14	93	1	13	0	$2\sqrt{7}$
15	121	1	15	0	$2^{\frac{5}{2}}$
16	122	1	15	$2^{\frac{5}{2}}$	0
17	154	1	17	6	0
18	155	1	17	0	6
19	191	1	19	0	$\sqrt{40}$
20	192	1	19	$\sqrt{40}$	0
21	232	1	21	$2\sqrt{11}$	0
22	233	1	21	0	$2\sqrt{11}$
23	277	1	23	0	$4\sqrt{3}$
24	278	1	23	$4\sqrt{3}$	0
25	326	1	25	$2\sqrt{13}$	0
26	327	1	25	0	$2\sqrt{13}$
27	379	1	27	0	$\sqrt{56}$
28	380	1	27	$\sqrt{56}$	0
29	436	1	29	$2\sqrt{15}$	0
30	437	1	29	0	$2\sqrt{15}$
31	497	1	31	0	8
32	498	1	31	8	0

Table 2.2 $Z_j(1, \epsilon)$ evaluated for the modes $j \leq 500$ with azimuthal frequency $m = 1$. Mode count is the number of contributing terms included in the evaluation of Eqn. (2.28).

Figures 2.2 through 2.9 show that the slope correlation function, Γ_s , and the slope structure function, D_s , are well represented by including the first four or six contributing terms to the average wavefront gradient. The choice between four or six terms depends on the turbulence power law and outer scale. Slope correlation, $\Gamma_s(\vec{u})$, is most often modeled as depending only on the second and third modes of the Zernike phase decomposition. Our Γ_s , Equation (2.28), does not make this assumption and includes all contributing terms. For computing Γ_s , we must limit the number of terms included in Eqn. (2.28). These figures show that the slope correlation is most dependent on the second, third, seventh, and eighth Zernike modes (a mode count of 4) and is dependent on the power law, α .

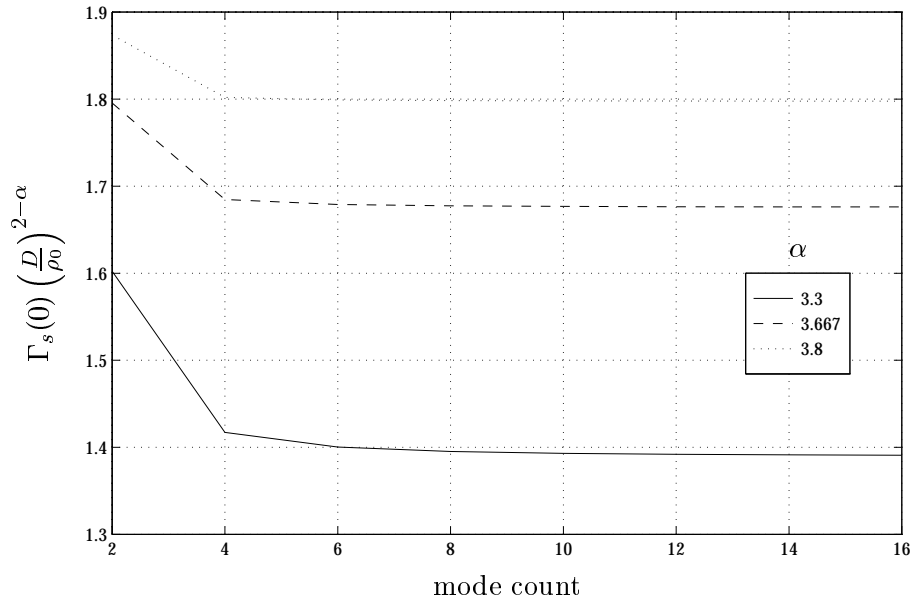


Figure 2.2 $\Gamma_s(0) \left(\frac{D}{\rho_0}\right)^{2-\alpha}$ vs. mode count for $L_0/D = \infty$ and various α .

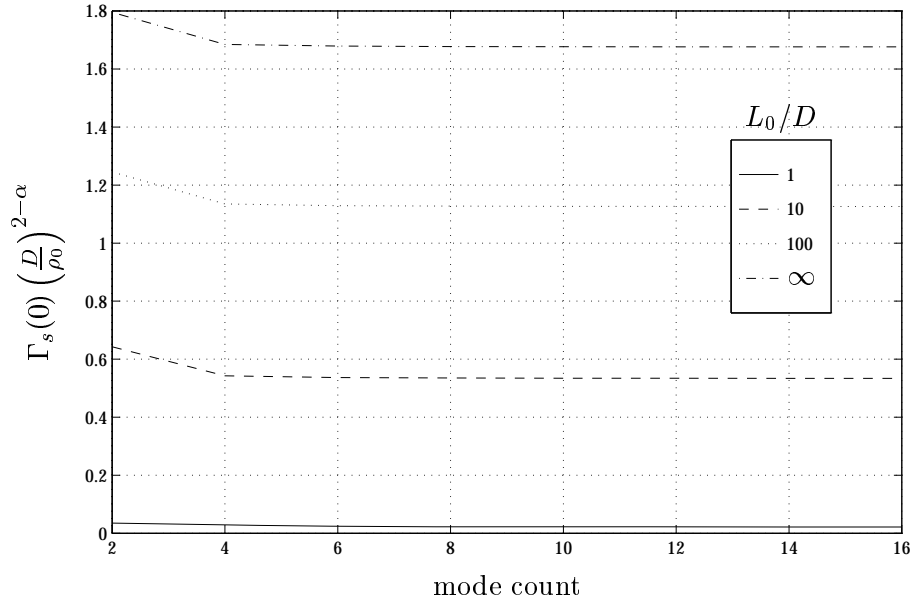


Figure 2.3 $\Gamma_s(0) \left(\frac{D}{\rho_0}\right)^{2-\alpha}$ vs. mode count for $\alpha = 11/3$ and various L_0/D .

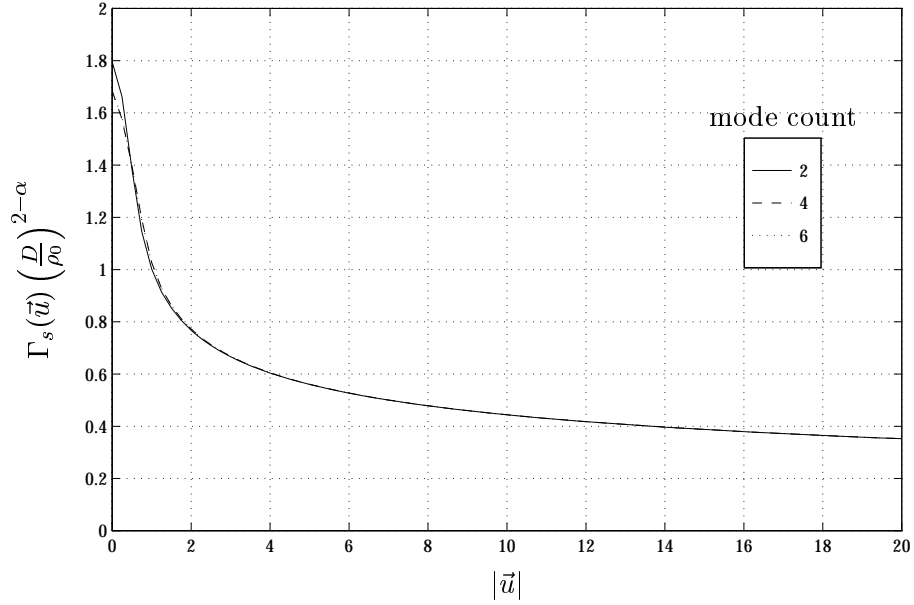


Figure 2.4 $\Gamma_s(\vec{u}) \left(\frac{D}{\rho_0}\right)^{2-\alpha}$ as a function of $|\vec{u}|$ for various mode counts, with $\alpha = 3.6667$, $\frac{L_0}{D} = \infty$, and $\theta_0 = 0$.

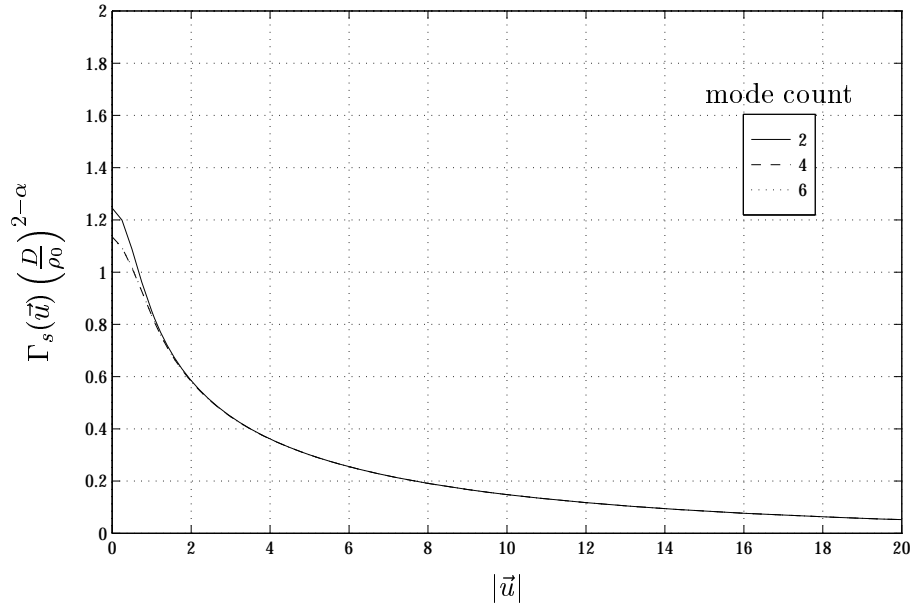


Figure 2.5 $\Gamma_s(\vec{u}) \left(\frac{D}{\rho_0}\right)^{2-\alpha}$ as a function of $|\vec{u}|$ for various mode counts, with $\alpha = 3.6667$, $\frac{L_0}{D} = 100.00$, and $\theta_0 = 0$.

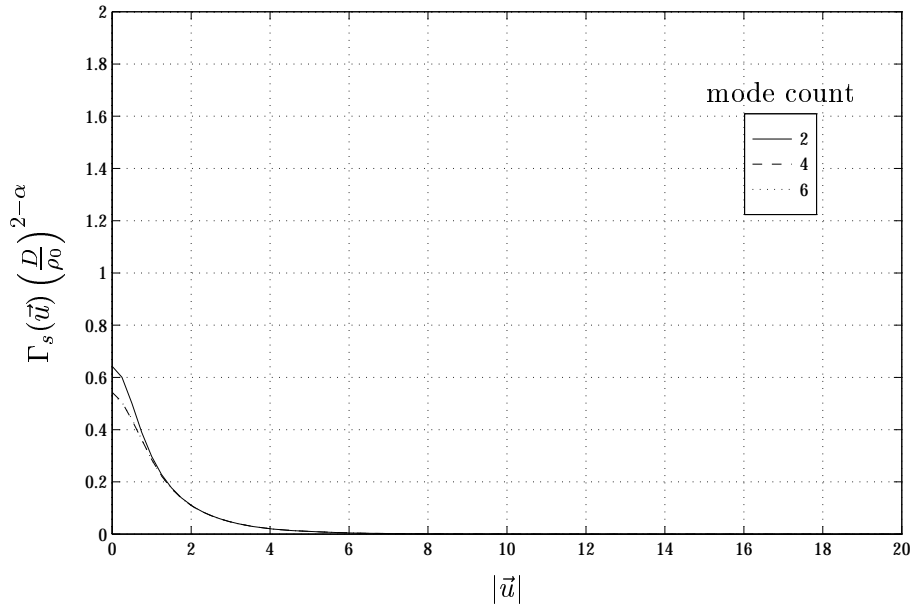


Figure 2.6 $\Gamma_s(\vec{u}) \left(\frac{D}{\rho_0}\right)^{2-\alpha}$ as a function of $|\vec{u}|$ for various mode counts, with $\alpha = 3.6667$, $\frac{L_0}{D} = 10.00$, and $\theta_0 = 0$.

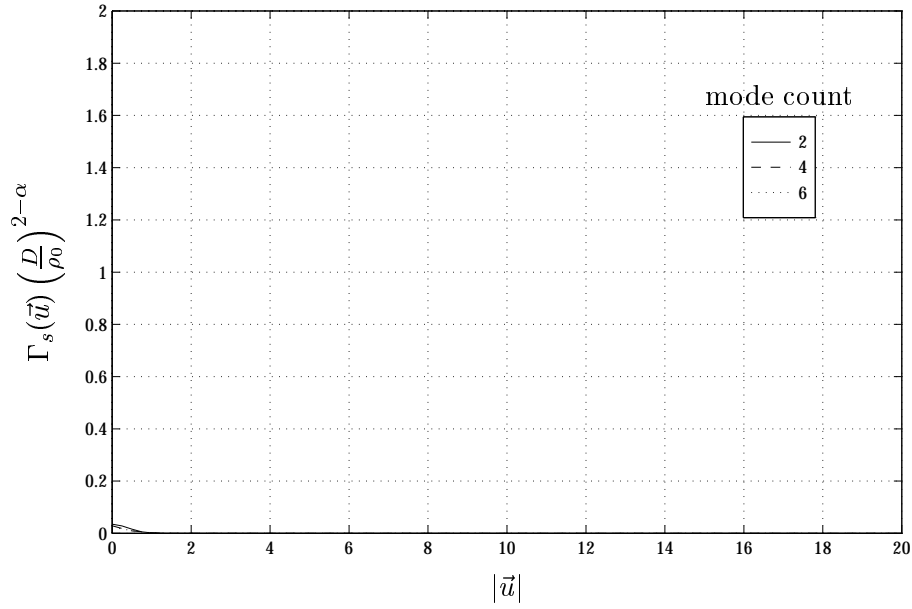


Figure 2.7 $\Gamma_s(\vec{u}) \left(\frac{D}{\rho_0}\right)^{2-\alpha}$ as a function of $|\vec{u}|$ for various mode counts, with $\alpha = 3.6667$, $\frac{L_0}{D} = 1.00$, and $\theta_0 = 0$.

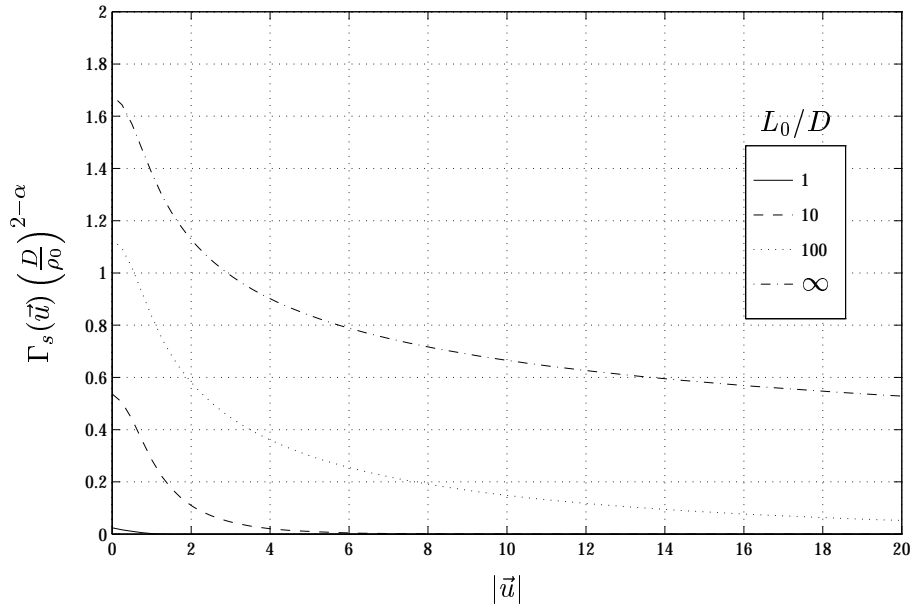


Figure 2.8 $\Gamma_s(\vec{u}) \left(\frac{D}{\rho_0}\right)^{2-\alpha}$ vs. $|u|$ for various L_0/D , with $\alpha = 3.6667$, and $\theta_0 = 0$.

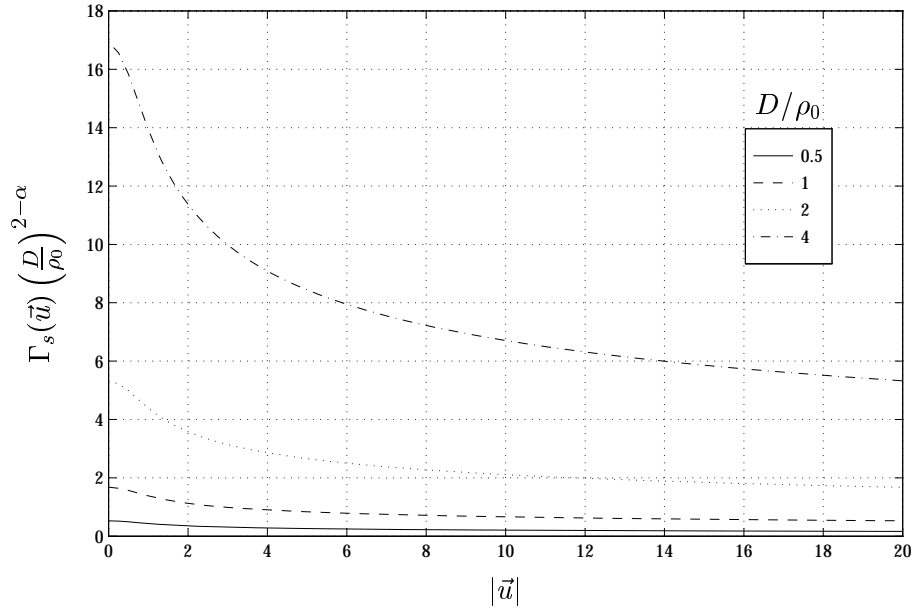


Figure 2.9 $\Gamma_s(\vec{u})$ for plane wave as a function of $|\vec{u}|$ for various $\frac{D}{\rho_0}$, with $\alpha = 3.6667$, $\frac{L_0}{D} = \infty$, and $\theta_0 = 0$.

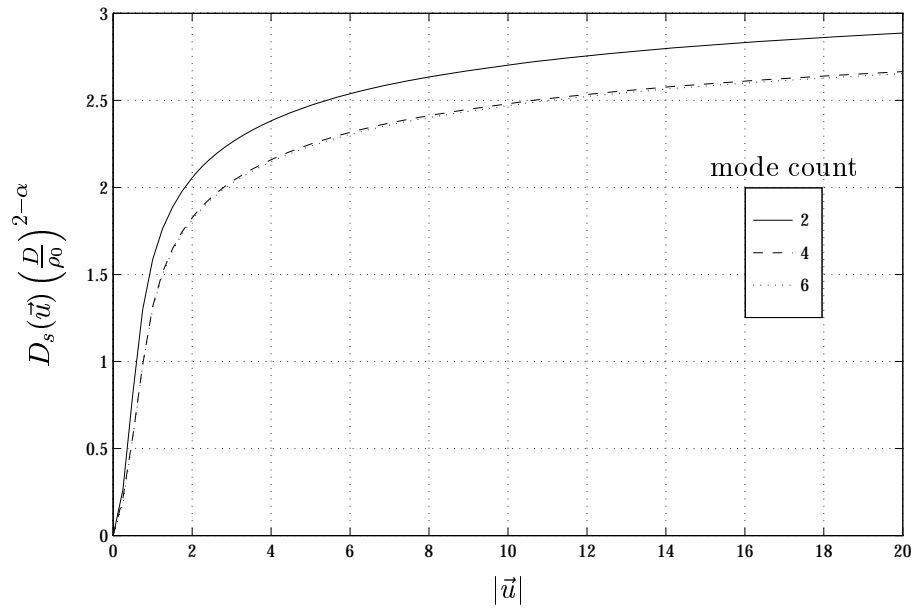


Figure 2.10 $D_s(\vec{u}) \left(\frac{D}{\rho_0}\right)^{2-\alpha}$ as a function of $|\vec{u}|$ for various mode counts, with $\alpha = 3.6667$, $\frac{L_0}{D} = \infty$, and $\theta_0 = 0$.

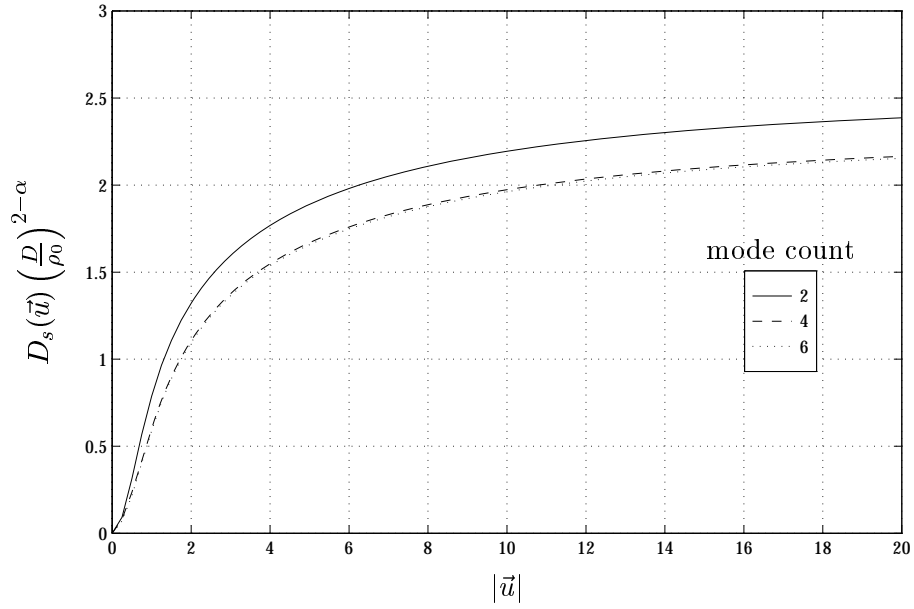


Figure 2.11 $D_s(\vec{u}) \left(\frac{D}{\rho_0}\right)^{2-\alpha}$ as a function of $|\vec{u}|$ for various mode counts, with $\alpha = 3.6667$, $\frac{L_0}{D} = 100.00$, and $\theta_0 = 0$.

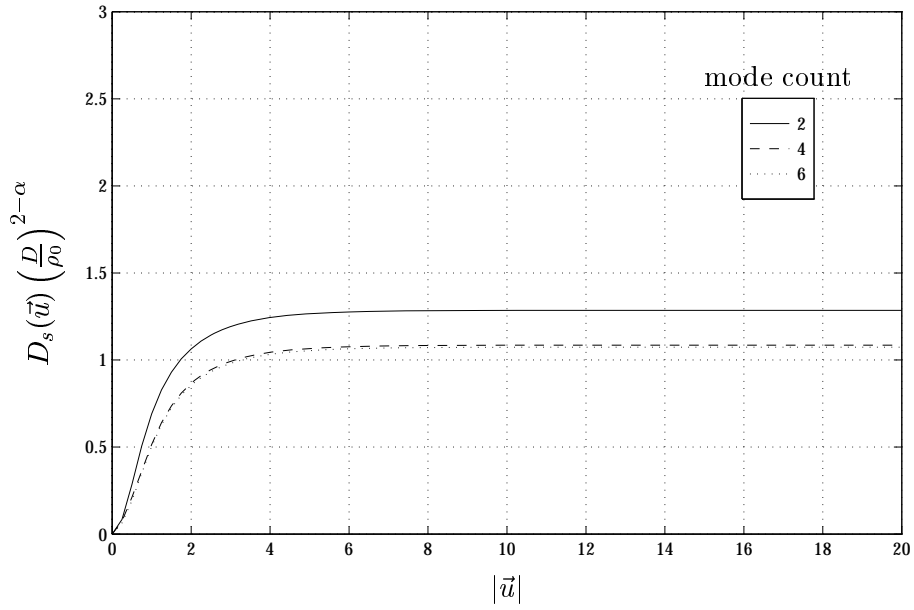


Figure 2.12 $D_s(\vec{u}) \left(\frac{D}{\rho_0}\right)^{2-\alpha}$ as a function of $|\vec{u}|$ for various mode counts, with $\alpha = 3.6667$, $\frac{L_0}{D} = 10.00$, and $\theta_0 = 0$.

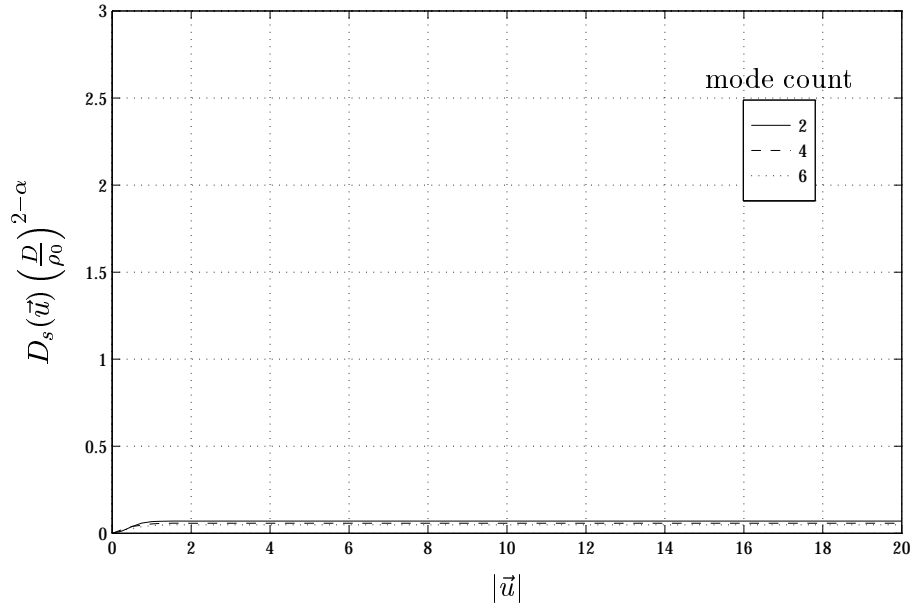


Figure 2.13 $D_s(\vec{u}) \left(\frac{D}{\rho_0}\right)^{2-\alpha}$ as a function of $|\vec{u}|$ for various mode counts, with $\alpha = 3.6667$, $\frac{L_0}{D} = 1.00$, and $\theta_0 = 0$.

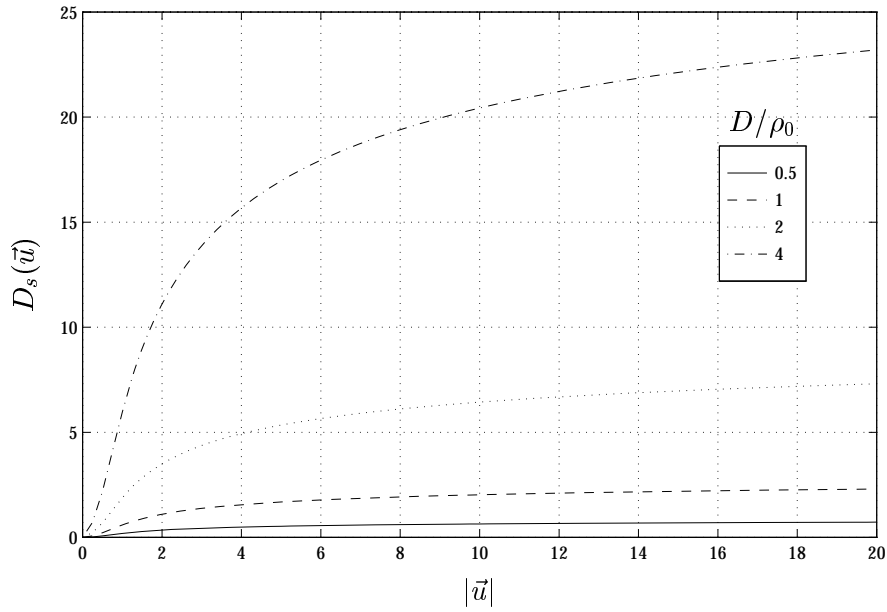


Figure 2.14 $D_s(\vec{u})$ as a function of $|\vec{u}|$ for various D/ρ_0 with $\alpha = 3.6667$, $\frac{L_0}{D} = \infty$, $\theta_0 = 0$, and mode count of 6.

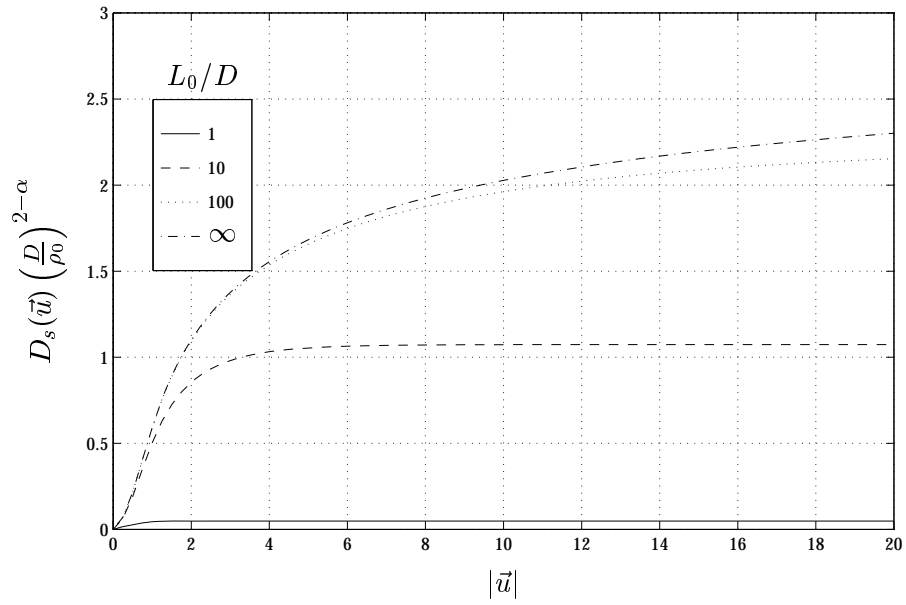


Figure 2.15 $D_s(\vec{u}) \left(\frac{D}{\rho_0}\right)^{2-\alpha}$ vs. $|u|$ for various L_0/D with $\alpha = 3.6667$, $\theta_0 = 0$, and mode count of 6.

III. SSF Estimator Signal-to-Noise Ratio

This chapter develops the SNR for the SSF estimator. First, the H-WFS geometry is presented. Then, the slope measurement model is presented. Next, the slope measurement correlation is evaluated. Then, the SNR is defined and the first and second moments of the SSF estimator are determined. Then, the final form for the SSF estimator SNR is summarized. Last, the extension to a multi-layered atmospheric model is addressed.

3.1 H-WFS Specification

Although many H-WFS's are composed of equally sized square subapertures, the Zernike polynomial approach requires equally sized circular subapertures. Thus every subaperture weighting function is defined in polar coordinates as

$$W(\vec{r}) = \begin{cases} 1/\pi & r \leq 1 \\ 0 & r > 1 \end{cases}, \quad (3.1)$$

where $r = |\vec{r}|$. In our analysis, a particular H-WFS is specified by a common subaperture diameter, D , and a list of vectors specified in rectangular coordinates whose vertices locate the subaperture centers and whose magnitudes are measured in units of diameter. For example, the H-WFS shown in Fig. 1.1 (b) is specified by

i	$\vec{x}_i(\frac{x}{D}, \frac{y}{D})$	i	$\vec{x}_i(\frac{x}{D}, \frac{y}{D})$
1	(0,0)	9	(0,2)
2	(1,0)	10	(1,2)
3	(2,0)	11	(2,2)
4	(3,0)	12	(3,2)
5	(0,1)	13	(0,3)
6	(1,1)	14	(1,3)
7	(2,1)	15	(2,3)
8	(3,1)	16	(3,3)

and some subaperture diameter D . The coordinate system origin is arbitrary.

3.2 Slope Measurement Model

The measured wavefront slope, $\hat{s}_a(\vec{p}, t)$, is modeled as a sum of the true wavefront slope, $s_a(\vec{p}, t)$, and an additive noise term, $n(\vec{p}, t)$, each a function of position and time,

$$\hat{s}_a(\vec{p}, t) = s_a(\vec{p}, t) + n(\vec{p}, t). \quad (3.2)$$

The true wavefront slope is taken as the average wavefront gradient over the subaperture and is defined in Eqn. (2.22). Both the wavefront slope and the additive noise are modeled as zero mean, Gaussian, wide-sense stationary random processes. Additionally, the following properties are assumed:

- Noise in one subaperture is uncorrelated to that in any other subaperture.
- Noise in different temporal frames is uncorrelated.
- Noise variance, σ_n^2 , within all subapertures is the same.
- Noise is uncorrelated with the true wavefront slope.

3.3 Slope Measurement Correlation

The correlation between slope measurements taken at different times, in different subapertures, is defined as

$$\mathcal{E} \{ \hat{s}(\vec{p}, t_1) \hat{s}(\vec{q}, t_2) \}. \quad (3.3)$$

Taylor's frozen flow hypothesis allows Eqn. (3.3) to be written as a function of $\vec{q} - \vec{p} + \vec{v}(t_2 - t_1)$ where \vec{v} is the velocity vector for the turbulent layer. Substituting Eqn. (3.2) into Eqn. (3.3), applying the wavefront slope and noise assumptions listed above, and assuming isotropic turbulence, Eqn. (3.3) may be expanded as

$$\begin{aligned} & \mathcal{E} \{ \hat{s}(\vec{p}, t_1) \hat{s}(\vec{q}, t_2) \} \\ &= \mathcal{E} \{ [s(\vec{p}, t_1) + n(\vec{p}, t_1)] [s(\vec{q}, t_2) + n(\vec{q}, t_2)] \} \\ &= \mathcal{E} \{ s(\vec{p}, t_1) s(\vec{q}, t_2) \} + \mathcal{E} \{ s(\vec{p}, t_1) n(\vec{q}, t_2) \} + \\ & \quad \mathcal{E} \{ s(\vec{q}, t_2) n(\vec{p}, t_1) \} + \mathcal{E} \{ n(\vec{p}, t_1) n(\vec{q}, t_2) \} \end{aligned}$$

$$= \begin{cases} \Gamma_s(0) + \sigma_n^2 & , \vec{p} = \vec{q} \text{ and } t_1 = t_2 \\ \Gamma_s(\vec{q} - \vec{p} + \vec{v}(t_2 - t_1)) & , \text{otherwise} \end{cases} \quad (3.4)$$

where Γ_s is the self slope correlation function defined in Eqn. (1.11).

3.4 SSF Estimate SNR Definition

The SSF estimator of Eqn. (1.12) is a random function depending on the statistics of atmospheric turbulence, the number of measurement realizations, and the geometry of the H-WFS. The SNR of the random function $\hat{D}_s(\vec{\rho})$ is defined as the unbiased mean divided by the standard deviation,

$$SNR(\hat{D}_s(\vec{\rho})) = \frac{\mathcal{E}\{\hat{D}_s(\vec{\rho})\} - \text{bias}}{\left[\mathcal{E}\left\{\left(\hat{D}_s(\vec{\rho})\right)^2\right\} - \mathcal{E}\left\{\hat{D}_s(\vec{\rho})\right\}^2\right]^{1/2}}. \quad (3.5)$$

Thus, the first and second moments of $\hat{D}_s(\vec{\rho})$ must be computed.

3.5 First Moment of the SSF Estimator

The first moment of Eqn. (1.12) is

$$\begin{aligned} \mathcal{E}\{\hat{D}_s(\vec{\rho})\} &= \mathcal{E}\left\{\frac{1}{NM} \sum_{m=1}^M \sum_{n=1}^N [\hat{s}(\vec{q}, t_n) - \hat{s}(\vec{p}, t_n)]^2\right\} \\ &= \frac{1}{NM} \sum_{m=1}^M \sum_{n=1}^N \mathcal{E}\left\{[\hat{s}(\vec{q}, t_n) - \hat{s}(\vec{p}, t_n)]^2\right\} \\ &= \frac{1}{NM} \sum_{m=1}^M \sum_{n=1}^N \mathcal{E}\left\{[(s(\vec{q}, t_n) + n(\vec{q}, t_n)) - (s(\vec{p}, t_n) + n(\vec{p}, t_n))]^2\right\} \end{aligned} \quad (3.6)$$

where all variables are as defined in Sec. (1.3). Expanding the power within the expectation operator and using the slope and noise assumptions listed in Sec. (3.2) we find

$$\begin{aligned} \mathcal{E}\{\hat{D}_s(\vec{\rho})\} &= \frac{1}{NM} \sum_{m=1}^M \sum_{n=1}^N \left[2\sigma_n^2 + 2\Gamma_s(\vec{0}) - 2\Gamma_s(\vec{q} - \vec{p})\right] \\ &= 2\sigma_n^2 + 2\Gamma_s(\vec{0}) - 2\Gamma_s(\vec{\rho}). \end{aligned} \quad (3.7)$$

Comparing the mean of the SSF estimator, Eqn. (3.7), with the SSF, Eqn. (1.9), we see our estimator is biased by $2\sigma_n^2$. It is this bias which is subtracted in the numerator of Eqn. (3.5).

3.6 Second Moment of SSF Estimator

The second moment calculation unfortunately is not as simple as the first moment calculation. We begin with the definition of the second moment,

$$\mathcal{E} \left\{ \left[\hat{D}_s(\vec{\rho}) \right]^2 \right\} = \mathcal{E} \left\{ \left[\frac{1}{NM} \sum_{m=1}^M \sum_{n=1}^N [\hat{s}(\vec{q}, t_n) - \hat{s}(\vec{p}, t_n)]^2 \right]^2 \right\}. \quad (3.8)$$

We then use the identity

$$\left(\sum_{a=1}^A \sum_{b=1}^B f(a, b) \right)^2 = \sum_{a=1}^A \sum_{b=1}^B \sum_{c=1}^C \sum_{d=1}^D f(a, b) f(c, d) \quad (3.9)$$

to rewrite Eqn. (3.8) as

$$\begin{aligned} \mathcal{E} \left\{ \left[\hat{D}_s(\vec{\rho}) \right]^2 \right\} = \\ \mathcal{E} \left\{ \frac{1}{(NM)^2} \sum_{m=1}^M \sum_{n=1}^N \sum_{\mu=1}^M \sum_{\nu=1}^N [\hat{s}(\vec{q}_m, t_n) - \hat{s}(\vec{p}_m, t_n)]^2 [\hat{s}(\vec{q}_\mu, t_\nu) - \hat{s}(\vec{p}_\mu, t_\nu)]^2 \right\}. \end{aligned} \quad (3.10)$$

Exchanging order of summation and expectation, we can write

$$\mathcal{E} \left\{ \left[\hat{D}_s(\vec{\rho}) \right]^2 \right\} = \frac{1}{(NM)^2} \sum_{n=1}^N \sum_{\nu=1}^N \sum_{m=1}^M \sum_{\mu=1}^M \mathcal{E} \left\{ [\hat{s}(\vec{q}_m, t_n) - \hat{s}(\vec{p}_m, t_n)]^2 [\hat{s}(\vec{q}_\mu, t_\nu) - \hat{s}(\vec{p}_\mu, t_\nu)]^2 \right\}. \quad (3.11)$$

3.6.1 Expectation Simplification. Simplifying the expectation within Eqn. (3.11) is a tedious task. Using Taylor's frozen flow hypothesis of Sec. (1.2), the time dependence in Eqn. (3.11) is rewritten as a spatial dependence only. In making this notation change, we adopt a simpler notation and label the four unique time-position vectors of Eqn. (3.11)

in terms of the four unique position vectors,

$$\begin{aligned}
\vec{x}_1 &= \vec{p}_m + \vec{v}t_n \\
\vec{x}_2 &= \vec{q}_m + \vec{v}t_n \\
\vec{x}_3 &= \vec{p}_\mu + \vec{v}t_\nu \\
\vec{x}_4 &= \vec{q}_\mu + \vec{v}t_\nu
\end{aligned} \tag{3.12}$$

This geometry is shown in Fig. 3.1. The subapertures centered at \vec{x}_1 and \vec{x}_2 form a *subaperture pair*, as do the subapertures centered at \vec{x}_3 and \vec{x}_4 . These two pairs are referred to as a *set* of subaperture pairs. Figure 3.2 shows different arrangements for sets of subaperture pairs that must be considered in the following development.

We write the expectation within Eqn. (3.11) as

$$\mathcal{E} \left\{ [\hat{s}(\vec{x}_2) - \hat{s}(\vec{x}_1)]^2 [\hat{s}(\vec{x}_4) - \hat{s}(\vec{x}_3)]^2 \right\}. \tag{3.13}$$

Using our slope measurement model, we write Eqn. (3.13) as

$$\mathcal{E} \left\{ [(s(\vec{x}_2) + n(\vec{x}_2)) - (s(\vec{x}_1) + n(\vec{x}_1))]^2 [(s(\vec{x}_4) + n(\vec{x}_4)) - (s(\vec{x}_3) + n(\vec{x}_3))]^2 \right\}. \tag{3.14}$$

Multiplying out Eqn. (3.14) we obtain a sum of 100 fourth-order joint moments. For jointly Gaussian random variables, joint moments of order higher than two can always be expressed in terms of first and second order moments [5:39]. In particular, it can be shown for the zero-mean Gaussian random variables, u_1 , u_2 , u_3 , and u_4 , that

$$\mathcal{E} \{u_1 u_2 u_3 u_4\} = \mathcal{E} \{u_1 u_2\} \mathcal{E} \{u_3 u_4\} + \mathcal{E} \{u_1 u_3\} \mathcal{E} \{u_2 u_4\} + \mathcal{E} \{u_1 u_4\} \mathcal{E} \{u_2 u_3\}. \tag{3.15}$$

We can thus further simplify the 100 fourth-order joint moments into a 300 term summation with each term a product of two second-order moments. Each of these second order moments can be expressed in terms of the slope correlation function, Γ_s , and the noise variance, σ_n^2 , as shown in Sec. (3.3). Special attention must be given to properly account for each of the time-position cases shown in Fig. 3.2. This process is difficult to perform reliably

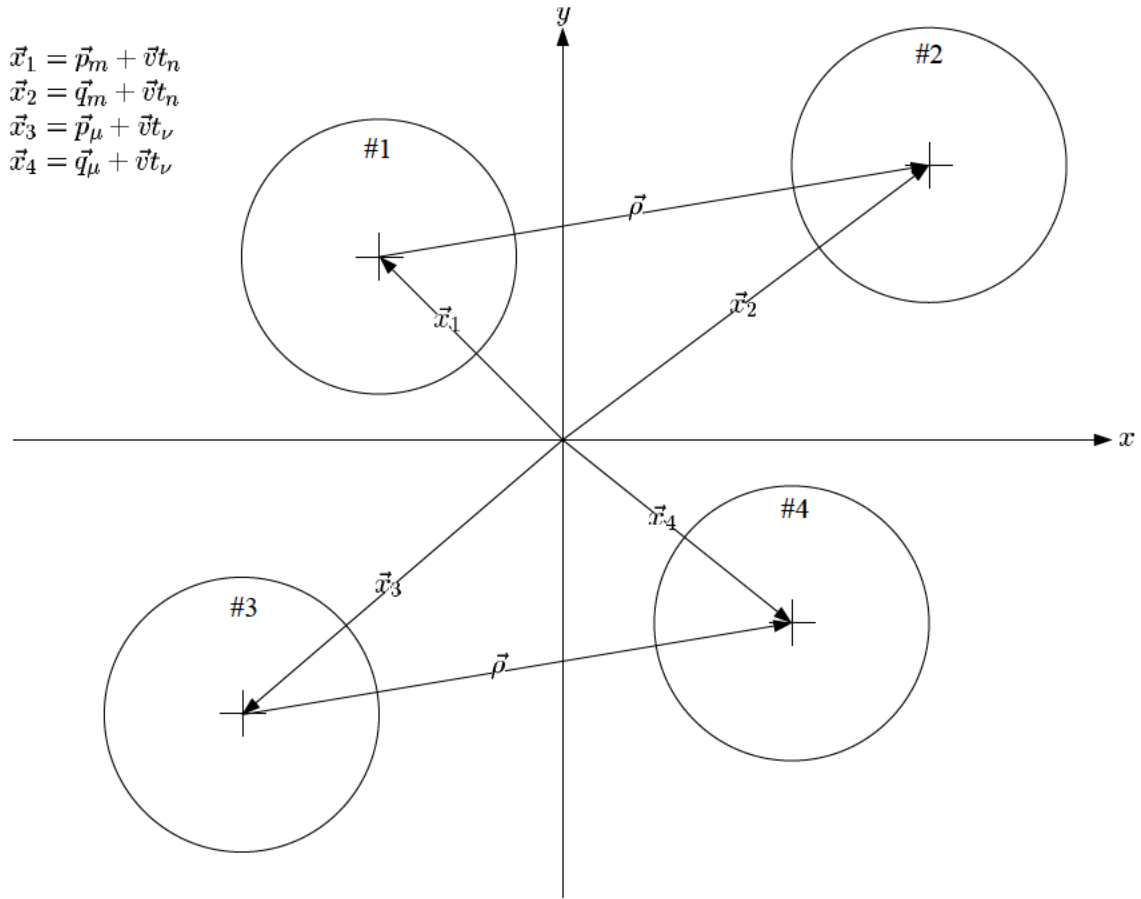


Figure 3.1 Geometry used in calculating second moment of SSF estimator: Application of Taylor's frozen flow hypothesis reduces the mixed temporal-spatial correlation of Eqn. (3.11) to spatial correlations only. The vector $\vec{\rho}$ is the separation for which the SSF is estimated. The subaperture centers are located by the vectors \vec{x}_1 , \vec{x}_2 , \vec{x}_3 , and \vec{x}_4 in the xy plane. Subapertures #1 and #2 form a pair whose vector separation is always $\vec{\rho}$ as do the pair #3 and #4. Each pair can be located anywhere in the xy plane. The two pairs are referred to as a set of subaperture pairs.

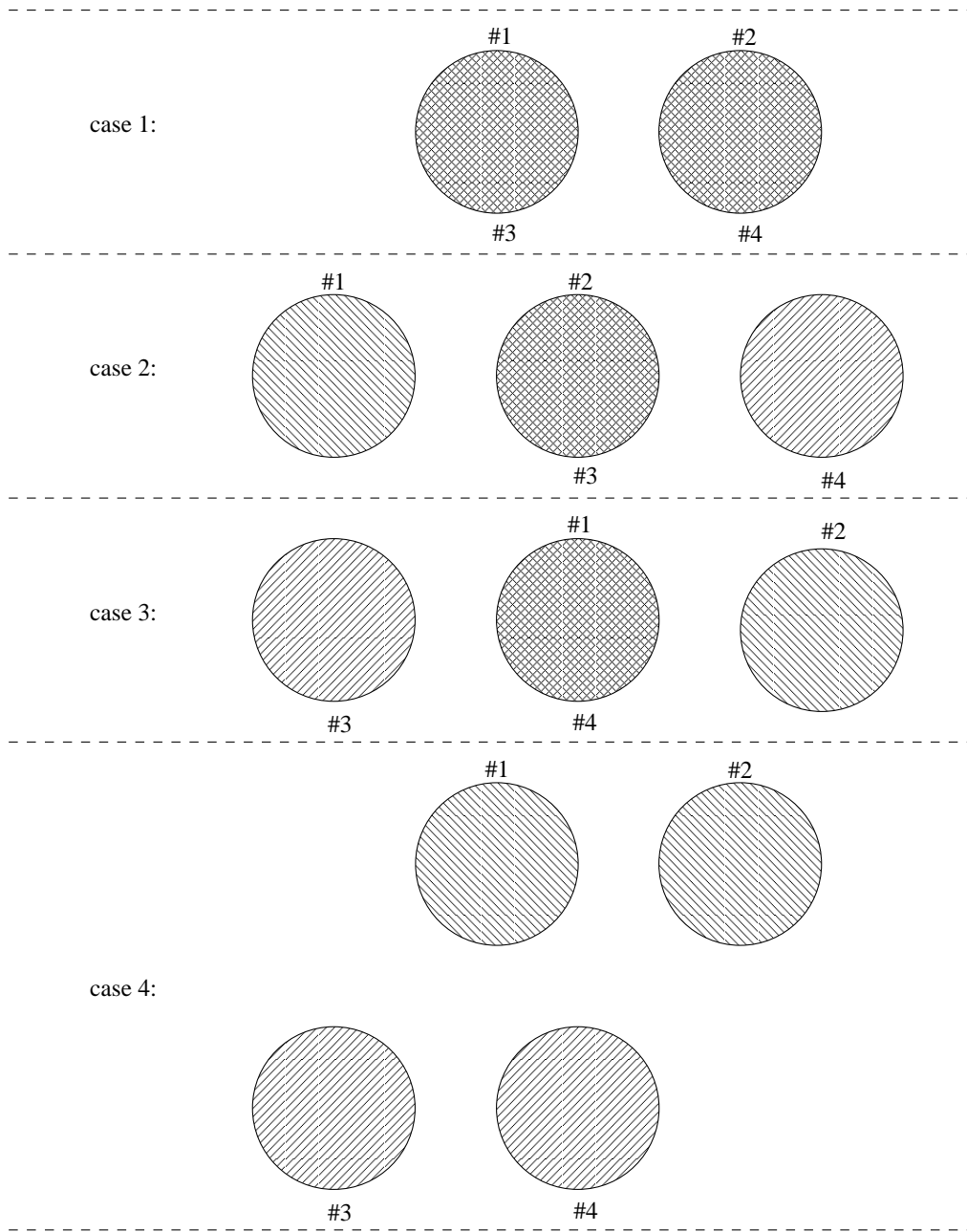


Figure 3.2 Four cases within SSF estimator second moment calculation: The subapertures are numbered one to four as in Fig. 3.1. Case 1 is when the set of subaperture pairs is located at the same position at the same time. Case 1 occurs in every H-WFS configuration. Case 2 and 3 are when two subapertures in the set of subaperture pairs share a common location at the same time. Case 2 or 3 occur only in H-WFS configurations with more than two subapertures. Case 4 is when neither set of subaperture pairs share a common location or when the time difference between the set of subaperture pairs is not zero. Case 4 occurs in all H-WFS configurations.

by hand, but the computer program Mathematica [23] is perfectly suited. Appendix C lists the Mathematica program used to express Eqn. (3.14) in terms of Γ_s and σ_n^2 .

Using Mathematica's results and further requiring that

$$\vec{v}(t_\nu - t_n) = \vec{v}\tau(\nu - n), \quad (3.16)$$

where τ is the time between temporally adjacent samples, and ν and n are integers, the expectation within Eqn. (3.11) can be written as

$$\mathcal{E} \left\{ [\hat{s}(\vec{q}_m, t_n) - \hat{s}(\vec{p}_m, t_n)]^2 [\hat{s}(\vec{q}_\mu, t_\nu) - \hat{s}(\vec{p}_\mu, t_\nu)]^2 \right\} = F_{sm}(\vec{\rho}, \sigma_n, \vec{v}\tau(\nu - n), \vec{p}_m, \vec{q}_m, \vec{p}_\mu, \vec{q}_\mu) \quad (3.17)$$

where

$$\begin{aligned}
F_{sm}(\vec{\rho}, \sigma_n, \vec{v}\tau(\nu - n), \vec{p}_m, \vec{q}_m, \vec{p}_\mu, \vec{q}_\mu) = & \\
\left\{ \begin{array}{l}
12\sigma_n^4 + 24\sigma_n^2\Gamma_s(0) + 12\Gamma_s^2(0) - 24\sigma_n^2\Gamma_s(\vec{\rho}) \\
- 24\Gamma_s(0)\Gamma_s(\vec{\rho}) + 12\Gamma_s^2(\vec{\rho}) \\
6\sigma_n^4 + 12\sigma_n^2\Gamma_s(0) + 6\Gamma_s^2(0) - 16\sigma_n^2\Gamma_s(\vec{\rho}) \\
- 16\Gamma_s(0)\Gamma_s(\vec{\rho}) + 12\Gamma_s^2(\vec{\rho}) + 4\sigma_n^2\Gamma_s(2\vec{\rho}) \\
+ 4\Gamma_s(0)\Gamma_s(2\vec{\rho}) - 8\Gamma_s(\rho)\Gamma_s(2\vec{\rho}) \\
+ 2\Gamma_s^2(2\vec{\rho}) \\
4\sigma_n^4 + 8\sigma_n^2\Gamma_s(0) + 4\Gamma_s^2(0) - 8\sigma_n^2\Gamma_s(\vec{\rho}) \\
- 8\Gamma_s(0)\Gamma_s(\vec{\rho}) + 4\Gamma_s^2(\vec{\rho}) + 8\Gamma_s^2(\vec{p}_\mu - \vec{p}_m + \vec{v}\tau(\nu - n)) \\
- 8\Gamma_s(\vec{p}_\mu - \vec{p}_m + \vec{v}\tau(\nu - n))\Gamma_s(\vec{p}_\mu - \vec{q}_m + \vec{v}\tau(\nu - n)) \\
+ 2\Gamma_s^2(\vec{p}_\mu - \vec{q}_m + \vec{v}\tau(\nu - n)) \\
- 8\Gamma_s(\vec{p}_\mu - \vec{p}_m + \vec{v}\tau(\nu - n))\Gamma_s(\vec{q}_\mu - \vec{p}_m + \vec{v}\tau(\nu - n)) \\
+ 4\Gamma_s(\vec{p}_\mu - \vec{q}_m + \vec{v}\tau(\nu - n))\Gamma_s(\vec{q}_\mu - \vec{p}_m + \vec{v}\tau(\nu - n)) \\
+ 2\Gamma_s^2(\vec{q}_\mu - \vec{p}_m + \vec{v}\tau(\nu - n))
\end{array} \right. \quad \begin{array}{l}
\text{case 1:} \\
\text{if } \vec{p}_m = \vec{p}_\mu \\
\text{and } \vec{q}_m = \vec{q}_\mu; \\
\nu - n = 0 \\
\\
\text{cases 2 and 3:} \\
\text{if } \vec{q}_m = \vec{p}_\mu \\
\text{or } \vec{q}_\mu = \vec{p}_m; \\
\nu - n = 0 \\
\\
\text{case 4:} \\
\text{otherwise}
\end{array} \quad . \quad (3.18)
\end{aligned}$$

3.6.2 Four Dimensional Summation Simplification. Evaluating the four dimensional summation in Eqn. (3.11) presents a serious computational problem. Here, we show that the four dimensional summation may be replaced by a two dimensional summation.

Since the double summation in Eqn. (3.11) with respect to time depends only on the difference $\nu - n$, the equality

$$\sum_{a=1}^N \sum_{b=1}^N f(a-b) = N \sum_{c=-N}^N \left(1 - \frac{|c|}{N}\right) f(c) \quad (3.19)$$

can be used [19]. A triangular weighting function properly accounts for the repetition of terms through the range of index differences. Additionally, if $f(a-b) = f(b-a)$, Eqn. (3.19) can be further reduced to

$$\sum_{a=1}^N \sum_{b=1}^N f(a-b) = (2 - \delta_{0,c})N \sum_{c=0}^N \left(1 - \frac{|c|}{N}\right) f(c), \quad (3.20)$$

where

$$\delta_{0,c} = \begin{cases} 1 & \text{if } c = 0 \\ 0 & \text{otherwise} \end{cases} . \quad (3.21)$$

It is shown in Eqn. (2.31) that the slope correlation function, Γ_s , has this property and therefore so does Eqn. (3.18).

The double summation with respect to subaperture pairs, indexes m and μ , also simplifies to a one dimensional summation. Unfortunately, the new index range and weighting function are not as simple as the time index range and weighting function in Eqn. (3.20).

The two dimensional arrangement of H-WFS subapertures must be considered in combination with the particular vector separation, $\vec{\rho}$, for which the SSF estimate is to be calculated. Figure 3.1 shows the geometry for a single evaluation of Eqn. (3.11) for a particular set of indexed values. For a fixed time index difference, only the relative orientation of the pair \vec{x}_1 and \vec{x}_2 to the pair \vec{x}_3 and \vec{x}_4 effect the expectation. Any other *set of subaperture pairs* with the same relative orientation will give the same numerical answer for Eqn. (3.14). We write the final form of the second-moment of the SSF estimator as

$$\mathcal{E} \left\{ \left[\hat{D}_s(\vec{\rho}) \right]^2 \right\} = \frac{1}{NM^2} \sum_{i=0}^N (2 - \delta_{0,i}) \left(1 - \frac{|i|}{N} \right) \sum_{j=1}^{M_r} w(j) F_{sm}(\vec{\rho}, \sigma_n, \vec{v}\tau i, \vec{p}_m^{(j)}, \vec{q}_m^{(j)}, \vec{p}_\mu^{(j)}, \vec{q}_\mu^{(j)}), \quad (3.22)$$

where the function F_{sm} is given in Eqn. (3.18) and $w(j)$ is a weighting function depending on H-WFS geometry. Let M_r represent the number of uniquely oriented sets of subaperture pairs (characterized by a subaperture pair separation of $\vec{\rho}$) with $M_r \leq M^2$. The summation over sets of subaperture pairs is indexed by j . Each j maps to $w(j)$ identically oriented sets of subaperture pairs. Any one of these $w(j)$ sets may be the source for the vectors $\vec{p}_\mu^{(j)}$, $\vec{p}_m^{(j)}$, $\vec{q}_\mu^{(j)}$, and $\vec{q}_m^{(j)}$. The summation over time is indexed by i . Additionally, it is required that

$$\sum_{j=1}^{M_r} w(j) = M^2. \quad (3.23)$$

Figure 3.3 illustrates how the spatial two dimensional summation over m and μ in Eqn. (3.11) can be replaced by a one dimensional summation over j as in Eqn. (3.22).

Figure 3.3 considers the simple H-WFS composed of an evenly spaced 2 by 3 grid of subapertures. As the number of sensor subapertures increase, the complexity of identifying like-oriented sets of pairs increase. This complicated process is best left to the software which evaluates the SNR for a particular H-WFS. Table 3.1 shows how this problem scales for larger H-WFS arrays.

Without this modification from a four dimensional summation to a two dimensional summation, computing the SNR for a large H-WFS array quickly becomes computationally improbable using available resources.

3.7 Final SSF Estimator SNR Expression

All expressions necessary to evaluate the SSF estimator SNR have now been developed. The SNR, defined in Eqn. (3.5), is in terms of the first and second moments of the SSF estimator, Eqns. (3.7) and (3.22). Both of these moments are in terms of the slope correlation function, Γ_s , which is evaluated using Eqn. (2.28). The SNR is independent of ρ_0 but does depend on L_0/D , α , the number of frames, N , and the H-WFS geometry.

3.8 Extension to a Multi-layer Atmospheric Model

Equation (1.12) is valid regardless of the atmospheric model. If the multi-layered atmospheric model of Sec. (1.2) is considered, our previous results can be modified.

Assuming near field conditions [11:72], optical phase is additive. Thus the total induced phase seen by the estimator, $\phi_{tot}(\vec{r}, t)$, is the sum of the phase induced by the Q individual layers,

$$\phi_{tot}(\vec{r}, t) = \sum_{l=1}^Q \phi_l(\vec{r}, t), \quad (3.24)$$

where $\phi_l(\vec{r}, t)$ is the phase induced by layer l . Using Eqn. (2.22), the average gradient for wavefront slope over a subaperture is

$$\begin{aligned} s_{\hat{a}_{tot}}(\vec{x}, t) &= \int d\vec{r} W(\vec{r} - \vec{x}) (\Delta \phi_{tot}(\vec{r}, t) \cdot \hat{a}) \\ &= \int d\vec{r} W(\vec{r} - \vec{x}) \left(\Delta \left(\sum_{l=1}^Q \phi_l(\vec{r}, t) \right) \cdot \hat{a} \right) \end{aligned}$$

Sensor	M	M^2	M_r
1×1	0	0	0
2×2	2	4	3
3×3	6	36	15
4×4	12	144	35
5×5	20	400	63
6×6	30	900	99
7×7	42	1764	143
8×8	56	3136	195
9×9	72	5184	255
10×10	90	8100	323
11×11	110	12100	399
12×12	132	17424	483
13×13	156	24336	575
14×14	182	33124	675
15×15	210	44100	783
16×16	240	57600	899
17×17	272	73984	1023
18×18	306	93636	1155
19×19	342	116964	1295
20×20	380	144400	1443
21×21	420	176400	1599
22×22	462	213444	1763
23×23	506	256036	1935
24×24	592	304704	2115
25×25	600	360000	2303
26×26	650	422500	2499

Table 3.1 Computational savings realized by identifying like-oriented sets of subaperture pairs: Sensor column specifies the H-WFS arrangement. For example, 10×10 refers to a H-WFS with 100 subapertures arranged in a 10×10 grid with adjacent subapertures spaced center-to-center one diameter D apart. The SSF estimate is to be computed for the vector separation $\vec{\rho} = (D, 0)$. There are M pair of subapertures in the sensor having vector separation $\vec{\rho}$. There are M^2 sets of subaperture pairs to consider if like-oriented sets of subaperture pairs is not exploited. There are only M_r unique sets of subaperture pairs within each sensor for the chosen $\vec{\rho}$. Each unique set, indexed by j in Eqn. (3.22), occur $w(j)$ (not shown) times in the sensor.

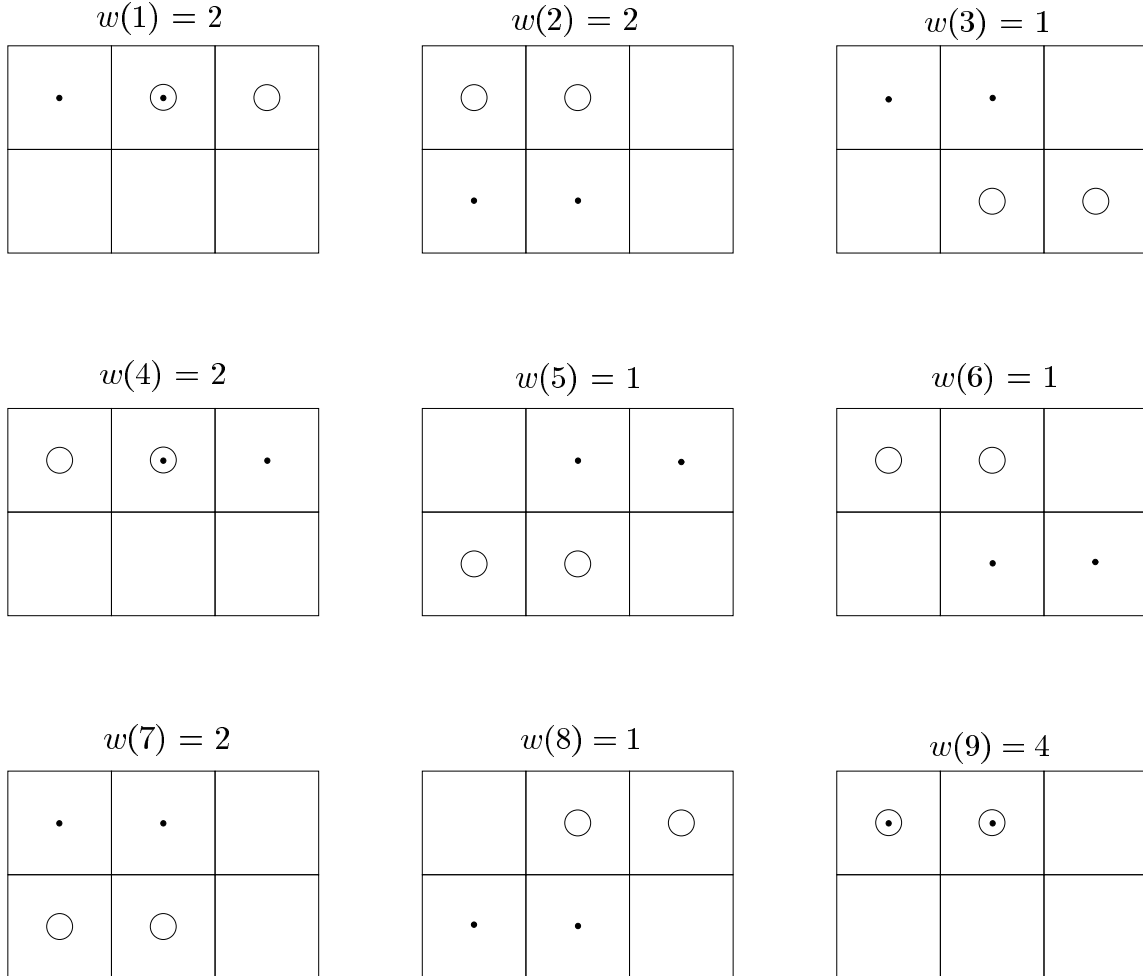


Figure 3.3 Duplication of $F_{sm}(\vec{\rho}, \sigma_n, \vec{\nu}\tau i, \vec{p}_m^{(j)}, \vec{q}_m^{(j)}, \vec{p}_\mu^{(j)}, \vec{q}_\mu^{(j)})$ for a 2 by 3 H-WFS: Assuming $\vec{\rho} = (D, 0^\circ)$ in Eqn. (3.11), the two dots represent a pair of subapertures indexed by n , and the two circle represent a pair of subapertures indexed by ν . We desire to reduce the two dimensional summation to a one dimensional summation by exploiting only the relative orientation of the set of subaperture pairs influence the evaluation of Eqn. (3.18). There are $M_r = 9$ unique sets of subaperture pairs out of the total sixteen sets of subaperture pairs. Each of these unique nine sets are shown above with the proper value for the weighting function, $w(j)$.

$$\begin{aligned}
&= \sum_{l=1}^Q \int d\vec{r} W(\vec{r} - \vec{x}) (\Delta\phi_l(\vec{r}, t) \cdot \hat{a}) \\
&= \sum_{l=1}^Q s_{\hat{a}_l}(\vec{x}, t).
\end{aligned} \tag{3.25}$$

Thus the total slope, $s_{\hat{a}_{tot}}$, is simply the sum of slopes for individual layers. Our multi-layered atmospheric model assumes independent layers, and thus so are the slopes for the individual layers. Since we model a single layer's slope as a zero-mean Gaussian random variable, so must be our total slope [5:39]. Because of this, the derived form for the SSF estimator SNR is unchanged when considering a multi-layered atmosphere. Only the form for the slope correlation function, Γ_s , must be modified.

We define a multi-layered slope correlation function, $\Gamma_{s_{tot}}$, as

$$\Gamma_{s_{tot}}(\vec{x}_2 - \vec{x}_1) = \mathcal{E} \{s_{tot}(\vec{x}_1) s_{tot}(\vec{x}_2)\}. \tag{3.26}$$

Equation (3.26) can be simplified as

$$\begin{aligned}
\Gamma_{s_{tot}}(\vec{x}_2 - \vec{x}_1) &= \mathcal{E} \{s_{tot}(\vec{x}_1) s_{tot}(\vec{x}_2)\} \\
&= \mathcal{E} \left\{ \sum_{l=1}^Q s_{\hat{a}_l}(\vec{x}_1) \sum_{l'=1}^Q s_{\hat{a}_{l'}}(\vec{x}_2) \right\} \\
&= \sum_{l=1}^Q \sum_{l'=1}^Q \mathcal{E} \{s_{\hat{a}_l}(\vec{x}_1) s_{\hat{a}_{l'}}(\vec{x}_2)\} \\
&= \sum_{l=1}^Q \mathcal{E} \{s_{\hat{a}_l}(\vec{x}_1) s_{\hat{a}_l}(\vec{x}_2)\} \\
&= \sum_{l=1}^Q \Gamma_{s_l}(\vec{x}_2 - \vec{x}_1),
\end{aligned} \tag{3.27}$$

where we have used the independence of turbulent layers as noted in Sec. (1.2), and where Γ_{s_l} is the self slope structure function for the l layer.

IV. SSF Estimator SNR Numerical Results

This chapter presents results for the SSF estimator SNR developed in Chapter III. The SNR equation is complex and difficult to intuitively understand. In addition, the SNR equation is non-trivial to implement and is computationally intensive to numerically evaluate. Representative results for the simplest H-WFS configuration, the DIMM, are presented and discussed. Additional DIMM results are included in Appendix D. For more complex H-WFS configurations, only how the SSF estimator SNR changes as the number of H-WFS subapertures increase is presented and discussed.

4.1 SSF Estimator SNR Numerical Results for the DIMM Geometry

A DIMM has two subapertures. Thus, a SSF estimate can be attained at only a single vector separation, $\vec{\rho}$. Within a single frame, wavefront slope measurements are correlated as a function of both the outer scale and the power law. To increase the SSF estimator SNR, multiple temporally spaced frames are included in the SSF estimate. If we assume that temporally spaced frames are uncorrelated, the SNR increases as the \sqrt{N} , where N is the number of frames [9, 19, 24]. But the wavefront slope measurements in different frames are correlated. This temporal correlation is a function of the turbulent layer's velocity and the time between frames. In addition, the noise inherent to the measurement process tends to decrease the SNR.

Figures 4.1 through 4.9 show representative SSF estimator SNR results for the DIMM geometry. As noted in the figure captions, these figures are selected from the five groups of results presented in Appendix D and summarized in Tab. D.1. The theoretical SSF estimator SNR predicted if temporal frames are assumed independent, an increase as the \sqrt{N} , is the thick solid top line shown in the figures. This \sqrt{N} line is always well above the other SNR curves and thus does not obscure the SSF estimator SNR predictions when temporal correlations are incorporated. All results are presented as SSF estimator SNR vs. the number of integration frames, N , included in the estimate. The wavefront slope is taken along the axis co-linear to the vector connecting the centers of the two DIMM subapertures.

Figures 4.1 through Fig. 4.3 show the theoretical SNR for a DIMM with subapertures separated by one diameter. Each plot shows the SNR for ratios of outer scale to subaperture diameter, L_0/D , ranging between one and infinity. The three plots assume different turbulence layer motion velocity magnitudes, $|\vec{v}\tau|$. As the outer scale decreases, the correlations between the temporal frames also decreases and tend to increase the SNR. But outer scale appears to have a rather weak effect on the SNR results. As the turbulence layer velocity increases, the correlations between temporal frames decrease and tend to increase the SNR. For a velocity magnitude of $2.50D$, outer scale has no effect on the SNR results for this DIMM geometry. Figures D.1 through D.24 include plots for other turbulence layer velocity magnitudes and with non-zero noise.

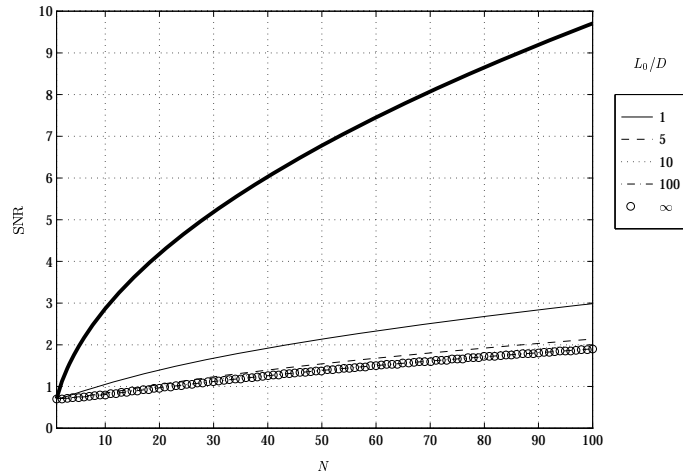


Figure 4.1 Slope structure function estimator SNR vs. number of integration frames, N , for the DIMM geometry with a subaperture separation of $\vec{\rho} = (1.00D, 0.00^\circ)$, a turbulence power law of $\alpha = 3.6667$, a turbulence layer motion velocity $\vec{v}\tau = (0.10D, 90.00^\circ)$, and a ratio of the slope measurement noise variance to the wavefront slope variance $\sigma_n^2/\Gamma_s(0) = 0\%$. The ratio L_0/D ranges from 1 to ∞ . The top solid line is the theoretical SNR predicted if temporal frames are assumed independent. (Same data as in Fig. D.1, Group A.)

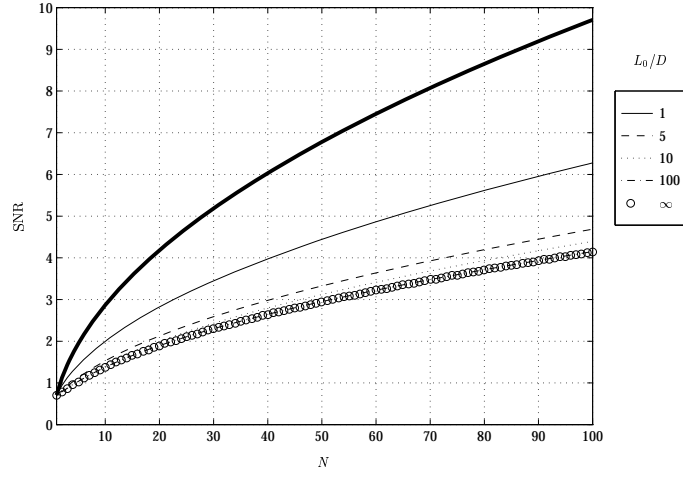


Figure 4.2 Slope structure function estimator SNR vs. number of integration frames, N , for the DIMM geometry with a subaperture separation of $\vec{\rho} = (1.00D, 0.00^\circ)$, a turbulence power law of $\alpha = 3.6667$, a turbulence layer motion velocity $\vec{v}\tau = (0.50D, 90.00^\circ)$, and a ratio of the slope measurement noise variance to the wavefront slope variance $\sigma_n^2/\Gamma_s(0) = 0\%$. The ratio L_0/D ranges from 1 to ∞ . The top solid line is the theoretical SNR predicted if temporal frames are assumed independent. (Same data as in Fig. D.3, Group A.)

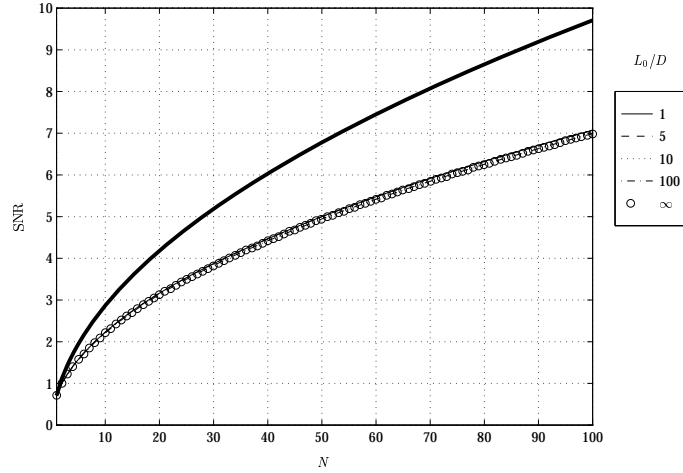


Figure 4.3 Slope structure function estimator SNR vs. number of integration frames, N , for the DIMM geometry with a subaperture separation of $\vec{\rho} = (1.00D, 0.00^\circ)$, a turbulence power law of $\alpha = 3.6667$, a turbulence layer motion velocity $\vec{v}\tau = (2.50D, 90.00^\circ)$, and a ratio of the slope measurement noise variance to the wavefront slope variance $\sigma_n^2/\Gamma_s(0) = 0\%$. The ratio L_0/D ranges from 1 to ∞ . The top solid line is the theoretical SNR predicted if temporal frames are assumed independent. (Same data as in Fig. D.4, Group A.)

Figures 4.4 through Fig. 4.6 assume identical turbulence properties as in Fig. 4.1 through Fig. 4.3 but is for a DIMM with subapertures separated by four diameters. This larger subaperture separation causes turbulence slope measurements within a frame to be less correlated since wavefront slope correlation decreases as separation increases (as shown in Sec. (2.3)). Hence, the SNR for identical turbulence conditions increase as the subaperture separation increases. Figures D.25 through D.48 include plots for other turbulence layer velocity magnitudes and with non-zero noise.

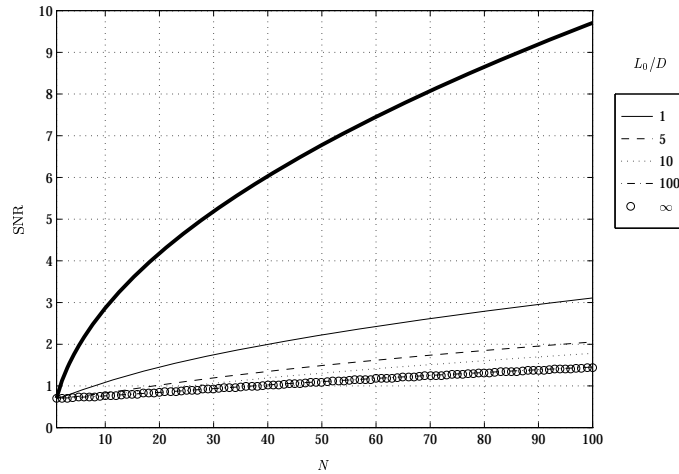


Figure 4.4 Slope structure function estimator SNR vs. number of integration frames, N , for the DIMM geometry with a subaperture separation of $\vec{\rho} = (4.00D, 0.00^\circ)$, a turbulence power law of $\alpha = 3.6667$, a turbulence layer motion velocity $\vec{v}\tau = (0.10D, 90.00^\circ)$, and a ratio of the slope measurement noise variance to the wavefront slope variance $\sigma_n^2/\Gamma_s(0) = 0\%$. The ratio L_0/D ranges from 1 to ∞ . The top solid line is the theoretical SNR predicted if temporal frames are assumed independent. (Same data as in Fig. D.25, Group B.)

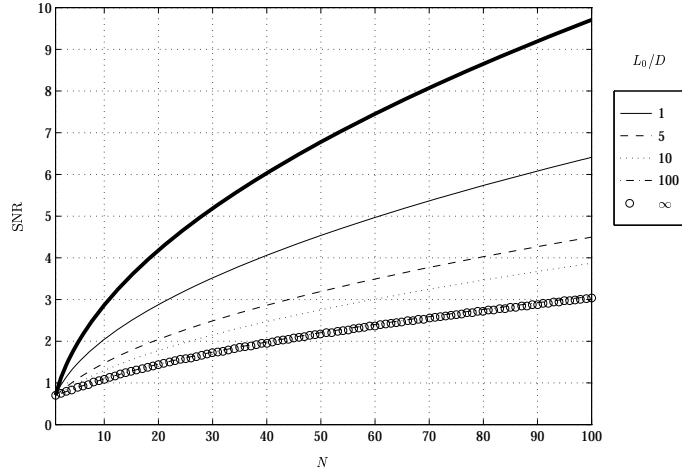


Figure 4.5 Slope structure function estimator SNR vs. number of integration frames, N , for the DIMM geometry with a subaperture separation of $\vec{\rho} = (4.00D, 0.00^\circ)$, a turbulence power law of $\alpha = 3.6667$, a turbulence layer motion velocity $\vec{v}\tau = (0.50D, 90.00^\circ)$, and a ratio of the slope measurement noise variance to the wavefront slope variance $\sigma_n^2/\Gamma_s(0) = 0\%$. The ratio L_0/D ranges from 1 to ∞ . The top solid line is the theoretical SNR predicted if temporal frames are assumed independent. (Same data as in Fig. D.26, Group B.)

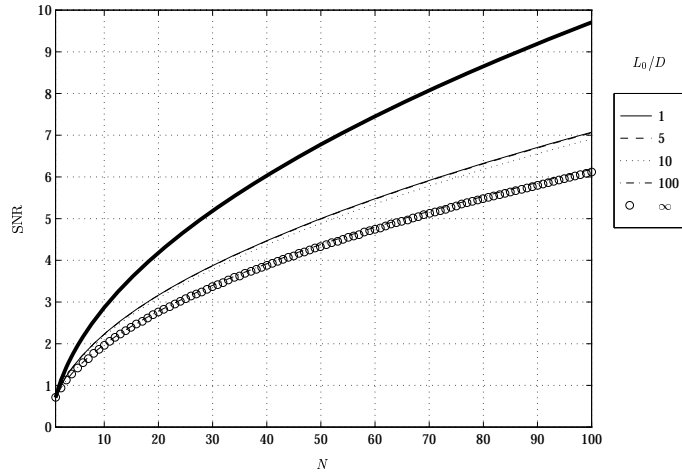


Figure 4.6 Slope structure function estimator SNR vs. number of integration frames, N , for the DIMM geometry with a subaperture separation of $\vec{\rho} = (4.00D, 0.00^\circ)$, a turbulence power law of $\alpha = 3.6667$, a turbulence layer motion velocity $\vec{v}\tau = (2.50D, 90.00^\circ)$, and a ratio of the slope measurement noise variance to the wavefront slope variance $\sigma_n^2/\Gamma_s(0) = 0\%$. The ratio L_0/D ranges from 1 to ∞ . The top solid line is the theoretical SNR predicted if temporal frames are assumed independent. (Same data as in Fig. D.28, Group B.)

Figure 4.7 shows how additive slope measurement noise decreases SNR. Noise is expressed as a ratio of the slope measurement noise variance to the wavefront slope variance $\sigma_n^2/\Gamma_s(0)$. As the noise increases, the SNR decreases. Figures D.49 through D.78 include plots for other turbulence layer velocity magnitudes and outer scales.

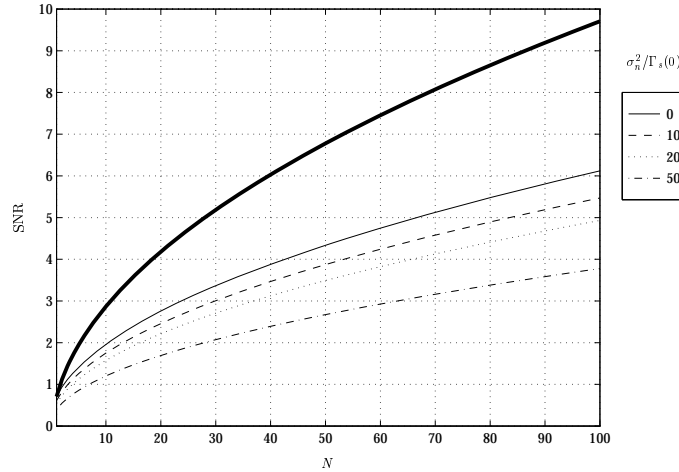


Figure 4.7 Slope structure function estimator SNR vs. number of integration frames, N , for the DIMM geometry with a subaperture separation of $\vec{\rho} = (4.00D, 0.00^\circ)$, a turbulence power law of $\alpha = 3.6667$, a turbulence layer motion velocity $\vec{v}\tau = (2.50D, 90.00^\circ)$, and a ratio $L_0/D = \infty$. The ratio of the slope measurement noise variance to the wavefront slope variance, $\sigma_n^2/\Gamma_s(0)$, varies from 0% to 50%. The top solid line is the theoretical SNR for zero noise, a \sqrt{N} increase, predicted if temporal frames are assumed independent. (Same data as in Fig. D.76, Group C.)

Figure 4.8 shows how turbulence layer velocity magnitude affects the the SNR. As the velocity magnitude increase, the temporal slope correlation between frames decrease and results in an increase in SNR. Figures D.79 through D.98 include similar plots for different outer scale and noise conditions.

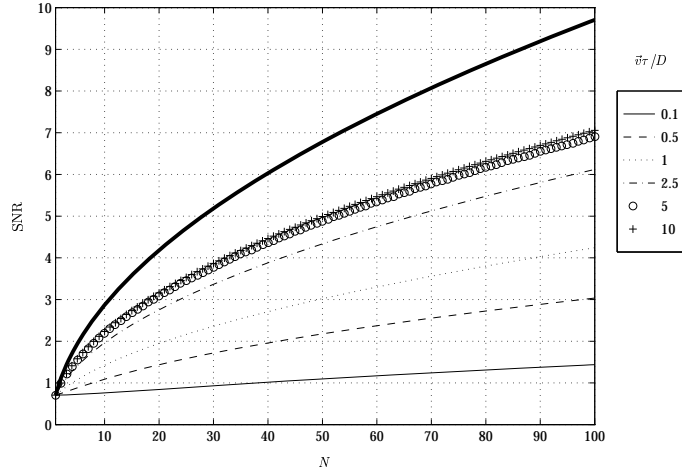


Figure 4.8 Slope structure function estimator SNR vs. number of integration frames, N , for the DIMM geometry with a subaperture separation of $\vec{\rho} = (4.00D, 0.00^\circ)$, a turbulence power law of $\alpha = 3.6667$, a turbulence layer motion velocity angle $\arg(\vec{v}) = 90.00^\circ$, a ratio $L_0/D = \infty$, and a ratio of the slope measurement noise variance to the wavefront slope variance $\sigma_n^2/\Gamma_s(0) = 0\%$. The magnitude of the turbulence layer motion velocity varies from $0.1D$ to $10D$. The top solid line is the theoretical SNR, a \sqrt{N} increase, predicted if temporal frames are assumed independent. (Same data as in Fig. D.95, Group D.)

Figure 4.9 demonstrates the effect of turbulence layer velocity direction with respect to the direction of a vector connecting the DIMM subaperture centers. As noted above, all slopes are taken in the direction of a vector connecting the DIMM subaperture centers. Equation (2.31) shows the slope correlation is symmetric with respect to this subaperture center-to-center vector. In the 0° case, the layer velocity direction is co-linear to a subaperture center-to-center vector. In the 90° case, the layer velocity direction is perpendicular to a subaperture center-to-center vector. The effect of turbulence layer velocity direction on the SNR is small. Figures D.99 through D.118 include similar plots for different outer scale and turbulence layer velocity magnitudes.

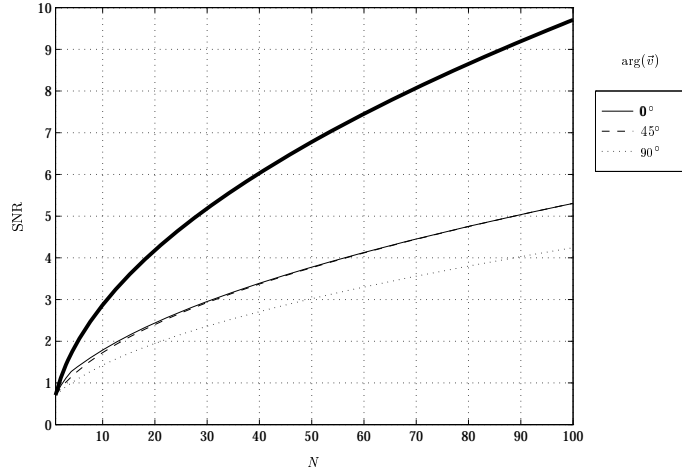


Figure 4.9 Slope structure function estimator SNR vs. number of integration frames, N , for the DIMM geometry with a subaperture separation of $\vec{\rho} = (4.00D, 0.00^\circ)$, a turbulence power law of $\alpha = 3.6667$, a turbulence layer motion velocity magnitude $|\vec{v}| = 1.00D$, a ratio $L_0/D = \infty$, and a ratio of the slope measurement noise variance to the wavefront slope variance $\sigma_n^2/\Gamma_s(0) = 0\%$. The angle of the turbulence layer motion velocity, $\arg(\vec{v})$, is 0, 45, or 90 degrees. The top solid line is the theoretical SNR, a \sqrt{N} increase, predicted if temporal frames are assumed independent. (Same as Fig. D.111, Group E.)

4.2 SSF Estimator SNR Numerical Results for non-DIMM Geometry

With non-DIMM arrays, SSF estimates for multiple vector separations are measured. Many SSF estimates at each $\vec{\rho}$ may be present within a single frame. Due to the difficulty in evaluating the SNR expression for large arrays over multiple frames, only single frame results are presented. The goal is to show how the SNR varies with the number of H-WFS subapertures. Figure 4.10 and Fig. 4.11 are different views of the same results. Figure 4.10 shows that a single frame SNR is a near-linear function of the number of subapertures on a single side of a square array of H-WFS subapertures.

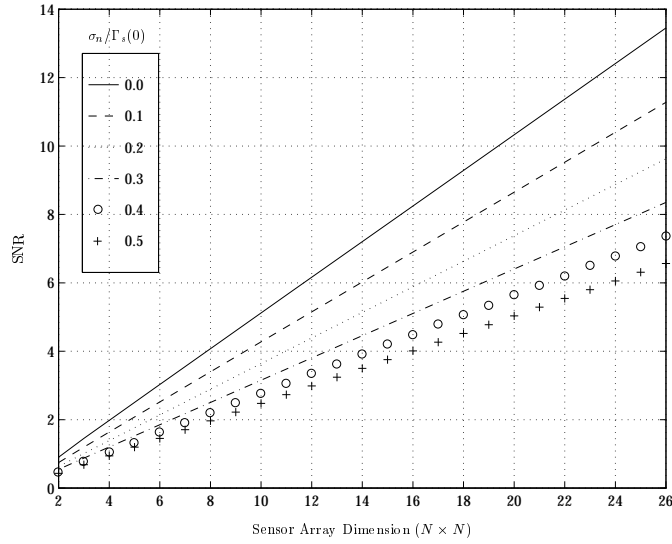


Figure 4.10 Slope structure function estimator SNR vs. sensor subaperture array size for a single temporal frame. The ratio $\sigma_n^2/\Gamma_s(0)$ ranges from 0% to 50%. The estimate is for a single frame of wavefront sensor measurements and at a vector separation $\vec{\rho} = (D, 0)$. The turbulence has an $\alpha = 11/3$ power law and outer scale $L_0/D = \infty$. The horizontal axis denotes the number subapertures on a side for a square H-WFS array whose subapertures are spaced one diameter center-to-center. For example, 26 denotes a 26×26 H-WFS array. A linear relationship is observed between the number of subapertures on a side in the H-WFS array and the SSF estimator SNR.

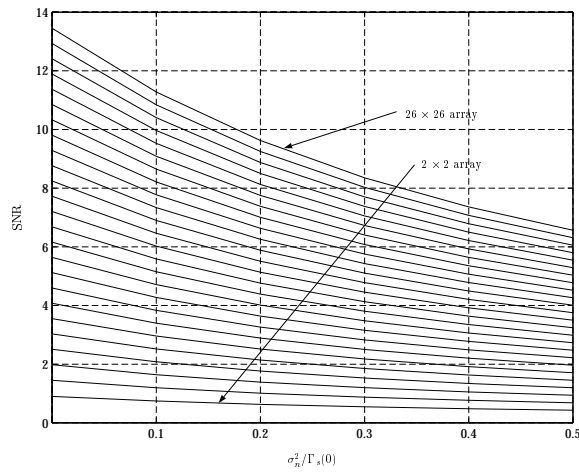


Figure 4.11 Slope structure function estimator SNR vs. the ratio $\sigma_n^2/\Gamma_s(0)$ for a single temporal frame. The estimate is for a single frame of wavefront sensor measurements and a vector separation $\vec{\rho} = (D, 0)$. The turbulence has an $\alpha = 11/3$ power law and outer scale $L_0/D = \infty$. Sensor subaperture arrays range from a 2×2 with the lowest SNR to a 26×26 with the highest SNR.

V. Results, Conclusions and Recommendations

This chapter summarizes the major results of this research and recommends related future research.

5.1 Summary of Theoretical Development

In Chapter II, the slope correlation function Γ_s , Eqn. (2.28), was developed based on a Zernike polynomial decomposition of phase over two circular apertures with arbitrary vector separation. Often, the wavefront average gradient is approximated by the second and third modes of the Zernike decomposition [4]. Equation (2.28) does not make this assumption and includes the effect of high order modes on wavefront average gradient. Figure 2.2 shows how $\Gamma_s(0)$ changes based on the number of modes included for various turbulence power laws. With this Γ_s expression, the theoretical slope structure function D_s , Eqn. (1.8), is calculated and presented in Figs. 2.10 through 2.15.

In Chapter III, the SNR of the SSF estimator is developed. For the SSF estimator defined in Eqn. (1.12), the first and second moment are calculated. The first moment is shown in Eqn. (3.7) and the second moment is shown in Eqn. (3.22). The SSF estimator is biased in the presence of noise by $2\sigma_n^2$. The SSF estimator SNR, defined in Eqn. (3.5), is formed with the resulting first and second moment expressions and depends on the H-WFS geometry, the number of frames included in the estimate, the outer scale of turbulence, and the power law of turbulence. The SNR expression does not depend on the atmospheric coherence diameter, ρ_0 .

5.2 Summary of Numerical Results

Selected numerical SSF estimator SNR results are presented in Chapter IV. Results focus on the simplest H-WFS geometry, the DIMM, with limited results presented for non-DIMM geometries. This is necessary due to the difficulty of numerically evaluating the SNR expression for non-DIMM geometries. The SSF estimator SNR is seen to be lower than that predicted if temporal frames are assumed uncorrelated. The single frame SSF

estimator SNR is observed to be a near-linear function of the number of subapertures on a single side of a square grid H-WFS array.

5.3 Recommendation for Future Research

In this section, recommendations for further research in this area are proposed.

- Develop a SSF estimator SNR simulation capability¹. The theoretical SSF estimator SNR is difficult to compute for large H-WFS—even for a single frame. Thus, predicting a theoretical SNR over dozens of frames is extremely difficult.
- Develop and simulate a method for retrieving atmospheric coherence diameter, outer scale, and power law from the SSF as estimated with a H-WFS. A H-WFS with more than two subapertures can estimate the SSF at more than one separation. Thus, a large H-WFS array allows many points on a theoretical SSF to be estimated. These multiple points should allow the turbulence parameters to be determined with greater confidence than with a DIMM.

¹This simulation should include a phase screen generator capable of including outer scale, power law, and temporal effects. This author has developed and tested a phase screen generator, with all these capabilities, based on Eqn. (2.18).

Appendix A. Zernike Expansion Coefficient Covariance Plots

This appendix shows the behavior the Zernike coefficient correlations required in the computation of the slope correlation function Γ_s , Eqn. (2.28), developed in Sec. (2.3). The desired coefficient correlation is given by the Equations (2.29), (2.30), (2.21), and (2.20) which are restated as

$$\mathcal{E} \{ a_j a_{j'}^* (\vec{u}) \} = 4c_1 \left(\frac{D}{\rho_0} \right)^{(\alpha-2)} \left[\frac{\Gamma(\frac{\alpha}{2})}{-\Gamma(\frac{2-\alpha}{2})} \right] [(n+1)(n'+1)]^{1/2} f_{jj'}(u, \theta_0, k_0), \quad (\text{A.1})$$

where

$$f_{jj'}(u, \theta_0, k_0) = \begin{cases} +(-1)^{(n+n')/2} \cos(2\theta_0) I_{2,n+1,n'+1}(2u, k_0) & \text{if } j, j' \text{ are both even} \\ +(-1)^{(n+n'+2)/2} I_{0,n+1,n'+1}(2u, k_0) & \\ -(-1)^{(n+n')/2} \cos(2\theta_0) I_{2,n+1,n'+1}(2u, k_0) & \text{if } j, j' \text{ are both odd} \\ +(-1)^{(n+n'+2)/2} I_{0,n+1,n'+1}(2u, k_0) & \end{cases}, \quad (\text{A.2})$$

$$k_0 = \pi \frac{D}{L_0}, \quad (\text{A.3})$$

$$I_{\kappa,\mu,\nu}(a, x_0) = \int_0^\infty \frac{x^{-1} J_\kappa(ax) J_\mu(x) J_\nu(x)}{(x^2 + x_0^2)^{\alpha/2}} dx, \quad (\text{A.4})$$

and c_1 is given by Eqn. (1.2), D is the aperture diameter, L_0 is the outer scale size, u and θ_0 are as shown in Fig. 2.1, and the functions $J_\kappa(x)$, $J_\mu(x)$, $J_\nu(x)$ are Bessel functions of the first kind and order κ , μ , and ν respectively

Figures A.1, A.2, and A.3 reproduce Takato and Yamaguchi's [15] Figs. 3, 4, and 5 and verify that the code developed for this thesis to evaluate Eqn. (A.1) produces results matching published results.

Figures A.4 through A.39 show Eqn. (A.1) evaluated as a function of aperture separation for various turbulence power laws α and outer scale LoD . Only the correlations for

Figure	modes	θ_0 ($^\circ$)	α	L_0/D
A.4	odd	0	3.3	10
A.5	odd	0	3.3	100
A.6	odd	0	3.3	0
A.7	odd	0	3.6667	10
A.8	odd	0	3.6667	100
A.9	odd	0	3.6667	0
A.10	odd	0	3.8	10
A.11	odd	0	3.8	100
A.12	odd	0	3.8	0
A.13	odd	90	3.3	10
A.14	odd	90	3.3	100
A.15	odd	90	3.3	0
A.16	odd	90	3.6667	10
A.17	odd	90	3.6667	100
A.18	odd	90	3.6667	0
A.19	odd	90	3.8	10
A.20	odd	90	3.8	100
A.21	odd	90	3.8	0
A.22	even	0	3.3	10
A.23	even	0	3.3	100
A.24	even	0	3.3	0
A.25	even	0	3.6667	10
A.26	even	0	3.6667	100
A.27	even	0	3.6667	0
A.28	even	0	3.8	10
A.29	even	0	3.8	100
A.30	even	0	3.8	0
A.31	even	90	3.3	10
A.32	even	90	3.3	100
A.33	even	90	3.3	0
A.34	even	90	3.6667	10
A.35	even	90	3.6667	100
A.36	even	90	3.6667	0
A.37	even	90	3.8	10
A.38	even	90	3.8	100
A.39	even	90	3.8	0

Table A.1 Summarization of Figures A.1 through A.39 showing Eqn. (A.1) evaluated as a function of aperture separation for various turbulence power laws and outer scale. Only the correlations for Zernike modes Z_2 through Z_{16} which contribute to the slope correlation Γ_s , Eqn. (2.28) developed in Sec. (2.3), are shown. The “modes” column refers to the mode correlations considered in each figure. The designator “odd” includes correlations between all combination of modes 3, 7, and 17. Likewise, the designator “even” includes correlations between all combinations of modes 2, 8, and 16.

Zernike modes Z_2 through Z_{16} which contribute to the slope correlation Γ_s , Eqn. (2.28), are shown. Tab. 2.3 shows that the wavefront slope in the $\theta_0 = 0$ direction depends only on the Zernike modes with even order j . Similarly, the wavefront slope in the $\theta_0 = \pi/2$ direction depends only on the Zernike modes with odd order j . The parameters examined in the figures are summarized in Tab. A.

The turbulence power law, α , determines how the power in the random process (the turbulence induced phase) is distributed as a function of Zernike mode order. The ratio of turbulence outer scale to subaperture diameter, L_0/D , determines the rate of correlation roll-off. The requested accuracy for numerical integration of the highly oscillatory

Eqn. (A.4) is $10E-12$. Thus, erroneous coefficient correlation results are seen when the magnitude of the numerical correlation is less than $10E-12$.

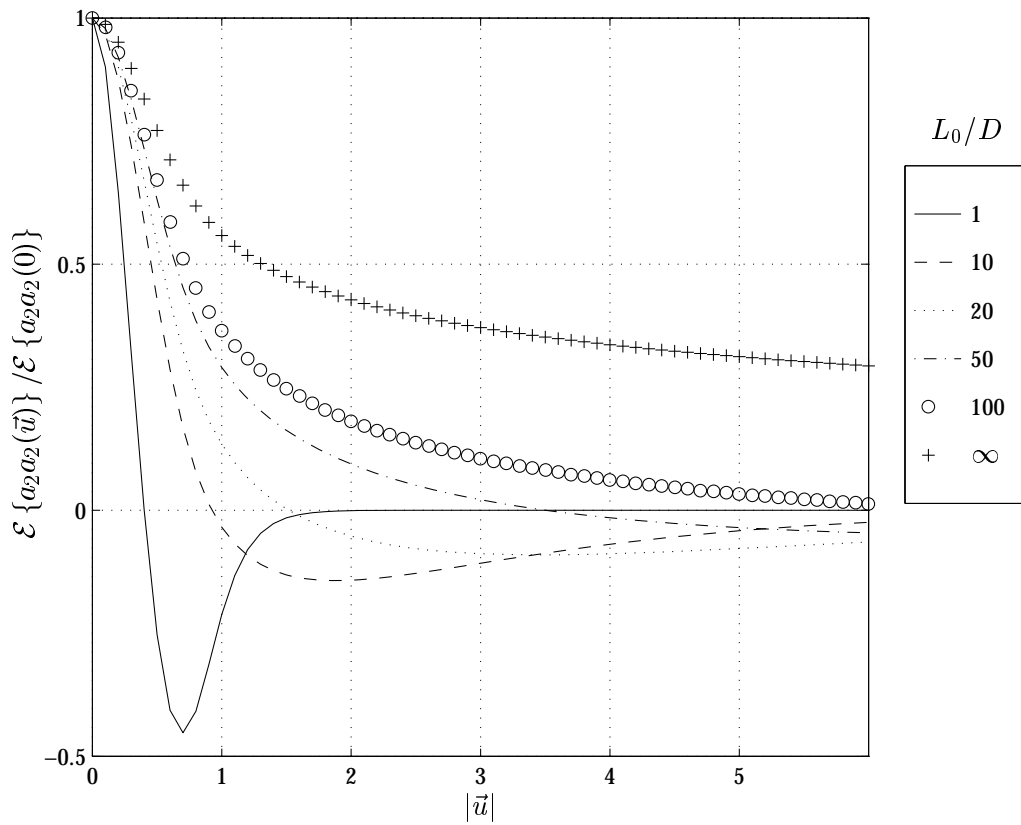


Figure A.1 $\mathcal{E}\{a_2 a_2(\vec{u})\} / \mathcal{E}\{a_2 a_2(0)\}$: Takato and Yamaguchi's Fig.3 [15] as generated by code developed in this thesis. $\theta_0 = 0$

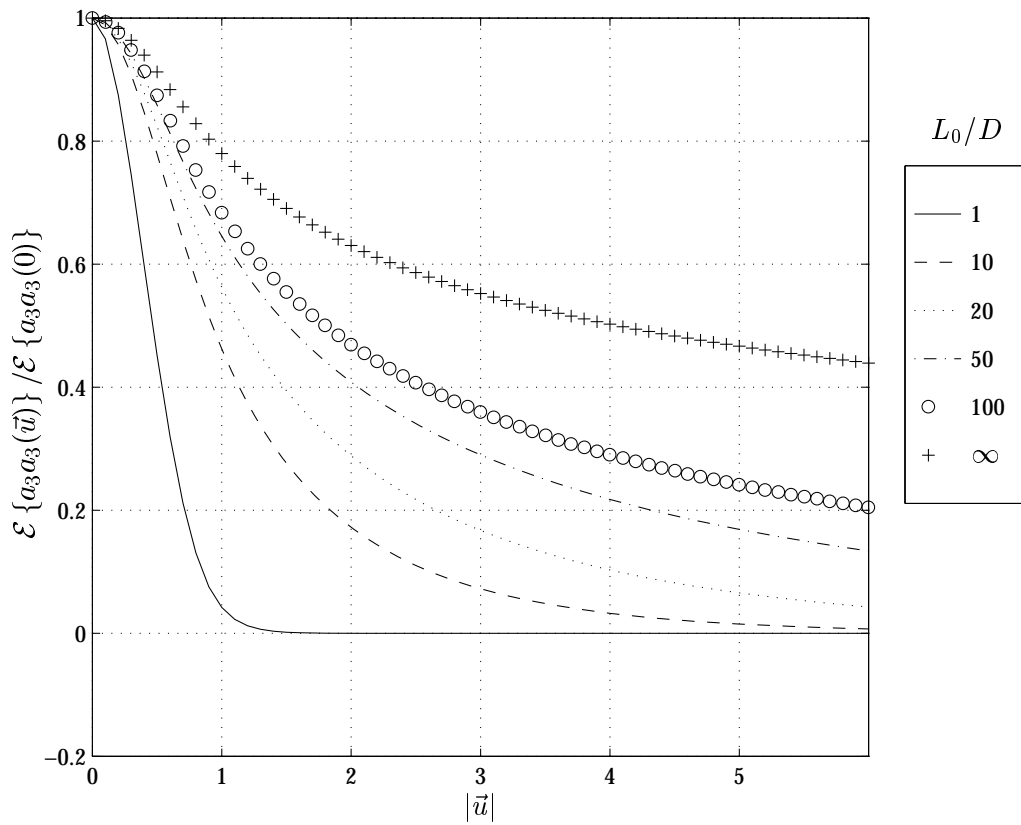


Figure A.2 $\mathcal{E}\{a_3 a_3(\vec{u})\} / \mathcal{E}\{a_3 a_3(0)\}$: Takato and Yamaguchi's Fig.4 [15] as generated by code developed in this thesis. $\theta_0 = 0$

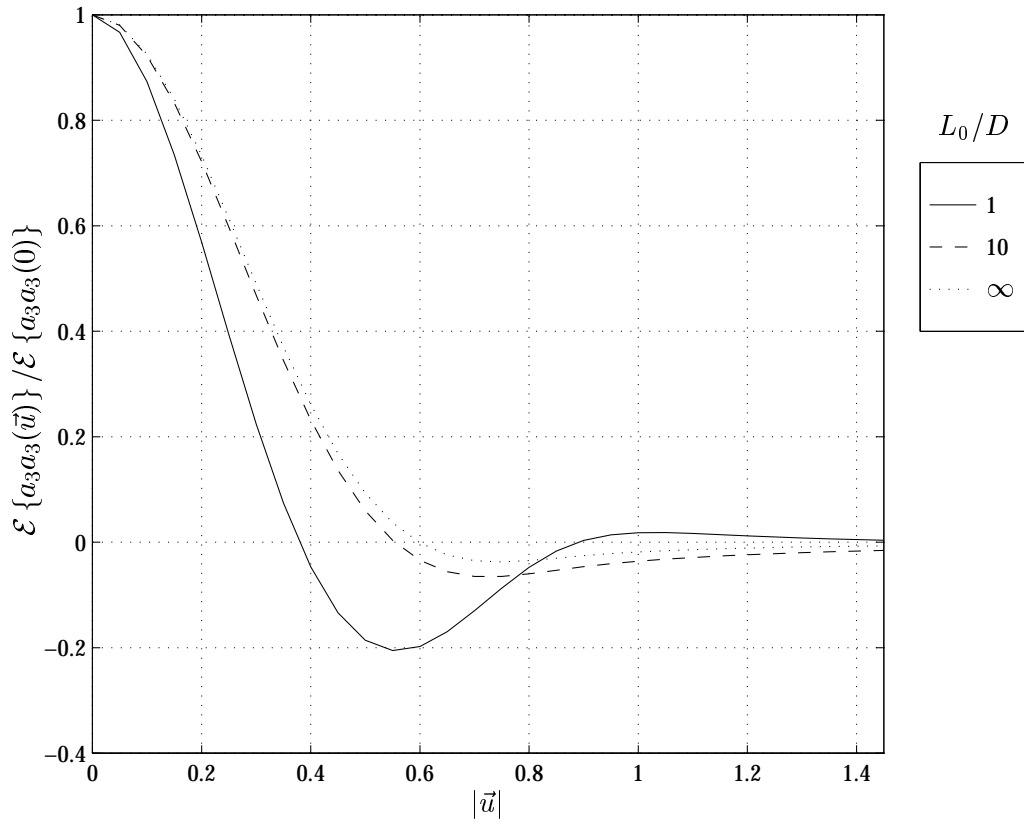


Figure A.3 $\mathcal{E}\{a_3 a_3(\vec{u})\} / \mathcal{E}\{a_3 a_3(0)\}$: Takato and Yamaguchi's Fig.5 [15] as generated by code developed in this thesis. $\theta_0 = 0$

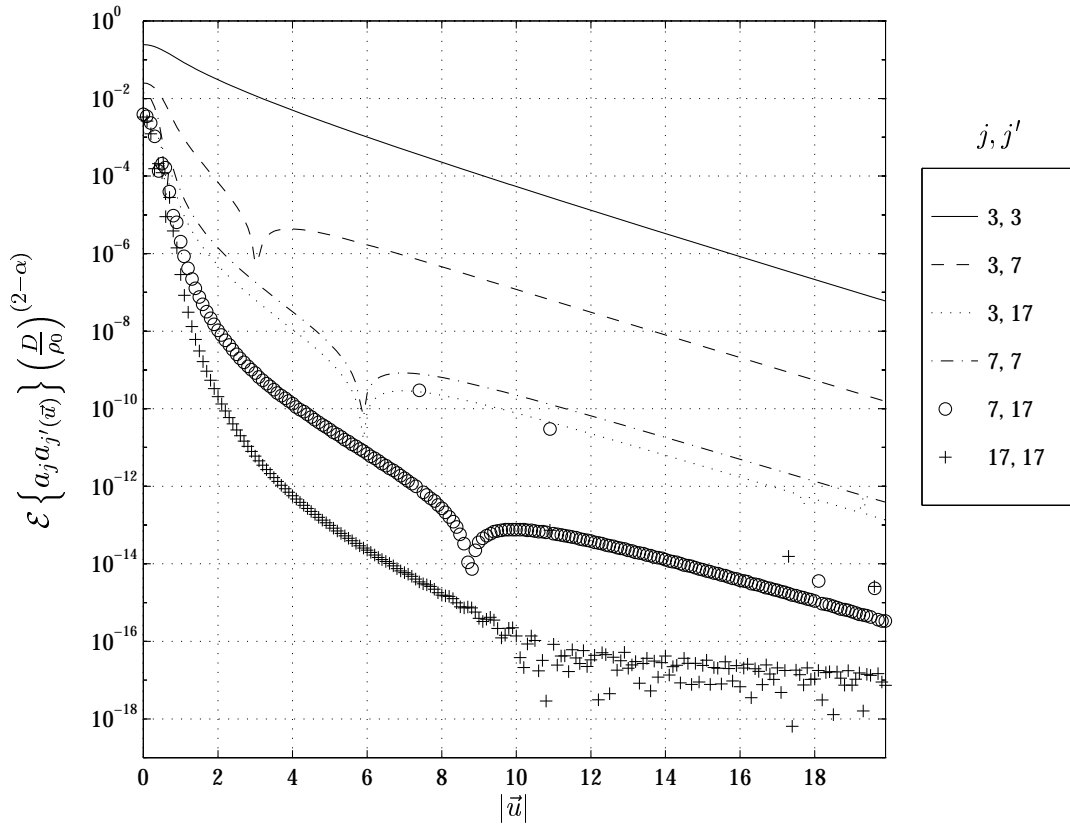


Figure A.4 $\mathcal{E} \left\{ a_j a_{j'}(\vec{u}) \right\} \left(\frac{D}{\rho_0} \right)^{(2-\alpha)}$, odd modes, $\theta_0 = 0^\circ$, $L_0/D = 10.00$, $\alpha = 3.3000$

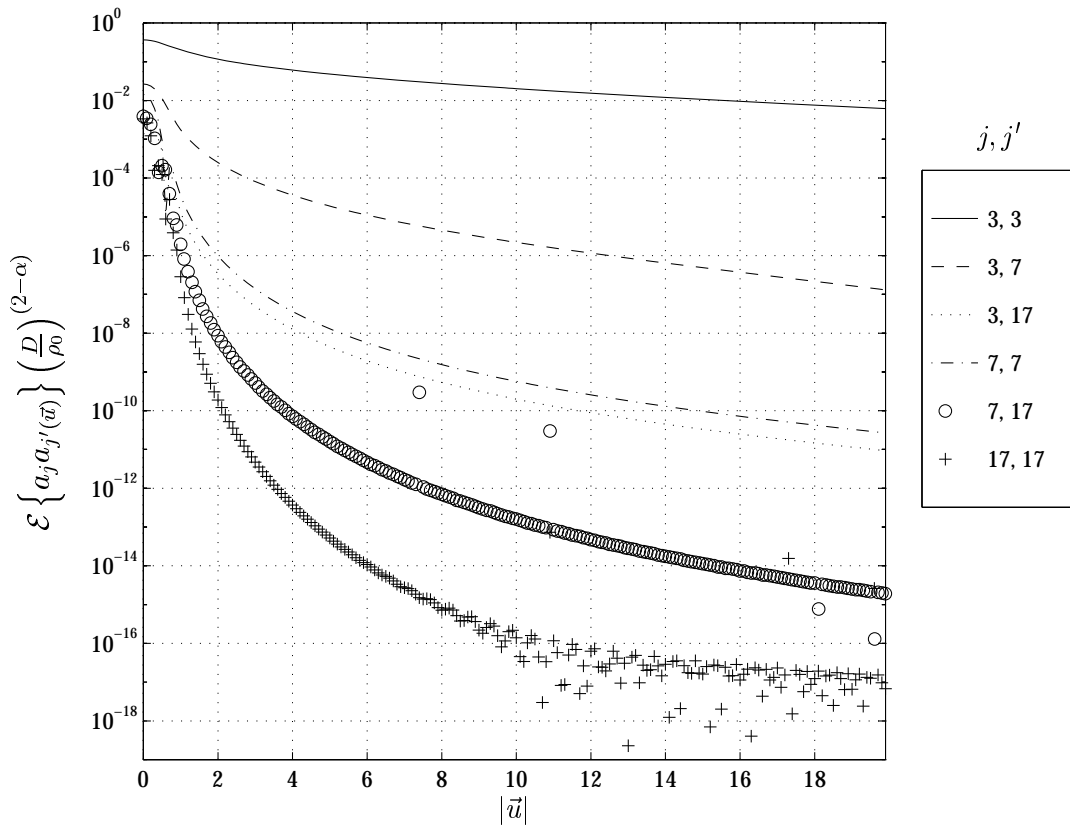


Figure A.5 $\mathcal{E} \left\{ a_j a_{j'}(\vec{u}) \right\} \left(\frac{D}{\rho_0} \right)^{(2-\alpha)}$, odd modes, $\theta_0 = 0^\circ$, $L_0/D = 100.00$, $\alpha = 3.3000$

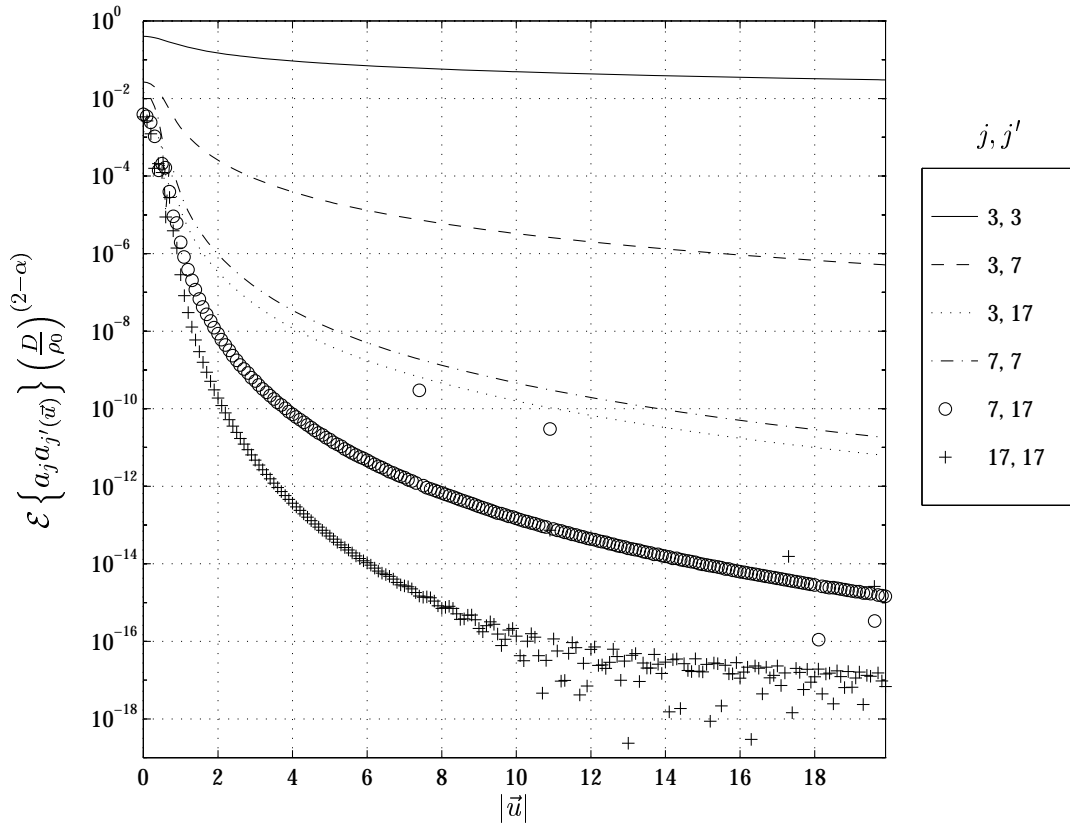


Figure A.6 $\mathcal{E} \left\{ a_j a_{j'}(\vec{u}) \right\} \left(\frac{D}{\rho_0} \right)^{(2-\alpha)}$, odd modes, $\theta_0 = 0^\circ$, $L_0/D = \infty$, $\alpha = 3.3000$

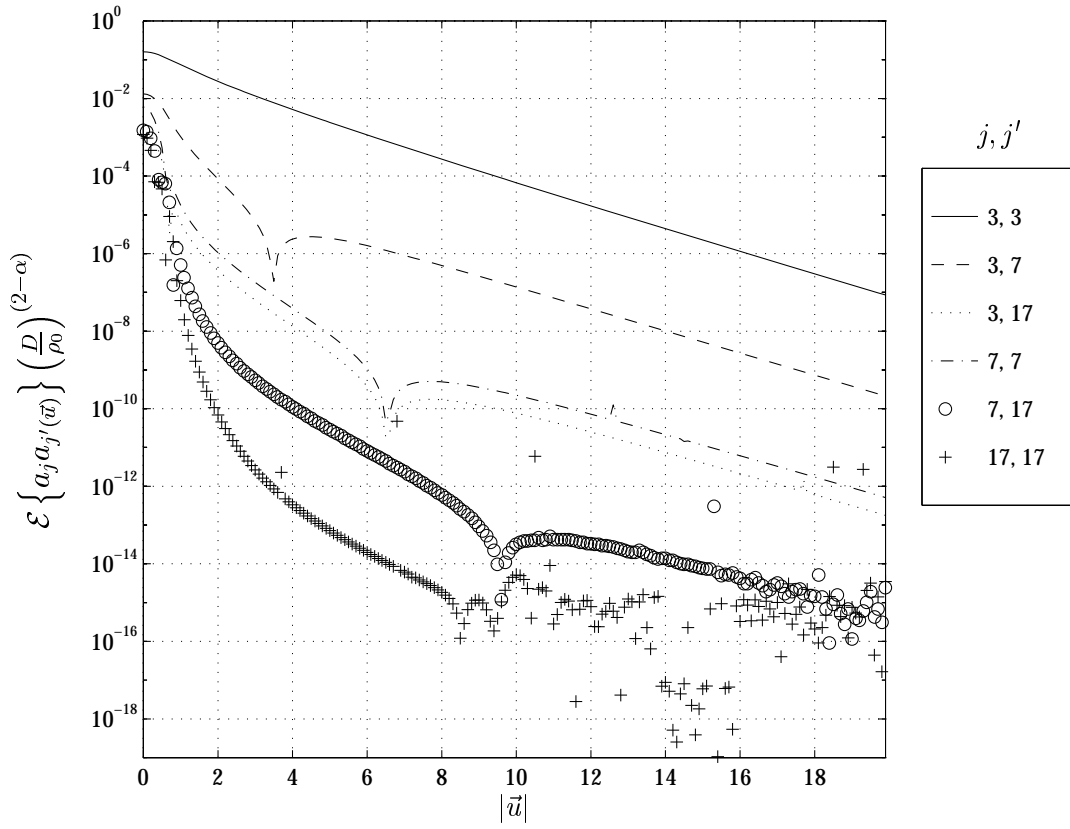


Figure A.7 $\mathcal{E} \left\{ a_j a_{j'}(\vec{u}) \right\} \left(\frac{D}{\rho_0} \right)^{(2-\alpha)}$, odd modes, $\theta_0 = 0^\circ$, $L_0/D = 10.00$, $\alpha = 3.6667$

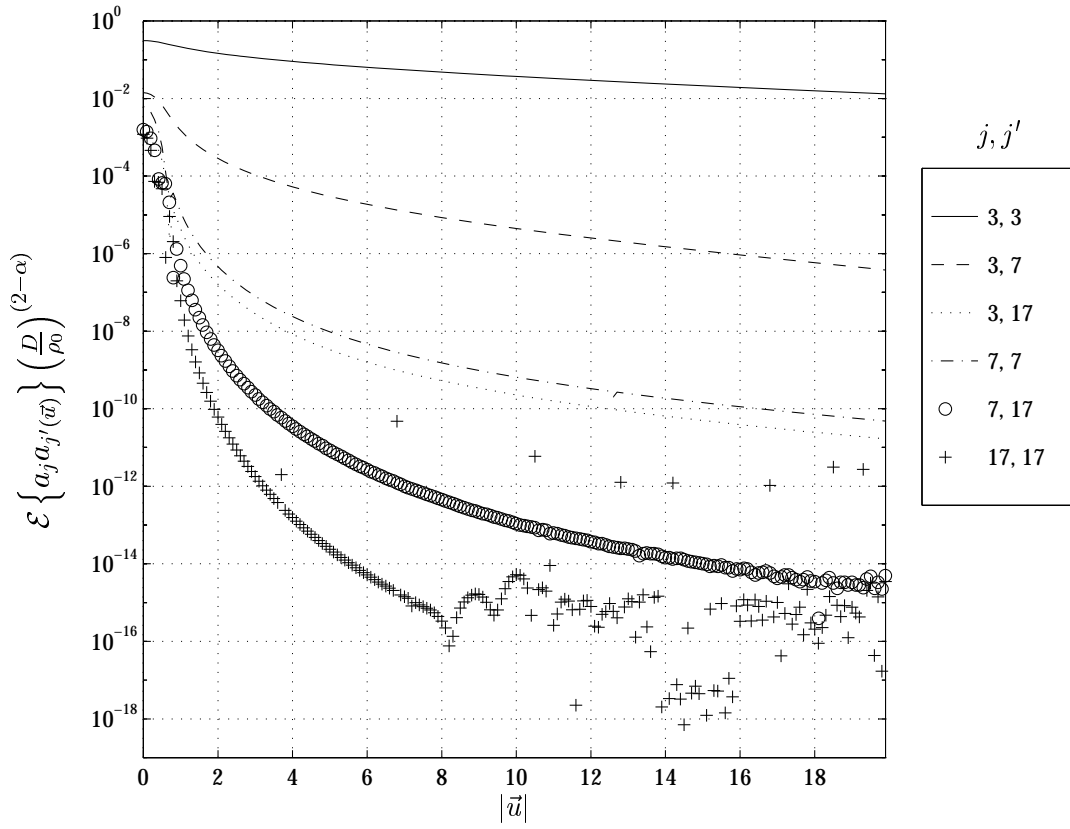


Figure A.8 $\mathcal{E} \left\{ a_j a_{j'}(\vec{u}) \right\} \left(\frac{D}{\rho_0} \right)^{(2-\alpha)}$, odd modes, $\theta_0 = 0^\circ$, $L_0/D = 100.00$, $\alpha = 3.6667$

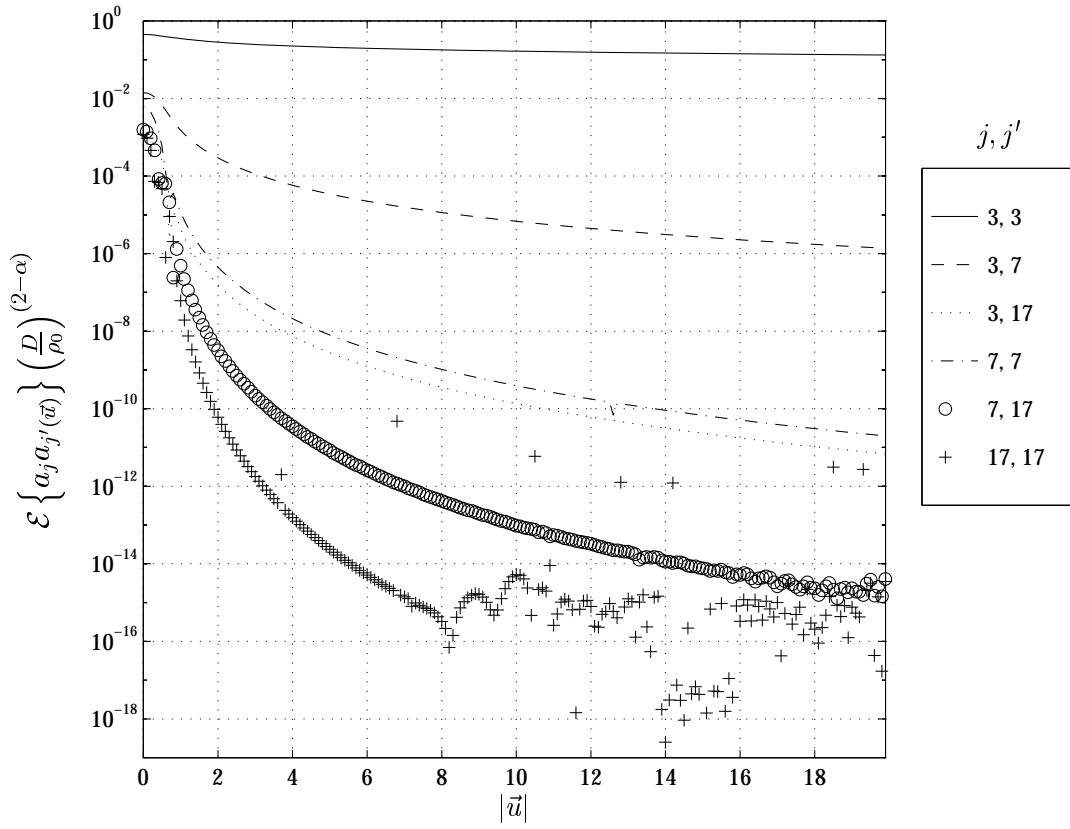


Figure A.9 $\mathcal{E} \left\{ a_j a_{j'}(\vec{u}) \right\} \left(\frac{D}{\rho_0} \right)^{(2-\alpha)}$, odd modes, $\theta_0 = 0^\circ$, $L_0/D = \infty$, $\alpha = 3.6667$

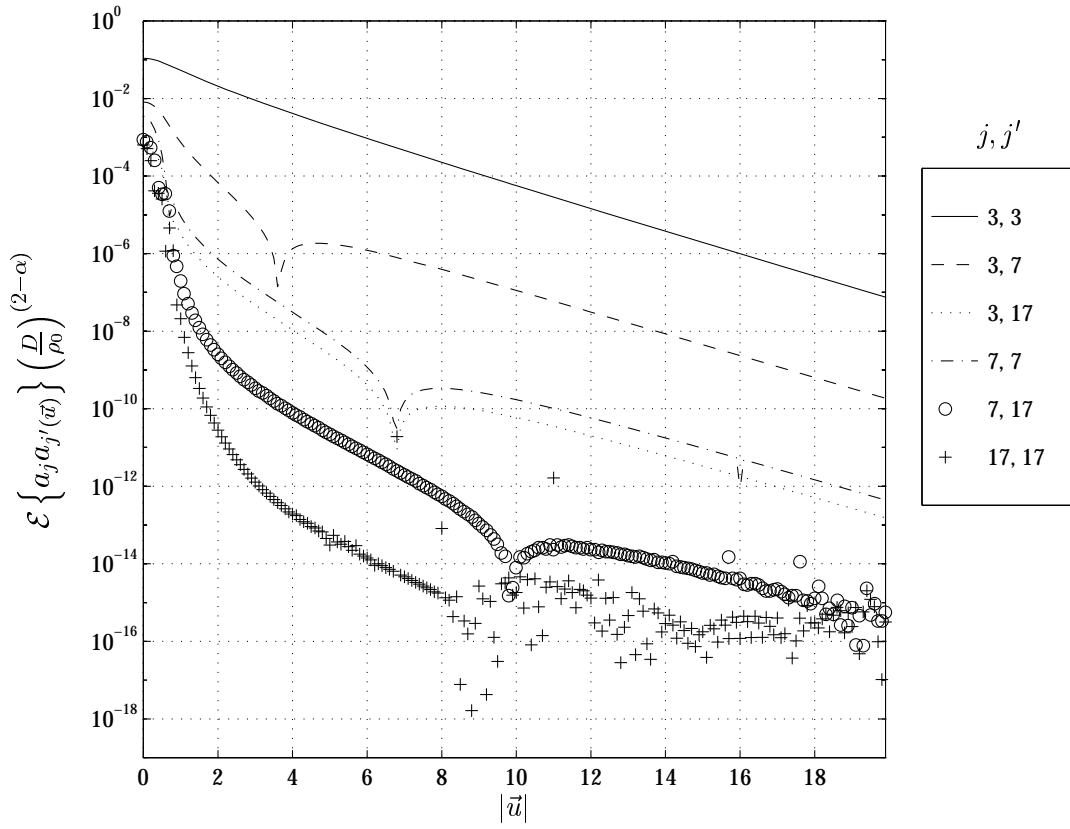


Figure A.10 $\mathcal{E} \left\{ a_j a_{j'}(\vec{u}) \right\} \left(\frac{D}{\rho_0} \right)^{(2-\alpha)}$, odd modes, $\theta_0 = 0^\circ$, $L_0/D = 10.00$, $\alpha = 3.8000$

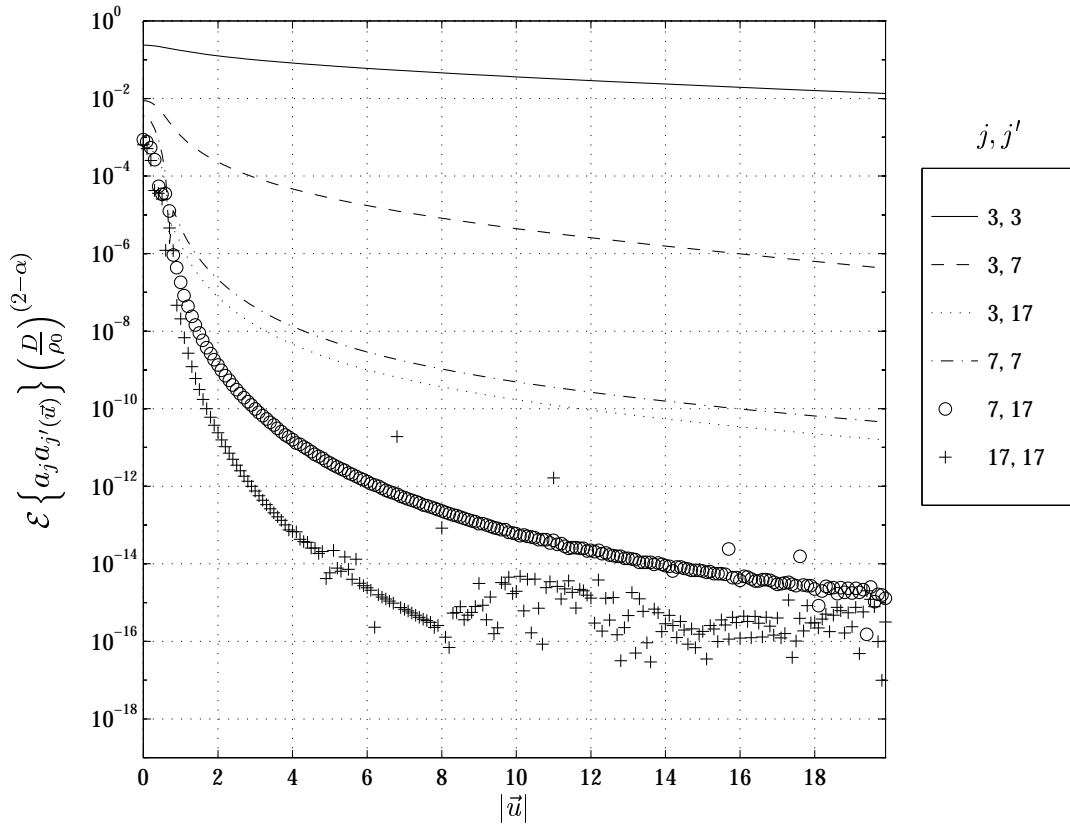


Figure A.11 $\mathcal{E} \left\{ a_j a_{j'}(\vec{u}) \right\} \left(\frac{D}{\rho_0} \right)^{(2-\alpha)}$, odd modes, $\theta_0 = 0^\circ$, $L_0/D = 100.00$, $\alpha = 3.8000$

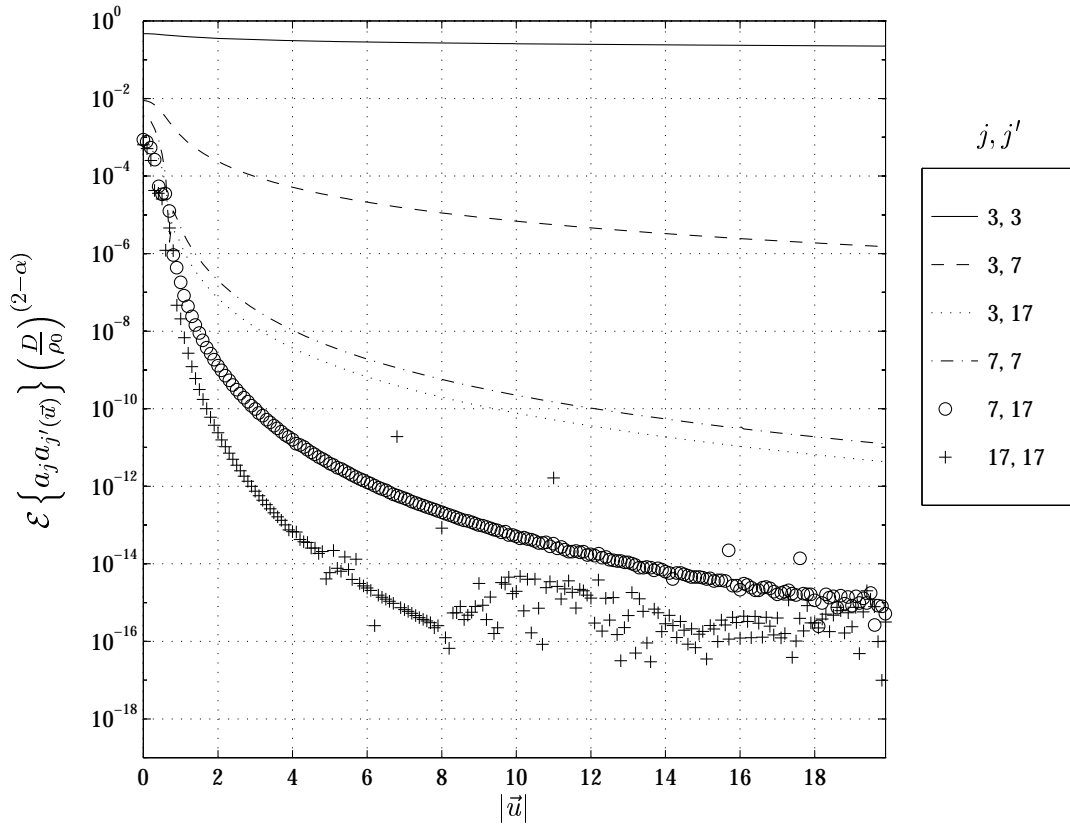


Figure A.12 $\mathcal{E} \left\{ a_j a_{j'}(\vec{u}) \right\} \left(\frac{D}{\rho_0} \right)^{(2-\alpha)}$, odd modes, $\theta_0 = 0^\circ$, $L_0/D = \infty$, $\alpha = 3.8000$

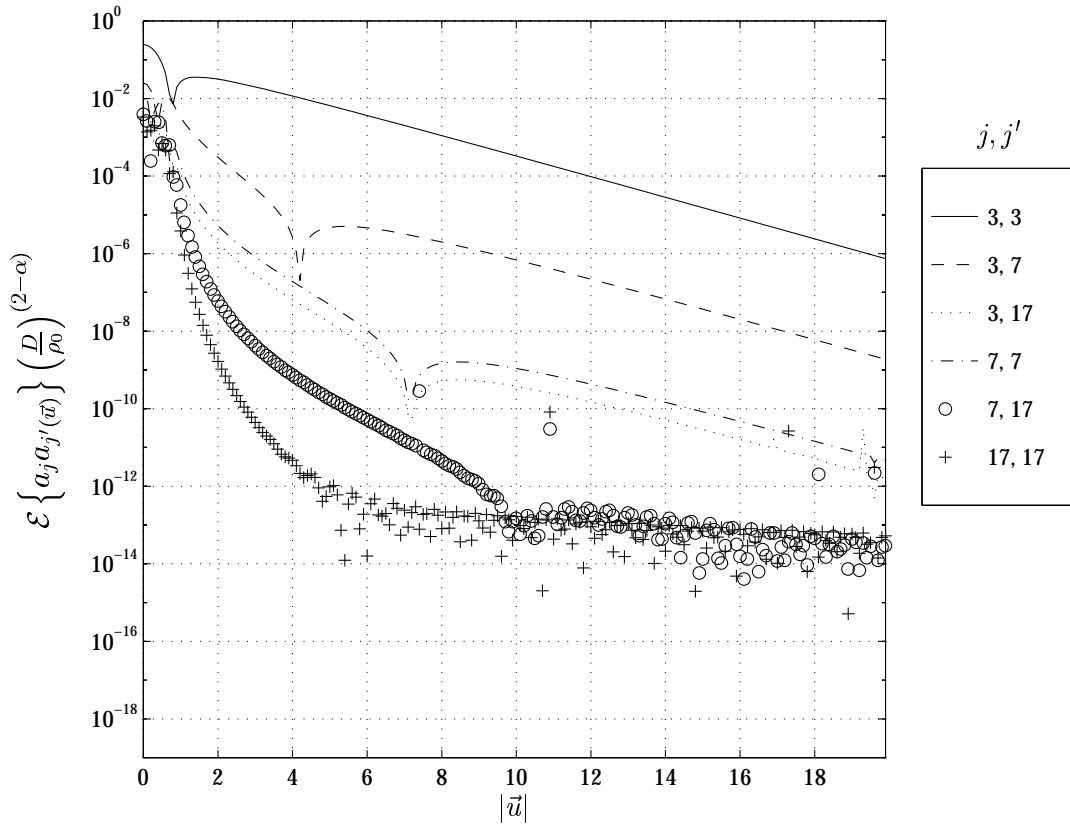


Figure A.13 $\mathcal{E} \left\{ a_j a_{j'}(\vec{u}) \right\} \left(\frac{D}{\rho_0} \right)^{(2-\alpha)}$, odd modes, $\theta_0 = 90^\circ$, $L_0/D = 10.00$, $\alpha = 3.3000$

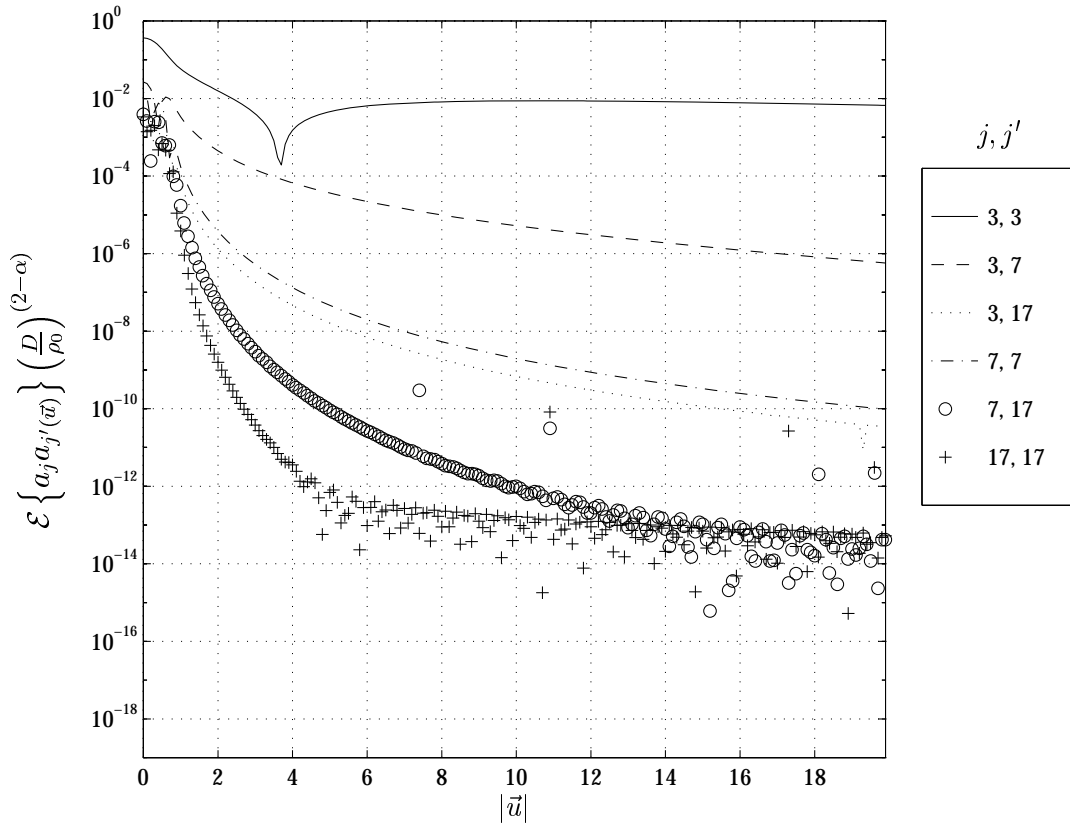


Figure A.14 $\mathcal{E} \left\{ a_j a_{j'}(\vec{u}) \right\} \left(\frac{D}{\rho_0} \right)^{(2-\alpha)}$, odd modes, $\theta_0 = 90^\circ$, $L_0/D = 100.00$, $\alpha = 3.3000$

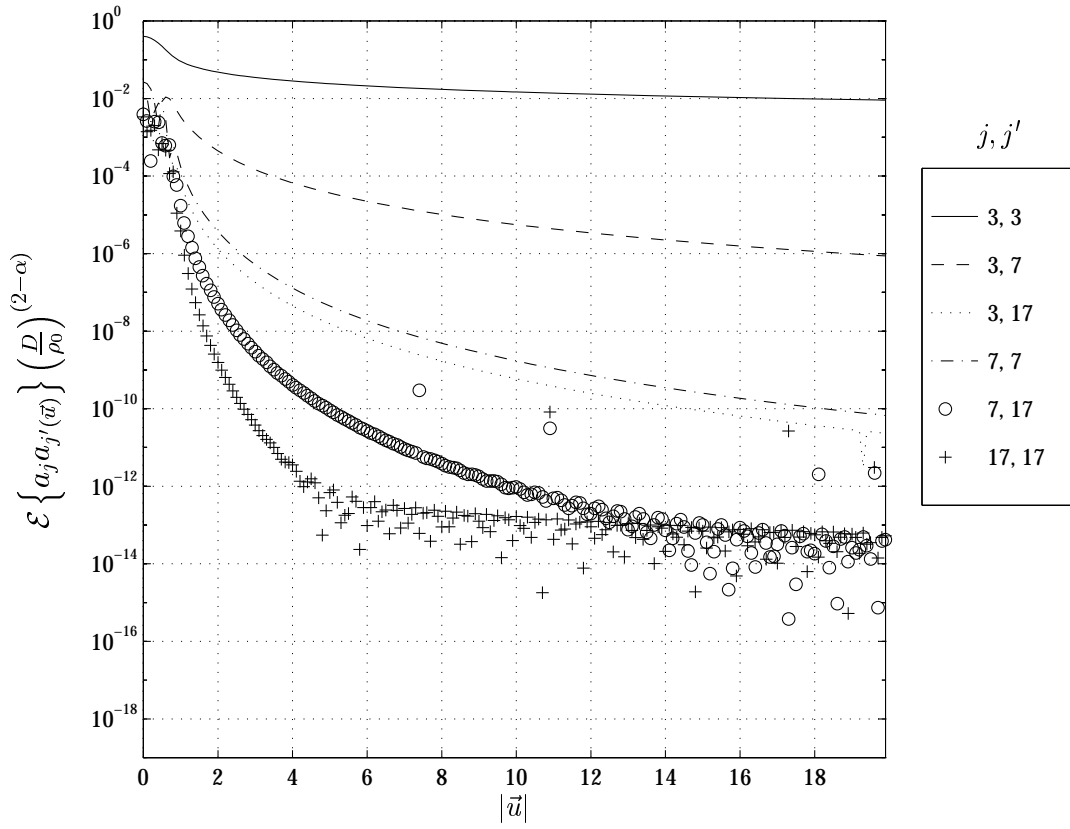


Figure A.15 $\mathcal{E} \left\{ a_j a_{j'}(\vec{u}) \right\} \left(\frac{D}{\rho_0} \right)^{(2-\alpha)}$, odd modes, $\theta_0 = 90^\circ$, $L_0/D = \infty$, $\alpha = 3.3000$

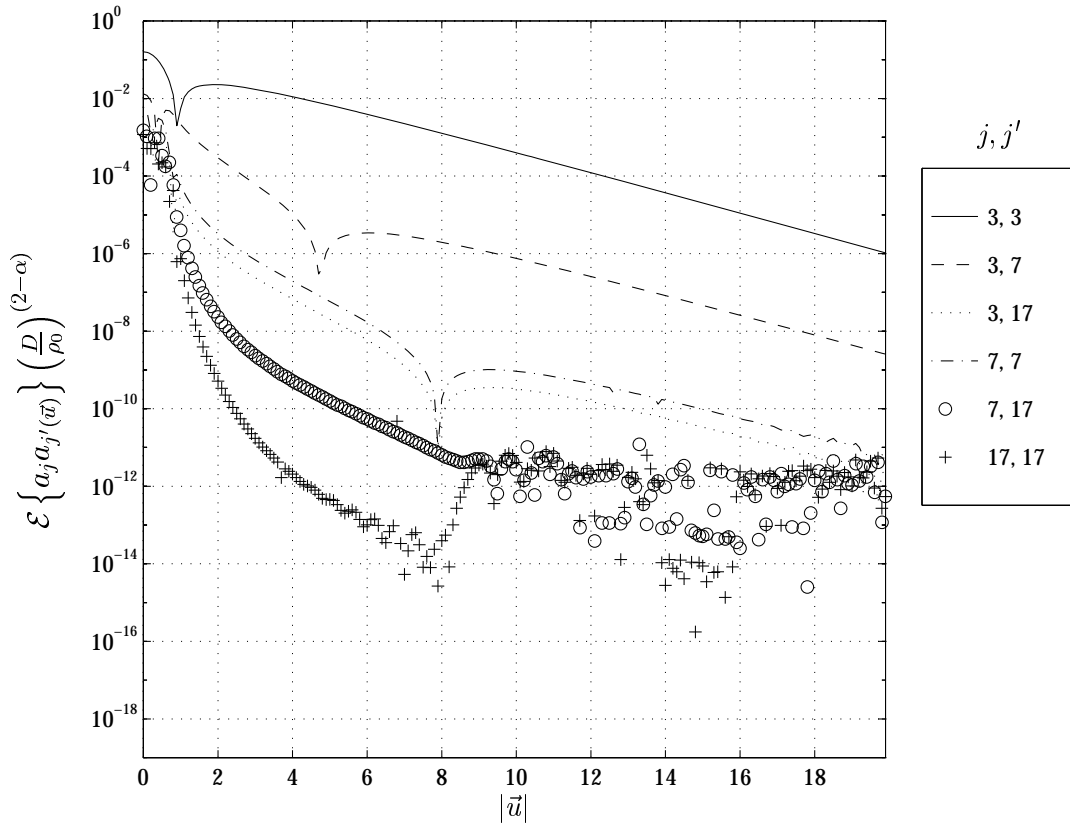


Figure A.16 $\mathcal{E} \left\{ a_j a_{j'}(\vec{u}) \right\} \left(\frac{D}{\rho_0} \right)^{(2-\alpha)}$, odd modes, $\theta_0 = 90^\circ$, $L_0/D = 10.00$, $\alpha = 3.6667$

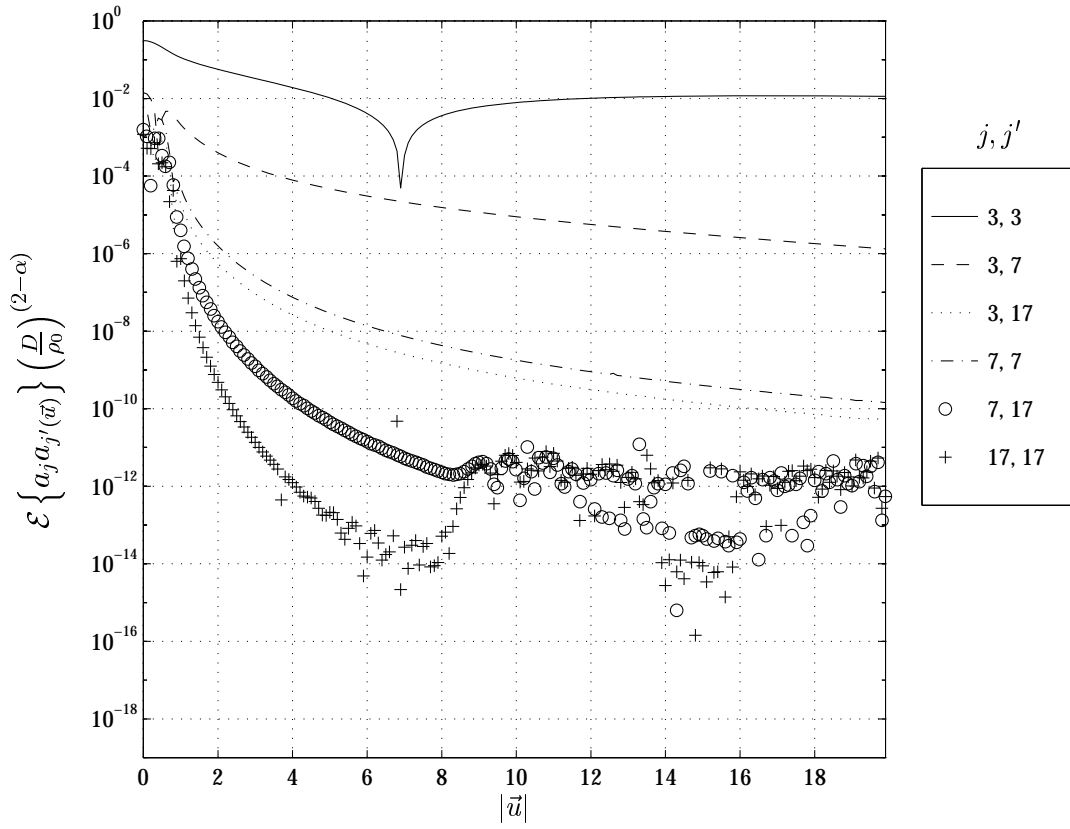


Figure A.17 $\mathcal{E} \left\{ a_j a_{j'}(\vec{u}) \right\} \left(\frac{D}{\rho_0} \right)^{(2-\alpha)}$, odd modes, $\theta_0 = 90^\circ$, $L_0/D = 100.00$, $\alpha = 3.6667$

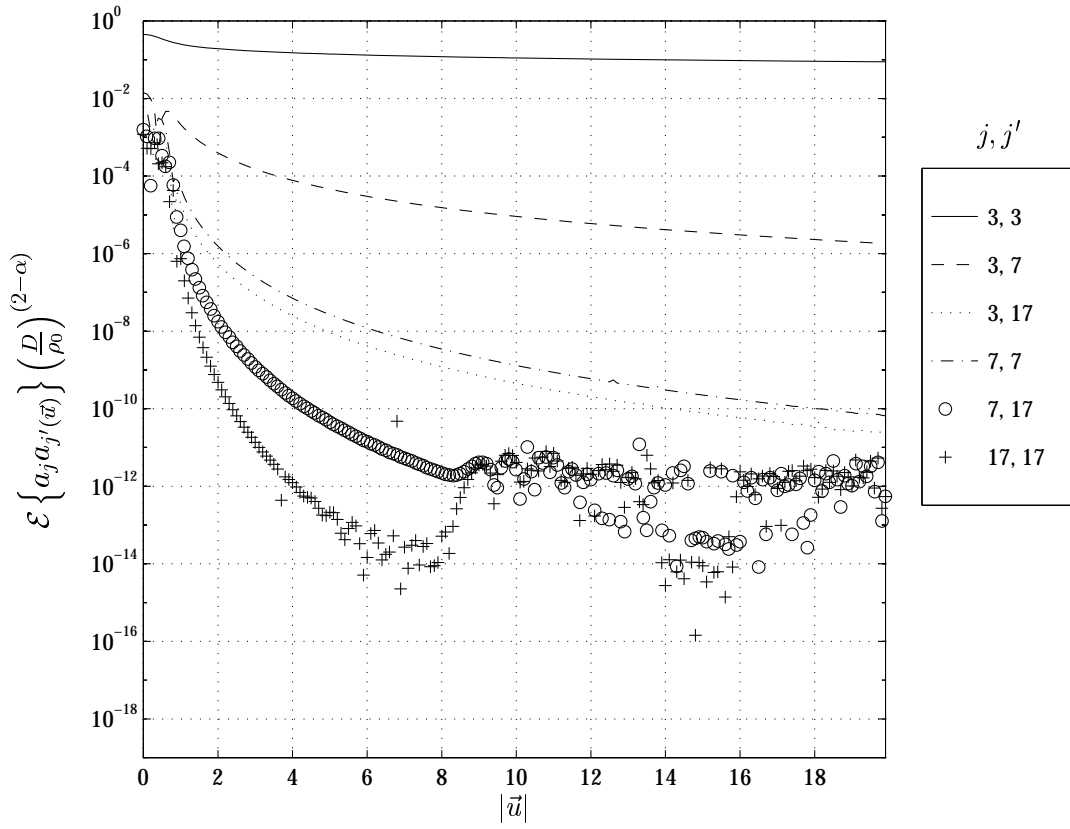


Figure A.18 $\mathcal{E} \left\{ a_j a_{j'}(\vec{u}) \right\} \left(\frac{D}{\rho_0} \right)^{(2-\alpha)}$, odd modes, $\theta_0 = 90^\circ$, $L_0/D = \infty$, $\alpha = 3.6667$

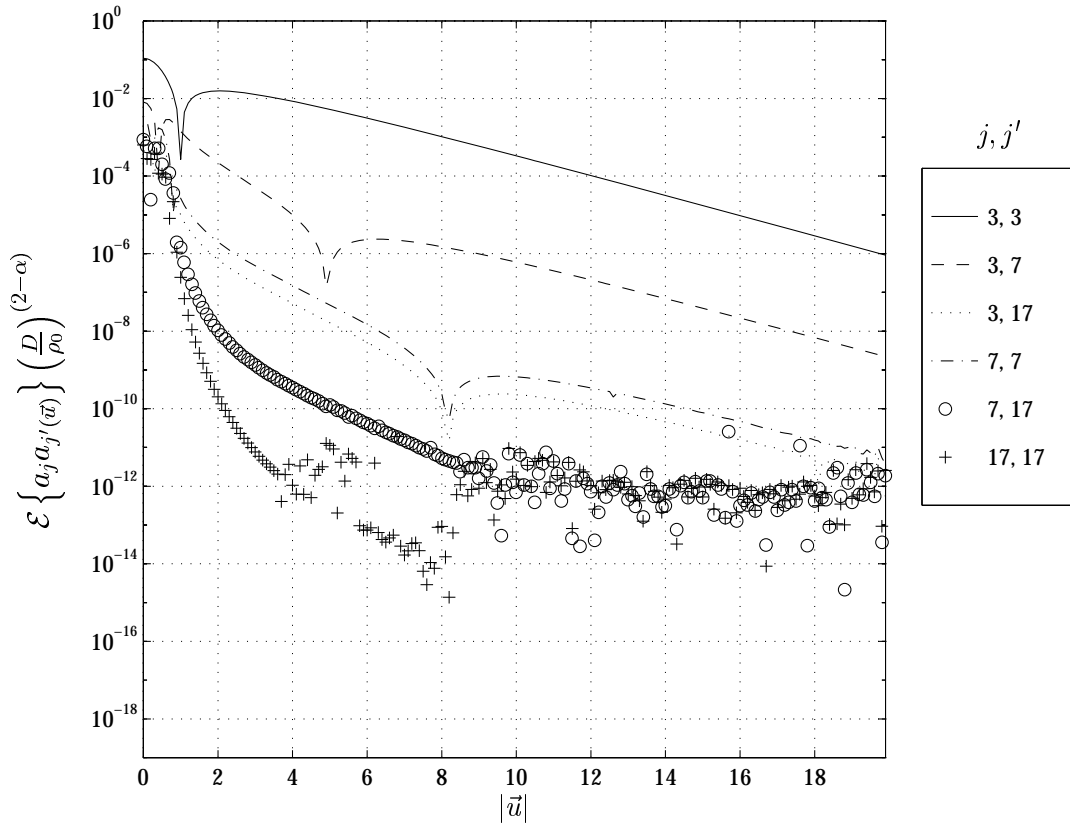


Figure A.19 $\mathcal{E} \left\{ a_j a_{j'}(\vec{u}) \right\} \left(\frac{D}{\rho_0} \right)^{(2-\alpha)}$, odd modes, $\theta_0 = 90^\circ$, $L_0/D = 10.00$, $\alpha = 3.8000$

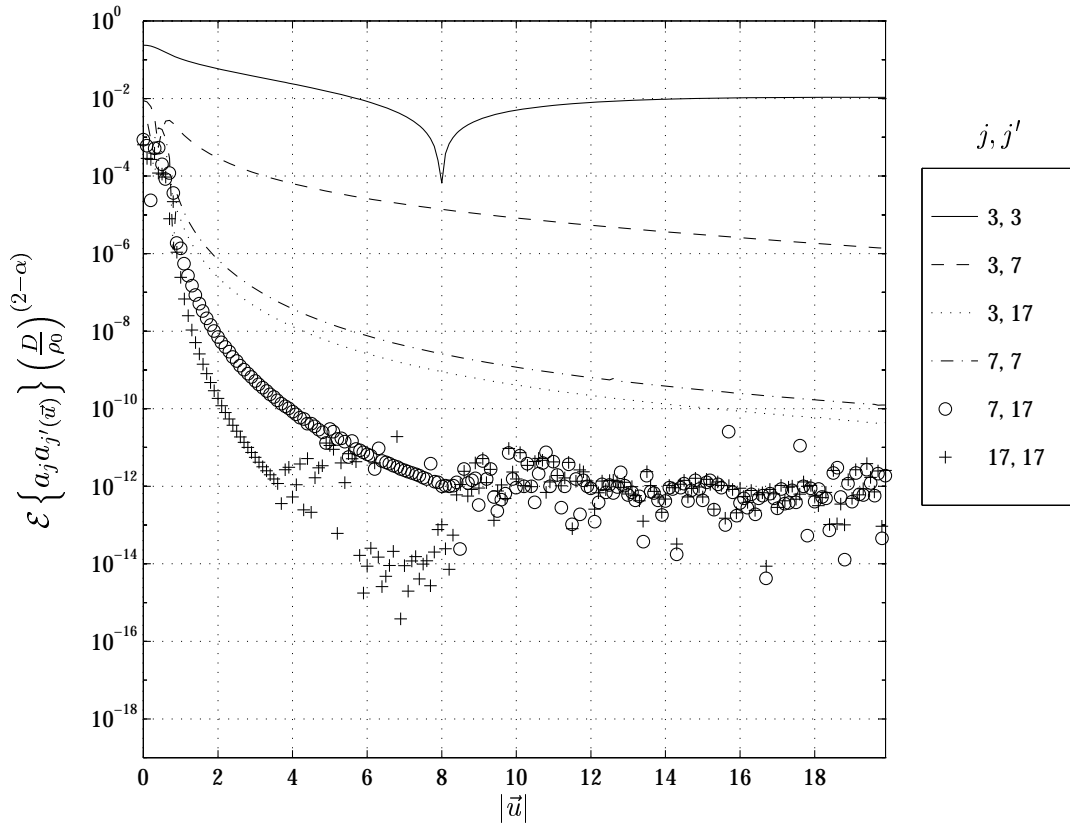


Figure A.20 $\mathcal{E} \left\{ a_j a_{j'}(\vec{u}) \right\} \left(\frac{D}{\rho_0} \right)^{(2-\alpha)}$, odd modes, $\theta_0 = 90^\circ$, $L_0/D = 100.00$, $\alpha = 3.8000$

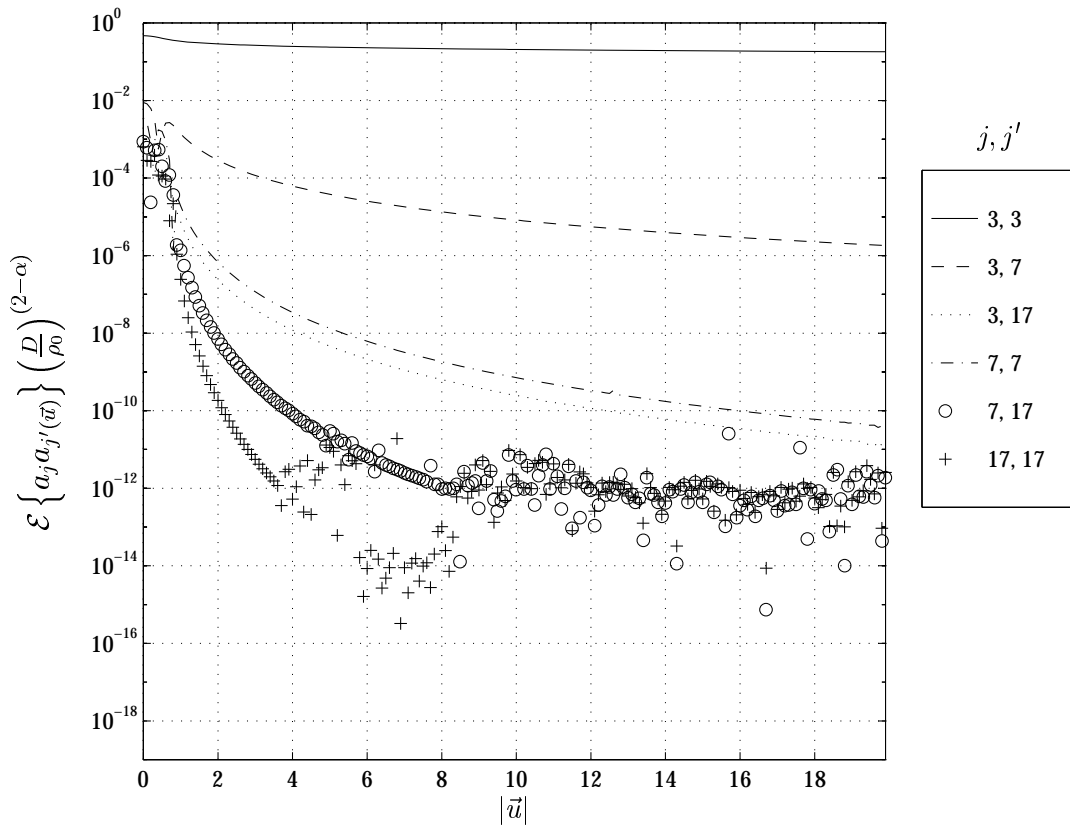


Figure A.21 $\mathcal{E} \left\{ a_j a_{j'}(\vec{u}) \right\} \left(\frac{D}{\rho_0} \right)^{(2-\alpha)}$, odd modes, $\theta_0 = 90^\circ$, $L_0/D = \infty$, $\alpha = 3.8000$

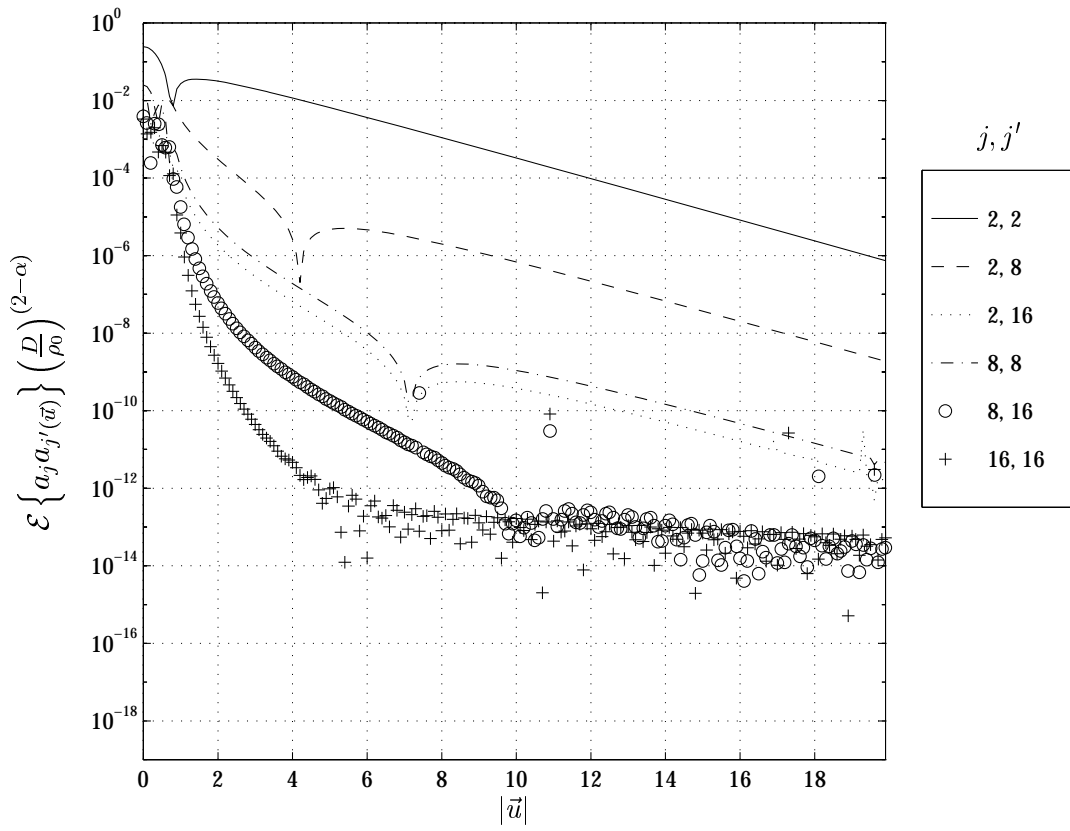


Figure A.22 $\mathcal{E} \left\{ a_j a_{j'}(\vec{u}) \right\} \left(\frac{D}{\rho_0} \right)^{(2-\alpha)}$, even modes, $\theta_0 = 0^\circ$, $L_0/D = 10.00$, $\alpha = 3.3000$

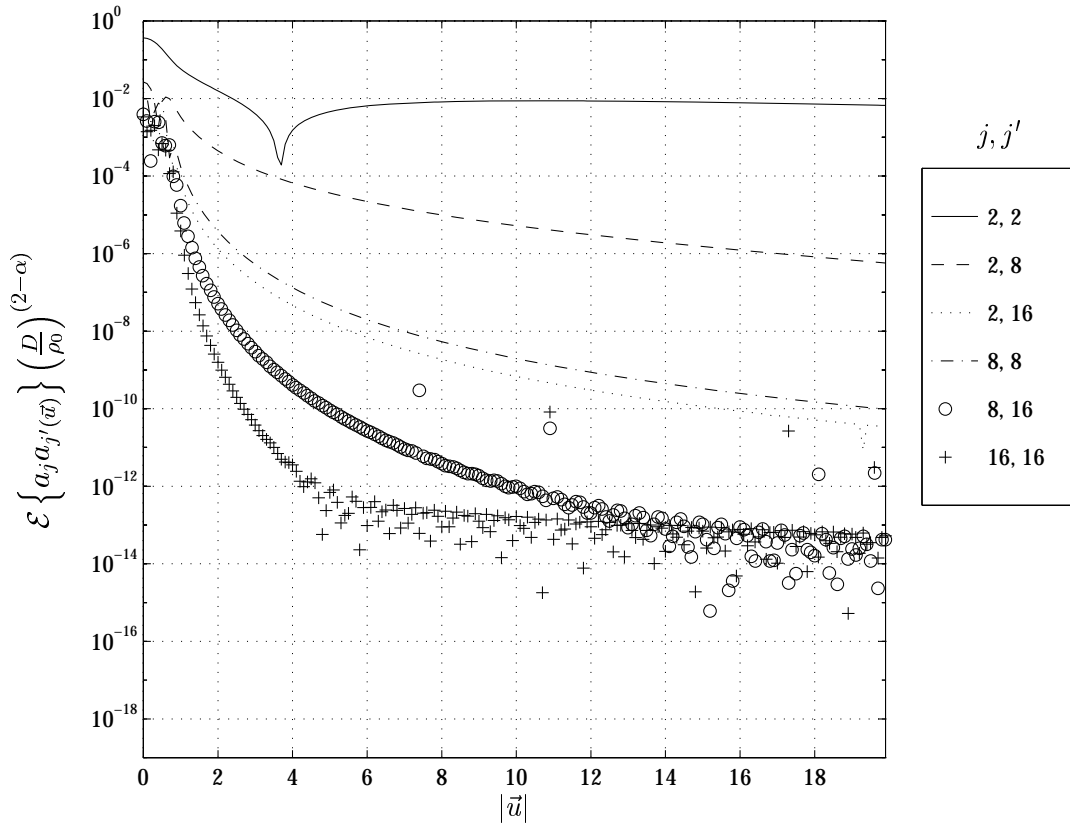


Figure A.23 $\mathcal{E} \left\{ a_j a_{j'}(\vec{u}) \right\} \left(\frac{D}{\rho_0} \right)^{(2-\alpha)}$, even modes, $\theta_0 = 0^\circ$, $L_0/D = 100.00$, $\alpha = 3.3000$

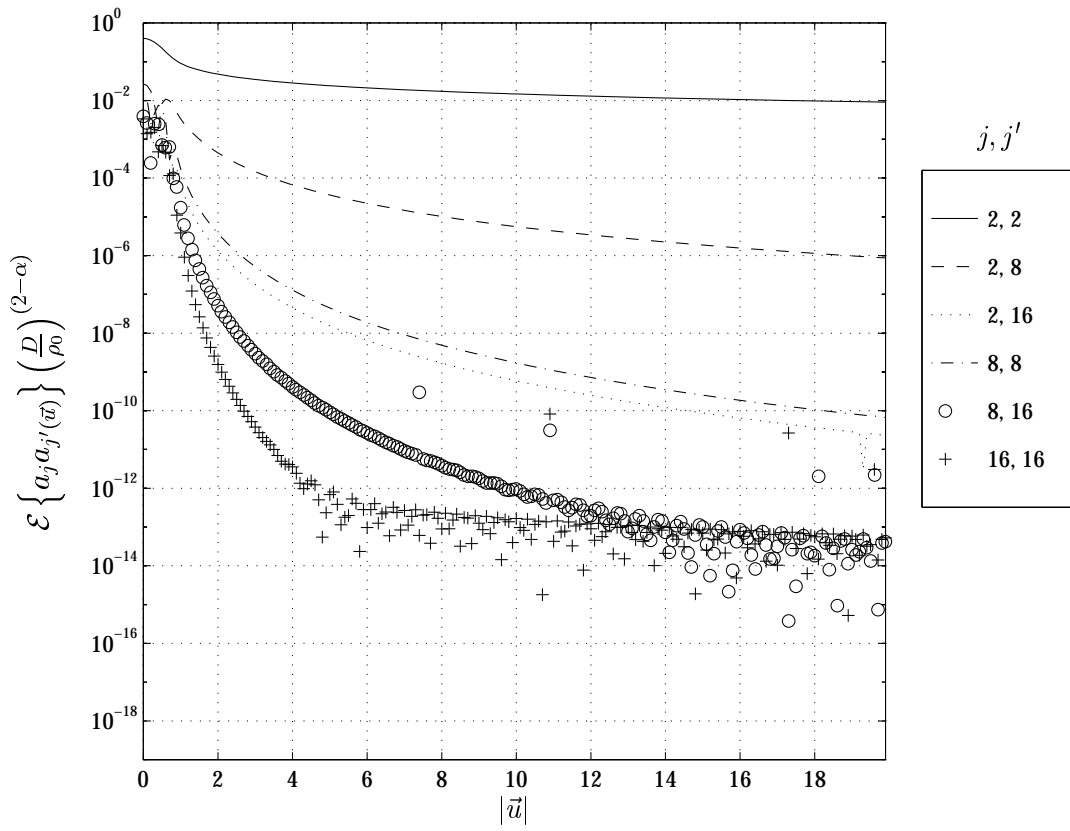


Figure A.24 $\mathcal{E} \left\{ a_j a_{j'}(\vec{u}) \right\} \left(\frac{D}{\rho_0} \right)^{(2-\alpha)}$, even modes, $\theta_0 = 0^\circ$, $L_0/D = \infty$, $\alpha = 3.3000$

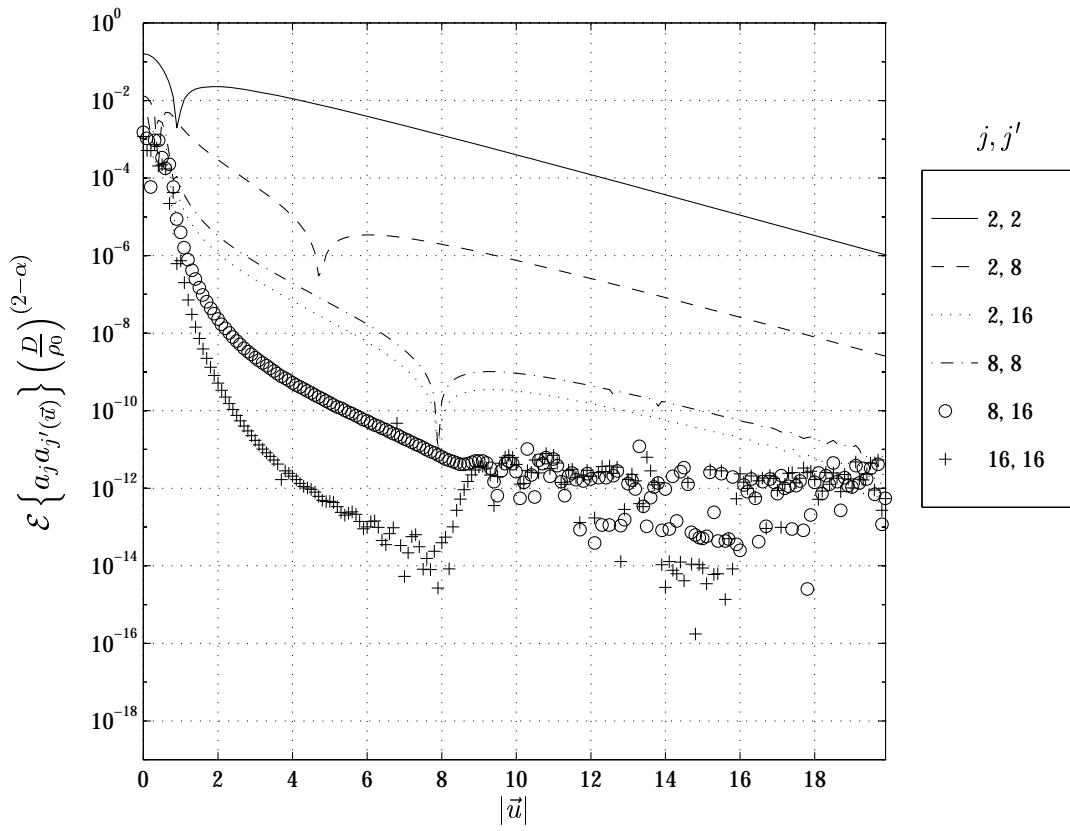


Figure A.25 $\mathcal{E} \left\{ a_j a_{j'}(\vec{u}) \right\} \left(\frac{D}{\rho_0} \right)^{(2-\alpha)}$, even modes, $\theta_0 = 0^\circ$, $L_0/D = 10.00$, $\alpha = 3.6667$

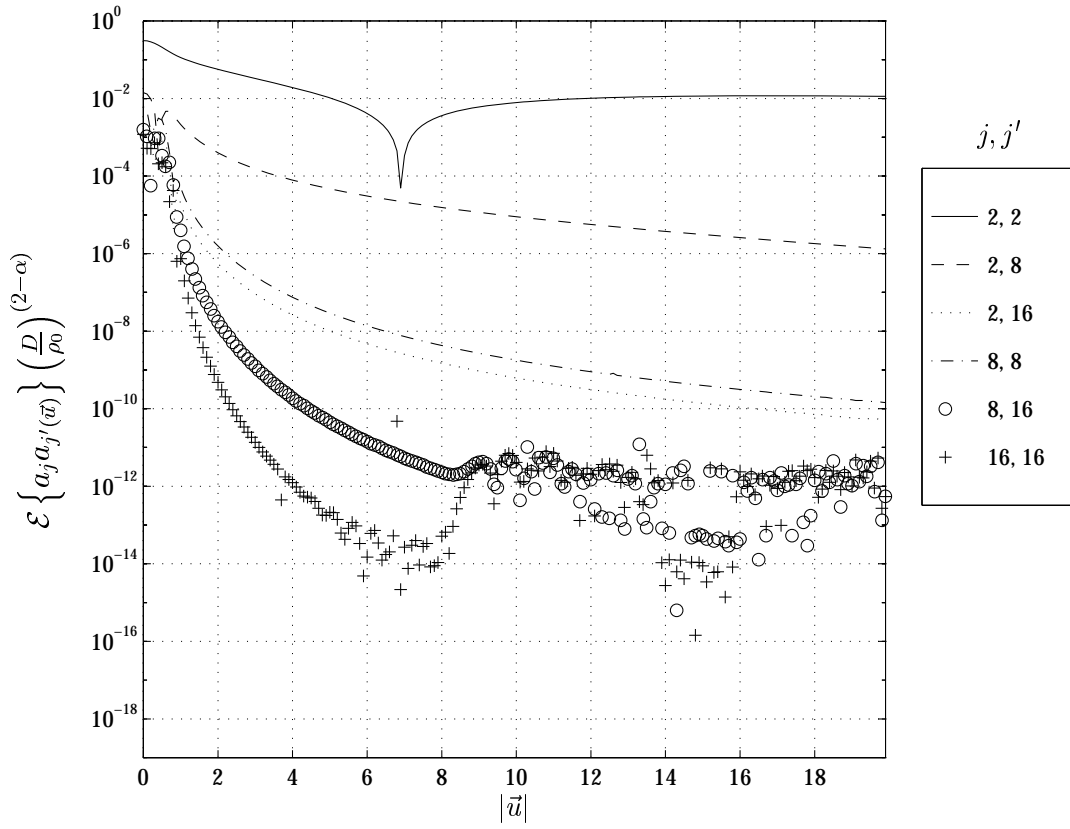


Figure A.26 $\mathcal{E} \left\{ a_j a_{j'}(\vec{u}) \right\} \left(\frac{D}{\rho_0} \right)^{(2-\alpha)}$, even modes, $\theta_0 = 0^\circ$, $L_0/D = 100.00$, $\alpha = 3.6667$

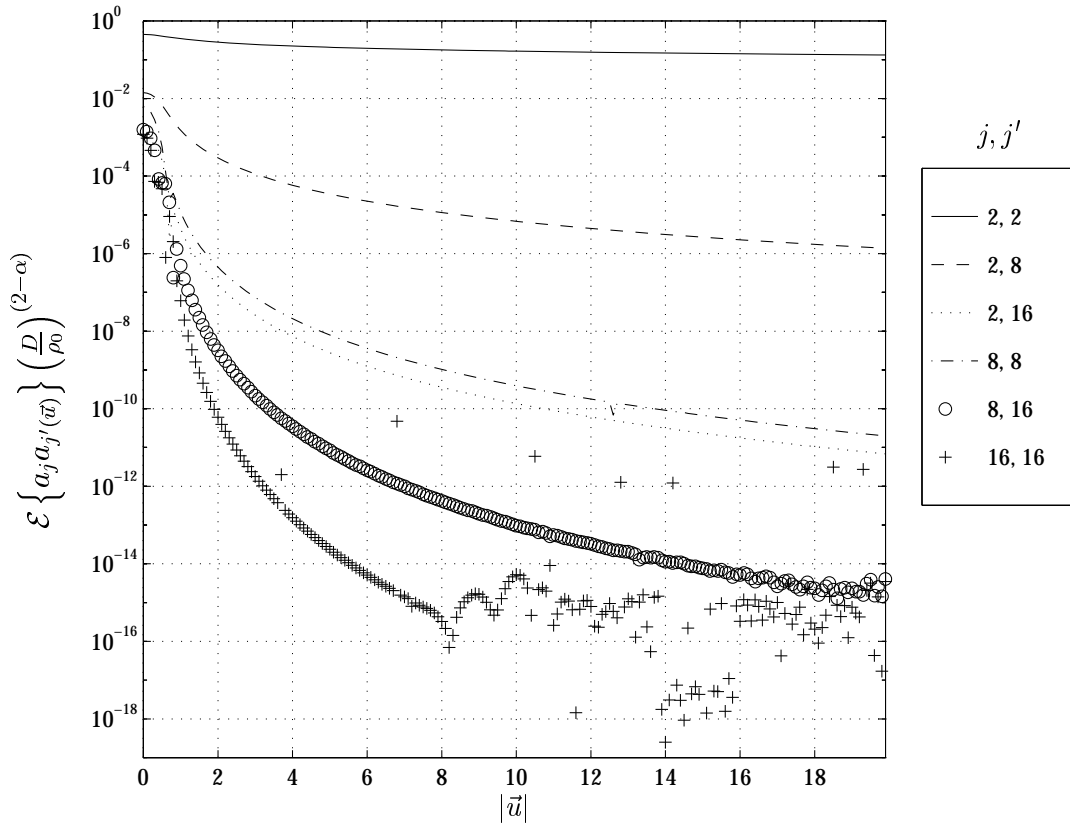


Figure A.27 $\mathcal{E} \left\{ a_j a_{j'}(\vec{u}) \right\} \left(\frac{D}{\rho_0} \right)^{(2-\alpha)}$, even modes, $\theta_0 = 90^\circ$, $L_0/D = \infty$, $\alpha = 3.6667$

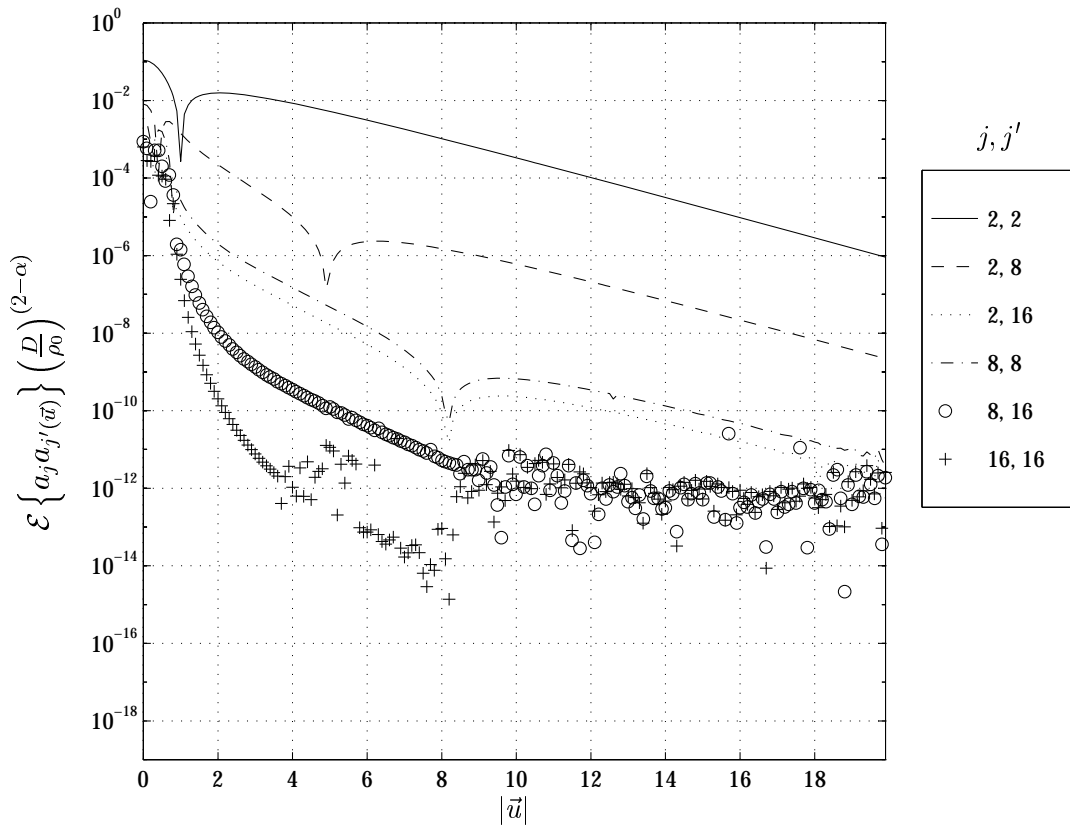


Figure A.28 $\mathcal{E} \left\{ a_j a_{j'}(\vec{u}) \right\} \left(\frac{D}{\rho_0} \right)^{(2-\alpha)}$, even modes, $\theta_0 = 0^\circ$, $L_0/D = 10.00$, $\alpha = 3.8000$

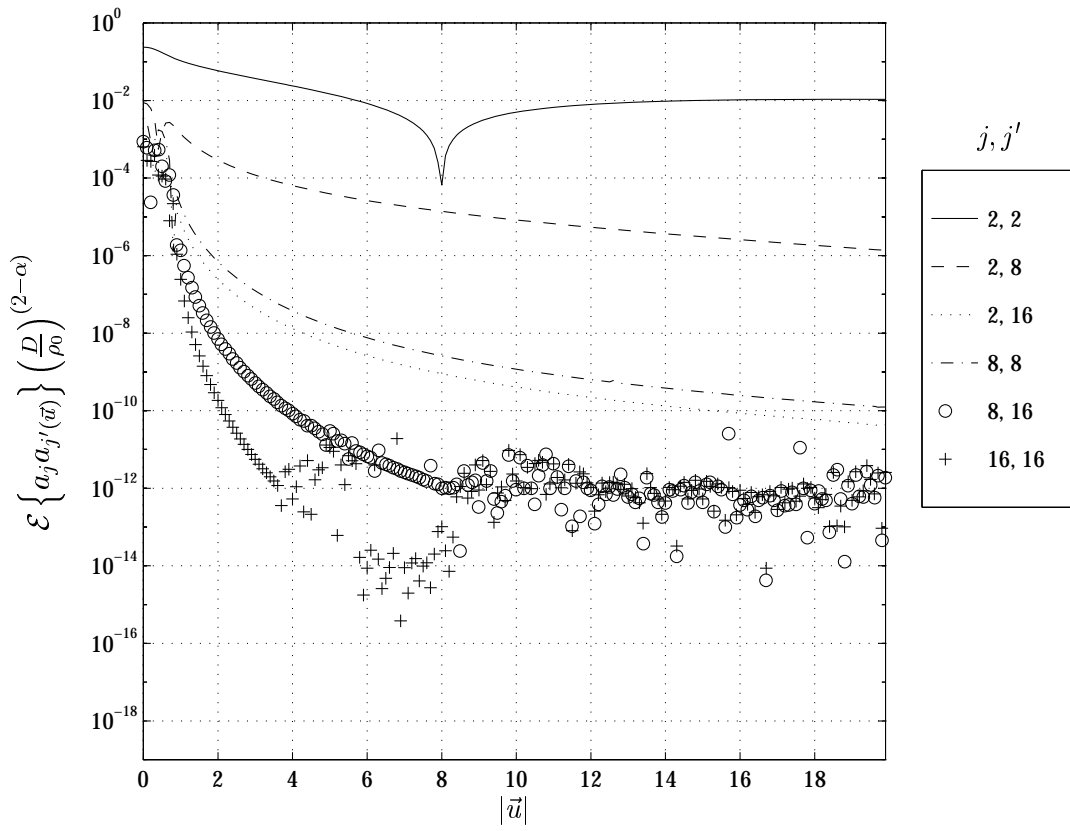


Figure A.29 $\mathcal{E} \left\{ a_j a_{j'}(\vec{u}) \right\} \left(\frac{D}{\rho_0} \right)^{(2-\alpha)}$, even modes, $\theta_0 = 0^\circ$, $L_0/D = 100.00$, $\alpha = 3.8000$

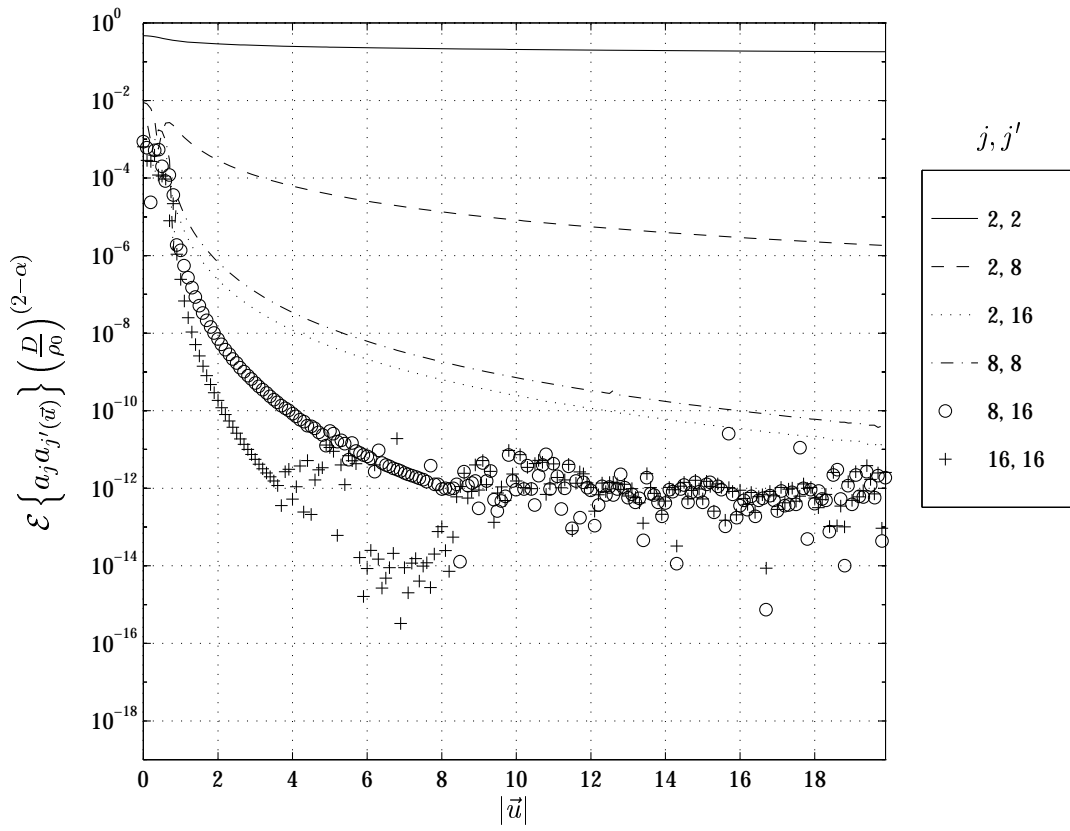


Figure A.30 $\mathcal{E} \left\{ a_j a_{j'}(\vec{u}) \right\} \left(\frac{D}{\rho_0} \right)^{(2-\alpha)}$, even modes, $\theta_0 = 0^\circ$, $L_0/D = \infty$, $\alpha = 3.8000$

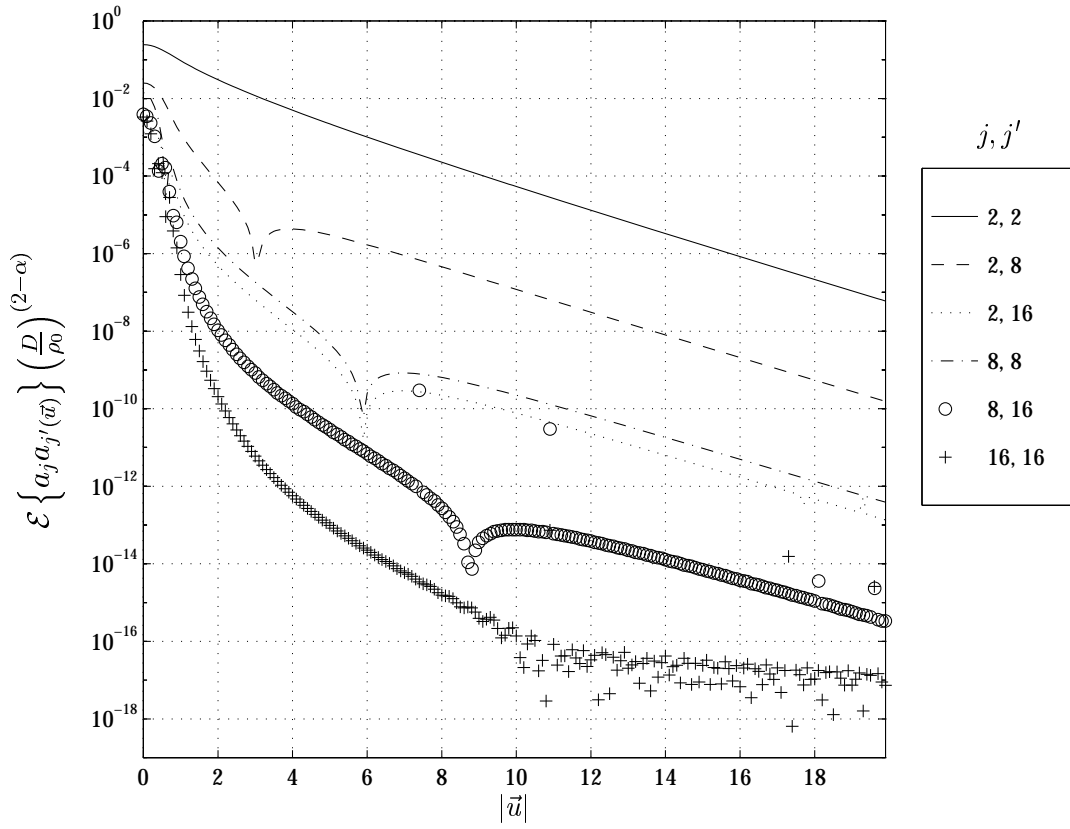


Figure A.31 $\mathcal{E} \left\{ a_j a_{j'}(\vec{u}) \right\} \left(\frac{D}{\rho_0} \right)^{(2-\alpha)}$, even modes, $\theta_0 = 90^\circ$, $L_0/D = 10.00$, $\alpha = 3.3000$

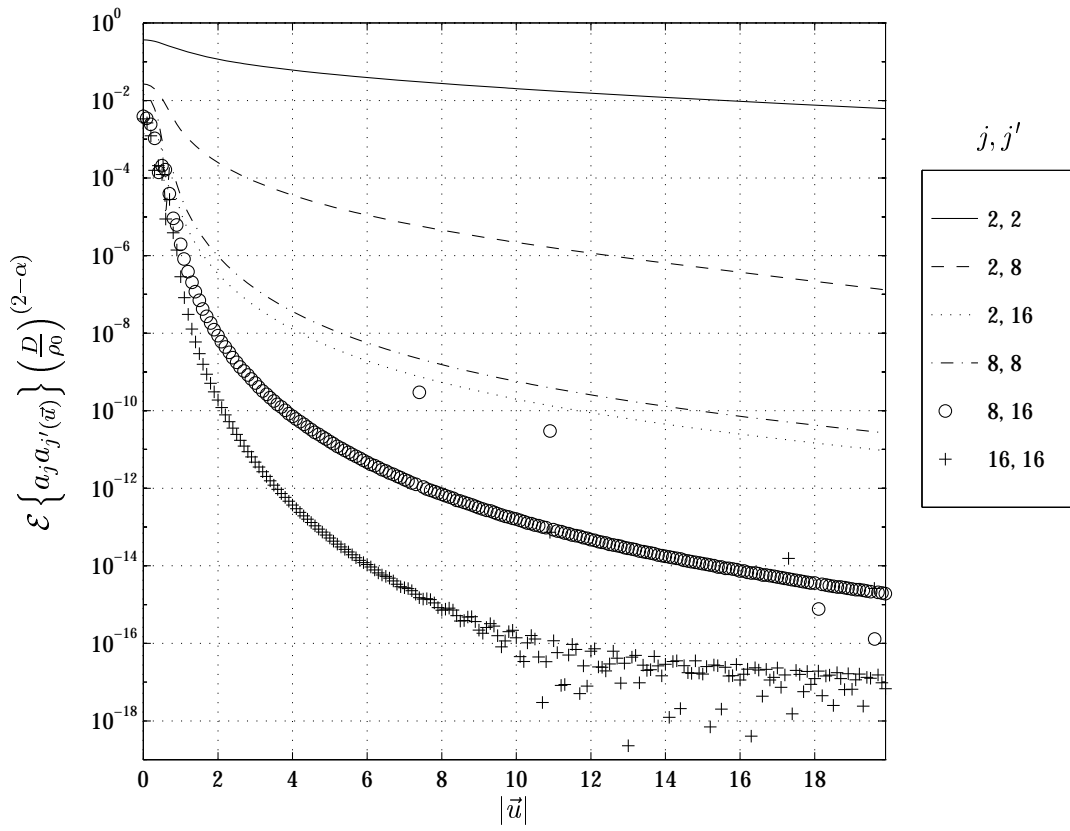


Figure A.32 $\mathcal{E} \left\{ a_j a_{j'}(\vec{u}) \right\} \left(\frac{D}{\rho_0} \right)^{(2-\alpha)}$, even modes, $\theta_0 = 90^\circ$, $L_0/D = 100.00$, $\alpha = 3.3000$

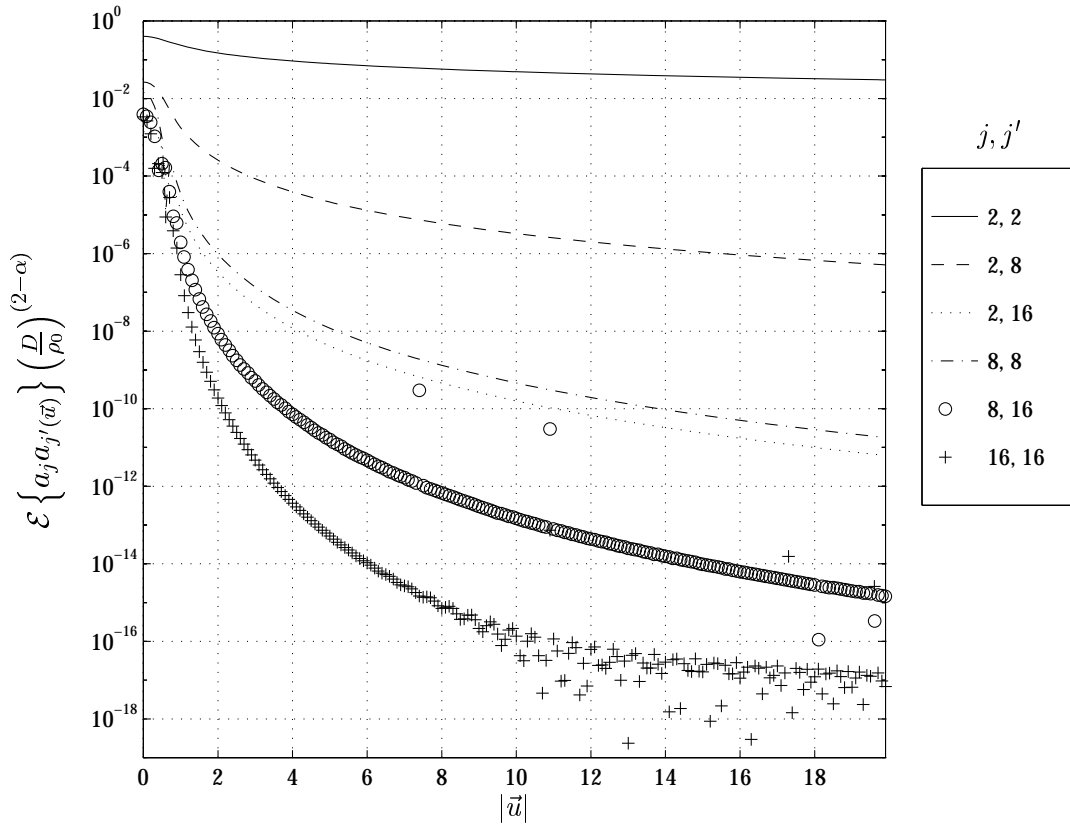


Figure A.33 $\mathcal{E} \left\{ a_j a_{j'}(\vec{u}) \right\} \left(\frac{D}{\rho_0} \right)^{(2-\alpha)}$, even modes, $\theta_0 = 90^\circ$, $L_0/D = \infty$, $\alpha = 3.3000$

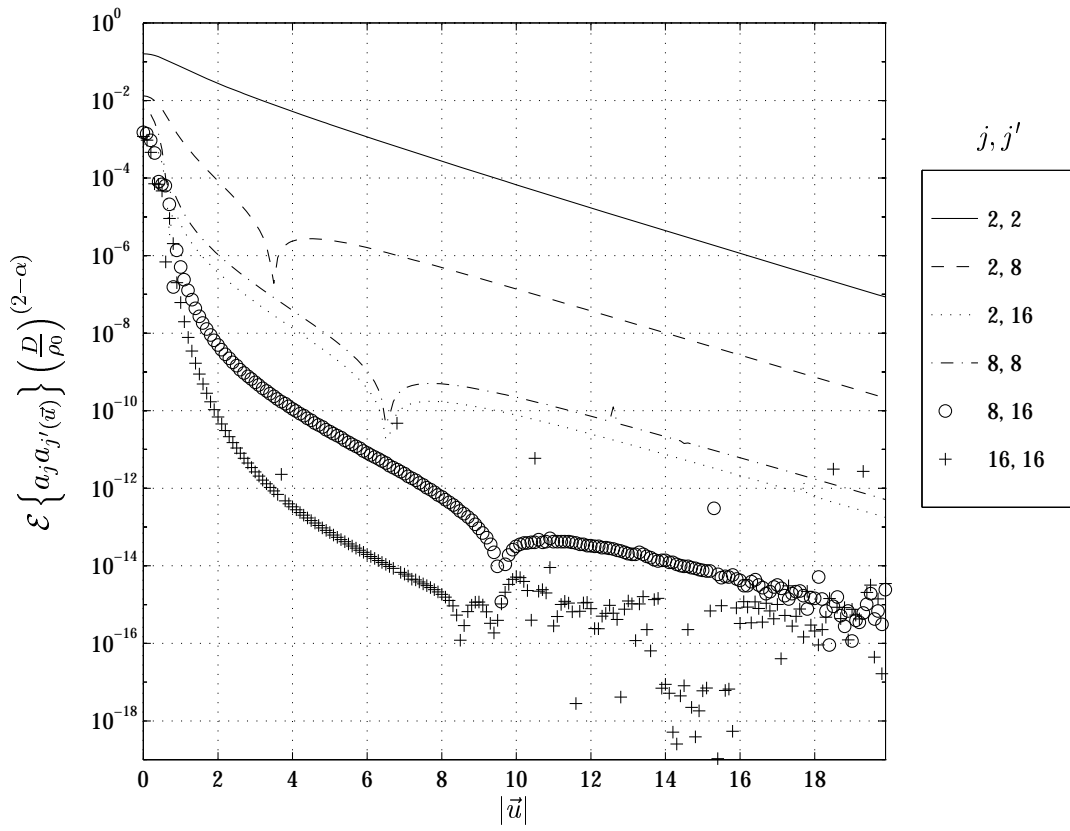


Figure A.34 $\mathcal{E} \left\{ a_j a_{j'}(\vec{u}) \right\} \left(\frac{D}{\rho_0} \right)^{(2-\alpha)}$, even modes, $\theta_0 = 90^\circ$, $L_0/D = 10.00$, $\alpha = 3.6667$

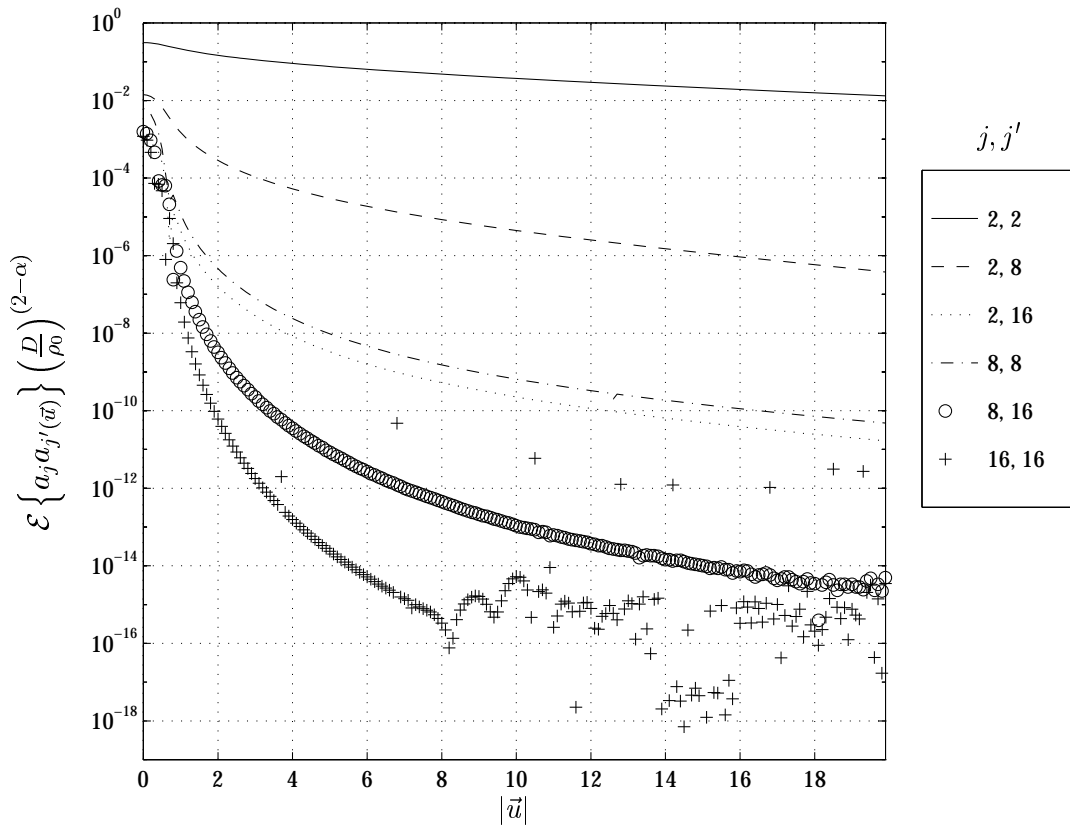


Figure A.35 $\mathcal{E} \left\{ a_j a_{j'}(\vec{u}) \right\} \left(\frac{D}{\rho_0} \right)^{(2-\alpha)}$, even modes, $\theta_0 = 90^\circ$, $L_0/D = 100.00$, $\alpha = 3.6667$

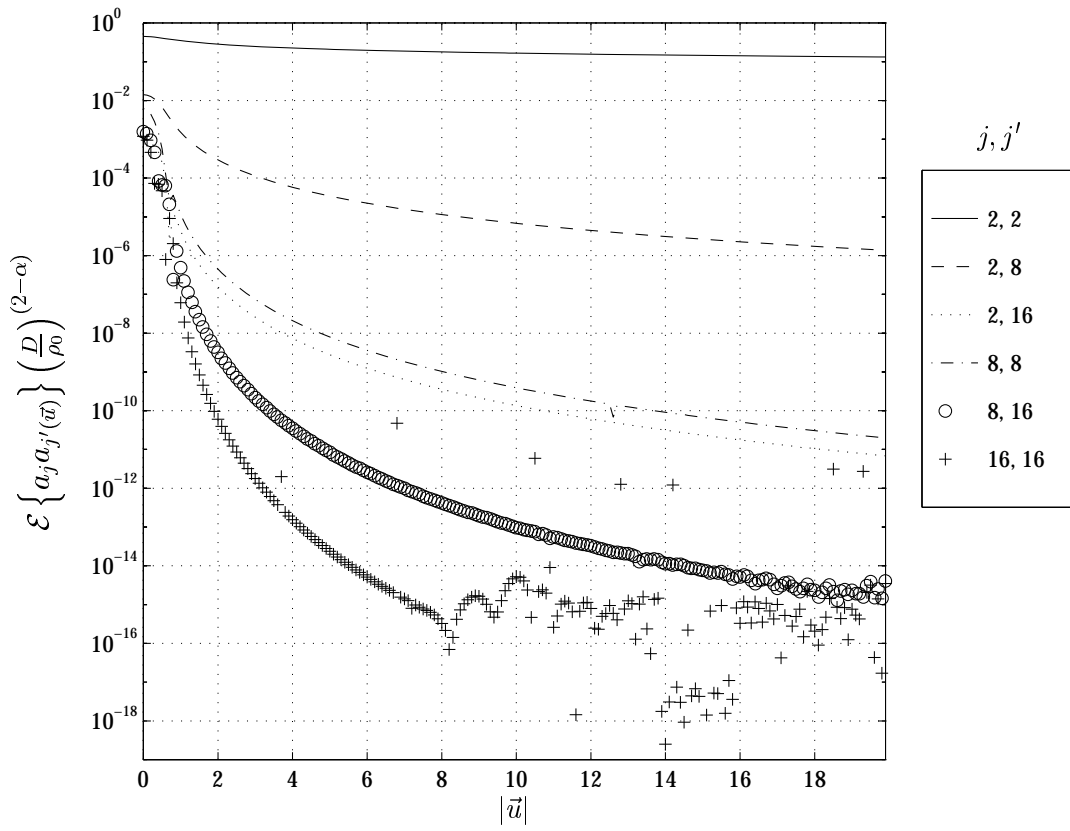


Figure A.36 $\mathcal{E} \left\{ a_j a_{j'}(\vec{u}) \right\} \left(\frac{D}{\rho_0} \right)^{(2-\alpha)}$, even modes, $\theta_0 = 90^\circ$, $L_0/D = \infty$, $\alpha = 3.6667$

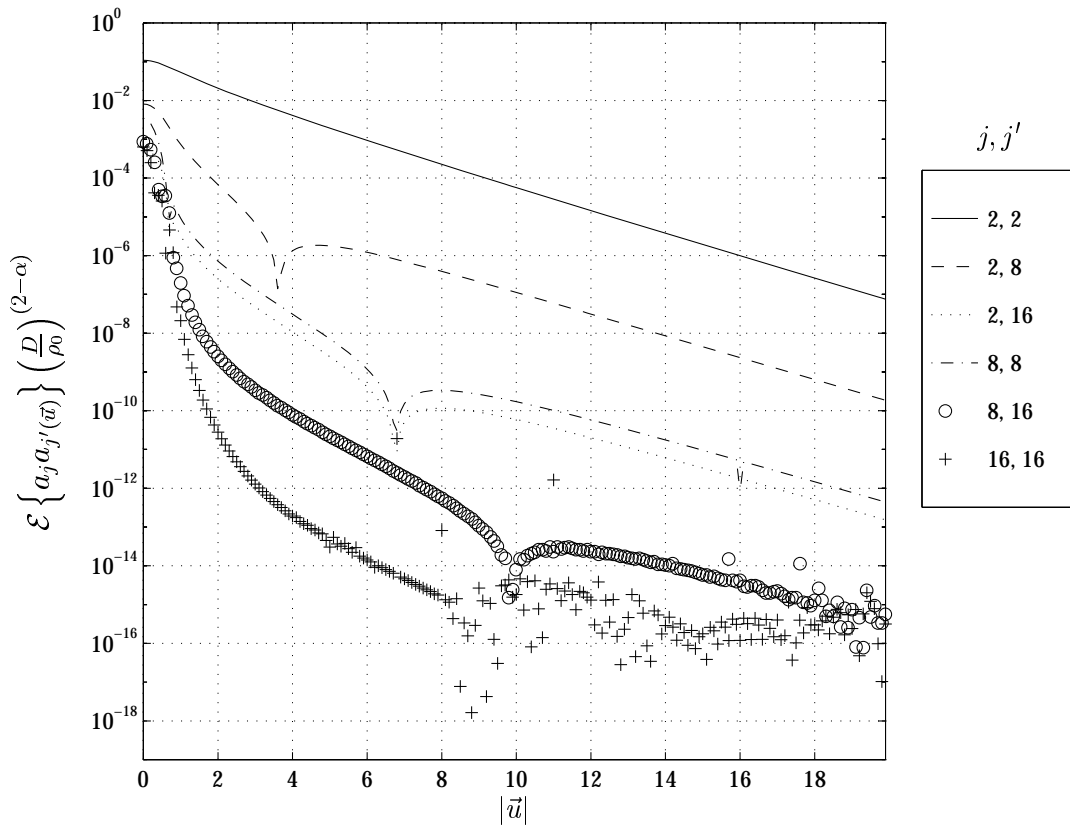


Figure A.37 $\mathcal{E} \left\{ a_j a_{j'}(\vec{u}) \right\} \left(\frac{D}{\rho_0} \right)^{(2-\alpha)}$, even modes, $\theta_0 = 90^\circ$, $L_0/D = 10.00$, $\alpha = 3.8000$

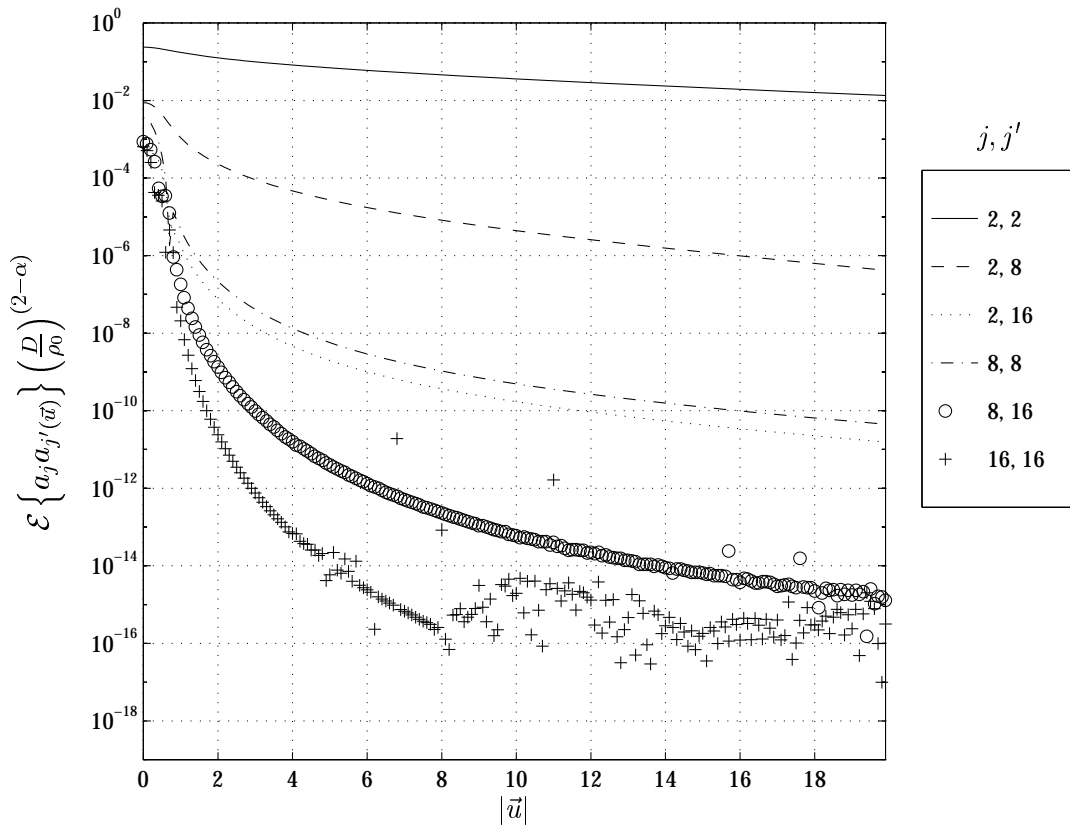


Figure A.38 $\mathcal{E} \left\{ a_j a_{j'}(\vec{u}) \right\} \left(\frac{D}{\rho_0} \right)^{(2-\alpha)}$, even modes, $\theta_0 = 90^\circ$, $L_0/D = 100.00$, $\alpha = 3.8000$

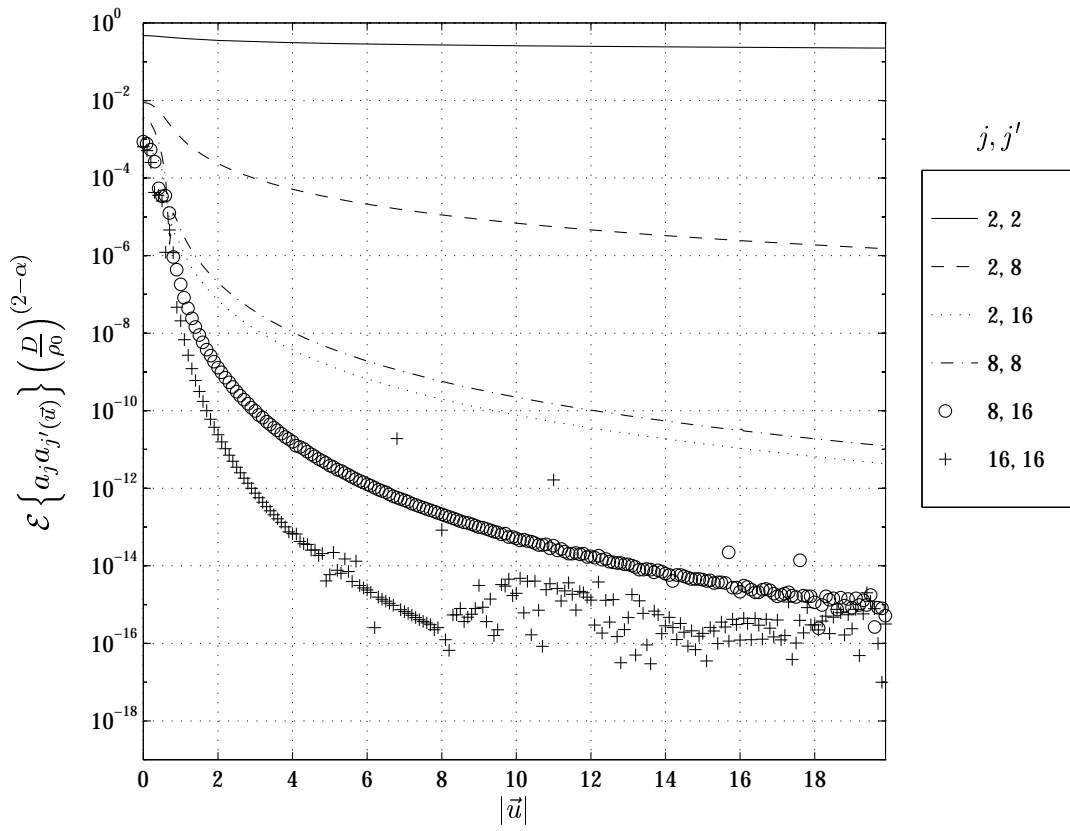


Figure A.39 $\mathcal{E} \left\{ a_j a_{j'}(\vec{u}) \right\} \left(\frac{D}{\rho_0} \right)^{(2-\alpha)}$, even modes, $\theta_0 = 90^\circ$, $L_0/D = \infty$, $\alpha = 3.8000$

Appendix B. Zernike Expansion Coefficient Covariance Tables

Noll's Eqns. (25) and (A2) in Ref. [8] give the closed form solution for the covariance between any two Zernike expansion coefficients, $\mathcal{E} \{a_j a_{j'}^*\}$, for atmospheric induced phase over a single subaperture. Noll's results are limited to a 11/3 power law with infinite outer scale. Winker's Eqn. (1) in Ref. [22] gives a closed form solution to $\mathcal{E} \{a_j^2\}$ for an 11/3 power law and finite outer scale. Setting $\vec{u} = 0$ in our Eqn. (2.18), $\mathcal{E} \{a_j a_{j'}^*\}$ may be numerically computed for *arbitrary powers laws and finite outer scale*. Tables B.2 through B.31 present selected numerical evaluations of $\mathcal{E} \{a_j a_{j'}^*\}$ as summarized in Tab. B.1

Table	α	L_0/D	Table	α	L_0/D
B.2	3.1	1	B.17	11/3	1
B.3	3.1	5	B.16	11/3	5
B.4	3.1	10	B.17	11/3	10
B.5	3.1	100	B.20	11/3	100
B.6	3.1	∞	B.21	11/3	∞
B.7	3.2	1	B.22	3.8	1
B.8	3.2	5	B.23	3.8	5
B.9	3.2	10	B.24	3.8	10
B.10	3.2	100	B.25	3.8	100
B.11	3.2	∞	B.26	3.8	∞
B.12	3.4	1	B.27	3.9	1
B.13	3.4	5	B.28	3.9	5
B.14	3.4	10	B.29	3.9	10
B.15	3.4	100	B.30	3.9	100
B.16	3.4	∞	B.31	3.9	∞

Table B.1 Summarization of Tables B.2 through B.31 listing $\mathcal{E} \{a_j a_{j'}^*\} \left(\frac{D}{\rho_0}\right)^{2-\alpha}$ for various turbulence power laws and outer scale.

The turbulence power law, α , determines how the power in the random process (the turbulence induced phase) is distributed as a function of Zernike mode order. The ratio of turbulence outer scale to subaperture diameter, L_0/D , determines the rate of correlation roll-off. For infinite outer scale, the piston variance, $\mathcal{E} \{a_1^2\}$, is infinite [8]. This causes the numerical integration to fail, as denoted in the tables by a question mark, for the piston variance when considering infinite outer scale. The “blank” table elements are zero.

	1	2	3	4	5	6	7	8	9	10	11	12
1	0.050213			-0.010201							-0.000399	
2		0.028387						-0.007338				
3			0.028387				-0.007338					
4	-0.010201			0.015906							-0.004724	
5					0.015906							
6						0.015906						-0.004724
7			-0.007338				0.009188					
8		-0.007338						0.009188				
9									0.009188			
10										0.009188		
11	-0.000399			-0.004724							0.005560	
12						-0.004724						0.005560

Table B.2 $\mathcal{E} \{a_j a_{j'}\} \left(\frac{D}{\rho_0}\right)^{2-\alpha}$ for $\alpha = 3.100$ and $\frac{L_0}{D} = 1.00$.

	1	2	3	4	5	6	7	8	9	10	11	12
1	1.335123			-0.095702							0.002851	
2		0.195475						-0.027639				
3			0.195475				-0.027639					
4	-0.095702			0.049258							-0.010827	
5					0.049258							
6						0.049258						-0.010827
7			-0.027639				0.018558					
8		-0.027639						0.018558				
9									0.018558			
10										0.018558		
11	0.002851			-0.010827							0.008875	
12						-0.010827						0.008875

Table B.3 $\mathcal{E} \{a_j a_{j'}\} \left(\frac{D}{\rho_0}\right)^{2-\alpha}$ for $\alpha = 3.100$ and $\frac{L_0}{D} = 5.00$.

	1	2	3	4	5	6	7	8	9	10	11	12
1	3.649597			-0.134876							0.003566	
2		0.265769						-0.030644				
3			0.265769				-0.030644					
4	-0.134876			0.053825							-0.011296	
5					0.053825							
6						0.053825						-0.011296
7			-0.030644				0.019237					
8		-0.030644						0.019237				
9									0.019237			
10										0.019237		
11	0.003566			-0.011296							0.009049	
12						-0.011296						0.009049

Table B.4 $\mathcal{E} \{a_j a_{j'}\} \left(\frac{D}{\rho_0}\right)^{2-\alpha}$ for $\alpha = 3.100$ and $\frac{L_0}{D} = 10.00$.

	1	2	3	4	5	6	7	8	9	10	11	12
1	57.178109			-0.189338							0.003921	
2		0.361194						-0.032035				
3			0.361194				-0.032035					
4	-0.189338			0.055904							-0.011465	
5					0.055904							
6						0.055904						-0.011465
7			-0.032035				0.019481					
8		-0.032035						0.019481				
9									0.019481			
10										0.019481		
11	0.003921			-0.011465							0.009109	
12						-0.011465						0.009109

Table B.5 $\mathcal{E} \{a_j a_{j'}\} \left(\frac{D}{\rho_0}\right)^{2-\alpha}$ for $\alpha = 3.100$ and $\frac{L_0}{D} = 100.00$.

	1	2	3	4	5	6	7	8	9	10	11	12
1	?			-0.198463							0.003926	
2		0.377013						-0.032053				
3			0.377013				-0.032053					
4	-0.198463			0.055931							-0.011467	
5					0.055931							
6						0.055931						-0.011467
7			-0.032053				0.019483					
8		-0.032053						0.019483				
9									0.019483			
10										0.019483		
11	0.003926			-0.011467							0.009110	
12						-0.011467						0.009110

Table B.6 $\mathcal{E}\{a_j a_{j'}\} \left(\frac{D}{\rho_0}\right)^{2-\alpha}$ for $\alpha = 3.100$ and $\frac{L_0}{D} = \infty$. A question mark indicates that the numerical integration failed to converge.

	1	2	3	4	5	6	7	8	9	10	11	12
1	0.044059			-0.008941							-0.000297	
2		0.024553						-0.006328				
3			0.024553				-0.006328					
4	-0.008941			0.013540							-0.004008	
5					0.013540							
6						0.013540						-0.004008
7			-0.006328				0.007697					
8		-0.006328						0.007697				
9									0.007697			
10										0.007697		
11	-0.000297			-0.004008							0.004586	
12						-0.004008						0.004586

Table B.7 $\mathcal{E} \{a_j a_{j'}\} \left(\frac{D}{\rho_0}\right)^{2-\alpha}$ for $\alpha = 3.200$ and $\frac{L_0^0}{D} = 1.00$.

	1	2	3	4	5	6	7	8	9	10	11	12
1	1.332826			-0.091201							0.002801	
2		0.184403						-0.025080				
3			0.184403				-0.025080					
4	-0.091201			0.044172							-0.009476	
5					0.044172							
6						0.044172						-0.009476
7			-0.025080				0.016044					
8		-0.025080						0.016044				
9									0.016044			
10										0.016044		
11	0.002801			-0.009476							0.007472	
12						-0.009476						0.007472

Table B.8 $\mathcal{E} \{a_j a_{j'}\} \left(\frac{D}{\rho_0}\right)^{2-\alpha}$ for $\alpha = 3.200$ and $\frac{L_0^0}{D} = 5.00$.

	1	2	3	4	5	6	7	8	9	10	11	12
1	3.850011			-0.131720							0.003508	
2		0.256936						-0.027999				
3			0.256936				-0.027999					
4	-0.131720			0.048589							-0.009908	
5					0.048589							
6						0.048589						-0.009908
7			-0.027999				0.016667					
8		-0.027999						0.016667				
9									0.016667			
10										0.016667		
11	0.003508			-0.009908							0.007626	
12						-0.009908						0.007626

Table B.9 $\mathcal{E} \{a_j a_{j'}\} \left(\frac{D}{\rho_0}\right)^{2-\alpha}$ for $\alpha = 3.200$ and $\frac{L_0}{D} = 10.00$.

	1	2	3	4	5	6	7	8	9	10	11	12
1	74.079729			-0.193801							0.003869	
2		0.365548						-0.029387				
3			0.365548				-0.029387					
4	-0.193801			0.050655							-0.010065	
5					0.050655							
6						0.050655						-0.010065
7			-0.029387				0.016892					
8		-0.029387						0.016892				
9									0.016892			
10										0.016892		
11	0.003869			-0.010065							0.007679	
12						-0.010065						0.007679

Table B.10 $\mathcal{E} \{a_j a_{j'}\} \left(\frac{D}{\rho_0}\right)^{2-\alpha}$ for $\alpha = 3.200$ and $\frac{L_0}{D} = 100.00$.

	1	2	3	4	5	6	7	8	9	10	11	12
1	?			-0.207083							0.003875	
2		0.388567						-0.029406				
3			0.388567				-0.029406					
4	-0.207083			0.050683							-0.010066	
5					0.050683							
6						0.050683						-0.010066
7			-0.029406				0.016894					
8		-0.029406						0.016894				
9									0.016894			
10										0.016894		
11	0.003875			-0.010066							0.007679	
12						-0.010066						0.007679

Table B.11 $\mathcal{E} \{a_j a_j\} \left(\frac{D}{\rho_0}\right)^{2-\alpha}$ for $\alpha = 3.200$ and $\frac{L_0}{D} = \infty$. A question mark indicates that the numerical integration failed to converge.

	1	2	3	4	5	6	7	8	9	10	11	12
1	0.032006			-0.006472							-0.000145	
2		0.017339						-0.004434				
3			0.017339				-0.004434					
4	-0.006472			0.009265							-0.002720	
5					0.009265							
6						0.009265						-0.002720
7			-0.004434				0.005100					
8		-0.004434						0.005100				
9									0.005100			
10										0.005100		
11	-0.000145			-0.002720							0.002947	
12						-0.002720						0.002947

Table B.12 $\mathcal{E} \{a_j a_{j'}\} \left(\frac{D}{\rho_0}\right)^{2-\alpha}$ for $\alpha = 3.400$ and $\frac{L_0}{D} = 1.00$.

	1	2	3	4	5	6	7	8	9	10	11	12
1	1.256955			-0.078395							0.002499	
2		0.155630						-0.019529				
3			0.155630				-0.019529					
4	-0.078395			0.033655							-0.006855	
5					0.033655							
6						0.033655						-0.006855
7			-0.019529				0.011347					
8		-0.019529						0.011347				
9									0.011347			
10										0.011347		
11	0.002499			-0.006855							0.005007	
12						-0.006855						0.005007

Table B.13 $\mathcal{E} \{a_j a_{j'}\} \left(\frac{D}{\rho_0}\right)^{2-\alpha}$ for $\alpha = 3.400$ and $\frac{L_0}{D} = 5.00$.

	1	2	3	4	5	6	7	8	9	10	11	12
1	4.065806			-0.119397							0.003151	
2		0.228718						-0.022136				
3			0.228718				-0.022136					
4	-0.119397			0.037568							-0.007202	
5					0.037568							
6						0.037568						-0.007202
7			-0.022136				0.011843					
8		-0.022136						0.011843				
9									0.011843			
10										0.011843		
11	0.003151			-0.007202							0.005121	
12						-0.007202						0.005121

Table B.14 $\mathcal{E} \{a_j a_{j'}\} \left(\frac{D}{\rho_0}\right)^{2-\alpha}$ for $\alpha = 3.400$ and $\frac{L_0^0}{D} = 10.00$.

	1	2	3	4	5	6	7	8	9	10	11	12
1	119.118810			-0.196789							0.003505	
2		0.363780						-0.023455				
3			0.363780				-0.023455					
4	-0.196789			0.039515							-0.007330	
5					0.039515							
6						0.039515						-0.007330
7			-0.023455				0.012023					
8		-0.023455						0.012023				
9									0.012023			
10										0.012023		
11	0.003505			-0.007330							0.005160	
12						-0.007330						0.005160

Table B.15 $\mathcal{E} \{a_j a_{j'}\} \left(\frac{D}{\rho_0}\right)^{2-\alpha}$ for $\alpha = 3.400$ and $\frac{D}{\rho_0} = 100.00$.

	1	2	3	4	5	6	7	8	9	10	11	12
1	?			-0.225207							0.003511	
2		0.413015						-0.023474				
3			0.413015				-0.023474					
4	-0.225207			0.039544							-0.007331	
5					0.039544							
6						0.039544						-0.007331
7			-0.023474				0.012025					
8		-0.023474						0.012025				
9									0.012025			
10										0.012025		
11	0.003511			-0.007331							0.005160	
12						-0.007331						0.005160

Table B.16 $\mathcal{E} \{a_j a_j\} \left(\frac{D}{\rho_0}\right)^{2-\alpha}$ for $\alpha = 3.400$ and $\frac{L_0}{D} = \infty$. A question mark indicates that the numerical integration failed to converge.

	1	2	3	4	5	6	7	8	9	10	11	12
1	0.016812			-0.003374							-0.000033	
2		0.008777						-0.002216				
3			0.008777				-0.002216					
4	-0.003374			0.004499							-0.001302	
5					0.004499							
6						0.004499						-0.001302
7			-0.002216				0.002374					
8		-0.002216						0.002374				
9									0.002374			
10										0.002374		
11	-0.000033			-0.001302							0.001317	
12						-0.001302						0.001317

Table B.17 $\mathcal{E} \{a_j a_{j'}\} \left(\frac{D}{\rho_0}\right)^{2-\alpha}$ for $\alpha = \frac{11}{3}$ and $\frac{L_0}{D} = 1.00$.

	1	2	3	4	5	6	7	8	9	10	11	12
1	0.940439			-0.051899							0.001675	
2		0.100897						-0.011315				
3			0.100897				-0.011315					
4	-0.051899			0.019006							-0.003591	
5					0.019006							
6						0.019006						-0.003591
7			-0.011315				0.005786					
8		-0.011315						0.005786				
9									0.005786			
10										0.005786		
11	0.001675			-0.003591							0.002371	
12						-0.003591						0.002371

Table B.18 $\mathcal{E} \{a_j a_{j'}\} \left(\frac{D}{\rho_0}\right)^{2-\alpha}$ for $\alpha = \frac{11}{3}$ and $\frac{L_0}{D} = 5.00$.

	1	2	3	4	5	6	7	8	9	10	11	12
1	3.555503			-0.085591							0.002147	
2		0.160671						-0.013132				
3			0.160671				-0.013132					
4	-0.085591			0.021709							-0.003800	
5					0.021709							
6						0.021709						-0.003800
7			-0.013132				0.006081					
8		-0.013132						0.006081				
9									0.006081			
10										0.006081		
11	0.002147			-0.003800							0.002433	
12						-0.003800						0.002433

Table B.19 $\mathcal{E} \{a_j a_{j'}\} \left(\frac{D}{\rho_0}\right)^{2-\alpha}$ for $\alpha = \frac{11}{3}$ and $\frac{L_0}{D} = 10.00$.

	1	2	3	4	5	6	7	8	9	10	11	12
1	185.201300			-0.172147							0.002429	
2		0.311356						-0.014146				
3			0.311356				-0.014146					
4	-0.172147			0.023192							-0.003878	
5					0.023192							
6						0.023192						-0.003878
7			-0.014146				0.006190					
8		-0.014146						0.006190				
9									0.006190			
10										0.006190		
11	0.002429			-0.003878							0.002454	
12						-0.003878						0.002454

Table B.20 $\mathcal{E}\{a_j a_{j'}\} \left(\frac{D}{\rho_0}\right)^{2-\alpha}$ for $\alpha = \frac{11}{3}$ and $\frac{L_0}{D} = 100.00$.

	1	2	3	4	5	6	7	8	9	10	11	12
1	?			-0.251538							0.002434	
2		0.448879						-0.014164				
3			0.448879				-0.014164					
4	-0.251538			0.023218							-0.003879	
5					0.023218							
6						0.023218						-0.003879
7							0.006191					
8		-0.014164						0.006191				
9									0.006191			
10										0.006191		
11	0.002434			-0.003879							0.002454	
12						-0.003879						0.002454

Table B.21 $\mathcal{E} \{a_j a_j\} \left(\frac{D}{\rho_0}\right)^{2-\alpha}$ for $\alpha = \frac{11}{3}$ and $\frac{L_0^0}{D} = \infty$. A question mark indicates that the numerical integration failed to converge.

	1	2	3	4	5	6	7	8	9	10	11	12
1	0.009744			-0.001947							-0.000008	
2		0.004996						-0.001252				
3			0.004996				-0.001252					
4	-0.001947			0.002509							-0.000720	
5					0.002509							
6						0.002509						-0.000720
7			-0.001252				0.001296					
8		-0.001252						0.001296				
9									0.001296			
10										0.001296		
11	-0.000008			-0.000720							0.000705	
12						-0.000720						0.000705

Table B.22 $\mathcal{E} \{a_j a_{j'}\} \left(\frac{D}{\rho_0}\right)^{2-\alpha}$ for $\alpha = 3.800$ and $\frac{L_0}{D} = 1.00$.

	1	2	3	4	5	6	7	8	9	10	11	12
1	0.652068			-0.033878							0.001087	
2		0.065262						-0.006906				
3			0.065262				-0.006906					
4	-0.033878			0.011467							-0.002082	
5					0.011467							
6						0.011467						-0.002082
7			-0.006906				0.003313					
8		-0.006906						0.003313				
9									0.003313			
10										0.003313		
11	0.001087			-0.002082							0.001308	
12						-0.002082						0.001308

Table B.23 $\mathcal{E} \{a_j a_{j'}\} \left(\frac{D}{\rho_0}\right)^{2-\alpha}$ for $\alpha = 3.800$ and $\frac{L_0}{D} = 5.00$.

	1	2	3	4	5	6	7	8	9	10	11	12
1	2.670352			-0.058364							0.001409	
2		0.108616						-0.008125				
3			0.108616				-0.008125					
4	-0.058364			0.013272							-0.002211	
5					0.013272							
6						0.013272						-0.002211
7			-0.008125				0.003495					
8		-0.008125						0.003495				
9									0.003495			
10										0.003495		
11	0.001409			-0.002211							0.001344	
12						-0.002211						0.001344

Table B.24 $\mathcal{E} \{a_j a_{j'}\} \left(\frac{D}{\rho_0}\right)^{2-\alpha}$ for $\alpha = 3.800$ and $\frac{L_0}{D} = 10.00$.

	1	2	3	4	5	6	7	8	9	10	11	12
1	186.340090			-0.132721							0.001612	
2		0.237945						-0.008843				
3			0.237945				-0.008843					
4	-0.132721			0.014319							-0.002261	
5					0.014319							
6						0.014319						-0.002261
7			-0.008843				0.003564					
8		-0.008843						0.003564				
9									0.003564			
10										0.003564		
11	0.001612			-0.002261							0.001356	
12						-0.002261						0.001356

Table B.25 $\mathcal{E} \{a_j a_{j'}\} \left(\frac{D}{\rho_0}\right)^{2-\alpha}$ for $\alpha = 3.800$ and $\frac{D}{\rho_0} = 100.00$.

	1	2	3	4	5	6	7	8	9	10	11	12
1	?			-0.265780							0.001616	
2		0.468420						-0.008857				
3			0.468420				-0.008857					
4	-0.265780			0.014339							-0.002261	
5					0.014339							
6						0.014339						-0.002261
7							0.003565					
8		-0.008857						0.003565				
9									0.003565			
10										0.003565		
11	0.001616			-0.002261							0.001356	
12						-0.002261						0.001356

Table B.26 $\mathcal{E} \{a_j a_j\} \left(\frac{D}{\rho_0}\right)^{2-\alpha}$ for $\alpha = 3.800$ and $\frac{L_0}{D} = \infty$. A question mark indicates that the numerical integration failed to converge.

	1	2	3	4	5	6	7	8	9	10	11	12
1	0.004732			-0.000942							-0.000000	
2		0.002394						-0.000596				
3			0.002394				-0.000596					
4	-0.000942			0.001184							-0.000338	
5					0.001184							
6						0.001184						-0.000338
7			-0.000596				0.000602					
8		-0.000596						0.000602				
9									0.000602			
10										0.000602		
11	-0.000000			-0.000338							0.000322	
12						-0.000338						0.000322

Table B.27 $\mathcal{E} \{a_j a_{j'}\} \left(\frac{D}{\rho_0}\right)^{2-\alpha}$ for $\alpha = 3.900$ and $\frac{L_0}{D} = 1.00$.

	1	2	3	4	5	6	7	8	9	10	11	12
1	0.362566			-0.018012							0.000573	
2		0.034478						-0.003491				
3			0.034478				-0.003491					
4	-0.018012			0.005749							-0.001012	
5					0.005749							
6						0.005749						-0.001012
7			-0.003491				0.001596					
8		-0.003491						0.001596				
9									0.001596			
10										0.001596		
11	0.000573			-0.001012							0.000612	
12						-0.001012						0.000612

Table B.28 $\mathcal{E} \{a_j a_{j'}\} \left(\frac{D}{\rho_0}\right)^{2-\alpha}$ for $\alpha = 3.900$ and $\frac{L_0}{D} = 5.00$.

	1	2	3	4	5	6	7	8	9	10	11	12
1	1.577670			-0.032118							0.000749	
2		0.059419						-0.004152				
3			0.059419				-0.004152					
4	-0.032118			0.006726							-0.001078	
5					0.006726							
6						0.006726						-0.001078
7			-0.004152				0.001689					
8		-0.004152						0.001689				
9									0.001689			
10										0.001689		
11	0.000749			-0.001078							0.000630	
12						-0.001078						0.000630

Table B.29 $\mathcal{E} \{a_j a_{j'}\} \left(\frac{D}{\rho_0}\right)^{2-\alpha}$ for $\alpha = 3.900$ and $\frac{L_0^0}{D} = 10.00$.

	1	2	3	4	5	6	7	8	9	10	11	12
1	137.306270			-0.080958							0.000866	
2		0.144317						-0.004560				
3			0.144317				-0.004560					
4	-0.080958			0.007318							-0.001104	
5					0.007318							
6						0.007318						-0.001104
7			-0.004560				0.001725					
8		-0.004560						0.001725				
9									0.001725			
10										0.001725		
11	0.000866			-0.001104							0.000636	
12						-0.001104						0.000636

Table B.30 $\mathcal{E} \{a_j a_{j'}\} \left(\frac{D}{\rho_0}\right)^{2-\alpha}$ for $\alpha = 3.900$ and $\frac{D}{\rho_0} = 100.00$.

	1	2	3	4	5	6	7	8	9	10	11	12
1	?			-2.527445							0.000869	
2		?						-0.004569				
3			?				-0.004569					
4	-2.527445			0.007331							-0.001104	
5					0.007331							
6						0.007331						-0.001104
7			-0.004569				0.001725					
8		-0.004569						0.001725				
9									0.001725			
10										0.001725		
11	0.000869			-0.001104							0.000636	
12						-0.001104						0.000636

Table B.31 $\mathcal{E} \{a_j a_j\} \left(\frac{D}{\rho_0}\right)^{2-\alpha}$ for $\alpha = 3.900$ and $\frac{L_0}{D} = \infty$. A question mark indicates that the numerical integration failed to converge.

Appendix C. SSF Estimator Second Moment Simplification

To simplify the expected value within Eqn. (3.11), the symbolic computation program Mathematica [23] is used. The program listed below substitutes the slope measurement model of Eqn. (3.2) into Eqn. (3.11), multiplies out all terms, applies the signal-noise assumptions listed in Sec. (3.2), applies the joint moments theorem of Eqn. (3.15), and rewrites the resulting expression in terms of the slope correlation function defined by Eqn. (1.11) and represented by $G[\dots]$.

```
(*-----  
This Mathematica code helps determine the second moment for the  
slope structure function estimator.  
  
x2-x1=p  
x4-x3=p  
  
case1: x1=x3 and x2=x4 and delta_time=0  
case2: x2=x3 and delta_time=0  
case3: x4=x1 and delta_time=0  
case4: x1,x2,x3,and x4 are four unique location (no overlap)  
  
Toby D. Reeves, July-Sept 1996  
)  
(*-----  
)  
Remove["Global`*"]  
(*-----  
Define the Expected Value Operator  
)  
EV[a_+b_] := EV[a]+EV[b]  
EV[a_Integer b_] := a EV[b]  
(*-----  
Define a Wrapper zmgrv[ ] for Zero Mean Gaussian Random Variable,  
then define rules that apply to zmgrv.  
)  
Format[zmgrv[x_]] := x  
EV[u1_zmgrv u2_zmgrv u3_zmgrv u4_zmgrv] := (  
    EV[u1 u2] EV[u3 u4] +  
    EV[u1 u3] EV[u2 u4] +  
    EV[u1 u4] EV[u2 u3]  
)  
EV[u1_zmgrv u1_zmgrv u3_zmgrv u4_zmgrv] := (  
    EV[u1 u2] EV[u3 u4] +
```

```

      EV[u1 u3] EV[u2 u4] +
      EV[u1 u4] EV[u2 u3]
    )/.u2->u1
EV[u1_zmgrv u1_zmgrv u3_zmgrv u3_zmgrv]:= (
      EV[u1 u2] EV[u3 u4] +
      EV[u1 u3] EV[u2 u4] +
      EV[u1 u4] EV[u2 u3]
    )/.{u2->u1,u4->u3}
EV[u1_zmgrv u1_zmgrv u1_zmgrv u4_zmgrv]:= (
      EV[u1 u2] EV[u3 u4] +
      EV[u1 u3] EV[u2 u4] +
      EV[u1 u4] EV[u2 u3]
    )/.{u2->u1,u3->u1}
EV[u1_zmgrv u1_zmgrv u1_zmgrv u1_zmgrv]:= (
      EV[u1 u2] EV[u3 u4] +
      EV[u1 u3] EV[u2 u4] +
      EV[u1 u4] EV[u2 u3]
    )/.{u2->u1,u3->u1,u4->u1}
(*-----
Properties of the Noise
*)
noiseRules= {
      EV[zmgrv[n[a_]] zmgrv[n[a_]]]->sig^2,
      EV[zmgrv[n[a_]] zmgrv[n[b_]]]->0,
      EV[zmgrv[n[a_]]]->0,
      EV[zmgrv[n[a_]] zmgrv[s[x_]]]->0
};
(*-----
      Apply these rules to my problem of calculating the expectation
      within the Second Moment formula
*)
f1= (a-b)^2 (c-d)^2 /.
      {a->zmgrv[s[x1]]+zmgrv[n[x1]],
      b->zmgrv[s[x2]]+zmgrv[n[x2]],
      c->zmgrv[s[x3]]+zmgrv[n[x3]],
      d->zmgrv[s[x4]]+zmgrv[n[x4]]
};
BigMess=EV[Expand[f1]];
convertRule={
      EV[zmgrv[s[x_]]^2]      ->G[0],

      EV[zmgrv[s[x1]] zmgrv[s[x2]]]  ->G[x2-x1],
      EV[zmgrv[s[x3]] zmgrv[s[x4]]]  ->G[x4-x3],

      EV[zmgrv[s[x1]] zmgrv[s[x3]]]  ->G[x3-x1],

```

```

        EV[zmgrv[s[x2]] zmgrv[s[x4]]]    ->G[x4-x2],

        EV[zmgrv[s[x1]] zmgrv[s[x4]]]    ->G[x4-x1],
        EV[zmgrv[s[x2]] zmgrv[s[x3]]]    ->G[x3-x2]
};

(* apply geometry and noiseRules for each case *)
case1Rule={x1->x3,x2->x4};
case1a=(BigMess/.case1Rule)/.noiseRules;

case2Rule={x2->x3};
case2a=(BigMess/.case2Rule)/.noiseRules;

case3Rule={x1->x4};
case3a=(BigMess/.case3Rule)/.noiseRules;

case4Rule={};
case4a=(BigMess/.case4Rule)/.noiseRules;

(* write in Gamma notation *)
case1b=case1a/.convertRule;
case2b=case2a/.convertRule;
case3b=case3a/.convertRule;
case4b=case4a/.convertRule;

(* use geometry to simplify more *)
geoRule={x2-x1->p,x4-x3->p,x4-x2->x3-x1} (*valid all cases*)
case1c=ExpandAll[case1b/.geoRule];
case2c=ExpandAll[(case2b/.geoRule)/.{x3-x1->p,x4-x1->2p}];
case3c=ExpandAll[(case3b/.geoRule)/.{x3-x1->-p,x3-x2->-2p}];
case4c=ExpandAll[case4b/.geoRule];

(* We know that for our case G[p]=G[-p] *)
q=case3c
case3c=case3c/.{-2p -> 2p, -p -> p};

(*-----
Drum roll please!!
*)
sout=OpenWrite["sf5n.txt",FormatType->OutputForm,PageWidth->75]

Write[sout,"BigMess= ",ExpandAll[BigMess]]

Write[sout,"case1a= ",case1a]
Write[sout,"case2a= ",case2a]

```

```
Write[sout,"case3a= ",case3a]
Write[sout,"case4a= ",case4a]
```

```
Write[sout,"case1b= ",case1b]
Write[sout,"case2b= ",case2b]
Write[sout,"case3b= ",case3b]
Write[sout,"case4b= ",case4b]
```

```
Write[sout,"case1c= ",case1c]
Write[sout,"case2c= ",case2c]
Write[sout,"case3c= ",case3c]
Write[sout,"case4c= ",case4c]
```

```
Close[sout]
```

$$\begin{aligned}
 \text{BigMess} &= 2 \text{EV}[n[x1] n[x3]]^2 - 4 \text{EV}[n[x1] n[x3]] \text{EV}[n[x2] n[x3]] + \\
 &> 2 \text{EV}[n[x2] n[x3]]^2 + \text{EV}[n[x1]]^2 \text{EV}[n[x3]]^2 - \\
 &> 2 \text{EV}[n[x1] n[x2]] \text{EV}[n[x3]]^2 + \text{EV}[n[x2]]^2 \text{EV}[n[x3]]^2 - \\
 &> 4 \text{EV}[n[x1] n[x3]] \text{EV}[n[x1] n[x4]] + \\
 &> 4 \text{EV}[n[x2] n[x3]] \text{EV}[n[x1] n[x4]] + 2 \text{EV}[n[x1] n[x4]]^2 + \\
 &> 4 \text{EV}[n[x1] n[x3]] \text{EV}[n[x2] n[x4]] - \\
 &> 4 \text{EV}[n[x2] n[x3]] \text{EV}[n[x2] n[x4]] - \\
 &> 4 \text{EV}[n[x1] n[x4]] \text{EV}[n[x2] n[x4]] + 2 \text{EV}[n[x2] n[x4]]^2 - \\
 &> 2 \text{EV}[n[x1]]^2 \text{EV}[n[x3] n[x4]] + 4 \text{EV}[n[x1] n[x2]] \text{EV}[n[x3] n[x4]] - \\
 &> 2 \text{EV}[n[x2]]^2 \text{EV}[n[x3] n[x4]] + \text{EV}[n[x1]]^2 \text{EV}[n[x4]]^2 - \\
 &> 2 \text{EV}[n[x1] n[x2]] \text{EV}[n[x4]]^2 + \text{EV}[n[x2]]^2 \text{EV}[n[x4]]^2 + \\
 & \quad 2
 \end{aligned}$$

$$\begin{aligned}
&> 2 \text{EV}[n[x3]]^2 \text{EV}[n[x1] s[x1]] - 4 \text{EV}[n[x3] n[x4]] \text{EV}[n[x1] s[x1]] + \\
&> 2 \text{EV}[n[x4]]^2 \text{EV}[n[x1] s[x1]] - 2 \text{EV}[n[x3]]^2 \text{EV}[n[x2] s[x1]] + \\
&> 4 \text{EV}[n[x3] n[x4]] \text{EV}[n[x2] s[x1]] - 2 \text{EV}[n[x4]]^2 \text{EV}[n[x2] s[x1]] + \\
&> 4 \text{EV}[n[x1] n[x3]] \text{EV}[n[x3] s[x1]] - \\
&> 4 \text{EV}[n[x2] n[x3]] \text{EV}[n[x3] s[x1]] - \\
&> 4 \text{EV}[n[x1] n[x4]] \text{EV}[n[x3] s[x1]] + \\
&> 4 \text{EV}[n[x2] n[x4]] \text{EV}[n[x3] s[x1]] + 2 \text{EV}[n[x3] s[x1]]^2 - \\
&> 4 \text{EV}[n[x1] n[x3]] \text{EV}[n[x4] s[x1]] + \\
&> 4 \text{EV}[n[x2] n[x3]] \text{EV}[n[x4] s[x1]] + \\
&> 4 \text{EV}[n[x1] n[x4]] \text{EV}[n[x4] s[x1]] - \\
&> 4 \text{EV}[n[x2] n[x4]] \text{EV}[n[x4] s[x1]] - \\
&> 4 \text{EV}[n[x3] s[x1]] \text{EV}[n[x4] s[x1]] + 2 \text{EV}[n[x4] s[x1]]^2 + \\
&> \text{EV}[n[x3]]^2 \text{EV}[s[x1]]^2 - 2 \text{EV}[n[x3] n[x4]] \text{EV}[s[x1]]^2 + \\
&> \text{EV}[n[x4]]^2 \text{EV}[s[x1]]^2 - 2 \text{EV}[n[x3]]^2 \text{EV}[n[x1] s[x2]] + \\
&> 4 \text{EV}[n[x3] n[x4]] \text{EV}[n[x1] s[x2]] - 2 \text{EV}[n[x4]]^2 \text{EV}[n[x1] s[x2]] + \\
&> 2 \text{EV}[n[x3]]^2 \text{EV}[n[x2] s[x2]] - 4 \text{EV}[n[x3] n[x4]] \text{EV}[n[x2] s[x2]] + \\
&> 2 \text{EV}[n[x4]]^2 \text{EV}[n[x2] s[x2]] - 4 \text{EV}[n[x1] n[x3]] \text{EV}[n[x3] s[x2]] + \\
&> 4 \text{EV}[n[x2] n[x3]] \text{EV}[n[x3] s[x2]] +
\end{aligned}$$

$$\begin{aligned}
&> 4 \text{EV}[n[x1] \ n[x4]] \ \text{EV}[n[x3] \ s[x2]] \ - \\
&> 4 \text{EV}[n[x2] \ n[x4]] \ \text{EV}[n[x3] \ s[x2]] \ - \\
&> 4 \text{EV}[n[x3] \ s[x1]] \ \text{EV}[n[x3] \ s[x2]] \ + \\
&> 4 \text{EV}[n[x4] \ s[x1]] \ \text{EV}[n[x3] \ s[x2]] \ + 2 \text{EV}[n[x3] \ s[x2]]^2 \ + \\
&> 4 \text{EV}[n[x1] \ n[x3]] \ \text{EV}[n[x4] \ s[x2]] \ - \\
&> 4 \text{EV}[n[x2] \ n[x3]] \ \text{EV}[n[x4] \ s[x2]] \ - \\
&> 4 \text{EV}[n[x1] \ n[x4]] \ \text{EV}[n[x4] \ s[x2]] \ + \\
&> 4 \text{EV}[n[x2] \ n[x4]] \ \text{EV}[n[x4] \ s[x2]] \ + \\
&> 4 \text{EV}[n[x3] \ s[x1]] \ \text{EV}[n[x4] \ s[x2]] \ - \\
&> 4 \text{EV}[n[x4] \ s[x1]] \ \text{EV}[n[x4] \ s[x2]] \ - \\
&> 4 \text{EV}[n[x3] \ s[x2]] \ \text{EV}[n[x4] \ s[x2]] \ + 2 \text{EV}[n[x4] \ s[x2]]^2 \ - \\
&> 2 \text{EV}[n[x3]]^2 \ \text{EV}[s[x1] \ s[x2]] \ + 4 \text{EV}[n[x3] \ n[x4]] \ \text{EV}[s[x1] \ s[x2]] \ - \\
&> 2 \text{EV}[n[x4]]^2 \ \text{EV}[s[x1] \ s[x2]] \ + \text{EV}[n[x3]]^2 \ \text{EV}[s[x2]]^2 \ - \\
&> 2 \text{EV}[n[x3] \ n[x4]] \ \text{EV}[s[x2]]^2 \ + \text{EV}[n[x4]]^2 \ \text{EV}[s[x2]]^2 \ + \\
&> 4 \text{EV}[n[x1] \ n[x3]] \ \text{EV}[n[x1] \ s[x3]] \ - \\
&> 4 \text{EV}[n[x2] \ n[x3]] \ \text{EV}[n[x1] \ s[x3]] \ - \\
&> 4 \text{EV}[n[x1] \ n[x4]] \ \text{EV}[n[x1] \ s[x3]] \ + \\
&> 4 \text{EV}[n[x2] \ n[x4]] \ \text{EV}[n[x1] \ s[x3]] \ + \\
&> 4 \text{EV}[n[x3] \ s[x1]] \ \text{EV}[n[x1] \ s[x3]] \ - \\
&> 4 \text{EV}[n[x4] \ s[x1]] \ \text{EV}[n[x1] \ s[x3]] \ -
\end{aligned}$$

$$\begin{aligned}
&> 4 \text{EV}[n[x3] \ s[x2]] \ \text{EV}[n[x1] \ s[x3]] \ + \\
&> 4 \text{EV}[n[x4] \ s[x2]] \ \text{EV}[n[x1] \ s[x3]] \ + 2 \text{EV}[n[x1] \ s[x3]]^2 \ - \\
&> 4 \text{EV}[n[x1] \ n[x3]] \ \text{EV}[n[x2] \ s[x3]] \ + \\
&> 4 \text{EV}[n[x2] \ n[x3]] \ \text{EV}[n[x2] \ s[x3]] \ + \\
&> 4 \text{EV}[n[x1] \ n[x4]] \ \text{EV}[n[x2] \ s[x3]] \ - \\
&> 4 \text{EV}[n[x2] \ n[x4]] \ \text{EV}[n[x2] \ s[x3]] \ - \\
&> 4 \text{EV}[n[x3] \ s[x1]] \ \text{EV}[n[x2] \ s[x3]] \ + \\
&> 4 \text{EV}[n[x4] \ s[x1]] \ \text{EV}[n[x2] \ s[x3]] \ + \\
&> 4 \text{EV}[n[x3] \ s[x2]] \ \text{EV}[n[x2] \ s[x3]] \ - \\
&> 4 \text{EV}[n[x4] \ s[x2]] \ \text{EV}[n[x2] \ s[x3]] \ - \\
&> 4 \text{EV}[n[x1] \ s[x3]] \ \text{EV}[n[x2] \ s[x3]] \ + 2 \text{EV}[n[x2] \ s[x3]]^2 \ + \\
&> 2 \text{EV}[n[x1]]^2 \ \text{EV}[n[x3] \ s[x3]] \ - 4 \text{EV}[n[x1] \ n[x2]] \ \text{EV}[n[x3] \ s[x3]] \ + \\
&> 2 \text{EV}[n[x2]]^2 \ \text{EV}[n[x3] \ s[x3]] \ + 4 \text{EV}[n[x1] \ s[x1]] \ \text{EV}[n[x3] \ s[x3]] \ - \\
&> 4 \text{EV}[n[x2] \ s[x1]] \ \text{EV}[n[x3] \ s[x3]] \ + 2 \text{EV}[s[x1]]^2 \ \text{EV}[n[x3] \ s[x3]] \ - \\
&> 4 \text{EV}[n[x1] \ s[x2]] \ \text{EV}[n[x3] \ s[x3]] \ + \\
&> 4 \text{EV}[n[x2] \ s[x2]] \ \text{EV}[n[x3] \ s[x3]] \ - \\
&> 4 \text{EV}[s[x1] \ s[x2]] \ \text{EV}[n[x3] \ s[x3]] \ + 2 \text{EV}[s[x2]]^2 \ \text{EV}[n[x3] \ s[x3]] \ - \\
&> 2 \text{EV}[n[x1]]^2 \ \text{EV}[n[x4] \ s[x3]] \ + 4 \text{EV}[n[x1] \ n[x2]] \ \text{EV}[n[x4] \ s[x3]] \ - \\
&> 2 \text{EV}[n[x2]]^2 \ \text{EV}[n[x4] \ s[x3]] \ - 4 \text{EV}[n[x1] \ s[x1]] \ \text{EV}[n[x4] \ s[x3]] \ +
\end{aligned}$$

$$\begin{aligned}
&> 4 \text{EV}[\text{n}[\text{x4}] \text{s}[\text{x2}]] \text{EV}[\text{s}[\text{x2}] \text{s}[\text{x3}]] - \\
&> 4 \text{EV}[\text{n}[\text{x1}] \text{s}[\text{x3}]] \text{EV}[\text{s}[\text{x2}] \text{s}[\text{x3}]] + \\
&> 4 \text{EV}[\text{n}[\text{x2}] \text{s}[\text{x3}]] \text{EV}[\text{s}[\text{x2}] \text{s}[\text{x3}]] - \\
&> 4 \text{EV}[\text{s}[\text{x1}] \text{s}[\text{x3}]] \text{EV}[\text{s}[\text{x2}] \text{s}[\text{x3}]] + 2 \text{EV}[\text{s}[\text{x2}] \text{s}[\text{x3}]]^2 + \\
&> \text{EV}[\text{n}[\text{x1}]]^2 \text{EV}[\text{s}[\text{x3}]]^2 - 2 \text{EV}[\text{n}[\text{x1}] \text{n}[\text{x2}]] \text{EV}[\text{s}[\text{x3}]]^2 + \\
&> \text{EV}[\text{n}[\text{x2}]]^2 \text{EV}[\text{s}[\text{x3}]]^2 + 2 \text{EV}[\text{n}[\text{x1}] \text{s}[\text{x1}]] \text{EV}[\text{s}[\text{x3}]]^2 - \\
&> 2 \text{EV}[\text{n}[\text{x2}] \text{s}[\text{x1}]] \text{EV}[\text{s}[\text{x3}]]^2 + \text{EV}[\text{s}[\text{x1}]]^2 \text{EV}[\text{s}[\text{x3}]]^2 - \\
&> 2 \text{EV}[\text{n}[\text{x1}] \text{s}[\text{x2}]] \text{EV}[\text{s}[\text{x3}]]^2 + 2 \text{EV}[\text{n}[\text{x2}] \text{s}[\text{x2}]] \text{EV}[\text{s}[\text{x3}]]^2 - \\
&> 2 \text{EV}[\text{s}[\text{x1}] \text{s}[\text{x2}]] \text{EV}[\text{s}[\text{x3}]]^2 + \text{EV}[\text{s}[\text{x2}]]^2 \text{EV}[\text{s}[\text{x3}]]^2 - \\
&> 4 \text{EV}[\text{n}[\text{x1}] \text{n}[\text{x3}]] \text{EV}[\text{n}[\text{x1}] \text{s}[\text{x4}]] + \\
&> 4 \text{EV}[\text{n}[\text{x2}] \text{n}[\text{x3}]] \text{EV}[\text{n}[\text{x1}] \text{s}[\text{x4}]] + \\
&> 4 \text{EV}[\text{n}[\text{x1}] \text{n}[\text{x4}]] \text{EV}[\text{n}[\text{x1}] \text{s}[\text{x4}]] - \\
&> 4 \text{EV}[\text{n}[\text{x2}] \text{n}[\text{x4}]] \text{EV}[\text{n}[\text{x1}] \text{s}[\text{x4}]] - \\
&> 4 \text{EV}[\text{n}[\text{x3}] \text{s}[\text{x1}]] \text{EV}[\text{n}[\text{x1}] \text{s}[\text{x4}]] + \\
&> 4 \text{EV}[\text{n}[\text{x4}] \text{s}[\text{x1}]] \text{EV}[\text{n}[\text{x1}] \text{s}[\text{x4}]] + \\
&> 4 \text{EV}[\text{n}[\text{x3}] \text{s}[\text{x2}]] \text{EV}[\text{n}[\text{x1}] \text{s}[\text{x4}]] - \\
&> 4 \text{EV}[\text{n}[\text{x4}] \text{s}[\text{x2}]] \text{EV}[\text{n}[\text{x1}] \text{s}[\text{x4}]] - \\
&> 4 \text{EV}[\text{n}[\text{x1}] \text{s}[\text{x3}]] \text{EV}[\text{n}[\text{x1}] \text{s}[\text{x4}]] + \\
&> 4 \text{EV}[\text{n}[\text{x2}] \text{s}[\text{x3}]] \text{EV}[\text{n}[\text{x1}] \text{s}[\text{x4}]] -
\end{aligned}$$

$$\begin{aligned}
&> 4 \text{EV}[s[x1] \ s[x3]] \ \text{EV}[n[x1] \ s[x4]] \ + \\
&> 4 \text{EV}[s[x2] \ s[x3]] \ \text{EV}[n[x1] \ s[x4]] \ + \ 2 \text{EV}[n[x1] \ s[x4]]^2 \ + \\
&> 4 \text{EV}[n[x1] \ n[x3]] \ \text{EV}[n[x2] \ s[x4]] \ - \\
&> 4 \text{EV}[n[x2] \ n[x3]] \ \text{EV}[n[x2] \ s[x4]] \ - \\
&> 4 \text{EV}[n[x1] \ n[x4]] \ \text{EV}[n[x2] \ s[x4]] \ + \\
&> 4 \text{EV}[n[x2] \ n[x4]] \ \text{EV}[n[x2] \ s[x4]] \ + \\
&> 4 \text{EV}[n[x3] \ s[x1]] \ \text{EV}[n[x2] \ s[x4]] \ - \\
&> 4 \text{EV}[n[x4] \ s[x1]] \ \text{EV}[n[x2] \ s[x4]] \ - \\
&> 4 \text{EV}[n[x3] \ s[x2]] \ \text{EV}[n[x2] \ s[x4]] \ + \\
&> 4 \text{EV}[n[x4] \ s[x2]] \ \text{EV}[n[x2] \ s[x4]] \ + \\
&> 4 \text{EV}[n[x1] \ s[x3]] \ \text{EV}[n[x2] \ s[x4]] \ - \\
&> 4 \text{EV}[n[x2] \ s[x3]] \ \text{EV}[n[x2] \ s[x4]] \ + \\
&> 4 \text{EV}[s[x1] \ s[x3]] \ \text{EV}[n[x2] \ s[x4]] \ - \\
&> 4 \text{EV}[s[x2] \ s[x3]] \ \text{EV}[n[x2] \ s[x4]] \ - \\
&> 4 \text{EV}[n[x1] \ s[x4]] \ \text{EV}[n[x2] \ s[x4]] \ + \ 2 \text{EV}[n[x2] \ s[x4]]^2 \ - \\
&> 2 \text{EV}[n[x1]]^2 \ \text{EV}[n[x3] \ s[x4]] \ + \ 4 \text{EV}[n[x1] \ n[x2]] \ \text{EV}[n[x3] \ s[x4]] \ - \\
&> 2 \text{EV}[n[x2]]^2 \ \text{EV}[n[x3] \ s[x4]] \ - \ 4 \text{EV}[n[x1] \ s[x1]] \ \text{EV}[n[x3] \ s[x4]] \ + \\
&> 4 \text{EV}[n[x2] \ s[x1]] \ \text{EV}[n[x3] \ s[x4]] \ - \ 2 \text{EV}[s[x1]]^2 \ \text{EV}[n[x3] \ s[x4]] \ + \\
&> 4 \text{EV}[n[x1] \ s[x2]] \ \text{EV}[n[x3] \ s[x4]] \ - \\
&> 4 \text{EV}[n[x2] \ s[x2]] \ \text{EV}[n[x3] \ s[x4]] \ +
\end{aligned}$$

$$\begin{aligned}
&> 4 \text{EV}[s[x1] s[x2]] \text{EV}[n[x3] s[x4]] - 2 \text{EV}[s[x2]^2] \text{EV}[n[x3] s[x4]] + \\
&2 \text{EV}[n[x1]^2] \text{EV}[n[x4] s[x4]] - 4 \text{EV}[n[x1] n[x2]] \text{EV}[n[x4] s[x4]] + \\
&2 \text{EV}[n[x2]^2] \text{EV}[n[x4] s[x4]] + 4 \text{EV}[n[x1] s[x1]] \text{EV}[n[x4] s[x4]] - \\
&4 \text{EV}[n[x2] s[x1]] \text{EV}[n[x4] s[x4]] + 2 \text{EV}[s[x1]^2] \text{EV}[n[x4] s[x4]] - \\
&4 \text{EV}[n[x1] s[x2]] \text{EV}[n[x4] s[x4]] + \\
&4 \text{EV}[n[x2] s[x2]] \text{EV}[n[x4] s[x4]] - \\
&4 \text{EV}[s[x1] s[x2]] \text{EV}[n[x4] s[x4]] + 2 \text{EV}[s[x2]^2] \text{EV}[n[x4] s[x4]] - \\
&4 \text{EV}[n[x1] n[x3]] \text{EV}[s[x1] s[x4]] + \\
&4 \text{EV}[n[x2] n[x3]] \text{EV}[s[x1] s[x4]] + \\
&4 \text{EV}[n[x1] n[x4]] \text{EV}[s[x1] s[x4]] - \\
&4 \text{EV}[n[x2] n[x4]] \text{EV}[s[x1] s[x4]] - \\
&4 \text{EV}[n[x3] s[x1]] \text{EV}[s[x1] s[x4]] + \\
&4 \text{EV}[n[x4] s[x1]] \text{EV}[s[x1] s[x4]] + \\
&4 \text{EV}[n[x3] s[x2]] \text{EV}[s[x1] s[x4]] - \\
&4 \text{EV}[n[x4] s[x2]] \text{EV}[s[x1] s[x4]] - \\
&4 \text{EV}[n[x1] s[x3]] \text{EV}[s[x1] s[x4]] + \\
&4 \text{EV}[n[x2] s[x3]] \text{EV}[s[x1] s[x4]] - \\
&4 \text{EV}[s[x1] s[x3]] \text{EV}[s[x1] s[x4]] + \\
&4 \text{EV}[s[x2] s[x3]] \text{EV}[s[x1] s[x4]] + \\
&4 \text{EV}[n[x1] s[x4]] \text{EV}[s[x1] s[x4]] -
\end{aligned}$$

$$\begin{aligned}
&> 4 \text{EV}[\text{n}[\text{x2}] \text{s}[\text{x4}]] \text{EV}[\text{s}[\text{x1}] \text{s}[\text{x4}]] + 2 \text{EV}[\text{s}[\text{x1}] \text{s}[\text{x4}]]^2 + \\
&> 4 \text{EV}[\text{n}[\text{x1}] \text{n}[\text{x3}]] \text{EV}[\text{s}[\text{x2}] \text{s}[\text{x4}]] - \\
&> 4 \text{EV}[\text{n}[\text{x2}] \text{n}[\text{x3}]] \text{EV}[\text{s}[\text{x2}] \text{s}[\text{x4}]] - \\
&> 4 \text{EV}[\text{n}[\text{x1}] \text{n}[\text{x4}]] \text{EV}[\text{s}[\text{x2}] \text{s}[\text{x4}]] + \\
&> 4 \text{EV}[\text{n}[\text{x2}] \text{n}[\text{x4}]] \text{EV}[\text{s}[\text{x2}] \text{s}[\text{x4}]] + \\
&> 4 \text{EV}[\text{n}[\text{x3}] \text{s}[\text{x1}]] \text{EV}[\text{s}[\text{x2}] \text{s}[\text{x4}]] - \\
&> 4 \text{EV}[\text{n}[\text{x4}] \text{s}[\text{x1}]] \text{EV}[\text{s}[\text{x2}] \text{s}[\text{x4}]] - \\
&> 4 \text{EV}[\text{n}[\text{x3}] \text{s}[\text{x2}]] \text{EV}[\text{s}[\text{x2}] \text{s}[\text{x4}]] + \\
&> 4 \text{EV}[\text{n}[\text{x4}] \text{s}[\text{x2}]] \text{EV}[\text{s}[\text{x2}] \text{s}[\text{x4}]] + \\
&> 4 \text{EV}[\text{n}[\text{x1}] \text{s}[\text{x3}]] \text{EV}[\text{s}[\text{x2}] \text{s}[\text{x4}]] - \\
&> 4 \text{EV}[\text{n}[\text{x2}] \text{s}[\text{x3}]] \text{EV}[\text{s}[\text{x2}] \text{s}[\text{x4}]] + \\
&> 4 \text{EV}[\text{s}[\text{x1}] \text{s}[\text{x3}]] \text{EV}[\text{s}[\text{x2}] \text{s}[\text{x4}]] - \\
&> 4 \text{EV}[\text{s}[\text{x2}] \text{s}[\text{x3}]] \text{EV}[\text{s}[\text{x2}] \text{s}[\text{x4}]] - \\
&> 4 \text{EV}[\text{n}[\text{x1}] \text{s}[\text{x4}]] \text{EV}[\text{s}[\text{x2}] \text{s}[\text{x4}]] + \\
&> 4 \text{EV}[\text{n}[\text{x2}] \text{s}[\text{x4}]] \text{EV}[\text{s}[\text{x2}] \text{s}[\text{x4}]] - \\
&> 4 \text{EV}[\text{s}[\text{x1}] \text{s}[\text{x4}]] \text{EV}[\text{s}[\text{x2}] \text{s}[\text{x4}]] + 2 \text{EV}[\text{s}[\text{x2}] \text{s}[\text{x4}]]^2 - \\
&> 2 \text{EV}[\text{n}[\text{x1}]]^2 \text{EV}[\text{s}[\text{x3}] \text{s}[\text{x4}]] + 4 \text{EV}[\text{n}[\text{x1}] \text{n}[\text{x2}]] \text{EV}[\text{s}[\text{x3}] \text{s}[\text{x4}]] - \\
&> 2 \text{EV}[\text{n}[\text{x2}]]^2 \text{EV}[\text{s}[\text{x3}] \text{s}[\text{x4}]] - 4 \text{EV}[\text{n}[\text{x1}] \text{s}[\text{x1}]] \text{EV}[\text{s}[\text{x3}] \text{s}[\text{x4}]] + \\
&> 4 \text{EV}[\text{n}[\text{x2}] \text{s}[\text{x1}]] \text{EV}[\text{s}[\text{x3}] \text{s}[\text{x4}]] - 2 \text{EV}[\text{s}[\text{x1}]]^2 \text{EV}[\text{s}[\text{x3}] \text{s}[\text{x4}]] + \\
&> 4 \text{EV}[\text{n}[\text{x1}] \text{s}[\text{x2}]] \text{EV}[\text{s}[\text{x3}] \text{s}[\text{x4}]] -
\end{aligned}$$

> $4 \text{EV}[n[x2] \ s[x2]] \ \text{EV}[s[x3] \ s[x4]] +$
 > $4 \text{EV}[s[x1] \ s[x2]] \ \text{EV}[s[x3] \ s[x4]] - 2 \text{EV}[s[x2]]^2 \ \text{EV}[s[x3] \ s[x4]] +$
 > $\text{EV}[n[x1]]^2 \ \text{EV}[s[x4]]^2 - 2 \text{EV}[n[x1] \ n[x2]] \ \text{EV}[s[x4]]^2 +$
 > $\text{EV}[n[x2]]^2 \ \text{EV}[s[x4]]^2 + 2 \text{EV}[n[x1] \ s[x1]] \ \text{EV}[s[x4]]^2 -$
 > $2 \text{EV}[n[x2] \ s[x1]] \ \text{EV}[s[x4]]^2 + \text{EV}[s[x1]]^2 \ \text{EV}[s[x4]]^2 -$
 > $2 \text{EV}[n[x1] \ s[x2]] \ \text{EV}[s[x4]]^2 + 2 \text{EV}[n[x2] \ s[x2]] \ \text{EV}[s[x4]]^2 -$
 > $2 \text{EV}[s[x1] \ s[x2]] \ \text{EV}[s[x4]]^2 + \text{EV}[s[x2]]^2 \ \text{EV}[s[x4]]^2$
 case1a= $12 \text{sig}^4 + 12 \text{sig}^2 \ \text{EV}[s[x3]]^2 + 3 \text{EV}[s[x3]]^2 -$
 > $24 \text{sig}^2 \ \text{EV}[s[x3] \ s[x4]] - 12 \text{EV}[s[x3]]^2 \ \text{EV}[s[x3] \ s[x4]] +$
 > $4 \text{EV}[s[x3] \ s[x4]]^2 + 12 \text{sig}^2 \ \text{EV}[s[x4]]^2 + 2 \text{EV}[s[x3]]^2 \ \text{EV}[s[x4]]^2 -$
 > $12 \text{EV}[s[x3] \ s[x4]] \ \text{EV}[s[x4]]^2 + 3 \text{EV}[s[x4]]^2 +$
 > $4 (2 \text{EV}[s[x3] \ s[x4]]^2 + \text{EV}[s[x3]]^2 \ \text{EV}[s[x4]]^2)$
 case2a= $6 \text{sig}^4 + 2 \text{sig}^2 \ \text{EV}[s[x1]]^2 - 8 \text{sig}^2 \ \text{EV}[s[x1] \ s[x3]] +$
 > $2 \text{EV}[s[x1] \ s[x3]]^2 + 8 \text{sig}^2 \ \text{EV}[s[x3]]^2 + \text{EV}[s[x1]]^2 \ \text{EV}[s[x3]]^2 -$
 > $6 \text{EV}[s[x1] \ s[x3]] \ \text{EV}[s[x3]]^2 + 3 \text{EV}[s[x3]]^2 +$
 > $4 \text{sig}^2 \ \text{EV}[s[x1] \ s[x4]] + 2 \text{EV}[s[x1]]^2 \ \text{EV}[s[x4]]^2 -$

$$\begin{aligned}
&> 8 \operatorname{sig}^2 \operatorname{EV}[s[x3] s[x4]] - 6 \operatorname{EV}[s[x3]]^2 \operatorname{EV}[s[x3] s[x4]] + \\
&> 2 \operatorname{EV}[s[x3] s[x4]]^2 - 2 (2 \operatorname{EV}[s[x1] s[x3]] \operatorname{EV}[s[x1] s[x4]] + \\
&> \operatorname{EV}[s[x1]]^2 \operatorname{EV}[s[x3] s[x4]]) + \\
&> 4 (\operatorname{EV}[s[x3]]^2 \operatorname{EV}[s[x1] s[x4]] + 2 \operatorname{EV}[s[x1] s[x3]] \operatorname{EV}[s[x3] s[x4]]) + \\
&> 2 \operatorname{sig}^2 \operatorname{EV}[s[x4]]^2 + \operatorname{EV}[s[x1]]^2 \operatorname{EV}[s[x4]]^2 + \operatorname{EV}[s[x3]]^2 \operatorname{EV}[s[x4]]^2 - \\
&> 2 (2 \operatorname{EV}[s[x1] s[x4]] \operatorname{EV}[s[x3] s[x4]] + \operatorname{EV}[s[x1] s[x3]] \operatorname{EV}[s[x4]]^2) \\
\text{case3a} &= 6 \operatorname{sig}^4 + 2 \operatorname{sig}^2 \operatorname{EV}[s[x2]]^2 + 4 \operatorname{sig}^2 \operatorname{EV}[s[x2] s[x3]] + \\
&> 2 \operatorname{EV}[s[x2] s[x3]]^2 + 2 \operatorname{sig}^2 \operatorname{EV}[s[x3]]^2 + \operatorname{EV}[s[x2]]^2 \operatorname{EV}[s[x3]]^2 - \\
&> 8 \operatorname{sig}^2 \operatorname{EV}[s[x2] s[x4]] + 2 \operatorname{EV}[s[x2] s[x4]]^2 - \\
&> 8 \operatorname{sig}^2 \operatorname{EV}[s[x3] s[x4]] + 2 \operatorname{EV}[s[x3] s[x4]]^2 - \\
&> 2 (2 \operatorname{EV}[s[x2] s[x3]] \operatorname{EV}[s[x2] s[x4]] + \operatorname{EV}[s[x2]]^2 \operatorname{EV}[s[x3] s[x4]]) - \\
&> 2 (\operatorname{EV}[s[x3]]^2 \operatorname{EV}[s[x2] s[x4]] + 2 \operatorname{EV}[s[x2] s[x3]] \operatorname{EV}[s[x3] s[x4]]) + \\
&> 8 \operatorname{sig}^2 \operatorname{EV}[s[x4]]^2 + \operatorname{EV}[s[x2]]^2 \operatorname{EV}[s[x4]]^2 + \operatorname{EV}[s[x3]]^2 \operatorname{EV}[s[x4]]^2 - \\
&> 6 \operatorname{EV}[s[x2] s[x4]] \operatorname{EV}[s[x4]]^2 - 6 \operatorname{EV}[s[x3] s[x4]] \operatorname{EV}[s[x4]]^2 + \\
&> 3 \operatorname{EV}[s[x4]]^2 + 4 (2 \operatorname{EV}[s[x2] s[x4]] \operatorname{EV}[s[x3] s[x4]] +
\end{aligned}$$

2

```

>      EV[s[x2] s[x3]] EV[s[x4] ]
      4      2      2      2
case4a= 4 sig + 2 sig EV[s[x1] ] - 4 sig EV[s[x1] s[x2]] +
      2      2      2      2
> 2 sig EV[s[x2] ] + 2 EV[s[x1] s[x3]] + 2 EV[s[x2] s[x3]] +
      2      2      2      2      2      2
> 2 sig EV[s[x3] ] + EV[s[x1] ] EV[s[x3] ] + EV[s[x2] ] EV[s[x3] ] -
      2
> 2 (2 EV[s[x1] s[x3]] EV[s[x2] s[x3]] + EV[s[x1] s[x2]] EV[s[x3] ] ) +
      2      2      2
> 2 EV[s[x1] s[x4]] + 2 EV[s[x2] s[x4]] - 4 sig EV[s[x3] s[x4]] -
      2
> 2 (2 EV[s[x1] s[x3]] EV[s[x1] s[x4]] + EV[s[x1] ] EV[s[x3] s[x4]]) +
      2
> 4 (EV[s[x2] s[x3]] EV[s[x1] s[x4]] +
      EV[s[x1] s[x3]] EV[s[x2] s[x4]] + EV[s[x1] s[x2]] EV[s[x3] s[x4]])\
      2
> - 2 (2 EV[s[x2] s[x3]] EV[s[x2] s[x4]] +
      2      2      2
      EV[s[x2] ] EV[s[x3] s[x4]]) + 2 sig EV[s[x4] ] +
      2      2      2      2
> EV[s[x1] ] EV[s[x4] ] + EV[s[x2] ] EV[s[x4] ] -
      2
> 2 (2 EV[s[x1] s[x4]] EV[s[x2] s[x4]] + EV[s[x1] s[x2]] EV[s[x4] ] )
      4      2      2      2
case1b= 12 sig + 24 sig G[0] + 8 G[0] - 24 sig G[-x3 + x4] -
      2      2      2      2
> 24 G[0] G[-x3 + x4] + 4 G[-x3 + x4] + 4 (G[0] + 2 G[-x3 + x4] )
      4      2      2      2
case2b= 6 sig + 12 sig G[0] + 6 G[0] - 8 sig G[-x1 + x3] -
      2      2      2      2
> 6 G[0] G[-x1 + x3] + 2 G[-x1 + x3] + 4 sig G[-x1 + x4] +
      2      2

```

```

> 2 G[-x1 + x4] - 8 sig G[-x3 + x4] - 6 G[0] G[-x3 + x4] +
> 2 G[-x3 + x4] - 2 (2 G[-x1 + x3] G[-x1 + x4] + G[0] G[-x3 + x4]) +
> 4 (G[0] G[-x1 + x4] + 2 G[-x1 + x3] G[-x3 + x4]) -
> 2 (G[0] G[-x1 + x3] + 2 G[-x1 + x4] G[-x3 + x4])
case3b= 6 sig + 12 sig G[0] + 6 G[0] + 4 sig G[-x2 + x3] +
> 2 G[-x2 + x3] - 8 sig G[-x2 + x4] - 6 G[0] G[-x2 + x4] +
> 2 G[-x2 + x4] - 8 sig G[-x3 + x4] - 6 G[0] G[-x3 + x4] +
> 2 G[-x3 + x4] - 2 (2 G[-x2 + x3] G[-x2 + x4] + G[0] G[-x3 + x4]) -
> 2 (G[0] G[-x2 + x4] + 2 G[-x2 + x3] G[-x3 + x4]) +
> 4 (G[0] G[-x2 + x3] + 2 G[-x2 + x4] G[-x3 + x4])
case4b= 4 sig + 8 sig G[0] + 4 G[0] - 4 sig G[-x1 + x2] +
> 2 G[-x1 + x3] + 2 G[-x2 + x3] -
> 2 (G[0] G[-x1 + x2] + 2 G[-x1 + x3] G[-x2 + x3]) + 2 G[-x1 + x4] +
> 2 G[-x2 + x4] - 2 (G[0] G[-x1 + x2] + 2 G[-x1 + x4] G[-x2 + x4]) -
> 4 sig G[-x3 + x4] - 2 (2 G[-x1 + x3] G[-x1 + x4] +
> G[0] G[-x3 + x4]) - 2 (2 G[-x2 + x3] G[-x2 + x4] +
> G[0] G[-x3 + x4]) + 4 (G[-x2 + x3] G[-x1 + x4] +
> G[-x1 + x3] G[-x2 + x4] + G[-x1 + x2] G[-x3 + x4])
case1c= 12 sig + 24 sig G[0] + 12 G[0] - 24 sig G[p] - 24 G[0] G[p] +

```

$$12 G[p]^2$$

$$\text{case2c} = 6 \text{sig}^4 + 12 \text{sig}^2 G[0] + 6 G[0]^2 - 16 \text{sig}^2 G[p] - 16 G[0] G[p] +$$

$$12 G[p]^2 + 4 \text{sig}^2 G[2 p] + 4 G[0] G[2 p] - 8 G[p] G[2 p] + 2 G[2 p]^2$$

$$\text{case3c} = 6 \text{sig}^4 + 12 \text{sig}^2 G[0] + 6 G[0]^2 - 16 \text{sig}^2 G[p] - 16 G[0] G[p] +$$

$$12 G[p]^2 + 4 \text{sig}^2 G[2 p] + 4 G[0] G[2 p] - 8 G[p] G[2 p] + 2 G[2 p]^2$$

$$\text{case4c} = 4 \text{sig}^4 + 8 \text{sig}^2 G[0] + 4 G[0]^2 - 8 \text{sig}^2 G[p] - 8 G[0] G[p] +$$

$$4 G[p]^2 + 8 G[-x1 + x3]^2 - 8 G[-x1 + x3] G[-x2 + x3] +$$

$$2 G[-x2 + x3]^2 - 8 G[-x1 + x3] G[-x1 + x4] +$$

$$4 G[-x2 + x3] G[-x1 + x4] + 2 G[-x1 + x4]^2$$

Appendix D. SSF SNR Results for DIMM Geometry H-WFS

This appendix presents results for the SSF estimator SNR developed in Chapter III for the simplest H-WFS configuration—the DIMM. The results are divided into five groups of plots. Each plot shows the SSF estimator SNR vs. the number of integration frames, N , included in the SSF estimate. The five groups, as listed in Table D.1, are chosen to show the SNR behavior as different SSF estimate and turbulence parameters are varied. All plots are for a turbulence power law $\alpha = 11/3$ and a average gradient mode count of four. The wavefront slope is taken along the axis co-linear to the vector connecting the centers of the two DIMM subapertures.

Slightly modified versions of Figures D.1, D.3, D.4, D.25, D.26, D.28, D.76, D.95, and D.111 are discussed in Sec. (4.1). The remaining figures are similarly interpreted.

Group	Figures	DIMM Separation $\vec{\rho}$	Family of Curves in Each Figure	Varied Parameters	Constant Parameters
A	D.1-D.24	$(1D, 0^\circ)$	$L_0/D = \{1, 5, 10, 100, \infty\}$	$\sigma_n^2/\Gamma_s(0) = \{0\%, 10\%, 20\%, 50\%\}$ $ \vec{v}\tau/D = \{0.1, 0.5, 1.0, 2.5, 5, 10\}$	$\theta_0 = 0^\circ$ $\alpha = 11/3$
B	D.25-D.48	$(4D, 0^\circ)$	$L_0/D = \{1, 5, 10, 100, \infty\}$	$\sigma_n^2/\Gamma_s(0) = \{0\%, 10\%, 20\%, 50\%\}$ $ \vec{v}\tau/D = \{0.1, 0.5, 1.0, 2.5, 5, 10\}$	$\theta_0 = 0^\circ$ $\alpha = 11/3$
C	D.49-D.78	$(4D, 0^\circ)$	$\sigma_n^2/\Gamma_s(0) = \{0\%, 10\%, 20\%, 50\%\}$	$L_0/D = \{1, 5, 10, 100, \infty\}$ $ \vec{v}\tau/D = \{0.1, 0.5, 1.0, 2.5, 5, 10\}$	$\theta_0 = 0^\circ$ $\alpha = 11/3$
D	D.79-D.98	$(4D, 0^\circ)$	$ \vec{v}\tau/D = \{0.1, 0.5, 1.0, 2.5, 5, 10\}$	$L_0/D = \{1, 5, 10, 100, \infty\}$ $\sigma_n^2/\Gamma_s(0) = \{0\%, 10\%, 20\%, 50\%\}$	$\theta_0 = 0^\circ$ $\alpha = 11/3$
E	D.99-D.118	$(4D, \theta_0)$	$\theta_0 = \{0^\circ, 45^\circ, 90^\circ\}$	$ \vec{v}\tau/D = \{0.5, 1.0, 2.5, 5, 10\}$ $\sigma_n^2/\Gamma_s(0) = \{0\%, 10\%, 20\%, 50\%\}$	$L_0/D = \infty$ $\alpha = 11/3$

Table D.1 Summarization of numerical results for slope structure function estimator SNR vs. number of integration frames, N , for a DIMM H-WFS geometry. These results are shown in Figures D.1 through D.118 and are divided into five groups, A through E. Within a group, each plot shows a family of curves for a varied parameter. Across a group, two other parameters are varied to show how the family of curves change.

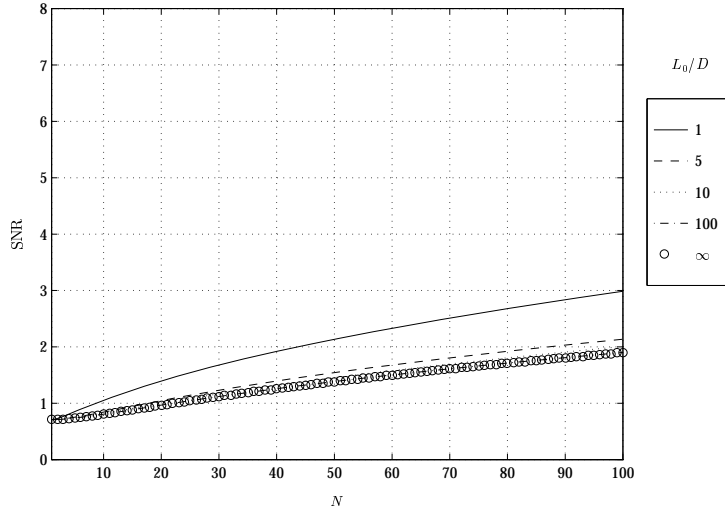


Figure D.1 Group A: Slope structure function estimator SNR vs. number of integration frames, N , for the DIMM geometry with a subaperture separation of $\vec{\rho} = (1.00D, 0.00^\circ)$, a turbulence power law of $\alpha = 3.6667$, a turbulence layer motion velocity $\vec{v}\tau = (0.10D, 90.00^\circ)$, and a ratio of the slope measurement noise variance to the wavefront slope variance $\sigma_n^2/\Gamma_s(0) = 0\%$. The ratio L_0/D ranges from 1 to ∞ .

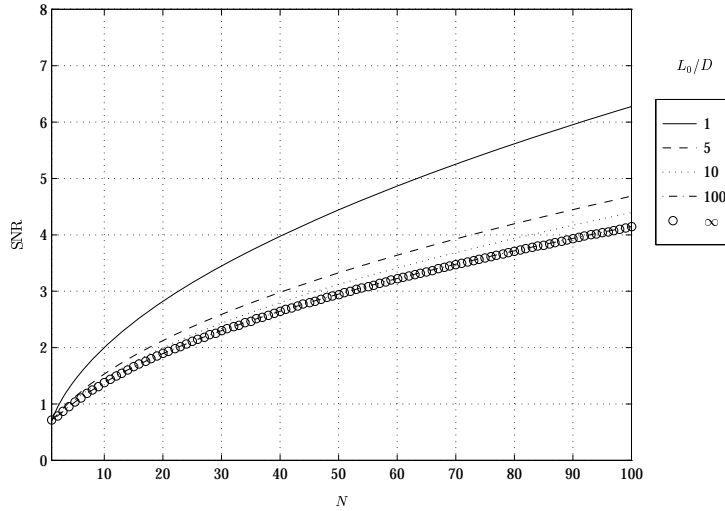


Figure D.2 Group A: Slope structure function estimator SNR vs. number of integration frames, N , for the DIMM geometry with a subaperture separation of $\vec{\rho} = (1.00D, 0.00^\circ)$, a turbulence power law of $\alpha = 3.6667$, a turbulence layer motion velocity $\vec{v}\tau = (0.50D, 90.00^\circ)$, and a ratio of the slope measurement noise variance to the wavefront slope variance $\sigma_n^2/\Gamma_s(0) = 0\%$. The ratio L_0/D ranges from 1 to ∞ .

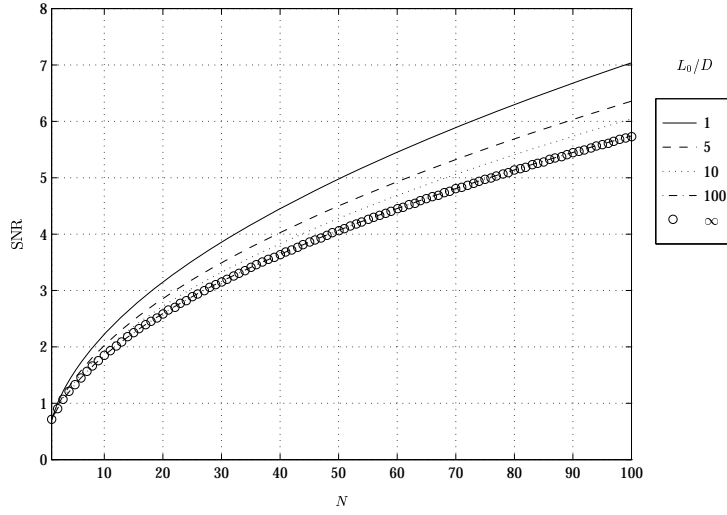


Figure D.3 Group A: Slope structure function estimator SNR vs. number of integration frames, N , for the DIMM geometry with a subaperture separation of $\vec{\rho} = (1.00D, 0.00^\circ)$, a turbulence power law of $\alpha = 3.6667$, a turbulence layer motion velocity $\vec{v}\tau = (1.00D, 90.00^\circ)$, and a ratio of the slope measurement noise variance to the wavefront slope variance $\sigma_n^2/\Gamma_s(0) = 0\%$. The ratio L_0/D ranges from 1 to ∞ .

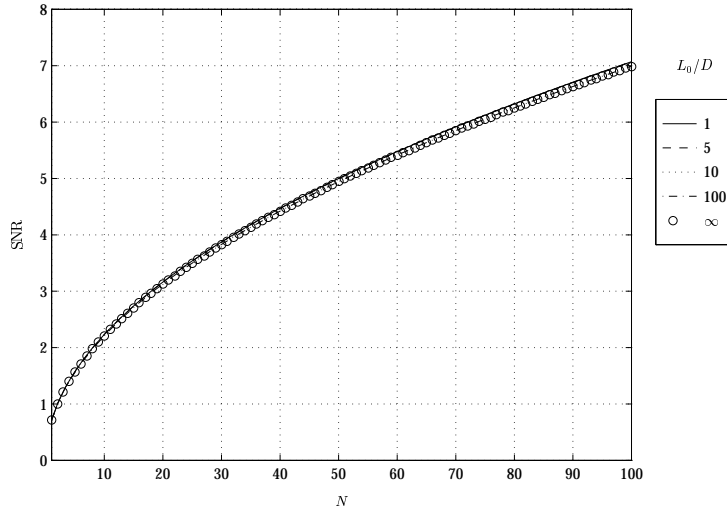


Figure D.4 Group A: Slope structure function estimator SNR vs. number of integration frames, N , for the DIMM geometry with a subaperture separation of $\vec{\rho} = (1.00D, 0.00^\circ)$, a turbulence power law of $\alpha = 3.6667$, a turbulence layer motion velocity $\vec{v}\tau = (2.50D, 90.00^\circ)$, and a ratio of the slope measurement noise variance to the wavefront slope variance $\sigma_n^2/\Gamma_s(0) = 0\%$. The ratio L_0/D ranges from 1 to ∞ .

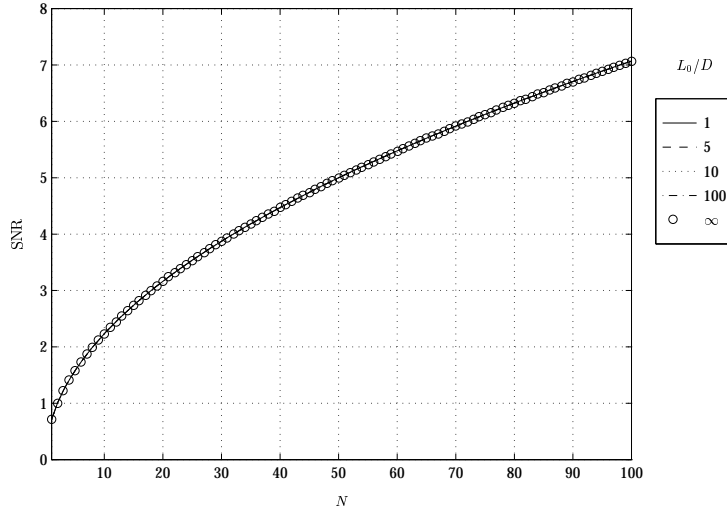


Figure D.5 Group A: Slope structure function estimator SNR vs. number of integration frames, N , for the DIMM geometry with a subaperture separation of $\vec{\rho} = (1.00D, 0.00^\circ)$, a turbulence power law of $\alpha = 3.6667$, a turbulence layer motion velocity $\vec{v}\tau = (5.00D, 90.00^\circ)$, and a ratio of the slope measurement noise variance to the wavefront slope variance $\sigma_n^2/\Gamma_s(0) = 0\%$. The ratio L_0/D ranges from 1 to ∞ .

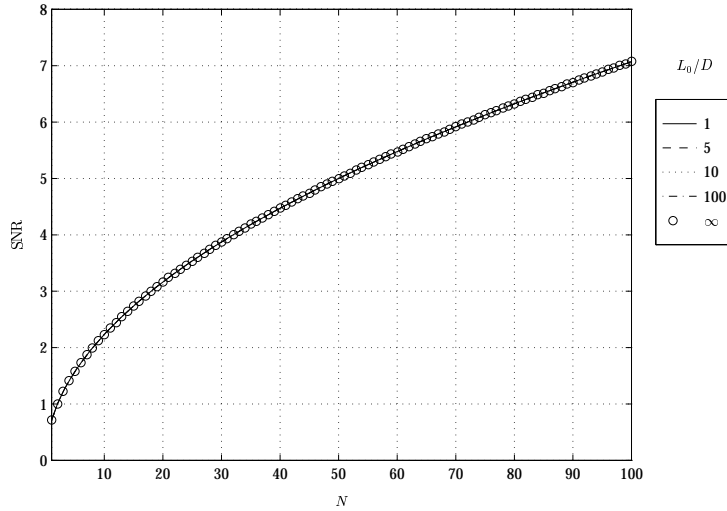


Figure D.6 Group A: Slope structure function estimator SNR vs. number of integration frames, N , for the DIMM geometry with a subaperture separation of $\vec{\rho} = (1.00D, 0.00^\circ)$, a turbulence power law of $\alpha = 3.6667$, a turbulence layer motion velocity $\vec{v}\tau = (10.00D, 90.00^\circ)$, and a ratio of the slope measurement noise variance to the wavefront slope variance $\sigma_n^2/\Gamma_s(0) = 0\%$. The ratio L_0/D ranges from 1 to ∞ .

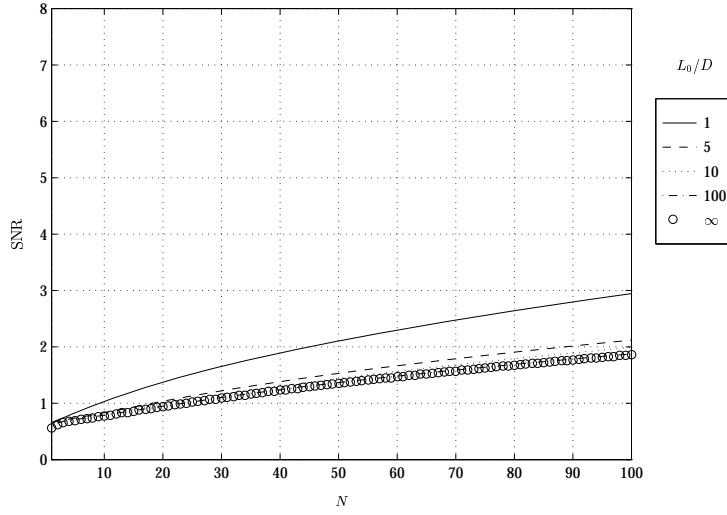


Figure D.7 Group A: Slope structure function estimator SNR vs. number of integration frames, N , for the DIMM geometry with a subaperture separation of $\vec{\rho} = (1.00D, 0.00^\circ)$, a turbulence power law of $\alpha = 3.6667$, a turbulence layer motion velocity $\vec{v}\tau = (0.10D, 90.00^\circ)$, and a ratio of the slope measurement noise variance to the wavefront slope variance $\sigma_n^2/\Gamma_s(0) = 10\%$. The ratio L_0/D ranges from 1 to ∞ .

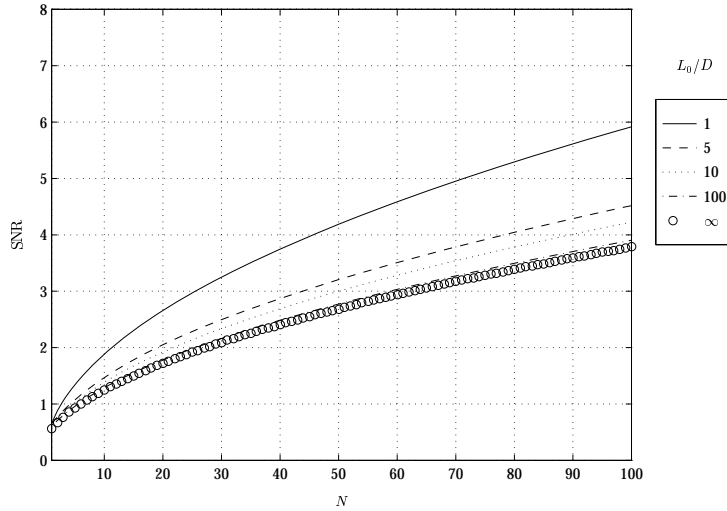


Figure D.8 Group A: Slope structure function estimator SNR vs. number of integration frames, N , for the DIMM geometry with a subaperture separation of $\vec{\rho} = (1.00D, 0.00^\circ)$, a turbulence power law of $\alpha = 3.6667$, a turbulence layer motion velocity $\vec{v}\tau = (0.50D, 90.00^\circ)$, and a ratio of the slope measurement noise variance to the wavefront slope variance $\sigma_n^2/\Gamma_s(0) = 10\%$. The ratio L_0/D ranges from 1 to ∞ .

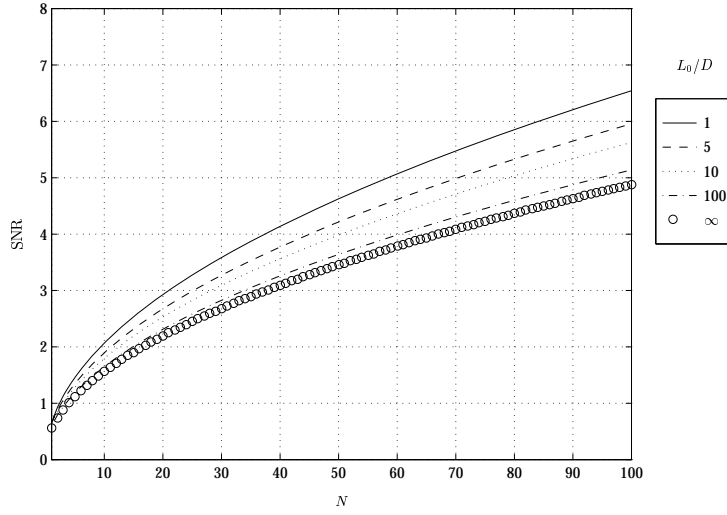


Figure D.9 Group A: Slope structure function estimator SNR vs. number of integration frames, N , for the DIMM geometry with a subaperture separation of $\vec{\rho} = (1.00D, 0.00^\circ)$, a turbulence power law of $\alpha = 3.6667$, a turbulence layer motion velocity $\vec{v}\tau = (1.00D, 90.00^\circ)$, and a ratio of the slope measurement noise variance to the wavefront slope variance $\sigma_n^2/\Gamma_s(0) = 10\%$. The ratio L_0/D ranges from 1 to ∞ .

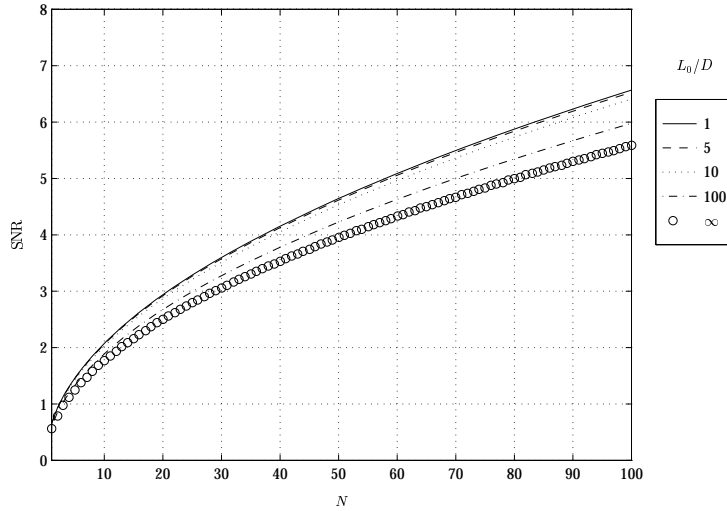


Figure D.10 Group A: Slope structure function estimator SNR vs. number of integration frames, N , for the DIMM geometry with a subaperture separation of $\vec{\rho} = (1.00D, 0.00^\circ)$, a turbulence power law of $\alpha = 3.6667$, a turbulence layer motion velocity $\vec{v}\tau = (2.50D, 90.00^\circ)$, and a ratio of the slope measurement noise variance to the wavefront slope variance $\sigma_n^2/\Gamma_s(0) = 10\%$. The ratio L_0/D ranges from 1 to ∞ .

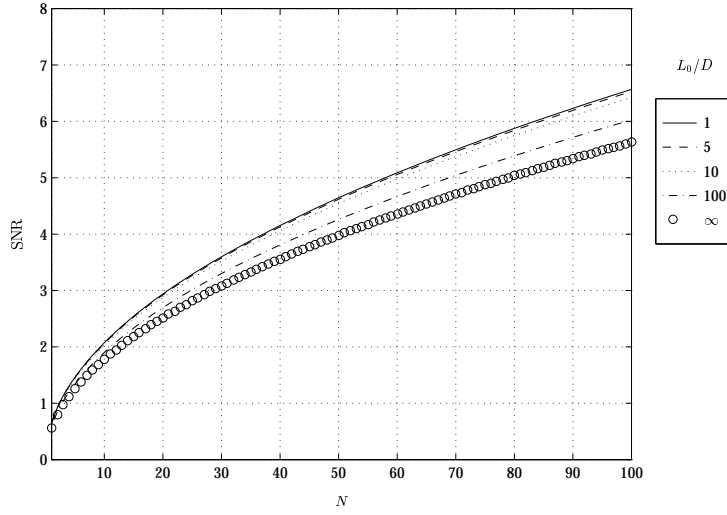


Figure D.11 Group A: Slope structure function estimator SNR vs. number of integration frames, N , for the DIMM geometry with a subaperture separation of $\vec{\rho} = (1.00D, 0.00^\circ)$, a turbulence power law of $\alpha = 3.6667$, a turbulence layer motion velocity $\vec{v}\tau = (5.00D, 90.00^\circ)$, and a ratio of the slope measurement noise variance to the wavefront slope variance $\sigma_n^2/\Gamma_s(0) = 10\%$. The ratio L_0/D ranges from 1 to ∞ .

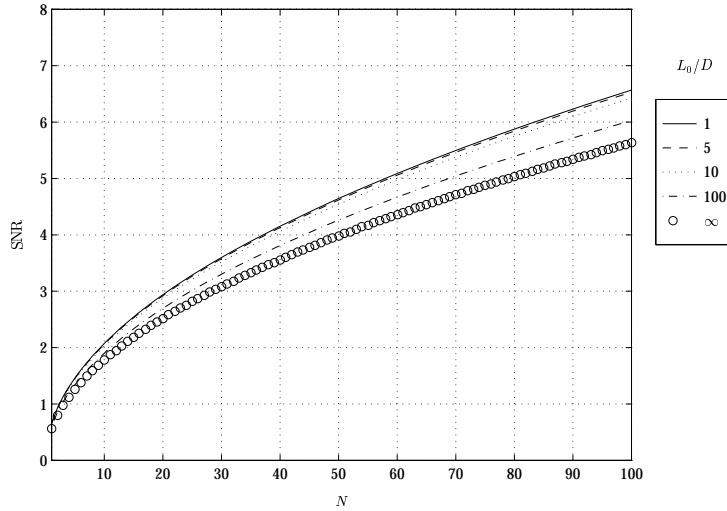


Figure D.12 Group A: Slope structure function estimator SNR vs. number of integration frames, N , for the DIMM geometry with a subaperture separation of $\vec{\rho} = (1.00D, 0.00^\circ)$, a turbulence power law of $\alpha = 3.6667$, a turbulence layer motion velocity $\vec{v}\tau = (10.00D, 90.00^\circ)$, and a ratio of the slope measurement noise variance to the wavefront slope variance $\sigma_n^2/\Gamma_s(0) = 10\%$. The ratio L_0/D ranges from 1 to ∞ .

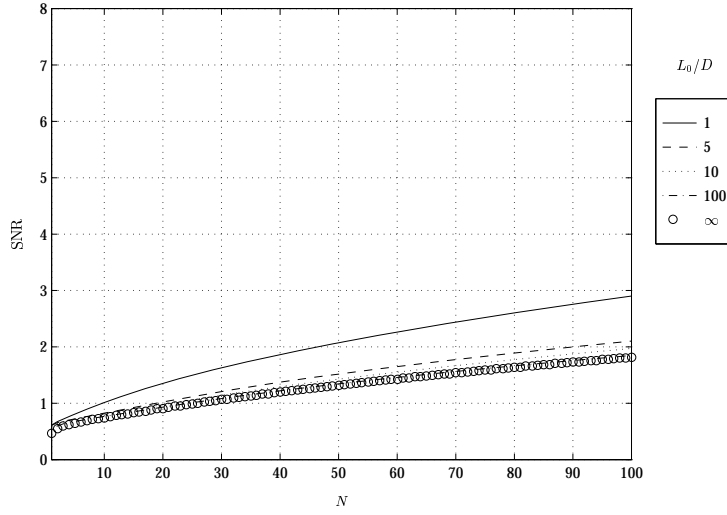


Figure D.13 Group A: Slope structure function estimator SNR vs. number of integration frames, N , for the DIMM geometry with a subaperture separation of $\vec{\rho} = (1.00D, 0.00^\circ)$, a turbulence power law of $\alpha = 3.6667$, a turbulence layer motion velocity $\vec{v}\tau = (0.10D, 90.00^\circ)$, and a ratio of the slope measurement noise variance to the wavefront slope variance $\sigma_n^2/\Gamma_s(0) = 20\%$. The ratio L_0/D ranges from 1 to ∞ .

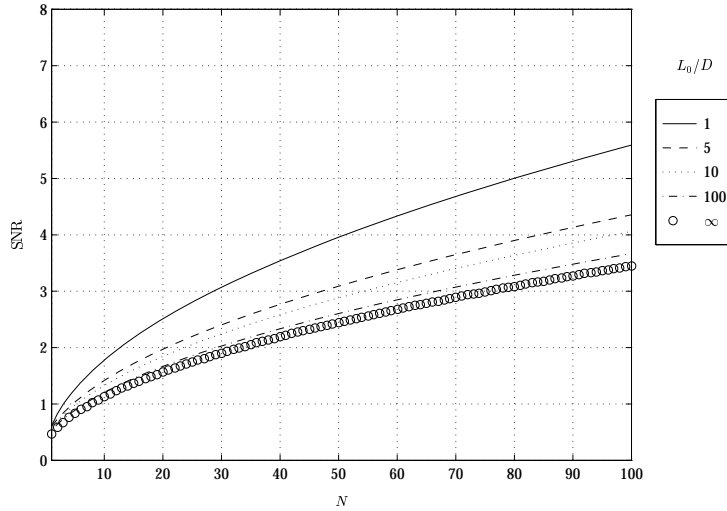


Figure D.14 Group A: Slope structure function estimator SNR vs. number of integration frames, N , for the DIMM geometry with a subaperture separation of $\vec{\rho} = (1.00D, 0.00^\circ)$, a turbulence power law of $\alpha = 3.6667$, a turbulence layer motion velocity $\vec{v}\tau = (0.50D, 90.00^\circ)$, and a ratio of the slope measurement noise variance to the wavefront slope variance $\sigma_n^2/\Gamma_s(0) = 20\%$. The ratio L_0/D ranges from 1 to ∞ .

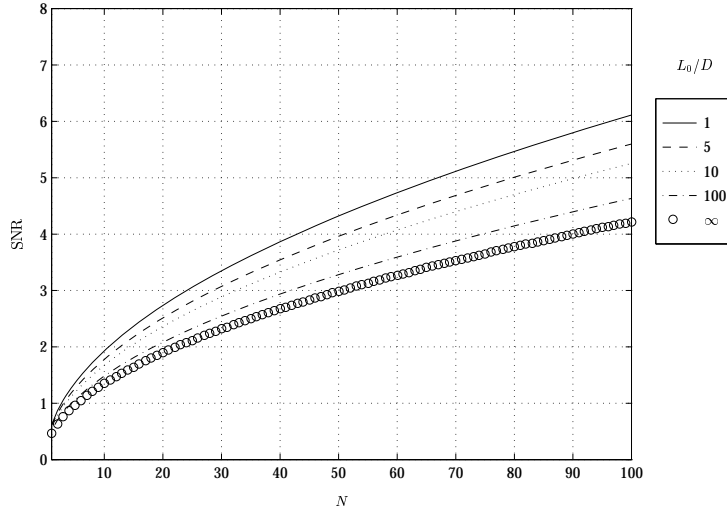


Figure D.15 Group A: Slope structure function estimator SNR vs. number of integration frames, N , for the DIMM geometry with a subaperture separation of $\vec{\rho} = (1.00D, 0.00^\circ)$, a turbulence power law of $\alpha = 3.6667$, a turbulence layer motion velocity $\vec{v}\tau = (1.00D, 90.00^\circ)$, and a ratio of the slope measurement noise variance to the wavefront slope variance $\sigma_n^2/\Gamma_s(0) = 20\%$. The ratio L_0/D ranges from 1 to ∞ .

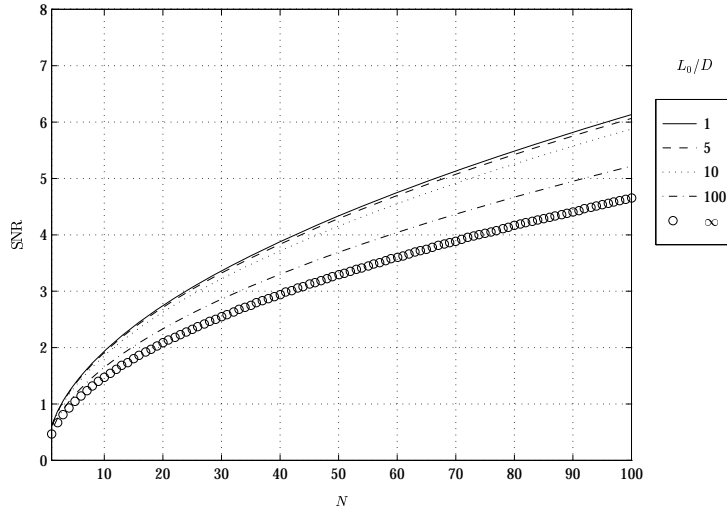


Figure D.16 Group A: Slope structure function estimator SNR vs. number of integration frames, N , for the DIMM geometry with a subaperture separation of $\vec{\rho} = (1.00D, 0.00^\circ)$, a turbulence power law of $\alpha = 3.6667$, a turbulence layer motion velocity $\vec{v}\tau = (2.50D, 90.00^\circ)$, and a ratio of the slope measurement noise variance to the wavefront slope variance $\sigma_n^2/\Gamma_s(0) = 20\%$. The ratio L_0/D ranges from 1 to ∞ .

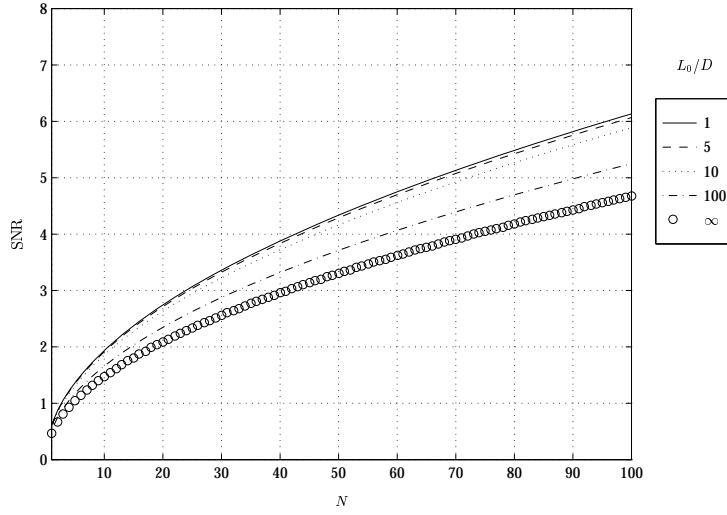


Figure D.17 Group A: Slope structure function estimator SNR vs. number of integration frames, N , for the DIMM geometry with a subaperture separation of $\vec{\rho} = (1.00D, 0.00^\circ)$, a turbulence power law of $\alpha = 3.6667$, a turbulence layer motion velocity $\vec{v}\tau = (5.00D, 90.00^\circ)$, and a ratio of the slope measurement noise variance to the wavefront slope variance $\sigma_n^2/\Gamma_s(0) = 20\%$. The ratio L_0/D ranges from 1 to ∞ .

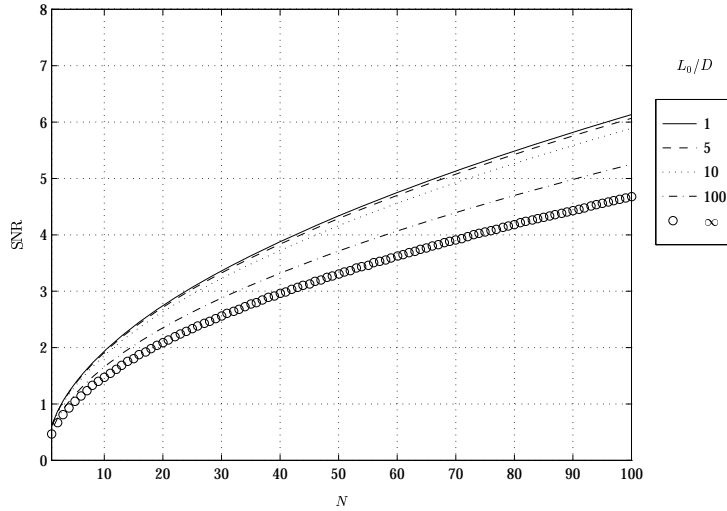


Figure D.18 Group A: Slope structure function estimator SNR vs. number of integration frames, N , for the DIMM geometry with a subaperture separation of $\vec{\rho} = (1.00D, 0.00^\circ)$, a turbulence power law of $\alpha = 3.6667$, a turbulence layer motion velocity $\vec{v}\tau = (10.00D, 90.00^\circ)$, and a ratio of the slope measurement noise variance to the wavefront slope variance $\sigma_n^2/\Gamma_s(0) = 20\%$. The ratio L_0/D ranges from 1 to ∞ .

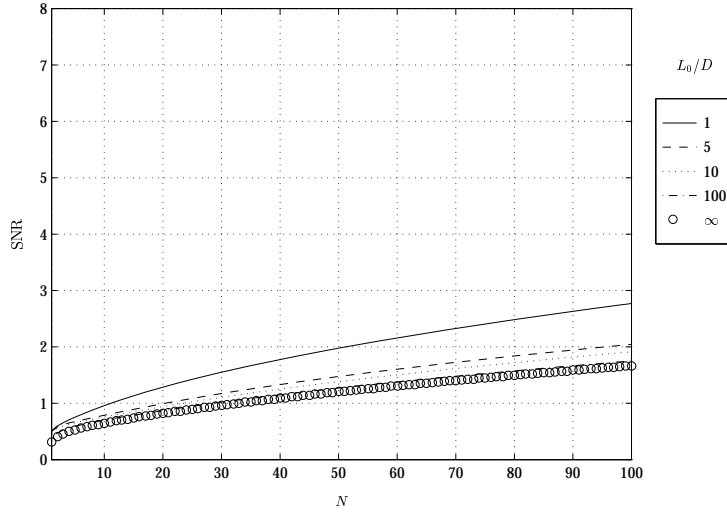


Figure D.19 Group A: Slope structure function estimator SNR vs. number of integration frames, N , for the DIMM geometry with a subaperture separation of $\vec{\rho} = (1.00D, 0.00^\circ)$, a turbulence power law of $\alpha = 3.6667$, a turbulence layer motion velocity $\vec{v}\tau = (0.10D, 90.00^\circ)$, and a ratio of the slope measurement noise variance to the wavefront slope variance $\sigma_n^2/\Gamma_s(0) = 50\%$. The ratio L_0/D ranges from 1 to ∞ .

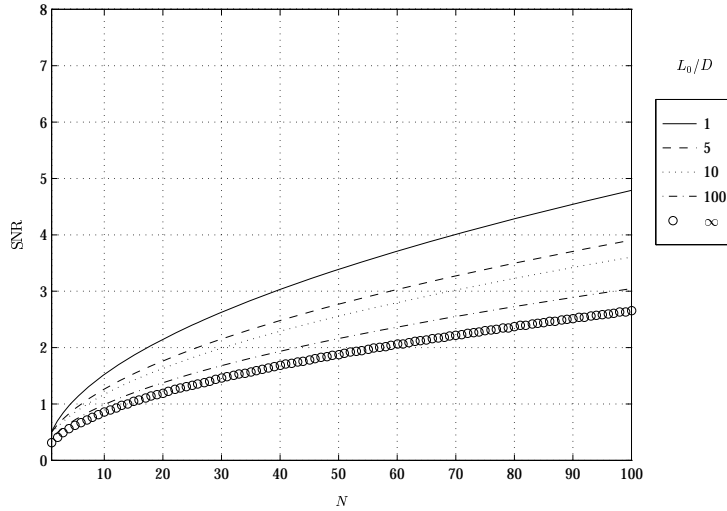


Figure D.20 Group A: Slope structure function estimator SNR vs. number of integration frames, N , for the DIMM geometry with a subaperture separation of $\vec{\rho} = (1.00D, 0.00^\circ)$, a turbulence power law of $\alpha = 3.6667$, a turbulence layer motion velocity $\vec{v}\tau = (0.50D, 90.00^\circ)$, and a ratio of the slope measurement noise variance to the wavefront slope variance $\sigma_n^2/\Gamma_s(0) = 50\%$. The ratio L_0/D ranges from 1 to ∞ .

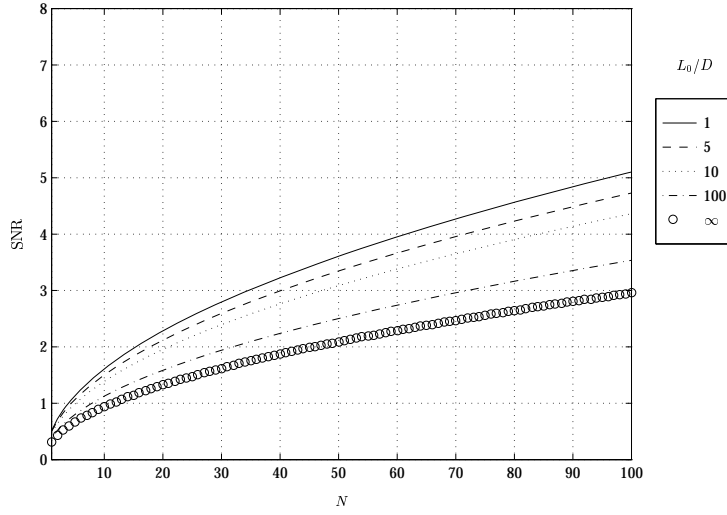


Figure D.21 Group A: Slope structure function estimator SNR vs. number of integration frames, N , for the DIMM geometry with a subaperture separation of $\vec{\rho} = (1.00D, 0.00^\circ)$, a turbulence power law of $\alpha = 3.6667$, a turbulence layer motion velocity $\vec{v}\tau = (1.00D, 90.00^\circ)$, and a ratio of the slope measurement noise variance to the wavefront slope variance $\sigma_n^2/\Gamma_s(0) = 50\%$. The ratio L_0/D ranges from 1 to ∞ .

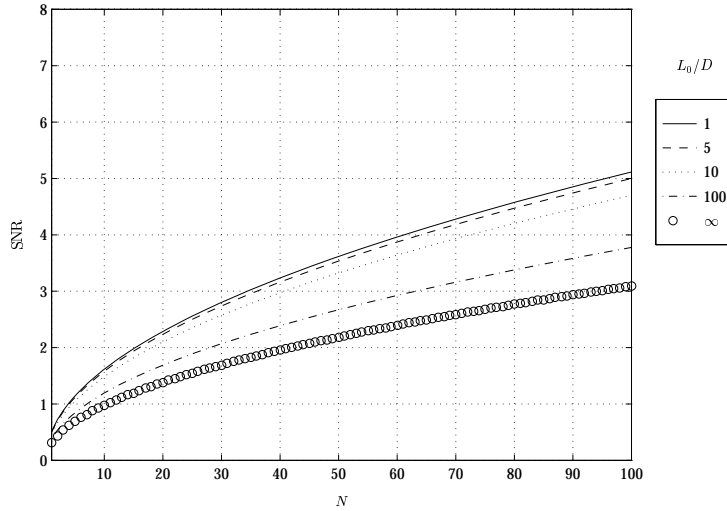


Figure D.22 Group A: Slope structure function estimator SNR vs. number of integration frames, N , for the DIMM geometry with a subaperture separation of $\vec{\rho} = (1.00D, 0.00^\circ)$, a turbulence power law of $\alpha = 3.6667$, a turbulence layer motion velocity $\vec{v}\tau = (2.50D, 90.00^\circ)$, and a ratio of the slope measurement noise variance to the wavefront slope variance $\sigma_n^2/\Gamma_s(0) = 50\%$. The ratio L_0/D ranges from 1 to ∞ .

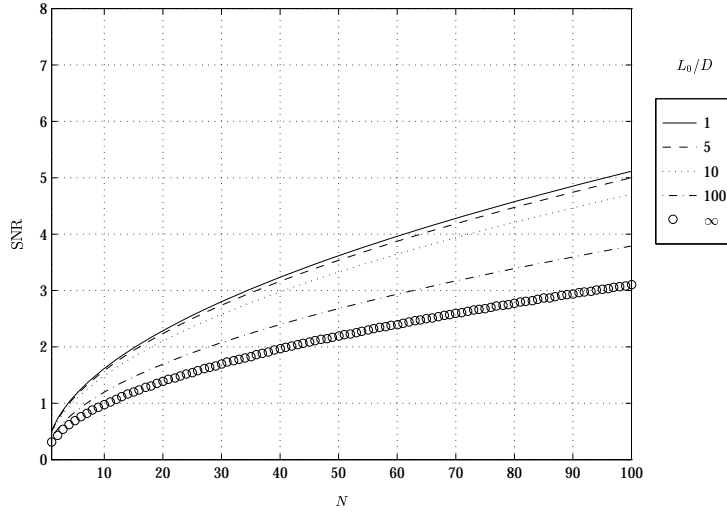


Figure D.23 Group A: Slope structure function estimator SNR vs. number of integration frames, N , for the DIMM geometry with a subaperture separation of $\vec{\rho} = (1.00D, 0.00^\circ)$, a turbulence power law of $\alpha = 3.6667$, a turbulence layer motion velocity $\vec{v}\tau = (5.00D, 90.00^\circ)$, and a ratio of the slope measurement noise variance to the wavefront slope variance $\sigma_n^2/\Gamma_s(0) = 50\%$. The ratio L_0/D ranges from 1 to ∞ .

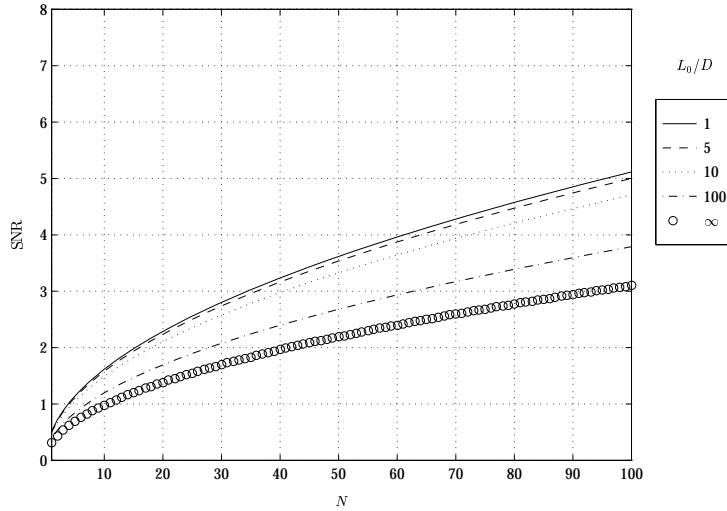


Figure D.24 Group A: Slope structure function estimator SNR vs. number of integration frames, N , for the DIMM geometry with a subaperture separation of $\vec{\rho} = (1.00D, 0.00^\circ)$, a turbulence power law of $\alpha = 3.6667$, a turbulence layer motion velocity $\vec{v}\tau = (10.00D, 90.00^\circ)$, and a ratio of the slope measurement noise variance to the wavefront slope variance $\sigma_n^2/\Gamma_s(0) = 50\%$. The ratio L_0/D ranges from 1 to ∞ .

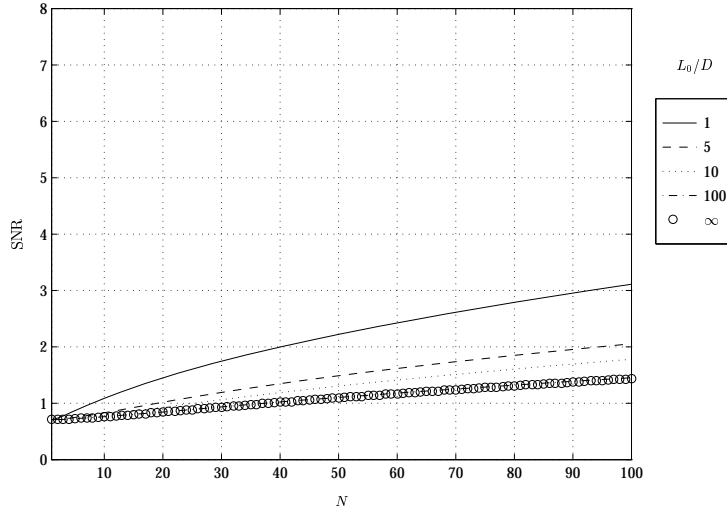


Figure D.25 Group B: Slope structure function estimator SNR vs. number of integration frames, N , for the DIMM geometry with a subaperture separation of $\vec{\rho} = (4.00D, 0.00^\circ)$, a turbulence power law of $\alpha = 3.6667$, a turbulence layer motion velocity $\vec{v}\tau = (0.10D, 90.00^\circ)$, and a ratio of the slope measurement noise variance to the wavefront slope variance $\sigma_n^2/\Gamma_s(0) = 0\%$. The ratio L_0/D ranges from 1 to ∞ .

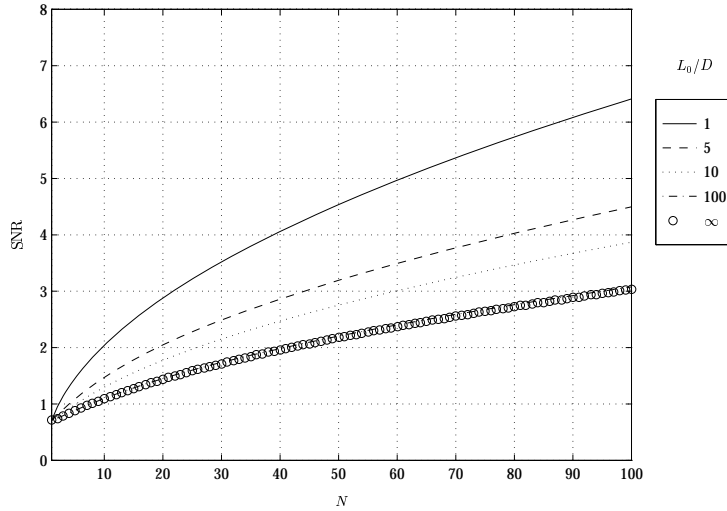


Figure D.26 Group B: Slope structure function estimator SNR vs. number of integration frames, N , for the DIMM geometry with a subaperture separation of $\vec{\rho} = (4.00D, 0.00^\circ)$, a turbulence power law of $\alpha = 3.6667$, a turbulence layer motion velocity $\vec{v}\tau = (0.50D, 90.00^\circ)$, and a ratio of the slope measurement noise variance to the wavefront slope variance $\sigma_n^2/\Gamma_s(0) = 0\%$. The ratio L_0/D ranges from 1 to ∞ .

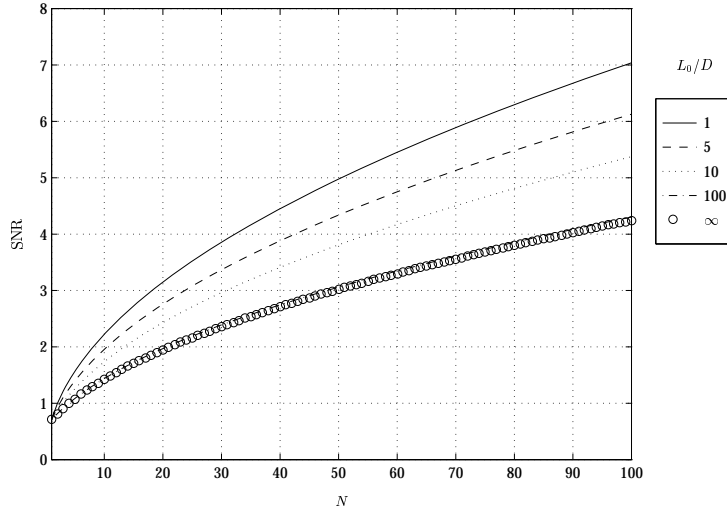


Figure D.27 Group B: Slope structure function estimator SNR vs. number of integration frames, N , for the DIMM geometry with a subaperture separation of $\vec{\rho} = (4.00D, 0.00^\circ)$, a turbulence power law of $\alpha = 3.6667$, a turbulence layer motion velocity $\vec{v}\tau = (1.00D, 90.00^\circ)$, and a ratio of the slope measurement noise variance to the wavefront slope variance $\sigma_n^2/\Gamma_s(0) = 0\%$. The ratio L_0/D ranges from 1 to ∞ .

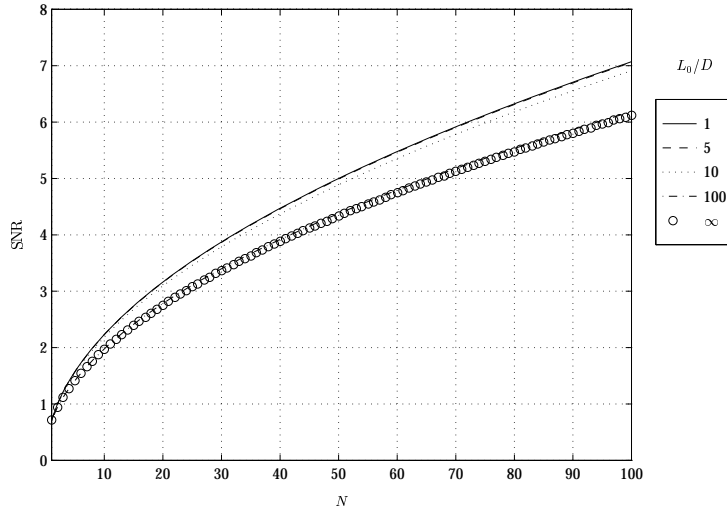


Figure D.28 Group B: Slope structure function estimator SNR vs. number of integration frames, N , for the DIMM geometry with a subaperture separation of $\vec{\rho} = (4.00D, 0.00^\circ)$, a turbulence power law of $\alpha = 3.6667$, a turbulence layer motion velocity $\vec{v}\tau = (2.50D, 90.00^\circ)$, and a ratio of the slope measurement noise variance to the wavefront slope variance $\sigma_n^2/\Gamma_s(0) = 0\%$. The ratio L_0/D ranges from 1 to ∞ .

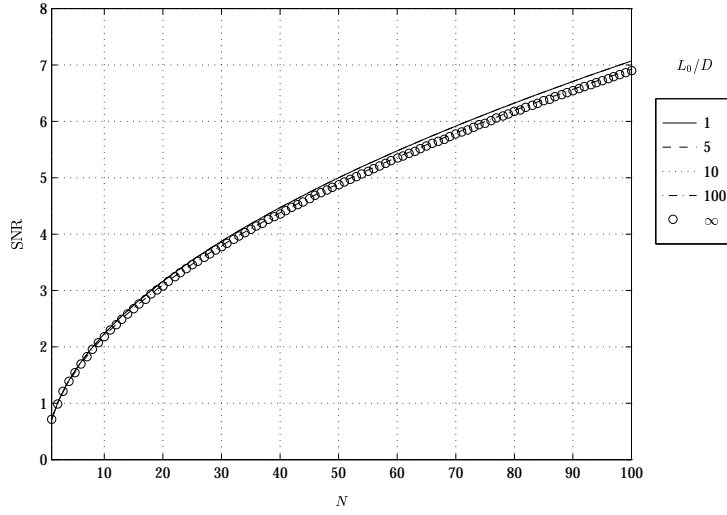


Figure D.29 Group B: Slope structure function estimator SNR vs. number of integration frames, N , for the DIMM geometry with a subaperture separation of $\vec{\rho} = (4.00D, 0.00^\circ)$, a turbulence power law of $\alpha = 3.6667$, a turbulence layer motion velocity $\vec{v}\tau = (5.00D, 90.00^\circ)$, and a ratio of the slope measurement noise variance to the wavefront slope variance $\sigma_n^2/\Gamma_s(0) = 0\%$. The ratio L_0/D ranges from 1 to ∞ .

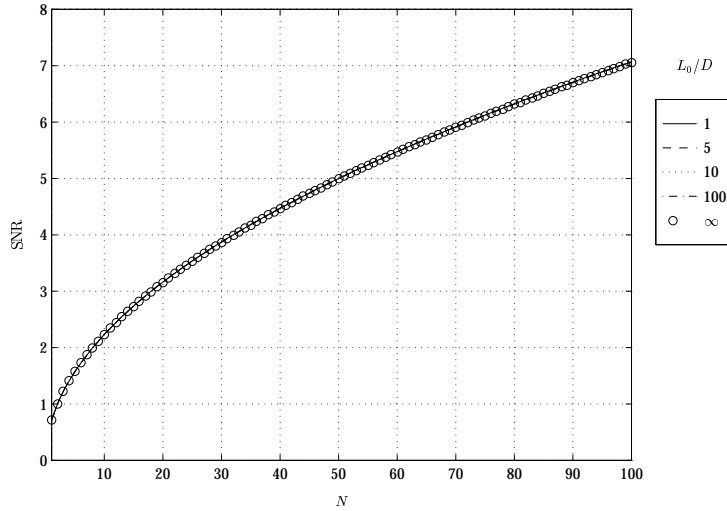


Figure D.30 Group B: Slope structure function estimator SNR vs. number of integration frames, N , for the DIMM geometry with a subaperture separation of $\vec{\rho} = (4.00D, 0.00^\circ)$, a turbulence power law of $\alpha = 3.6667$, a turbulence layer motion velocity $\vec{v}\tau = (10.00D, 90.00^\circ)$, and a ratio of the slope measurement noise variance to the wavefront slope variance $\sigma_n^2/\Gamma_s(0) = 0\%$. The ratio L_0/D ranges from 1 to ∞ .

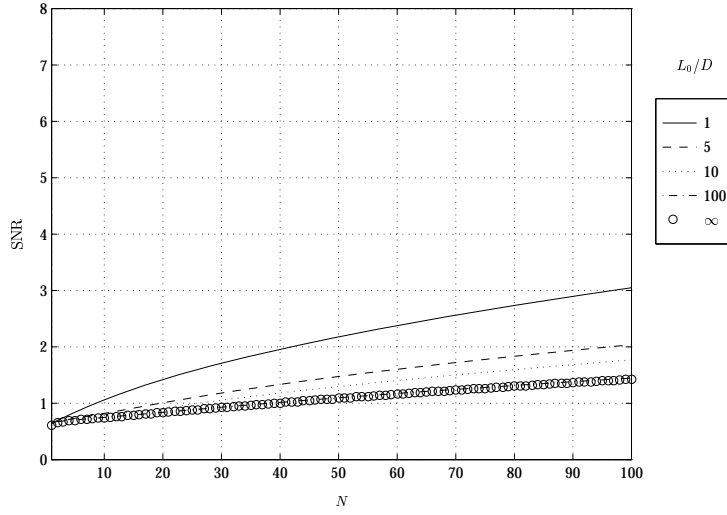


Figure D.31 Group B: Slope structure function estimator SNR vs. number of integration frames, N , for the DIMM geometry with a subaperture separation of $\vec{\rho} = (4.00D, 0.00^\circ)$, a turbulence power law of $\alpha = 3.6667$, a turbulence layer motion velocity $\vec{v}\tau = (0.10D, 90.00^\circ)$, and a ratio of the slope measurement noise variance to the wavefront slope variance $\sigma_n^2/\Gamma_s(0) = 10\%$. The ratio L_0/D ranges from 1 to ∞ .

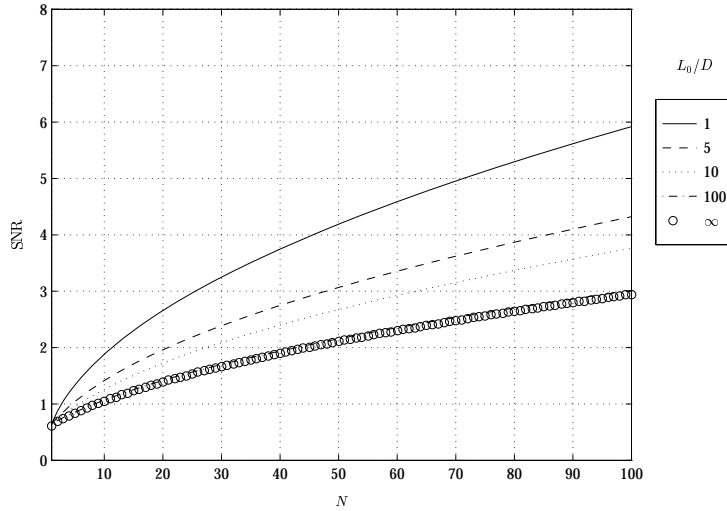


Figure D.32 Group B: Slope structure function estimator SNR vs. number of integration frames, N , for the DIMM geometry with a subaperture separation of $\vec{\rho} = (4.00D, 0.00^\circ)$, a turbulence power law of $\alpha = 3.6667$, a turbulence layer motion velocity $\vec{v}\tau = (0.50D, 90.00^\circ)$, and a ratio of the slope measurement noise variance to the wavefront slope variance $\sigma_n^2/\Gamma_s(0) = 10\%$. The ratio L_0/D ranges from 1 to ∞ .

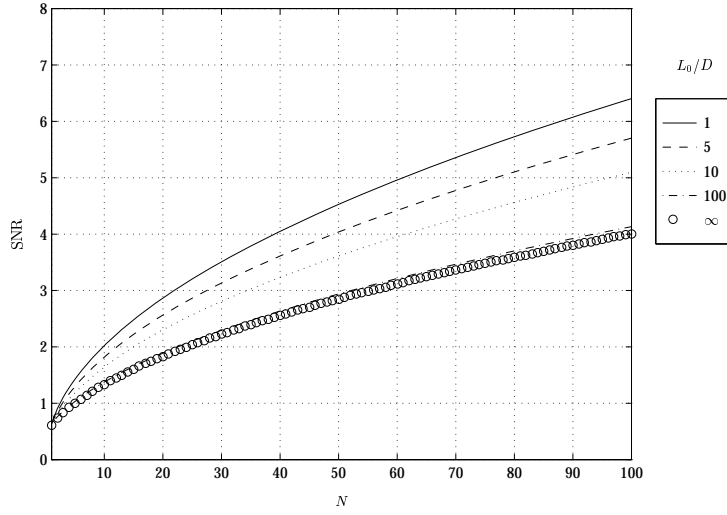


Figure D.33 Group B: Slope structure function estimator SNR vs. number of integration frames, N , for the DIMM geometry with a subaperture separation of $\vec{\rho} = (4.00D, 0.00^\circ)$, a turbulence power law of $\alpha = 3.6667$, a turbulence layer motion velocity $\vec{v}\tau = (1.00D, 90.00^\circ)$, and a ratio of the slope measurement noise variance to the wavefront slope variance $\sigma_n^2/\Gamma_s(0) = 10\%$. The ratio L_0/D ranges from 1 to ∞ .

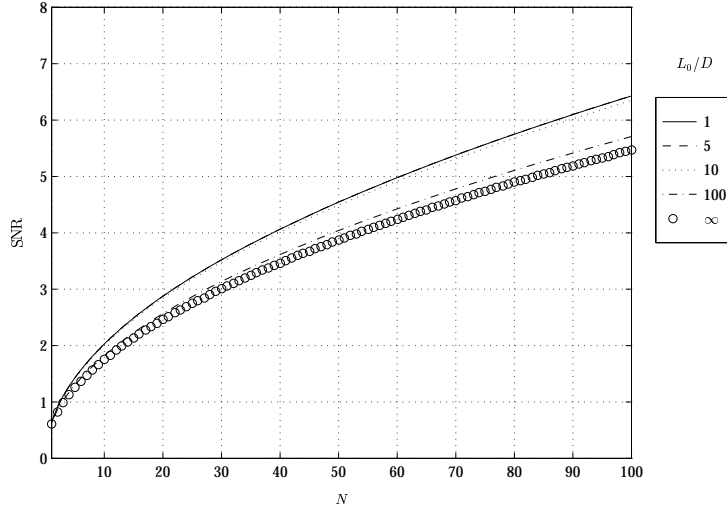


Figure D.34 Group B: Slope structure function estimator SNR vs. number of integration frames, N , for the DIMM geometry with a subaperture separation of $\vec{\rho} = (4.00D, 0.00^\circ)$, a turbulence power law of $\alpha = 3.6667$, a turbulence layer motion velocity $\vec{v}\tau = (2.50D, 90.00^\circ)$, and a ratio of the slope measurement noise variance to the wavefront slope variance $\sigma_n^2/\Gamma_s(0) = 10\%$. The ratio L_0/D ranges from 1 to ∞ .

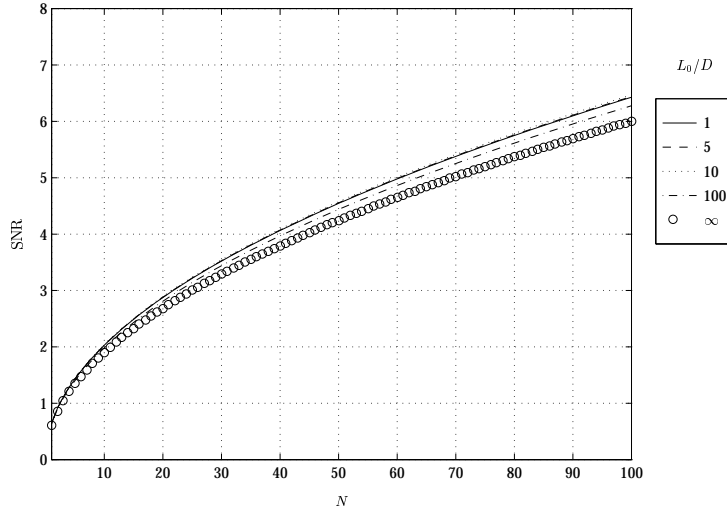


Figure D.35 Group B: Slope structure function estimator SNR vs. number of integration frames, N , for the DIMM geometry with a subaperture separation of $\vec{\rho} = (4.00D, 0.00^\circ)$, a turbulence power law of $\alpha = 3.6667$, a turbulence layer motion velocity $\vec{v}\tau = (5.00D, 90.00^\circ)$, and a ratio of the slope measurement noise variance to the wavefront slope variance $\sigma_n^2/\Gamma_s(0) = 10\%$. The ratio L_0/D ranges from 1 to ∞ .

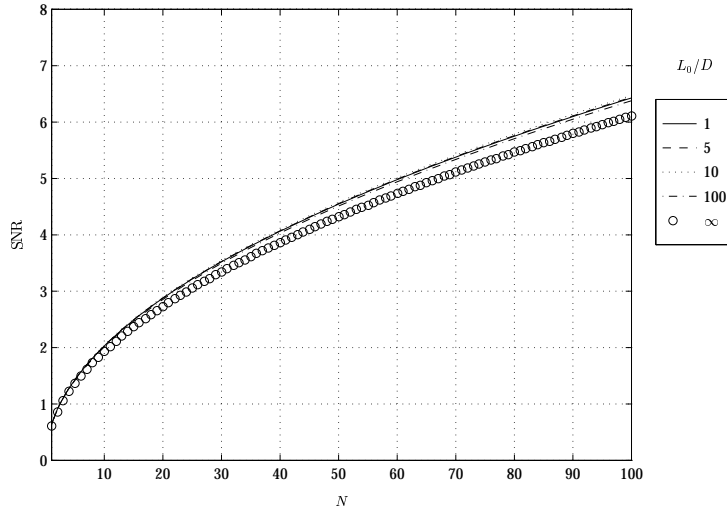


Figure D.36 Group B: Slope structure function estimator SNR vs. number of integration frames, N , for the DIMM geometry with a subaperture separation of $\vec{\rho} = (4.00D, 0.00^\circ)$, a turbulence power law of $\alpha = 3.6667$, a turbulence layer motion velocity $\vec{v}\tau = (10.00D, 90.00^\circ)$, and a ratio of the slope measurement noise variance to the wavefront slope variance $\sigma_n^2/\Gamma_s(0) = 10\%$. The ratio L_0/D ranges from 1 to ∞ .

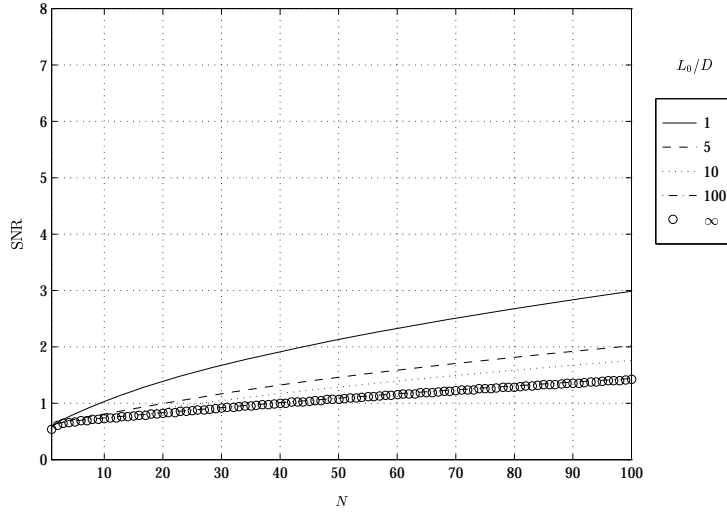


Figure D.37 Group B: Slope structure function estimator SNR vs. number of integration frames, N , for the DIMM geometry with a subaperture separation of $\vec{\rho} = (4.00D, 0.00^\circ)$, a turbulence power law of $\alpha = 3.6667$, a turbulence layer motion velocity $\vec{v}\tau = (0.10D, 90.00^\circ)$, and a ratio of the slope measurement noise variance to the wavefront slope variance $\sigma_n^2/\Gamma_s(0) = 20\%$. The ratio L_0/D ranges from 1 to ∞ .

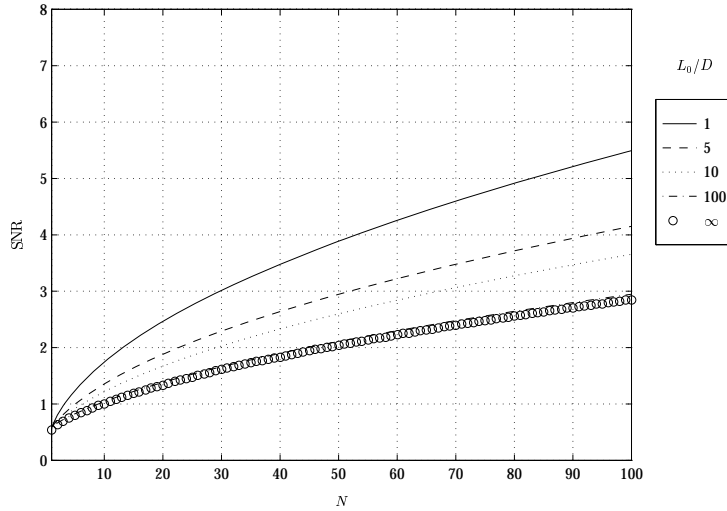


Figure D.38 Group B: Slope structure function estimator SNR vs. number of integration frames, N , for the DIMM geometry with a subaperture separation of $\vec{\rho} = (4.00D, 0.00^\circ)$, a turbulence power law of $\alpha = 3.6667$, a turbulence layer motion velocity $\vec{v}\tau = (0.50D, 90.00^\circ)$, and a ratio of the slope measurement noise variance to the wavefront slope variance $\sigma_n^2/\Gamma_s(0) = 20\%$. The ratio L_0/D ranges from 1 to ∞ .

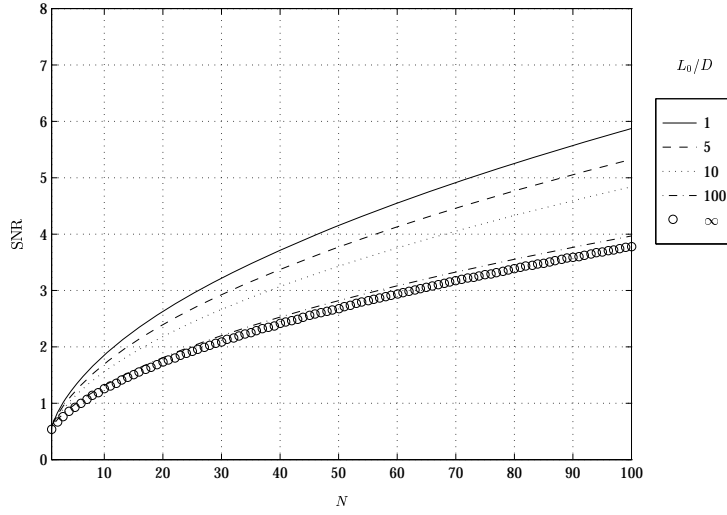


Figure D.39 Group B: Slope structure function estimator SNR vs. number of integration frames, N , for the DIMM geometry with a subaperture separation of $\vec{\rho} = (4.00D, 0.00^\circ)$, a turbulence power law of $\alpha = 3.6667$, a turbulence layer motion velocity $\vec{v}\tau = (1.00D, 90.00^\circ)$, and a ratio of the slope measurement noise variance to the wavefront slope variance $\sigma_n^2/\Gamma_s(0) = 20\%$. The ratio L_0/D ranges from 1 to ∞ .

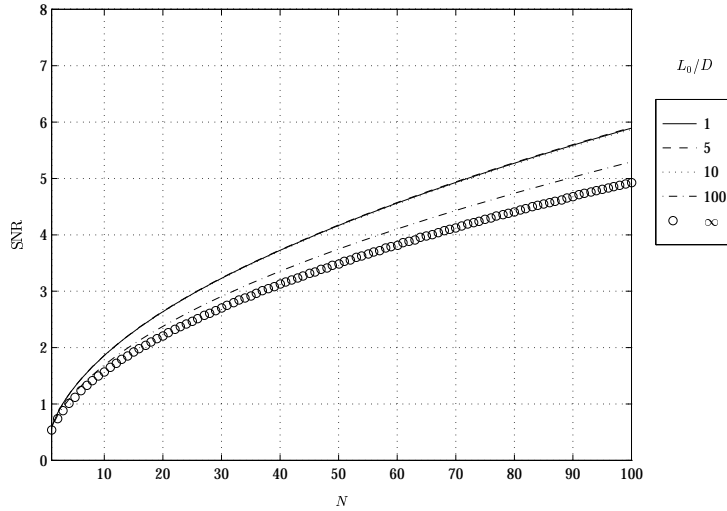


Figure D.40 Group B: Slope structure function estimator SNR vs. number of integration frames, N , for the DIMM geometry with a subaperture separation of $\vec{\rho} = (4.00D, 0.00^\circ)$, a turbulence power law of $\alpha = 3.6667$, a turbulence layer motion velocity $\vec{v}\tau = (2.50D, 90.00^\circ)$, and a ratio of the slope measurement noise variance to the wavefront slope variance $\sigma_n^2/\Gamma_s(0) = 20\%$. The ratio L_0/D ranges from 1 to ∞ .

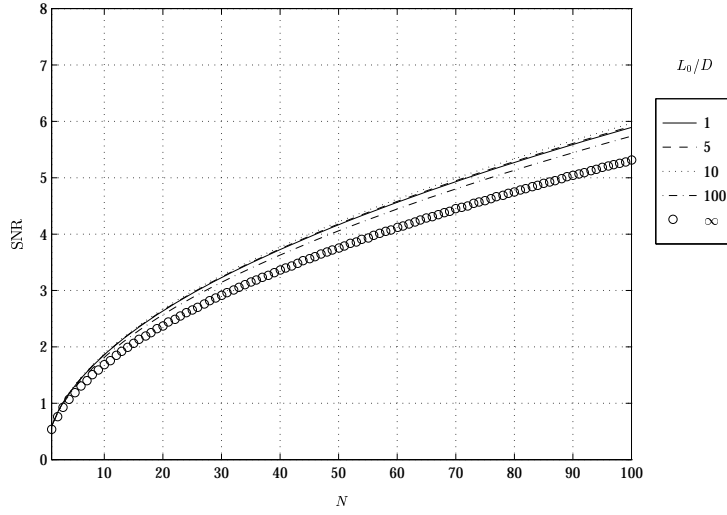


Figure D.41 Group B: Slope structure function estimator SNR vs. number of integration frames, N , for the DIMM geometry with a subaperture separation of $\vec{\rho} = (4.00D, 0.00^\circ)$, a turbulence power law of $\alpha = 3.6667$, a turbulence layer motion velocity $\vec{v}\tau = (5.00D, 90.00^\circ)$, and a ratio of the slope measurement noise variance to the wavefront slope variance $\sigma_n^2/\Gamma_s(0) = 20\%$. The ratio L_0/D ranges from 1 to ∞ .

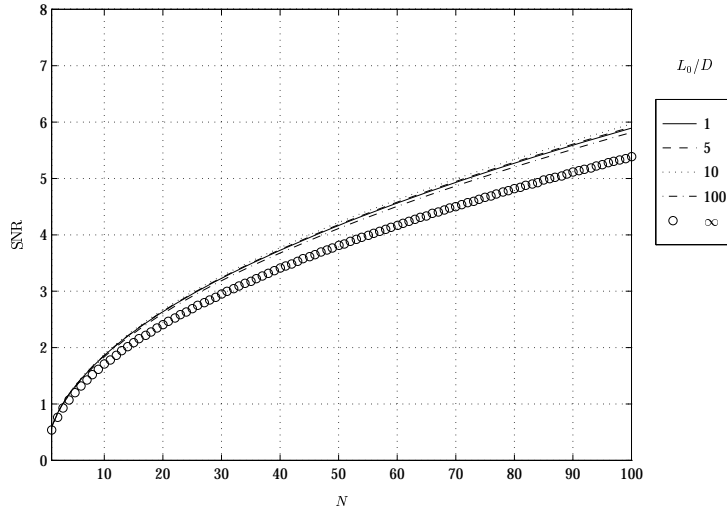


Figure D.42 Group B: Slope structure function estimator SNR vs. number of integration frames, N , for the DIMM geometry with a subaperture separation of $\vec{\rho} = (4.00D, 0.00^\circ)$, a turbulence power law of $\alpha = 3.6667$, a turbulence layer motion velocity $\vec{v}\tau = (10.00D, 90.00^\circ)$, and a ratio of the slope measurement noise variance to the wavefront slope variance $\sigma_n^2/\Gamma_s(0) = 20\%$. The ratio L_0/D ranges from 1 to ∞ .

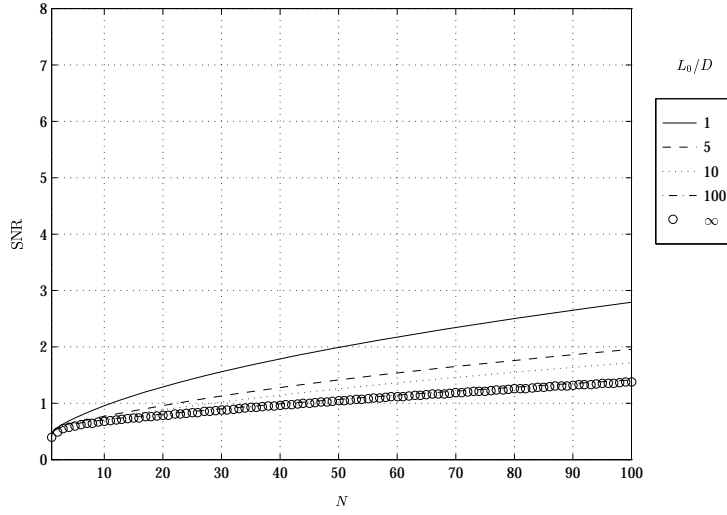


Figure D.43 Group B: Slope structure function estimator SNR vs. number of integration frames, N , for the DIMM geometry with a subaperture separation of $\vec{\rho} = (4.00D, 0.00^\circ)$, a turbulence power law of $\alpha = 3.6667$, a turbulence layer motion velocity $\vec{v}\tau = (0.10D, 90.00^\circ)$, and a ratio of the slope measurement noise variance to the wavefront slope variance $\sigma_n^2/\Gamma_s(0) = 50\%$. The ratio L_0/D ranges from 1 to ∞ .

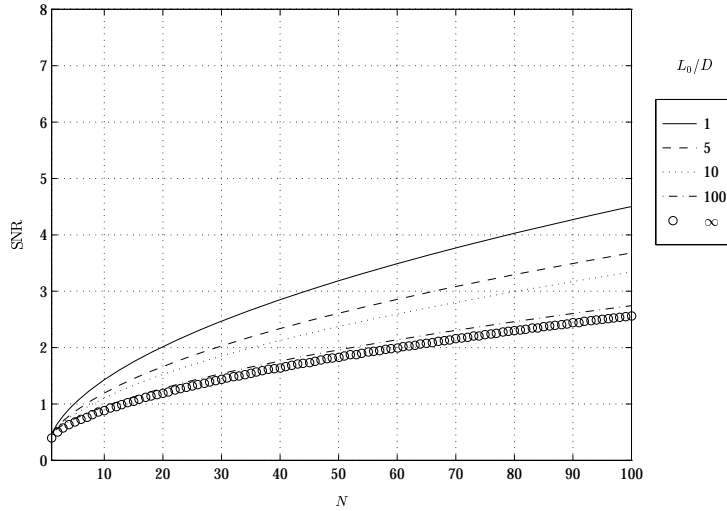


Figure D.44 Group B: Slope structure function estimator SNR vs. number of integration frames, N , for the DIMM geometry with a subaperture separation of $\vec{\rho} = (4.00D, 0.00^\circ)$, a turbulence power law of $\alpha = 3.6667$, a turbulence layer motion velocity $\vec{v}\tau = (0.50D, 90.00^\circ)$, and a ratio of the slope measurement noise variance to the wavefront slope variance $\sigma_n^2/\Gamma_s(0) = 50\%$. The ratio L_0/D ranges from 1 to ∞ .

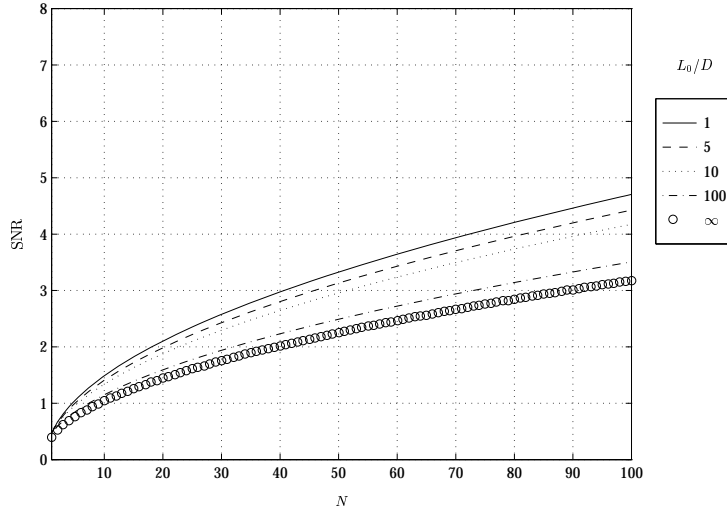


Figure D.45 Group B: Slope structure function estimator SNR vs. number of integration frames, N , for the DIMM geometry with a subaperture separation of $\vec{\rho} = (4.00D, 0.00^\circ)$, a turbulence power law of $\alpha = 3.6667$, a turbulence layer motion velocity $\vec{v}\tau = (1.00D, 90.00^\circ)$, and a ratio of the slope measurement noise variance to the wavefront slope variance $\sigma_n^2/\Gamma_s(0) = 50\%$. The ratio L_0/D ranges from 1 to ∞ .

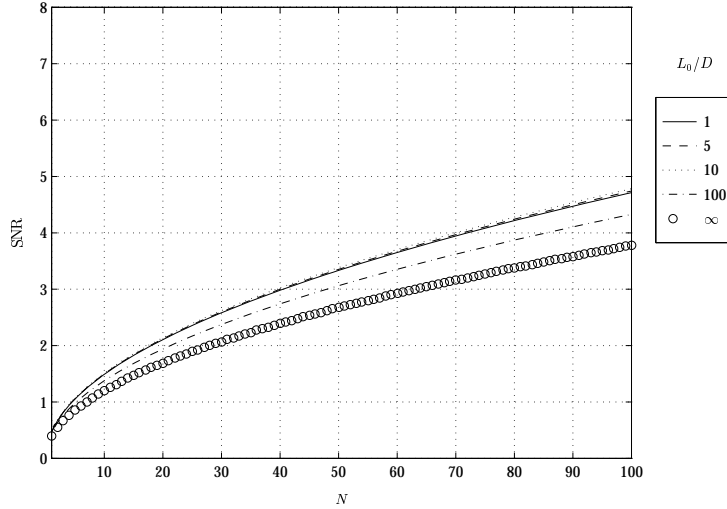


Figure D.46 Group B: Slope structure function estimator SNR vs. number of integration frames, N , for the DIMM geometry with a subaperture separation of $\vec{\rho} = (4.00D, 0.00^\circ)$, a turbulence power law of $\alpha = 3.6667$, a turbulence layer motion velocity $\vec{v}\tau = (2.50D, 90.00^\circ)$, and a ratio of the slope measurement noise variance to the wavefront slope variance $\sigma_n^2/\Gamma_s(0) = 50\%$. The ratio L_0/D ranges from 1 to ∞ .

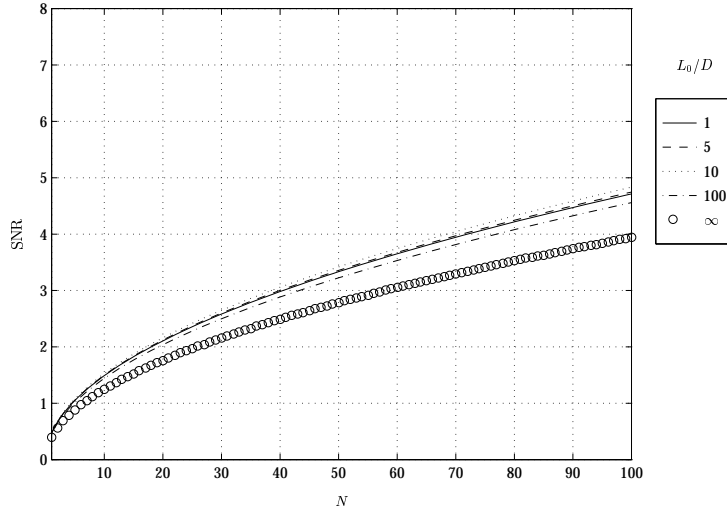


Figure D.47 Group B: Slope structure function estimator SNR vs. number of integration frames, N , for the DIMM geometry with a subaperture separation of $\vec{\rho} = (4.00D, 0.00^\circ)$, a turbulence power law of $\alpha = 3.6667$, a turbulence layer motion velocity $\vec{v}\tau = (5.00D, 90.00^\circ)$, and a ratio of the slope measurement noise variance to the wavefront slope variance $\sigma_n^2/\Gamma_s(0) = 50\%$. The ratio L_0/D ranges from 1 to ∞ .

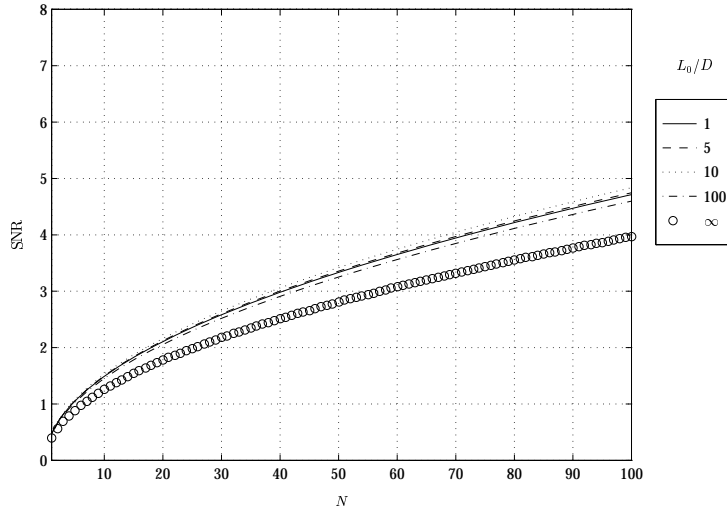


Figure D.48 Group B: Slope structure function estimator SNR vs. number of integration frames, N , for the DIMM geometry with a subaperture separation of $\vec{\rho} = (4.00D, 0.00^\circ)$, a turbulence power law of $\alpha = 3.6667$, a turbulence layer motion velocity $\vec{v}\tau = (10.00D, 90.00^\circ)$, and a ratio of the slope measurement noise variance to the wavefront slope variance $\sigma_n^2/\Gamma_s(0) = 50\%$. The ratio L_0/D ranges from 1 to ∞ .

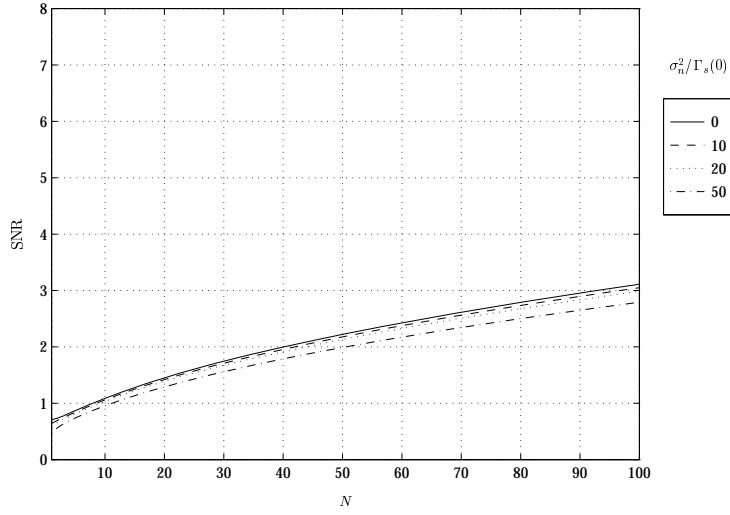


Figure D.49 Group C: Slope structure function estimator SNR vs. number of integration frames, N , for the DIMM geometry with a subaperture separation of $\vec{\rho} = (4.00D, 0.00^\circ)$, a turbulence power law of $\alpha = 3.6667$, a turbulence layer motion velocity $\vec{v}\tau = (0.10D, 90.00^\circ)$, and a ratio $L_0/D = 1.00$. The ratio of the slope measurement noise variance to the wavefront slope variance $\sigma_n^2/\Gamma_s(0)$ varies from 0% to 50%.

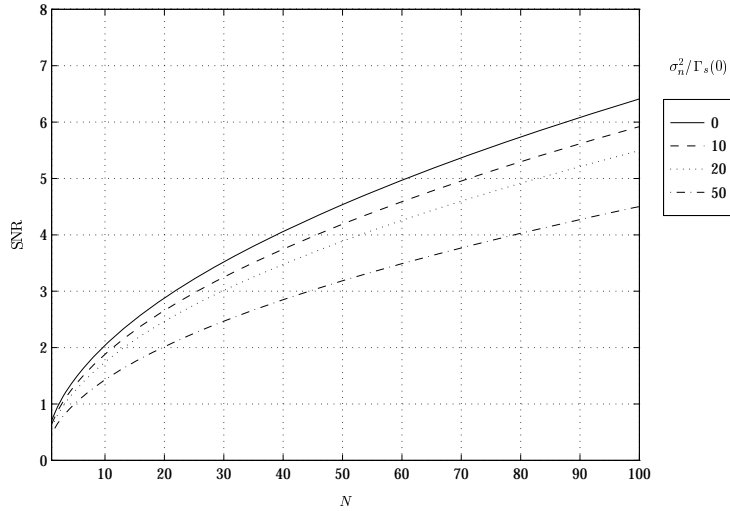


Figure D.50 Group C: Slope structure function estimator SNR vs. number of integration frames, N , for the DIMM geometry with a subaperture separation of $\vec{\rho} = (4.00D, 0.00^\circ)$, a turbulence power law of $\alpha = 3.6667$, a turbulence layer motion velocity $\vec{v}\tau = (0.50D, 90.00^\circ)$, and a ratio $L_0/D = 1.00$. The ratio of the slope measurement noise variance to the wavefront slope variance $\sigma_n^2/\Gamma_s(0)$ varies from 0% to 50%.

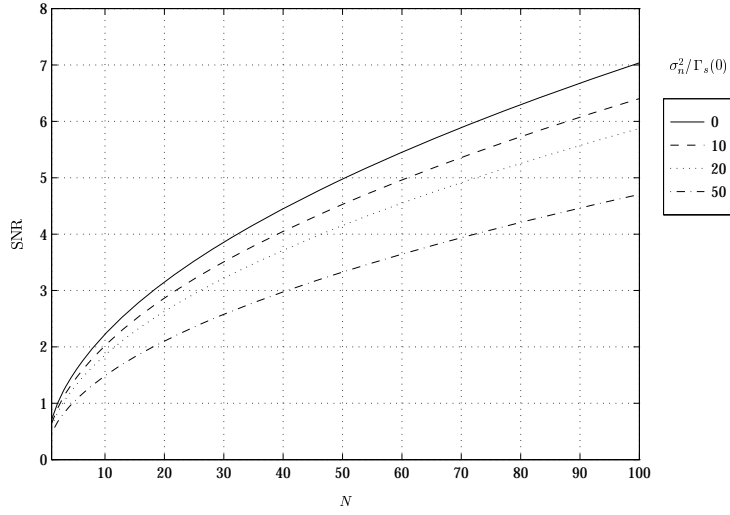


Figure D.51 Group C: Slope structure function estimator SNR vs. number of integration frames, N , for the DIMM geometry with a subaperture separation of $\vec{\rho} = (4.00D, 0.00^\circ)$, a turbulence power law of $\alpha = 3.6667$, a turbulence layer motion velocity $\vec{v}\tau = (1.00D, 90.00^\circ)$, and a ratio $L_0/D = 1.00$. The ratio of the slope measurement noise variance to the wavefront slope variance $\sigma_n^2/\Gamma_s(0)$ varies from 0% to 50%.

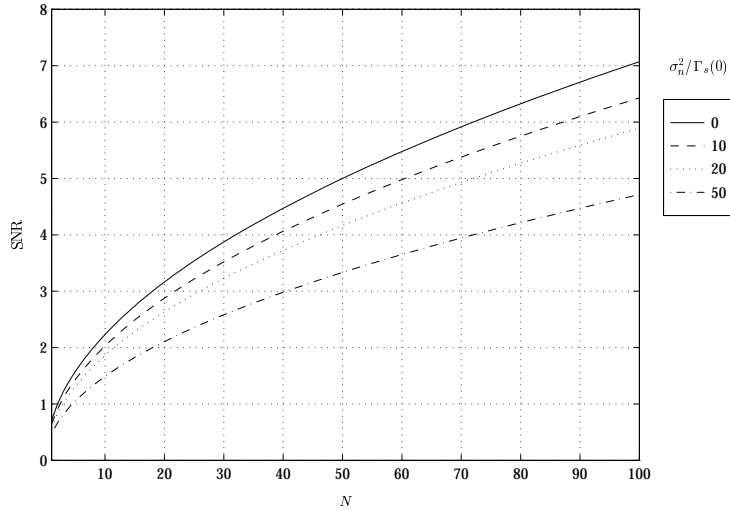


Figure D.52 Group C: Slope structure function estimator SNR vs. number of integration frames, N , for the DIMM geometry with a subaperture separation of $\vec{\rho} = (4.00D, 0.00^\circ)$, a turbulence power law of $\alpha = 3.6667$, a turbulence layer motion velocity $\vec{v}\tau = (2.50D, 90.00^\circ)$, and a ratio $L_0/D = 1.00$. The ratio of the slope measurement noise variance to the wavefront slope variance $\sigma_n^2/\Gamma_s(0)$ varies from 0% to 50%.

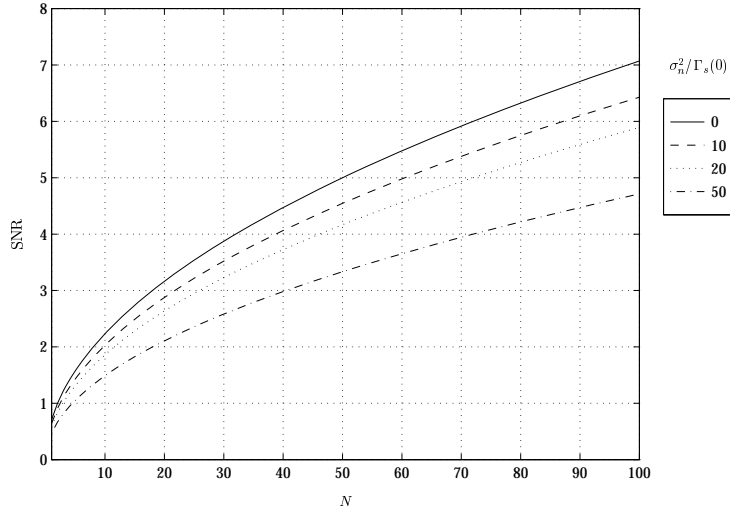


Figure D.53 Group C: Slope structure function estimator SNR vs. number of integration frames, N , for the DIMM geometry with a subaperture separation of $\vec{\rho} = (4.00D, 0.00^\circ)$, a turbulence power law of $\alpha = 3.6667$, a turbulence layer motion velocity $\vec{v}\tau = (5.00D, 90.00^\circ)$, and a ratio $L_0/D = 1.00$. The ratio of the slope measurement noise variance to the wavefront slope variance $\sigma_n^2/\Gamma_s(0)$ varies from 0% to 50%.

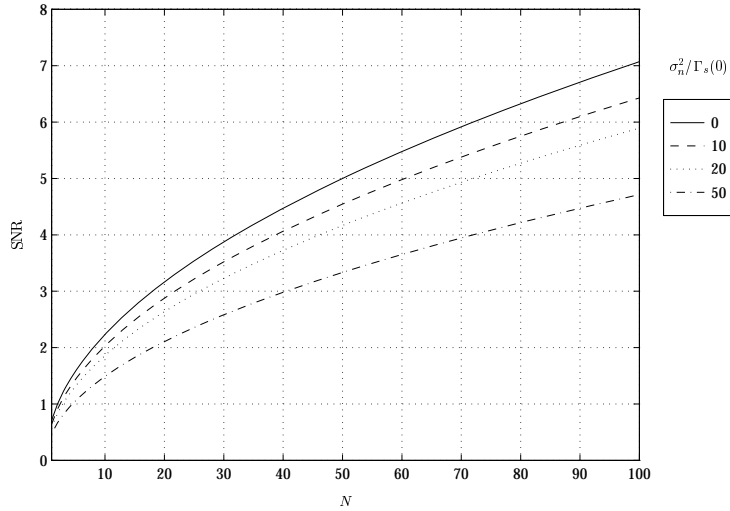


Figure D.54 Group C: Slope structure function estimator SNR vs. number of integration frames, N , for the DIMM geometry with a subaperture separation of $\vec{\rho} = (4.00D, 0.00^\circ)$, a turbulence power law of $\alpha = 3.6667$, a turbulence layer motion velocity $\vec{v}\tau = (10.00D, 90.00^\circ)$, and a ratio $L_0/D = 1.00$. The ratio of the slope measurement noise variance to the wavefront slope variance $\sigma_n^2/\Gamma_s(0)$ varies from 0% to 50%.

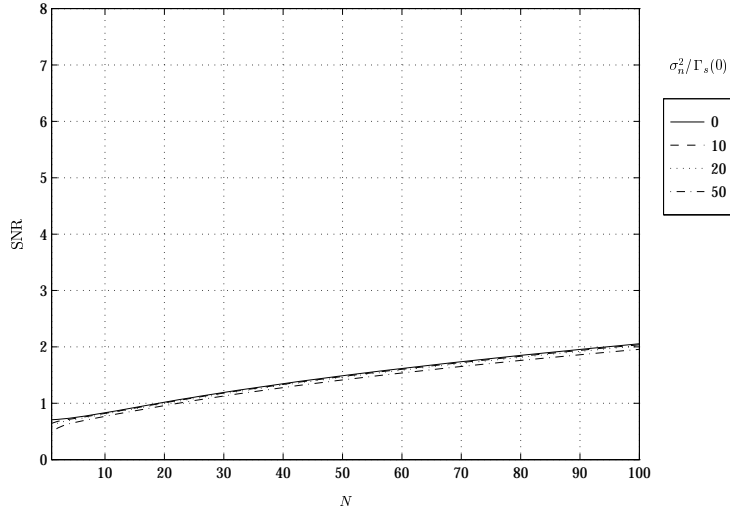


Figure D.55 Group C: Slope structure function estimator SNR vs. number of integration frames, N , for the DIMM geometry with a subaperture separation of $\vec{\rho} = (4.00D, 0.00^\circ)$, a turbulence power law of $\alpha = 3.6667$, a turbulence layer motion velocity $\vec{v}\tau = (0.10D, 90.00^\circ)$, and a ratio $L_0/D = 5.00$. The ratio of the slope measurement noise variance to the wavefront slope variance $\sigma_n^2/\Gamma_s(0)$ varies from 0% to 50%.

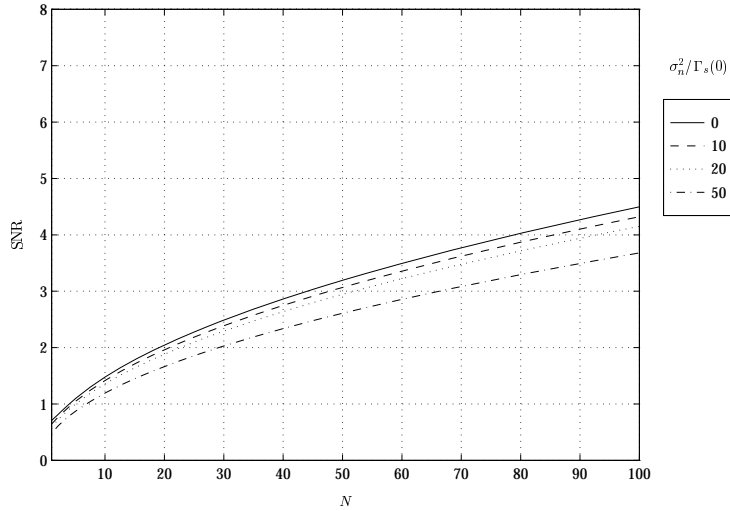


Figure D.56 Group C: Slope structure function estimator SNR vs. number of integration frames, N , for the DIMM geometry with a subaperture separation of $\vec{\rho} = (4.00D, 0.00^\circ)$, a turbulence power law of $\alpha = 3.6667$, a turbulence layer motion velocity $\vec{v}\tau = (0.50D, 90.00^\circ)$, and a ratio $L_0/D = 5.00$. The ratio of the slope measurement noise variance to the wavefront slope variance $\sigma_n^2/\Gamma_s(0)$ varies from 0% to 50%.

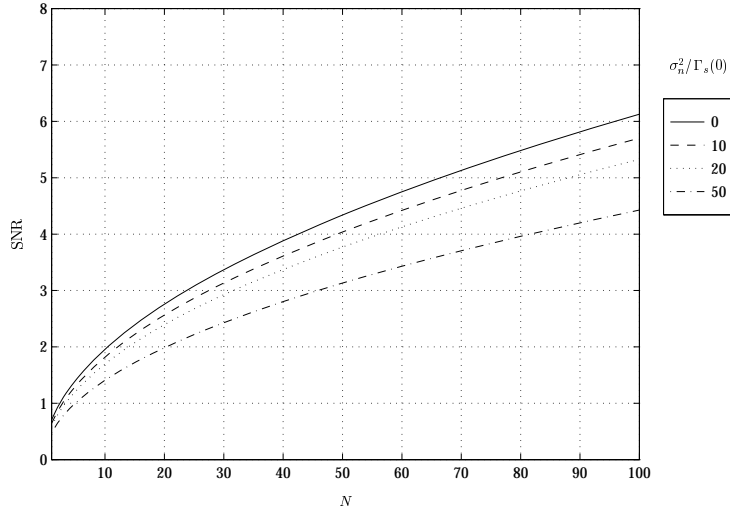


Figure D.57 Group C: Slope structure function estimator SNR vs. number of integration frames, N , for the DIMM geometry with a subaperture separation of $\vec{\rho} = (4.00D, 0.00^\circ)$, a turbulence power law of $\alpha = 3.6667$, a turbulence layer motion velocity $\vec{v}\tau = (1.00D, 90.00^\circ)$, and a ratio $L_0/D = 5.00$. The ratio of the slope measurement noise variance to the wavefront slope variance $\sigma_n^2/\Gamma_s(0)$ varies from 0% to 50%.

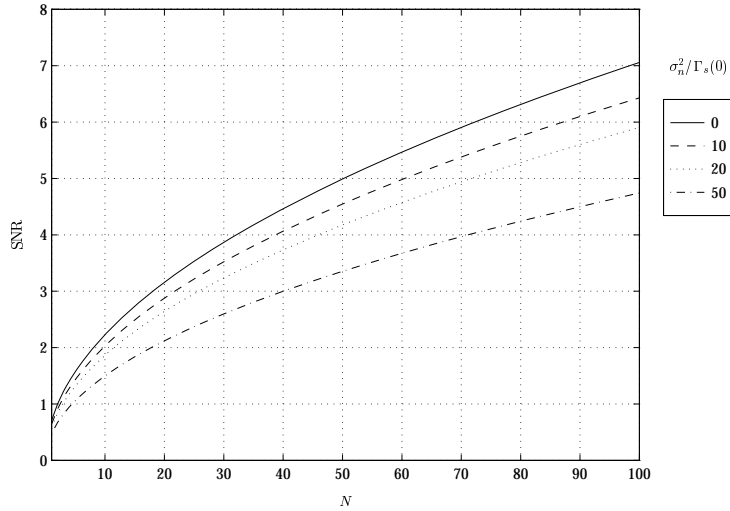


Figure D.58 Group C: Slope structure function estimator SNR vs. number of integration frames, N , for the DIMM geometry with a subaperture separation of $\vec{\rho} = (4.00D, 0.00^\circ)$, a turbulence power law of $\alpha = 3.6667$, a turbulence layer motion velocity $\vec{v}\tau = (2.50D, 90.00^\circ)$, and a ratio $L_0/D = 5.00$. The ratio of the slope measurement noise variance to the wavefront slope variance $\sigma_n^2/\Gamma_s(0)$ varies from 0% to 50%.

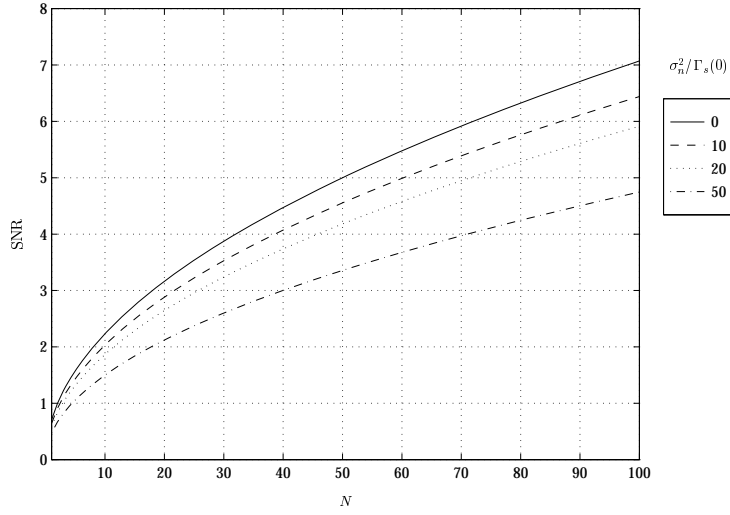


Figure D.59 Group C: Slope structure function estimator SNR vs. number of integration frames, N , for the DIMM geometry with a subaperture separation of $\vec{\rho} = (4.00D, 0.00^\circ)$, a turbulence power law of $\alpha = 3.6667$, a turbulence layer motion velocity $\vec{v}\tau = (5.00D, 90.00^\circ)$, and a ratio $L_0/D = 5.00$. The ratio of the slope measurement noise variance to the wavefront slope variance $\sigma_n^2/\Gamma_s(0)$ varies from 0% to 50%.

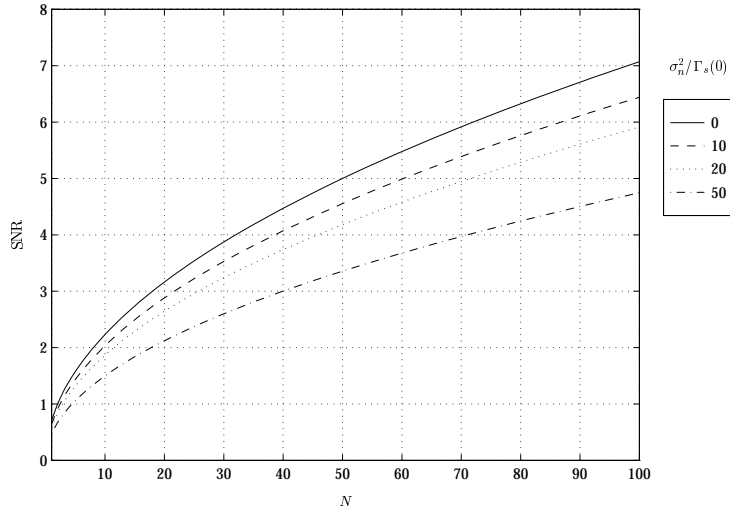


Figure D.60 Group C: Slope structure function estimator SNR vs. number of integration frames, N , for the DIMM geometry with a subaperture separation of $\vec{\rho} = (4.00D, 0.00^\circ)$, a turbulence power law of $\alpha = 3.6667$, a turbulence layer motion velocity $\vec{v}\tau = (10.00D, 90.00^\circ)$, and a ratio $L_0/D = 5.00$. The ratio of the slope measurement noise variance to the wavefront slope variance $\sigma_n^2/\Gamma_s(0)$ varies from 0% to 50%.

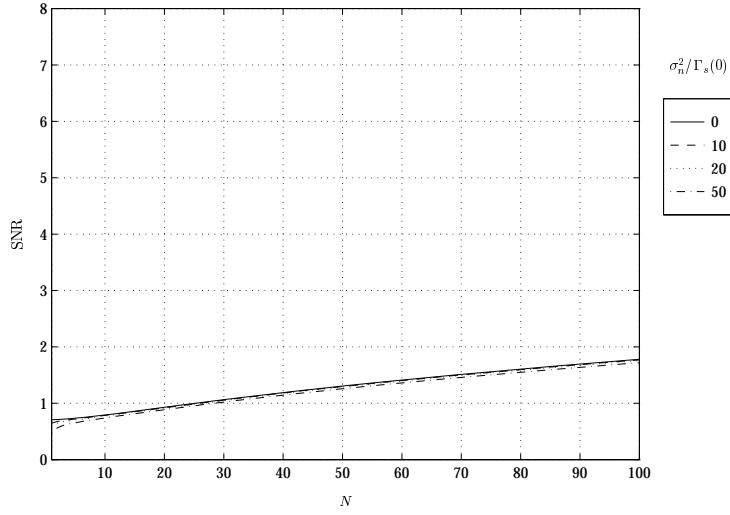


Figure D.61 Group C: Slope structure function estimator SNR vs. number of integration frames, N , for the DIMM geometry with a subaperture separation of $\vec{\rho} = (4.00D, 0.00^\circ)$, a turbulence power law of $\alpha = 3.6667$, a turbulence layer motion velocity $\vec{v}\tau = (0.10D, 90.00^\circ)$, and a ratio $L_0/D = 10.00$. The ratio of the slope measurement noise variance to the wavefront slope variance $\sigma_n^2/\Gamma_s(0)$ varies from 0% to 50%.

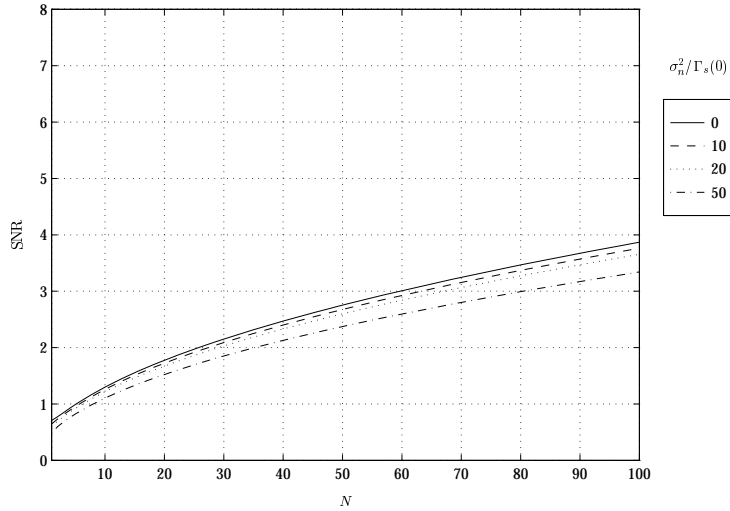


Figure D.62 Group C: Slope structure function estimator SNR vs. number of integration frames, N , for the DIMM geometry with a subaperture separation of $\vec{\rho} = (4.00D, 0.00^\circ)$, a turbulence power law of $\alpha = 3.6667$, a turbulence layer motion velocity $\vec{v}\tau = (0.50D, 90.00^\circ)$, and a ratio $L_0/D = 10.00$. The ratio of the slope measurement noise variance to the wavefront slope variance $\sigma_n^2/\Gamma_s(0)$ varies from 0% to 50%.

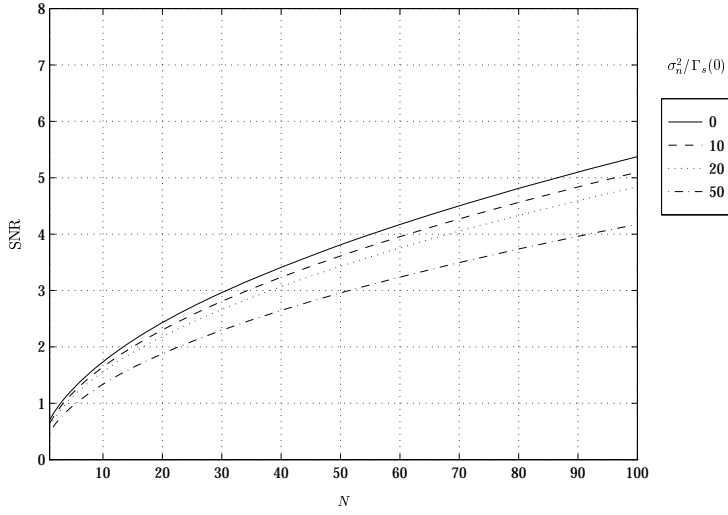


Figure D.63 Group C: Slope structure function estimator SNR vs. number of integration frames, N , for the DIMM geometry with a subaperture separation of $\vec{\rho} = (4.00D, 0.00^\circ)$, a turbulence power law of $\alpha = 3.6667$, a turbulence layer motion velocity $\vec{v}\tau = (1.00D, 90.00^\circ)$, and a ratio $L_0/D = 10.00$. The ratio of the slope measurement noise variance to the wavefront slope variance $\sigma_n^2/\Gamma_s(0)$ varies from 0% to 50%.

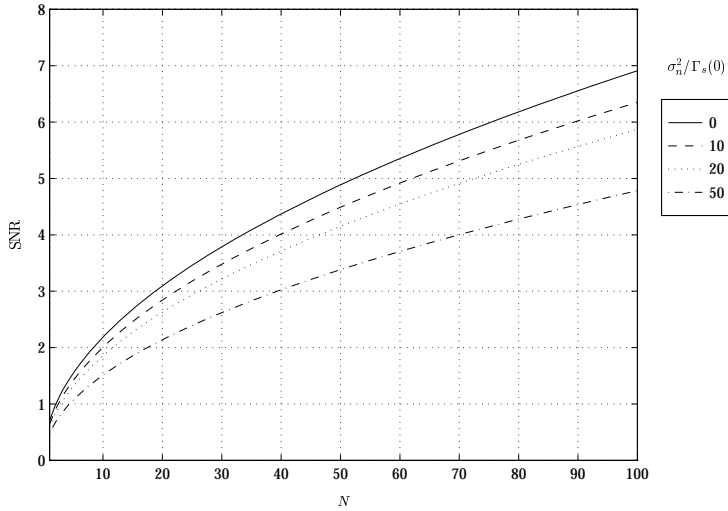


Figure D.64 Group C: Slope structure function estimator SNR vs. number of integration frames, N , for the DIMM geometry with a subaperture separation of $\vec{\rho} = (4.00D, 0.00^\circ)$, a turbulence power law of $\alpha = 3.6667$, a turbulence layer motion velocity $\vec{v}\tau = (2.50D, 90.00^\circ)$, and a ratio $L_0/D = 10.00$. The ratio of the slope measurement noise variance to the wavefront slope variance $\sigma_n^2/\Gamma_s(0)$ varies from 0% to 50%.

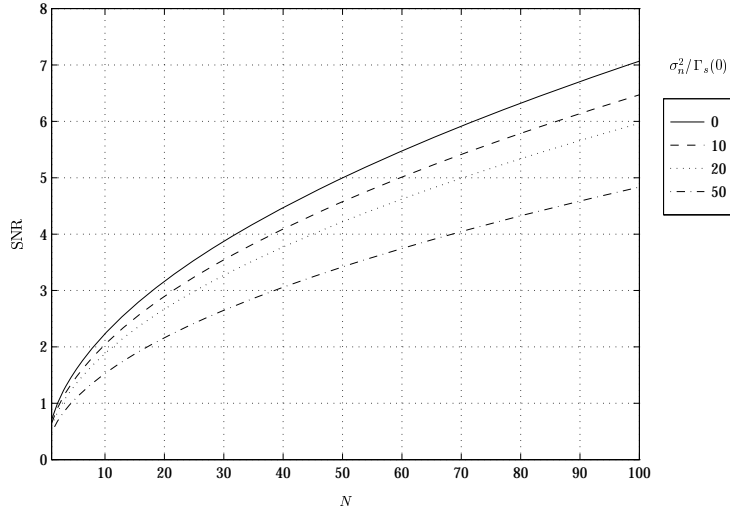


Figure D.65 Group C: Slope structure function estimator SNR vs. number of integration frames, N , for the DIMM geometry with a subaperture separation of $\vec{\rho} = (4.00D, 0.00^\circ)$, a turbulence power law of $\alpha = 3.6667$, a turbulence layer motion velocity $\vec{v}\tau = (5.00D, 90.00^\circ)$, and a ratio $L_0/D = 10.00$. The ratio of the slope measurement noise variance to the wavefront slope variance $\sigma_n^2/\Gamma_s(0)$ varies from 0% to 50%.

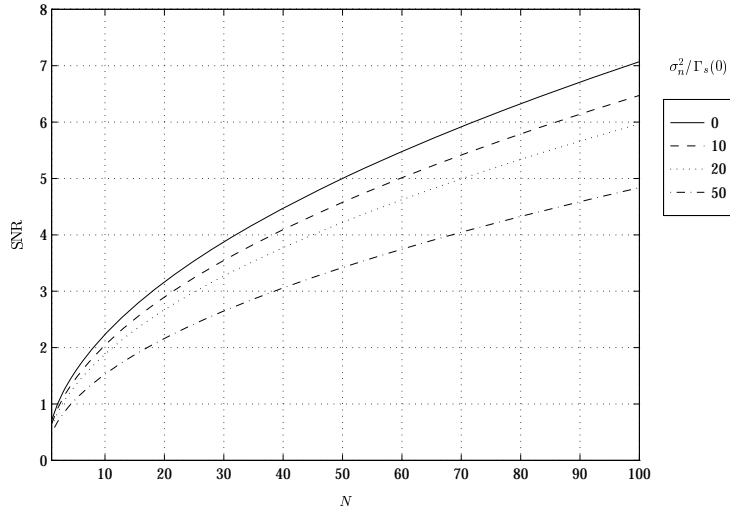


Figure D.66 Group C: Slope structure function estimator SNR vs. number of integration frames, N , for the DIMM geometry with a subaperture separation of $\vec{\rho} = (4.00D, 0.00^\circ)$, a turbulence power law of $\alpha = 3.6667$, a turbulence layer motion velocity $\vec{v}\tau = (10.00D, 90.00^\circ)$, and a ratio $L_0/D = 10.00$. The ratio of the slope measurement noise variance to the wavefront slope variance $\sigma_n^2/\Gamma_s(0)$ varies from 0% to 50%.

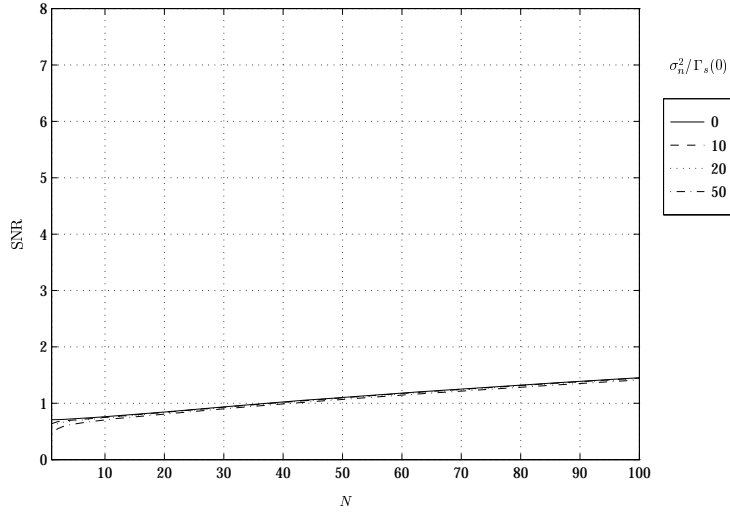


Figure D.67 Group C: Slope structure function estimator SNR vs. number of integration frames, N , for the DIMM geometry with a subaperture separation of $\vec{\rho} = (4.00D, 0.00^\circ)$, a turbulence power law of $\alpha = 3.6667$, a turbulence layer motion velocity $\vec{v}\tau = (0.10D, 90.00^\circ)$, and a ratio $L_0/D = 100.00$. The ratio of the slope measurement noise variance to the wavefront slope variance $\sigma_n^2/\Gamma_s(0)$ varies from 0% to 50%.

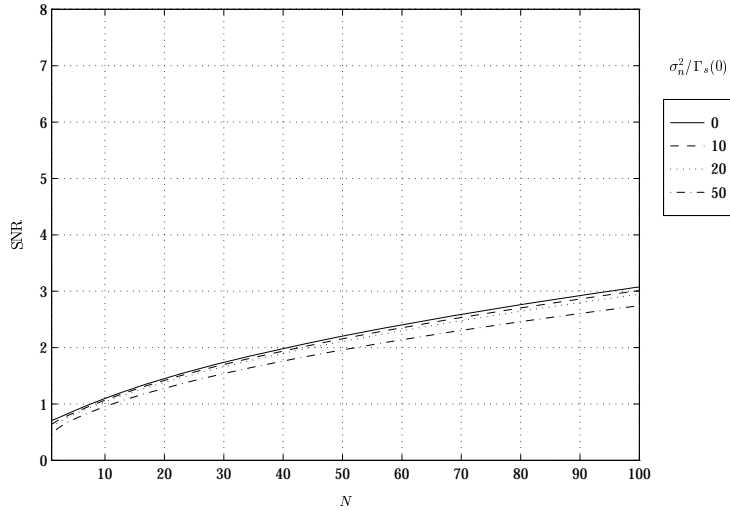


Figure D.68 Group C: Slope structure function estimator SNR vs. number of integration frames, N , for the DIMM geometry with a subaperture separation of $\vec{\rho} = (4.00D, 0.00^\circ)$, a turbulence power law of $\alpha = 3.6667$, a turbulence layer motion velocity $\vec{v}\tau = (0.50D, 90.00^\circ)$, and a ratio $L_0/D = 100.00$. The ratio of the slope measurement noise variance to the wavefront slope variance $\sigma_n^2/\Gamma_s(0)$ varies from 0% to 50%.

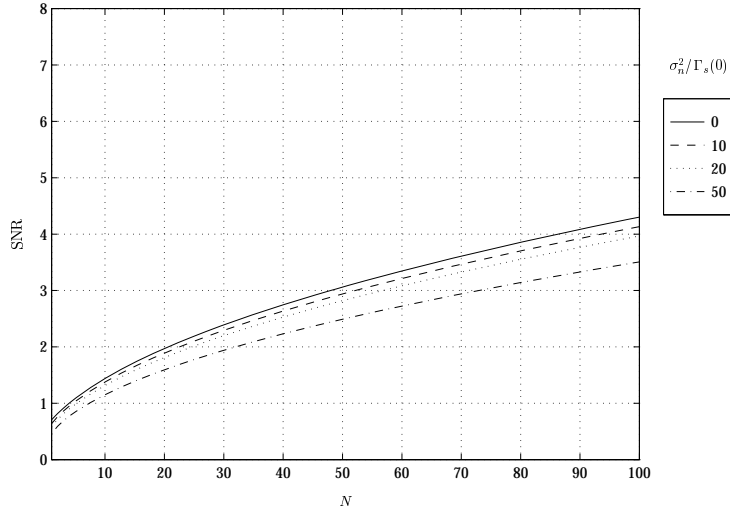


Figure D.69 Group C: Slope structure function estimator SNR vs. number of integration frames, N , for the DIMM geometry with a subaperture separation of $\vec{\rho} = (4.00D, 0.00^\circ)$, a turbulence power law of $\alpha = 3.6667$, a turbulence layer motion velocity $\vec{v}\tau = (1.00D, 90.00^\circ)$, and a ratio $L_0/D = 100.00$. The ratio of the slope measurement noise variance to the wavefront slope variance $\sigma_n^2/\Gamma_s(0)$ varies from 0% to 50%.

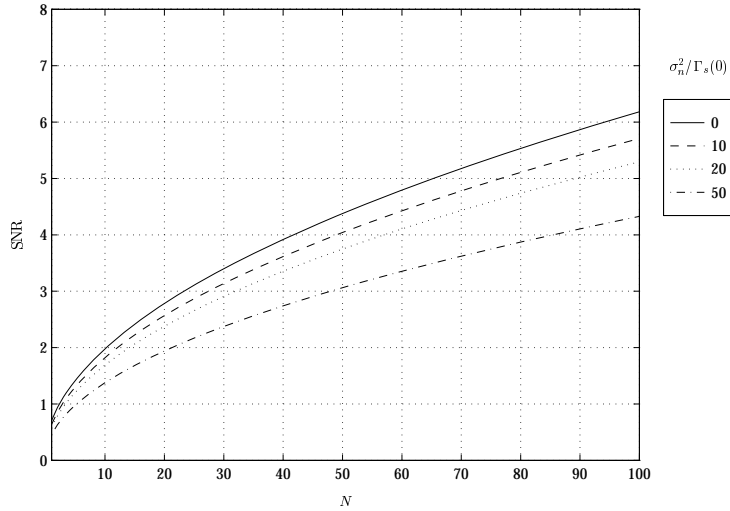


Figure D.70 Group C: Slope structure function estimator SNR vs. number of integration frames, N , for the DIMM geometry with a subaperture separation of $\vec{\rho} = (4.00D, 0.00^\circ)$, a turbulence power law of $\alpha = 3.6667$, a turbulence layer motion velocity $\vec{v}\tau = (2.50D, 90.00^\circ)$, and a ratio $L_0/D = 100.00$. The ratio of the slope measurement noise variance to the wavefront slope variance $\sigma_n^2/\Gamma_s(0)$ varies from 0% to 50%.

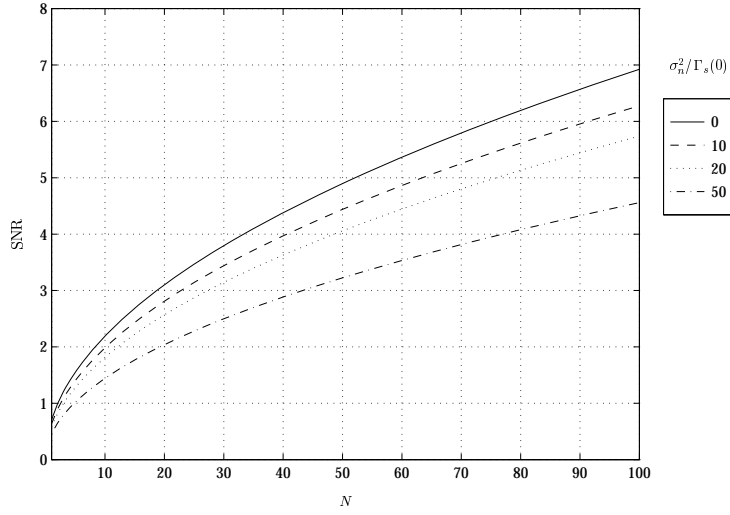


Figure D.71 Group C: Slope structure function estimator SNR vs. number of integration frames, N , for the DIMM geometry with a subaperture separation of $\vec{\rho} = (4.00D, 0.00^\circ)$, a turbulence power law of $\alpha = 3.6667$, a turbulence layer motion velocity $\vec{v}\tau = (5.00D, 90.00^\circ)$, and a ratio $L_0/D = 100.00$. The ratio of the slope measurement noise variance to the wavefront slope variance $\sigma_n^2/\Gamma_s(0)$ varies from 0% to 50%.

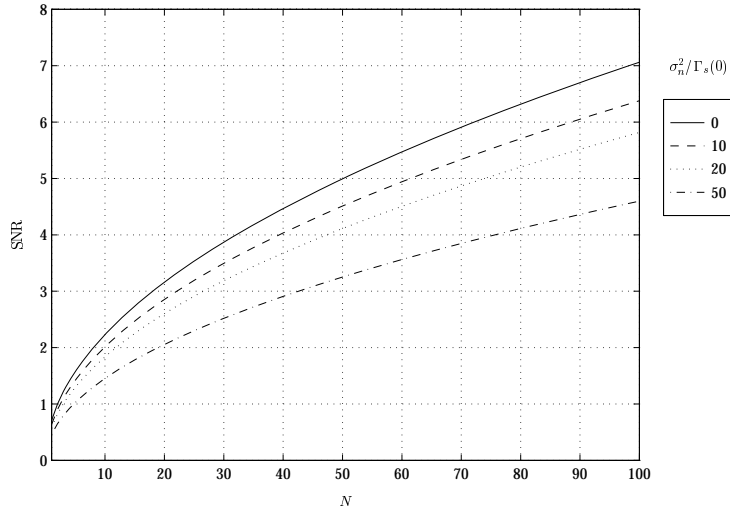


Figure D.72 Group C: Slope structure function estimator SNR vs. number of integration frames, N , for the DIMM geometry with a subaperture separation of $\vec{\rho} = (4.00D, 0.00^\circ)$, a turbulence power law of $\alpha = 3.6667$, a turbulence layer motion velocity $\vec{v}\tau = (10.00D, 90.00^\circ)$, and a ratio $L_0/D = 100.00$. The ratio of the slope measurement noise variance to the wavefront slope variance $\sigma_n^2/\Gamma_s(0)$ varies from 0% to 50%.

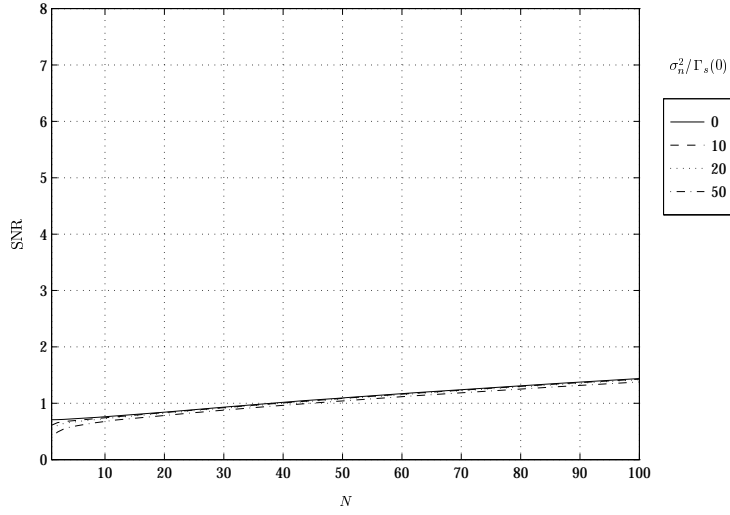


Figure D.73 Group C: Slope structure function estimator SNR vs. number of integration frames, N , for the DIMM geometry with a subaperture separation of $\vec{\rho} = (4.00D, 0.00^\circ)$, a turbulence power law of $\alpha = 3.6667$, a turbulence layer motion velocity $\vec{v}\tau = (0.10D, 90.00^\circ)$, and a ratio $L_0/D = \infty$. The ratio of the slope measurement noise variance to the wavefront slope variance $\sigma_n^2/\Gamma_s(0)$ varies from 0% to 50%.

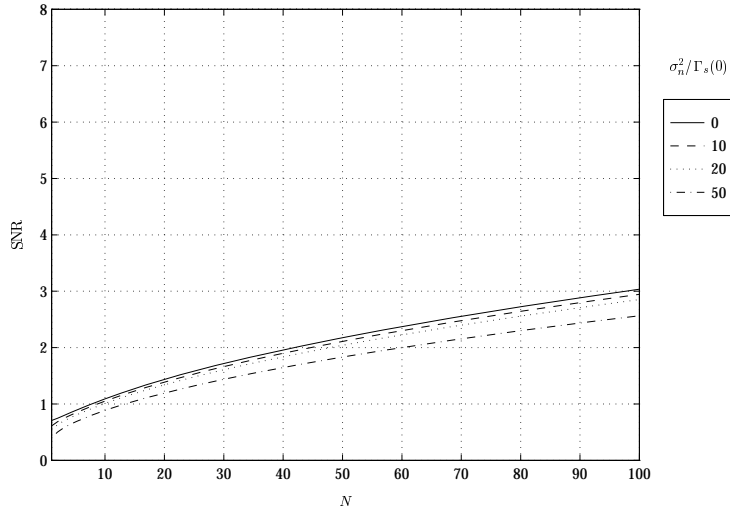


Figure D.74 Group C: Slope structure function estimator SNR vs. number of integration frames, N , for the DIMM geometry with a subaperture separation of $\vec{\rho} = (4.00D, 0.00^\circ)$, a turbulence power law of $\alpha = 3.6667$, a turbulence layer motion velocity $\vec{v}\tau = (0.50D, 90.00^\circ)$, and a ratio $L_0/D = \infty$. The ratio of the slope measurement noise variance to the wavefront slope variance $\sigma_n^2/\Gamma_s(0)$ varies from 0% to 50%.

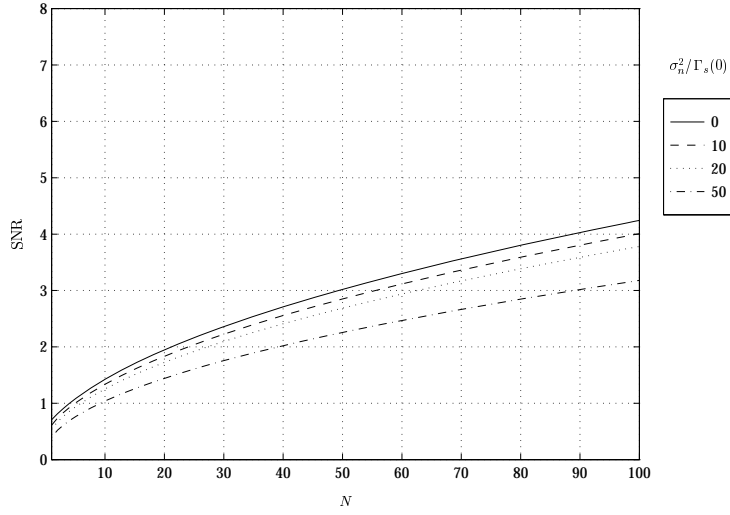


Figure D.75 Group C: Slope structure function estimator SNR vs. number of integration frames, N , for the DIMM geometry with a subaperture separation of $\vec{\rho} = (4.00D, 0.00^\circ)$, a turbulence power law of $\alpha = 3.6667$, a turbulence layer motion velocity $\vec{v}\tau = (1.00D, 90.00^\circ)$, and a ratio $L_0/D = \infty$. The ratio of the slope measurement noise variance to the wavefront slope variance $\sigma_n^2/\Gamma_s(0)$ varies from 0% to 50%.

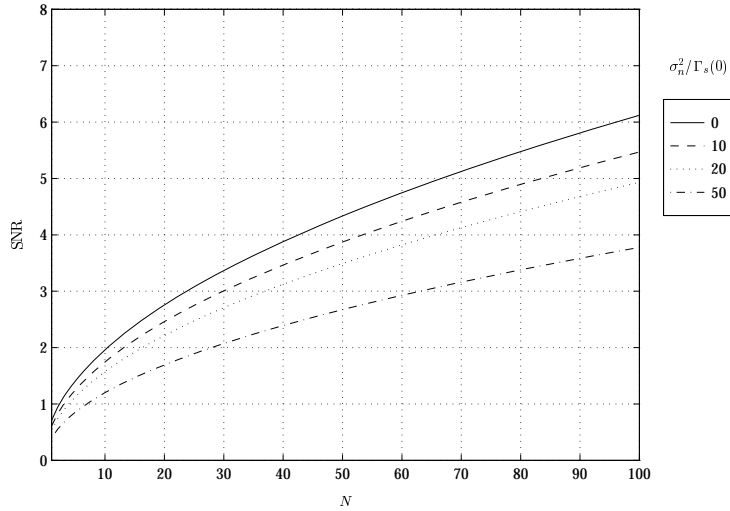


Figure D.76 Group C: Slope structure function estimator SNR vs. number of integration frames, N , for the DIMM geometry with a subaperture separation of $\vec{\rho} = (4.00D, 0.00^\circ)$, a turbulence power law of $\alpha = 3.6667$, a turbulence layer motion velocity $\vec{v}\tau = (2.50D, 90.00^\circ)$, and a ratio $L_0/D = \infty$. The ratio of the slope measurement noise variance to the wavefront slope variance $\sigma_n^2/\Gamma_s(0)$ varies from 0% to 50%.

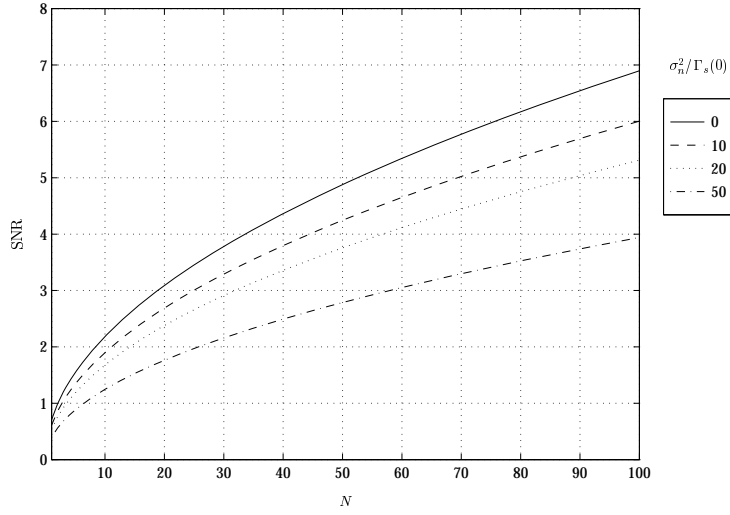


Figure D.77 Group C: Slope structure function estimator SNR vs. number of integration frames, N , for the DIMM geometry with a subaperture separation of $\vec{\rho} = (4.00D, 0.00^\circ)$, a turbulence power law of $\alpha = 3.6667$, a turbulence layer motion velocity $\vec{v}\tau = (5.00D, 90.00^\circ)$, and a ratio $L_0/D = \infty$. The ratio of the slope measurement noise variance to the wavefront slope variance $\sigma_n^2/\Gamma_s(0)$ varies from 0% to 50%.

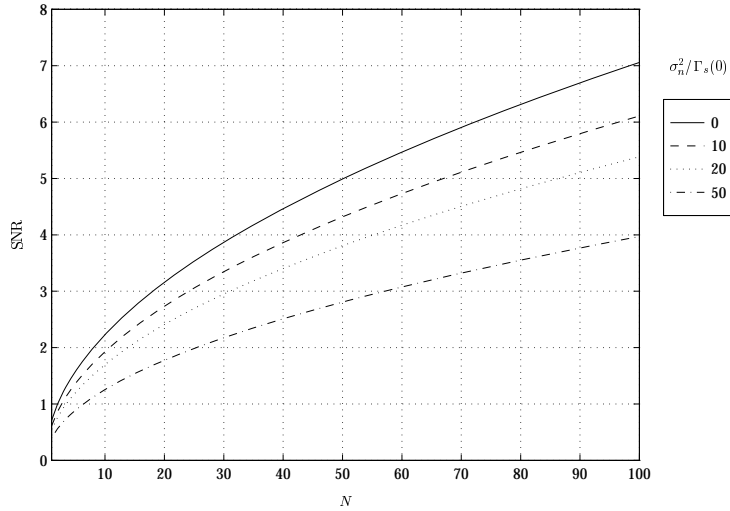


Figure D.78 Group C: Slope structure function estimator SNR vs. number of integration frames, N , for the DIMM geometry with a subaperture separation of $\vec{\rho} = (4.00D, 0.00^\circ)$, a turbulence power law of $\alpha = 3.6667$, a turbulence layer motion velocity $\vec{v}\tau = (10.00D, 90.00^\circ)$, and a ratio $L_0/D = \infty$. The ratio of the slope measurement noise variance to the wavefront slope variance $\sigma_n^2/\Gamma_s(0)$ varies from 0% to 50%.

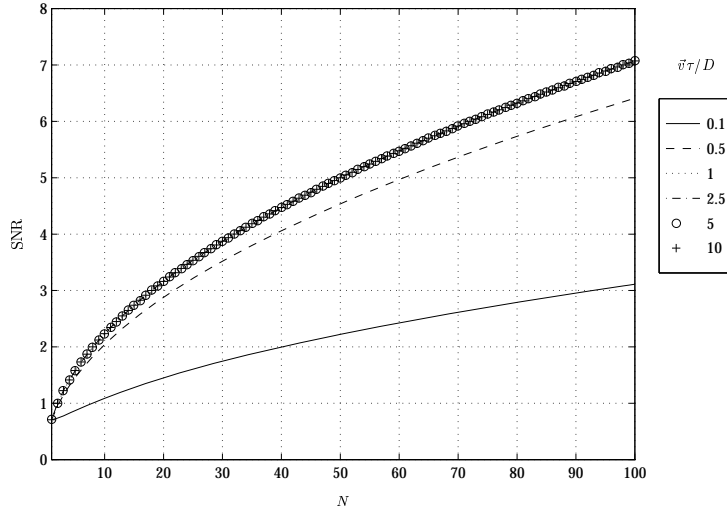


Figure D.79 Group D: Slope structure function estimator SNR vs. number of integration frames, N , for the DIMM geometry with a subaperture separation of $\vec{\rho} = (4.00D, 0.00^\circ)$, a turbulence power law of $\alpha = 3.6667$, a turbulence layer motion velocity angle $\arg(\vec{v}) = 90.00^\circ$, a ratio $L_0/D = 1.00$, and a ratio of the slope measurement noise variance to the wavefront slope variance $\sigma_n^2/\Gamma_s(0) = 0\%$. The magnitude of the turbulence layer motion velocity varies from $0.1D$ to $10D$.

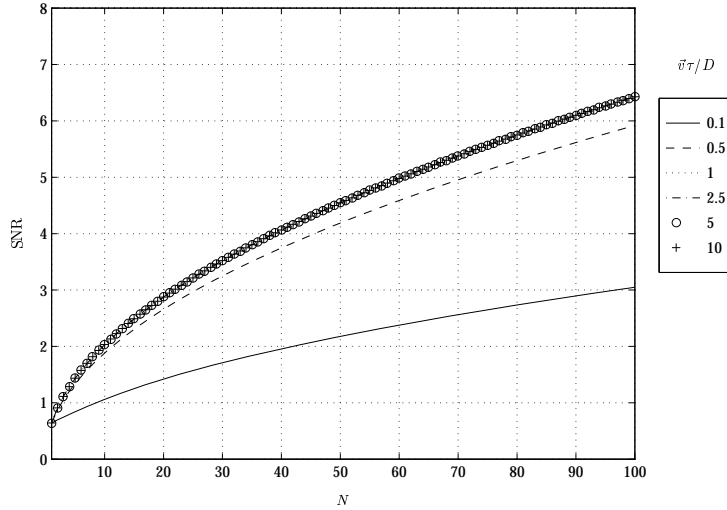


Figure D.80 Group D: Slope structure function estimator SNR vs. number of integration frames, N , for the DIMM geometry with a subaperture separation of $\vec{\rho} = (4.00D, 0.00^\circ)$, a turbulence power law of $\alpha = 3.6667$, a turbulence layer motion velocity angle $\arg(\vec{v}) = 90.00^\circ$, a ratio $L_0/D = 1.00$, and a ratio of the slope measurement noise variance to the wavefront slope variance $\sigma_n^2/\Gamma_s(0) = 10\%$. The magnitude of the turbulence layer motion velocity varies from $0.1D$ to $10D$.

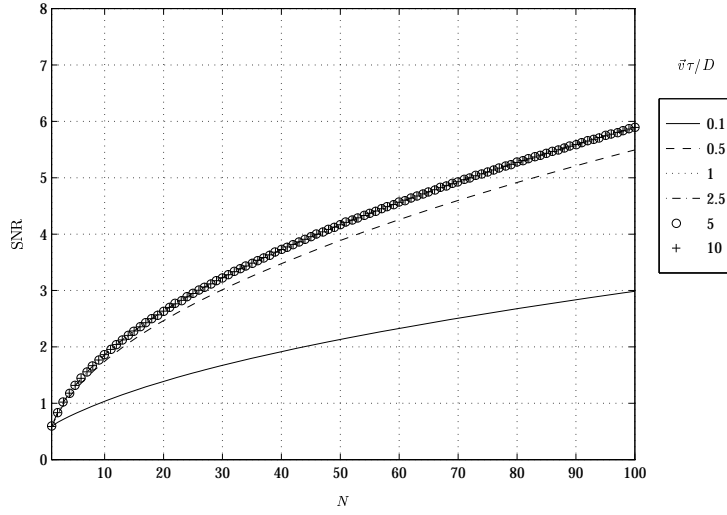


Figure D.81 Group D: Slope structure function estimator SNR vs. number of integration frames, N , for the DIMM geometry with a subaperture separation of $\vec{\rho} = (4.00D, 0.00^\circ)$, a turbulence power law of $\alpha = 3.6667$, a turbulence layer motion velocity angle $\arg(\vec{v}) = 90.00^\circ$, a ratio $L_0/D = 1.00$, and a ratio of the slope measurement noise variance to the wavefront slope variance $\sigma_n^2/\Gamma_s(0) = 20\%$. The magnitude of the turbulence layer motion velocity varies from $0.1D$ to $10D$.

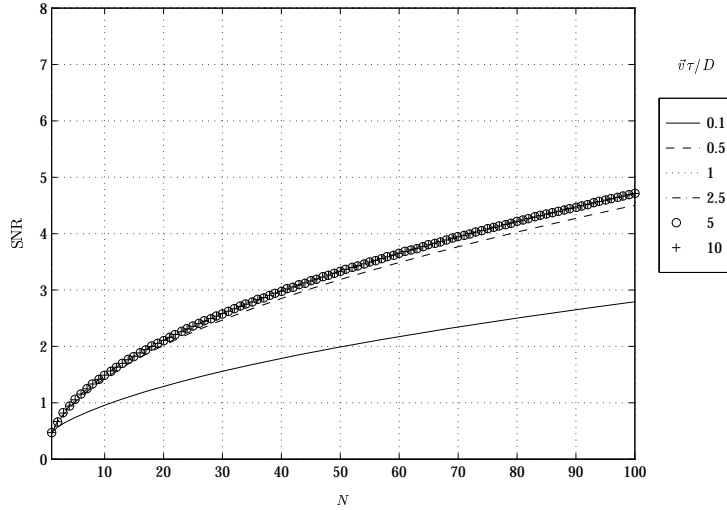


Figure D.82 Group D: Slope structure function estimator SNR vs. number of integration frames, N , for the DIMM geometry with a subaperture separation of $\vec{\rho} = (4.00D, 0.00^\circ)$, a turbulence power law of $\alpha = 3.6667$, a turbulence layer motion velocity angle $\arg(\vec{v}) = 90.00^\circ$, a ratio $L_0/D = 1.00$, and a ratio of the slope measurement noise variance to the wavefront slope variance $\sigma_n^2/\Gamma_s(0) = 50\%$. The magnitude of the turbulence layer motion velocity varies from $0.1D$ to $10D$.

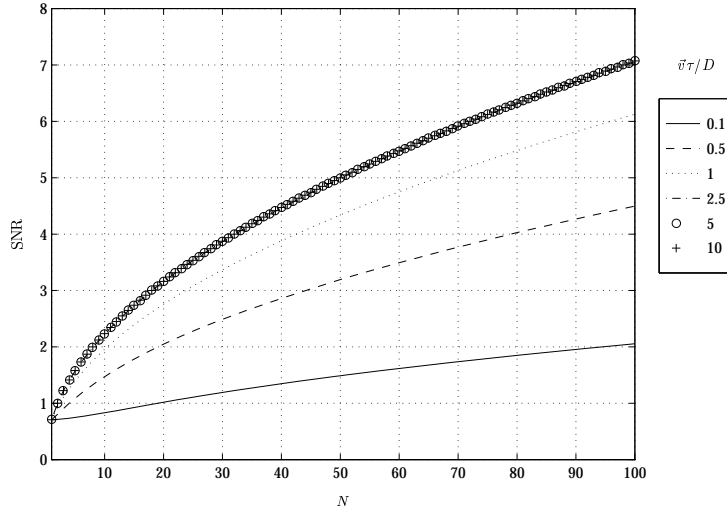


Figure D.83 Group D: Slope structure function estimator SNR vs. number of integration frames, N , for the DIMM geometry with a subaperture separation of $\vec{\rho} = (4.00D, 0.00^\circ)$, a turbulence power law of $\alpha = 3.6667$, a turbulence layer motion velocity angle $\arg(\vec{v}) = 90.00^\circ$, a ratio $L_0/D = 5.00$, and a ratio of the slope measurement noise variance to the wavefront slope variance $\sigma_n^2/\Gamma_s(0) = 0\%$. The magnitude of the turbulence layer motion velocity varies from $0.1D$ to $10D$.

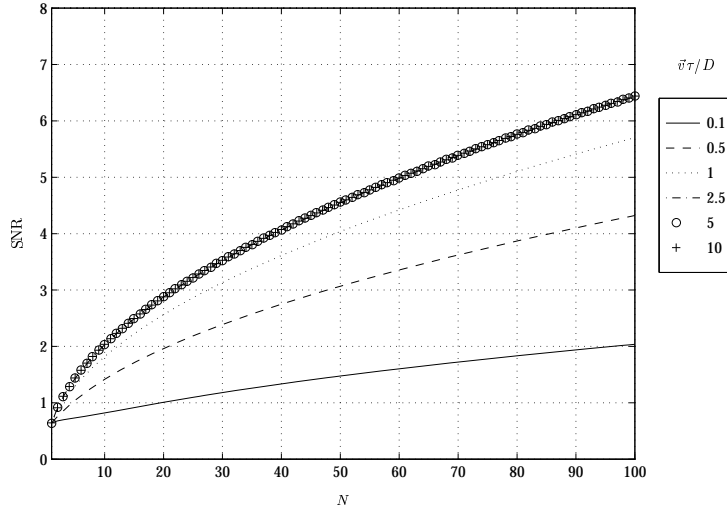


Figure D.84 Group D: Slope structure function estimator SNR vs. number of integration frames, N , for the DIMM geometry with a subaperture separation of $\vec{\rho} = (4.00D, 0.00^\circ)$, a turbulence power law of $\alpha = 3.6667$, a turbulence layer motion velocity angle $\arg(\vec{v}) = 90.00^\circ$, a ratio $L_0/D = 5.00$, and a ratio of the slope measurement noise variance to the wavefront slope variance $\sigma_n^2/\Gamma_s(0) = 10\%$. The magnitude of the turbulence layer motion velocity varies from $0.1D$ to $10D$.

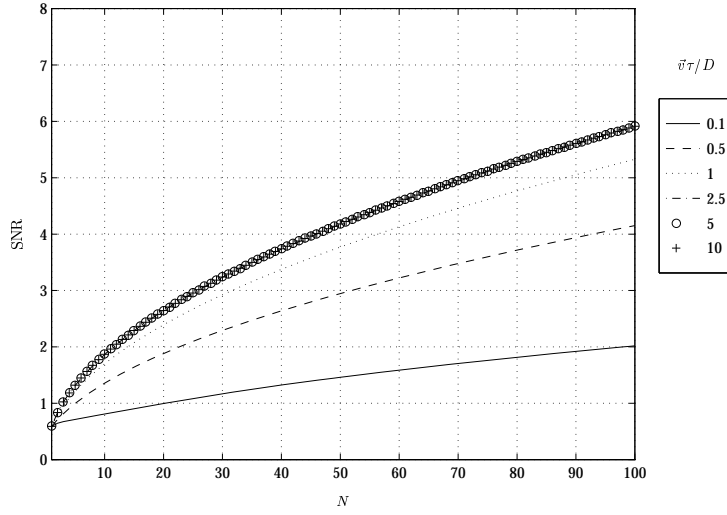


Figure D.85 Group D: Slope structure function estimator SNR vs. number of integration frames, N , for the DIMM geometry with a subaperture separation of $\vec{\rho} = (4.00D, 0.00^\circ)$, a turbulence power law of $\alpha = 3.6667$, a turbulence layer motion velocity angle $\arg(\vec{v}) = 90.00^\circ$, a ratio $L_0/D = 5.00$, and a ratio of the slope measurement noise variance to the wavefront slope variance $\sigma_n^2/\Gamma_s(0) = 20\%$. The magnitude of the turbulence layer motion velocity varies from $0.1D$ to $10D$.

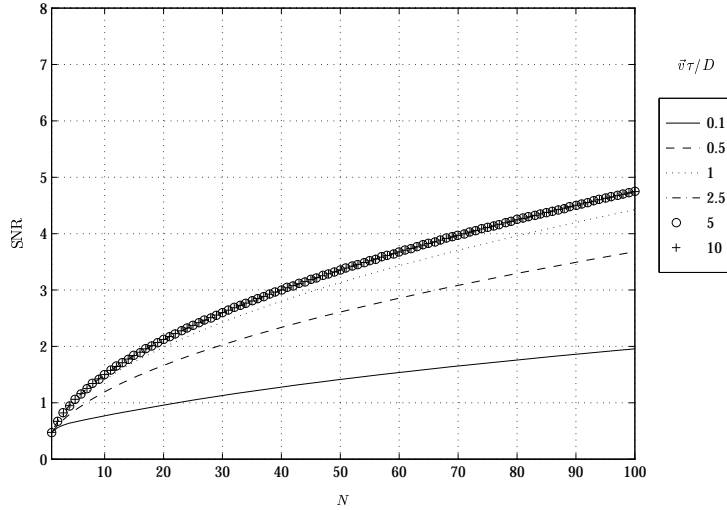


Figure D.86 Group D: Slope structure function estimator SNR vs. number of integration frames, N , for the DIMM geometry with a subaperture separation of $\vec{\rho} = (4.00D, 0.00^\circ)$, a turbulence power law of $\alpha = 3.6667$, a turbulence layer motion velocity angle $\arg(\vec{v}) = 90.00^\circ$, a ratio $L_0/D = 5.00$, and a ratio of the slope measurement noise variance to the wavefront slope variance $\sigma_n^2/\Gamma_s(0) = 50\%$. The magnitude of the turbulence layer motion velocity varies from $0.1D$ to $10D$.

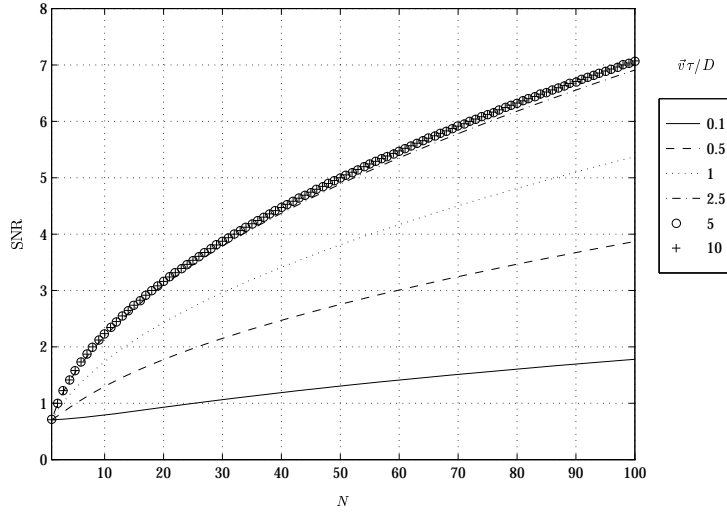


Figure D.87 Group D: Slope structure function estimator SNR vs. number of integration frames, N , for the DIMM geometry with a subaperture separation of $\vec{\rho} = (4.00D, 0.00^\circ)$, a turbulence power law of $\alpha = 3.6667$, a turbulence layer motion velocity angle $\arg(\vec{v}) = 90.00^\circ$, a ratio $L_0/D = 10.00$, and a ratio of the slope measurement noise variance to the wavefront slope variance $\sigma_n^2/\Gamma_s(0) = 0\%$. The magnitude of the turbulence layer motion velocity varies from $0.1D$ to $10D$.

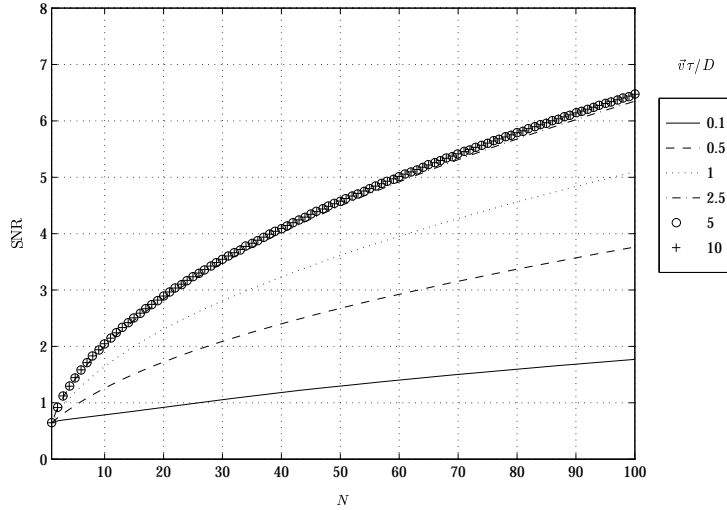


Figure D.88 Group D: Slope structure function estimator SNR vs. number of integration frames, N , for the DIMM geometry with a subaperture separation of $\vec{\rho} = (4.00D, 0.00^\circ)$, a turbulence power law of $\alpha = 3.6667$, a turbulence layer motion velocity angle $\arg(\vec{v}) = 90.00^\circ$, a ratio $L_0/D = 10.00$, and a ratio of the slope measurement noise variance to the wavefront slope variance $\sigma_n^2/\Gamma_s(0) = 10\%$. The magnitude of the turbulence layer motion velocity varies from $0.1D$ to $10D$.

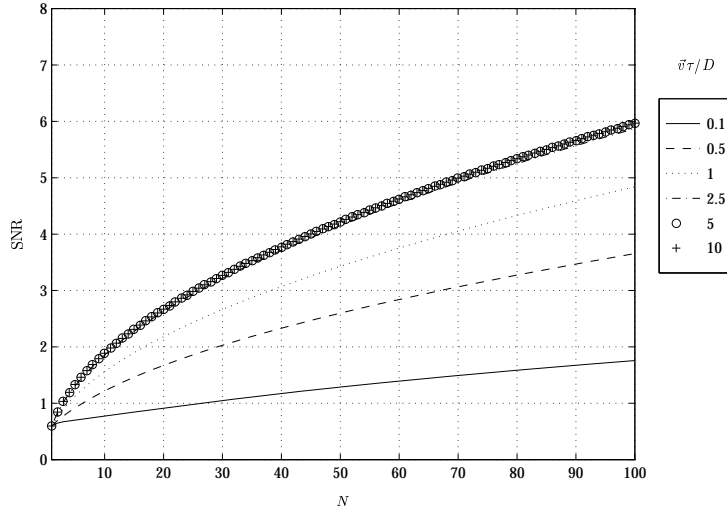


Figure D.89 Group D: Slope structure function estimator SNR vs. number of integration frames, N , for the DIMM geometry with a subaperture separation of $\vec{\rho} = (4.00D, 0.00^\circ)$, a turbulence power law of $\alpha = 3.6667$, a turbulence layer motion velocity angle $\arg(\vec{v}) = 90.00^\circ$, a ratio $L_0/D = 10.00$, and a ratio of the slope measurement noise variance to the wavefront slope variance $\sigma_n^2/\Gamma_s(0) = 20\%$. The magnitude of the turbulence layer motion velocity varies from $0.1D$ to $10D$.

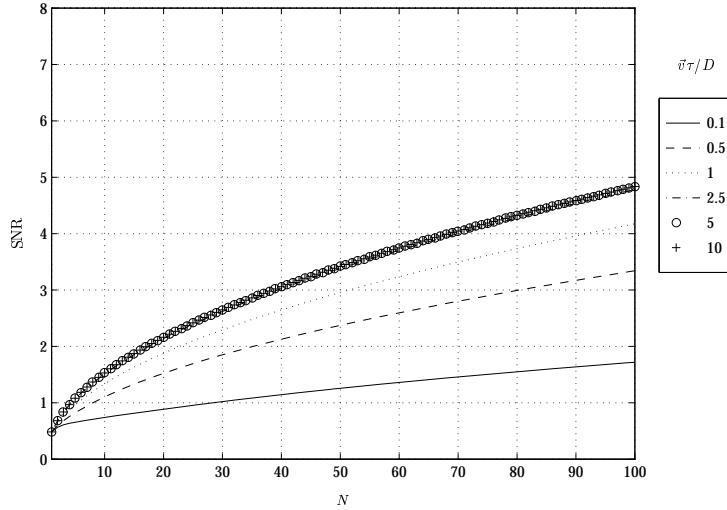


Figure D.90 Group D: Slope structure function estimator SNR vs. number of integration frames, N , for the DIMM geometry with a subaperture separation of $\vec{\rho} = (4.00D, 0.00^\circ)$, a turbulence power law of $\alpha = 3.6667$, a turbulence layer motion velocity angle $\arg(\vec{v}) = 90.00^\circ$, a ratio $L_0/D = 10.00$, and a ratio of the slope measurement noise variance to the wavefront slope variance $\sigma_n^2/\Gamma_s(0) = 50\%$. The magnitude of the turbulence layer motion velocity varies from $0.1D$ to $10D$.

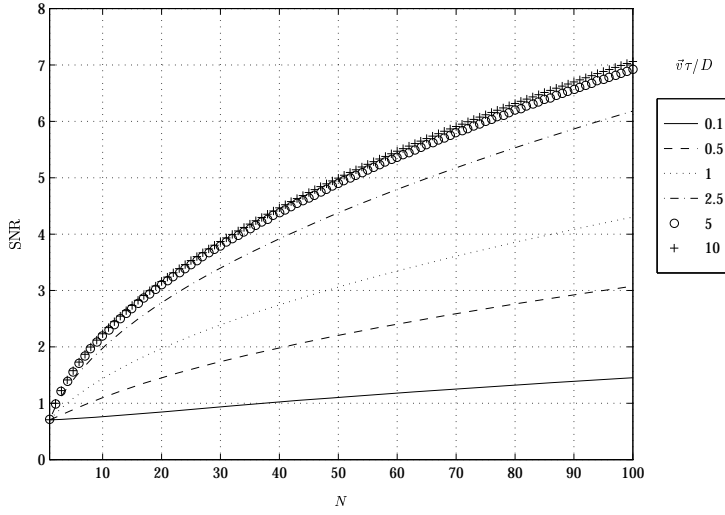


Figure D.91 Group D: Slope structure function estimator SNR vs. number of integration frames, N , for the DIMM geometry with a subaperture separation of $\vec{\rho} = (4.00D, 0.00^\circ)$, a turbulence power law of $\alpha = 3.6667$, a turbulence layer motion velocity angle $\arg(\vec{v}) = 90.00^\circ$, a ratio $L_0/D = 100.00$, and a ratio of the slope measurement noise variance to the wavefront slope variance $\sigma_n^2/\Gamma_s(0) = 0\%$. The magnitude of the turbulence layer motion velocity varies from $0.1D$ to $10D$.

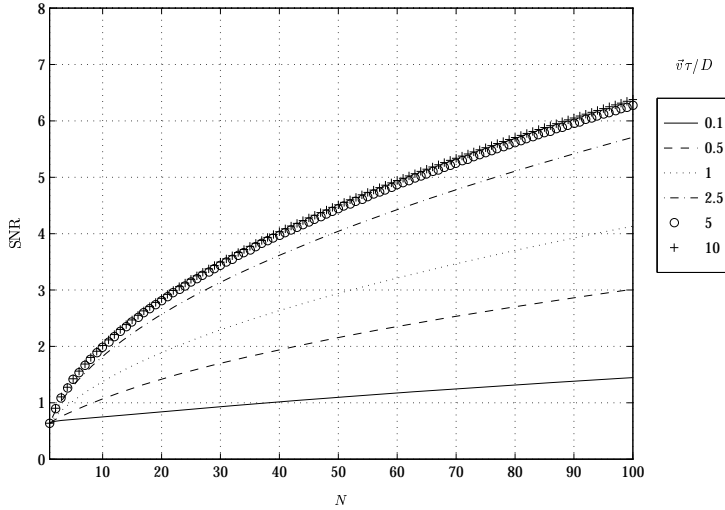


Figure D.92 Group D: Slope structure function estimator SNR vs. number of integration frames, N , for the DIMM geometry with a subaperture separation of $\vec{\rho} = (4.00D, 0.00^\circ)$, a turbulence power law of $\alpha = 3.6667$, a turbulence layer motion velocity angle $\arg(\vec{v}) = 90.00^\circ$, a ratio $L_0/D = 100.00$, and a ratio of the slope measurement noise variance to the wavefront slope variance $\sigma_n^2/\Gamma_s(0) = 10\%$. The magnitude of the turbulence layer motion velocity varies from $0.1D$ to $10D$.

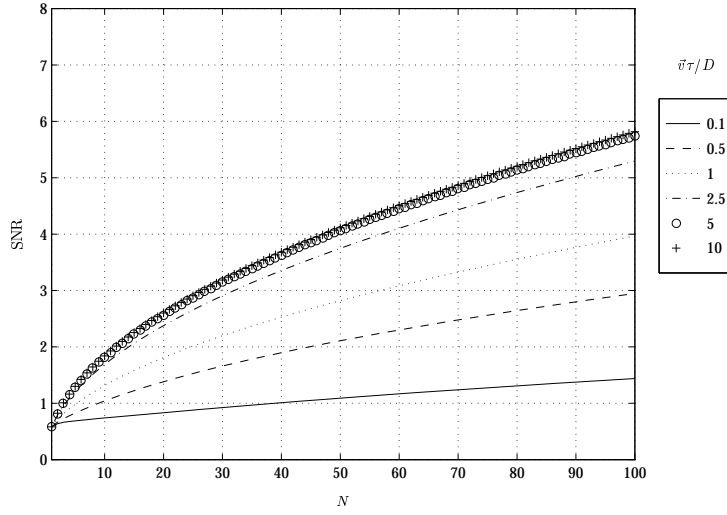


Figure D.93 Group D: Slope structure function estimator SNR vs. number of integration frames, N , for the DIMM geometry with a subaperture separation of $\vec{\rho} = (4.00D, 0.00^\circ)$, a turbulence power law of $\alpha = 3.6667$, a turbulence layer motion velocity angle $\arg(\vec{v}) = 90.00^\circ$, a ratio $L_0/D = 100.00$, and a ratio of the slope measurement noise variance to the wavefront slope variance $\sigma_n^2/\Gamma_s(0) = 20\%$. The magnitude of the turbulence layer motion velocity varies from $0.1D$ to $10D$.

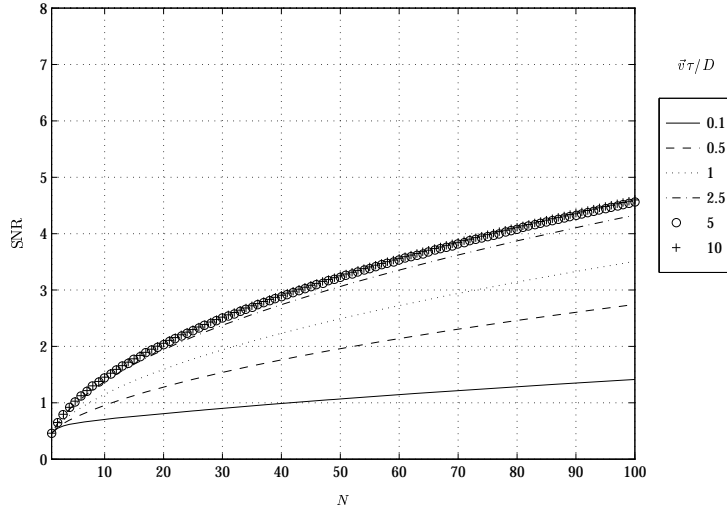


Figure D.94 Group D: Slope structure function estimator SNR vs. number of integration frames, N , for the DIMM geometry with a subaperture separation of $\vec{\rho} = (4.00D, 0.00^\circ)$, a turbulence power law of $\alpha = 3.6667$, a turbulence layer motion velocity angle $\arg(\vec{v}) = 90.00^\circ$, a ratio $L_0/D = 100.00$, and a ratio of the slope measurement noise variance to the wavefront slope variance $\sigma_n^2/\Gamma_s(0) = 50\%$. The magnitude of the turbulence layer motion velocity varies from $0.1D$ to $10D$.

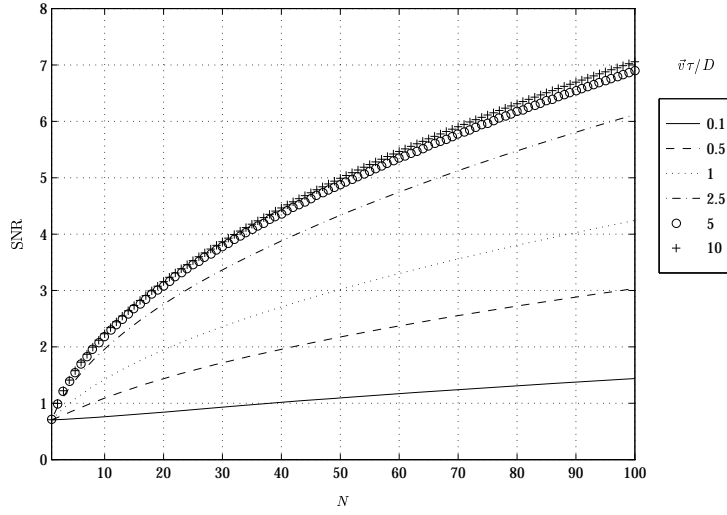


Figure D.95 Group D: Slope structure function estimator SNR vs. number of integration frames, N , for the DIMM geometry with a subaperture separation of $\vec{\rho} = (4.00D, 0.00^\circ)$, a turbulence power law of $\alpha = 3.6667$, a turbulence layer motion velocity angle $\arg(\vec{v}) = 90.00^\circ$, a ratio $L_0/D = \infty$, and a ratio of the slope measurement noise variance to the wavefront slope variance $\sigma_n^2/\Gamma_s(0) = 0\%$. The magnitude of the turbulence layer motion velocity varies from $0.1D$ to $10D$.

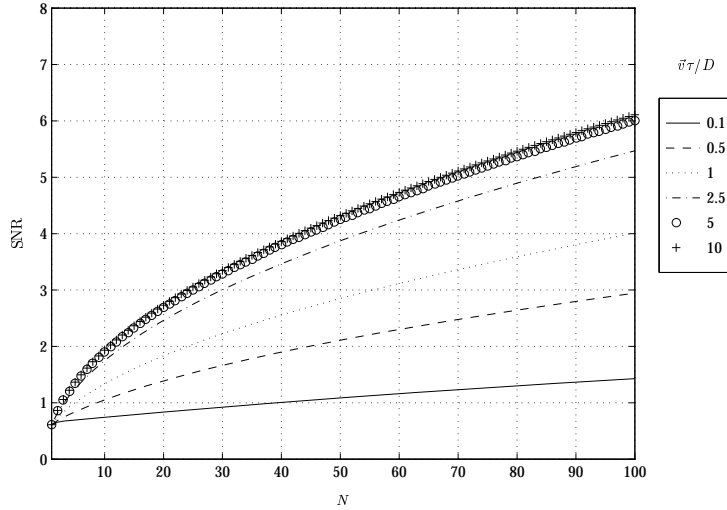


Figure D.96 Group D: Slope structure function estimator SNR vs. number of integration frames, N , for the DIMM geometry with a subaperture separation of $\vec{\rho} = (4.00D, 0.00^\circ)$, a turbulence power law of $\alpha = 3.6667$, a turbulence layer motion velocity angle $\arg(\vec{v}) = 90.00^\circ$, a ratio $L_0/D = \infty$, and a ratio of the slope measurement noise variance to the wavefront slope variance $\sigma_n^2/\Gamma_s(0) = 10\%$. The magnitude of the turbulence layer motion velocity varies from $0.1D$ to $10D$.

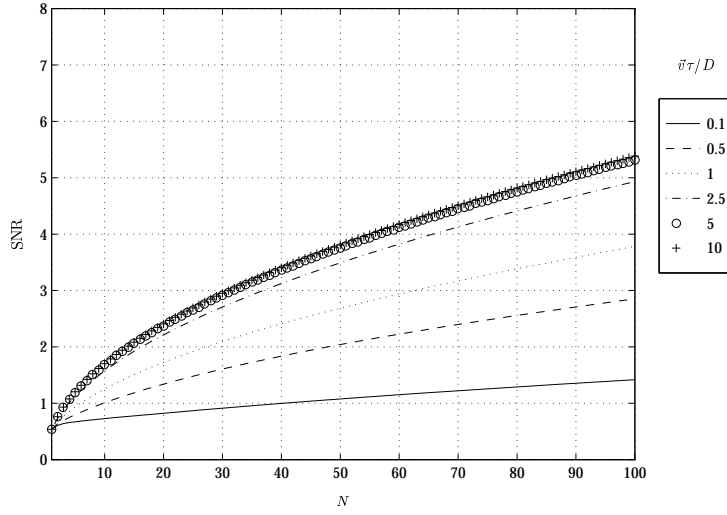


Figure D.97 Group D: Slope structure function estimator SNR vs. number of integration frames, N , for the DIMM geometry with a subaperture separation of $\vec{\rho} = (4.00D, 0.00^\circ)$, a turbulence power law of $\alpha = 3.6667$, a turbulence layer motion velocity angle $\arg(\vec{v}) = 90.00^\circ$, a ratio $L_0/D = \infty$, and a ratio of the slope measurement noise variance to the wavefront slope variance $\sigma_n^2/\Gamma_s(0) = 20\%$. The magnitude of the turbulence layer motion velocity varies from $0.1D$ to $10D$.

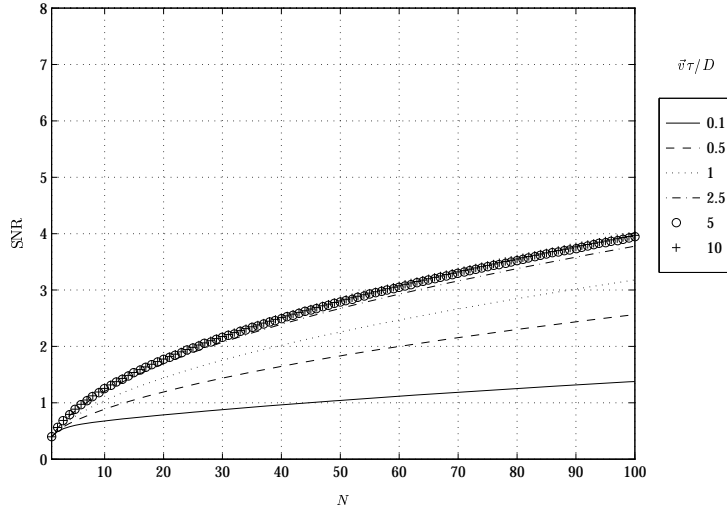


Figure D.98 Group D: Slope structure function estimator SNR vs. number of integration frames, N , for the DIMM geometry with a subaperture separation of $\vec{\rho} = (4.00D, 0.00^\circ)$, a turbulence power law of $\alpha = 3.6667$, a turbulence layer motion velocity angle $\arg(\vec{v}) = 90.00^\circ$, a ratio $L_0/D = \infty$, and a ratio of the slope measurement noise variance to the wavefront slope variance $\sigma_n^2/\Gamma_s(0) = 50\%$. The magnitude of the turbulence layer motion velocity varies from $0.1D$ to $10D$.

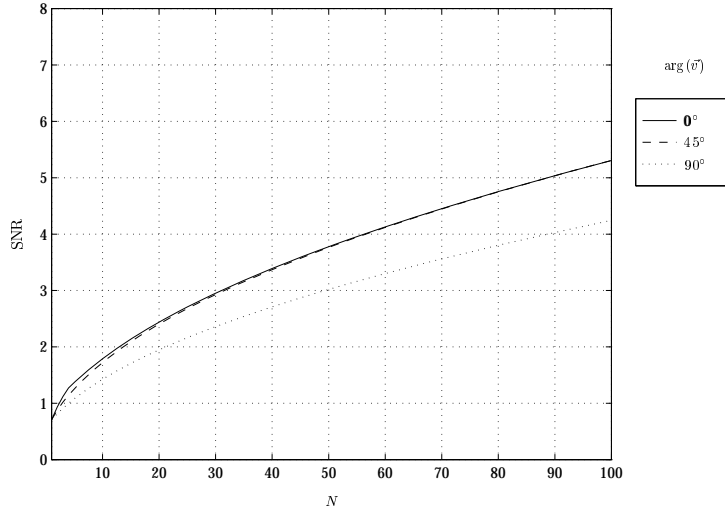


Figure D.99 Group E: Slope structure function estimator SNR vs. number of integration frames, N , for the DIMM geometry with a subaperture separation of $\vec{\rho} = (4.00D, 0.00^\circ)$, a turbulence power law of $\alpha = 3.6667$, a turbulence layer motion velocity magnitude $|\vec{v}| = 1.00D$, a ratio $L_0/D = \infty$, and a ratio of the slope measurement noise variance to the wavefront slope variance $\sigma_n^2/\Gamma_s(0) = 0\%$. The angle of the turbulence layer motion velocity, $\arg(\vec{v})$, is 0, 45, or 90 degrees.

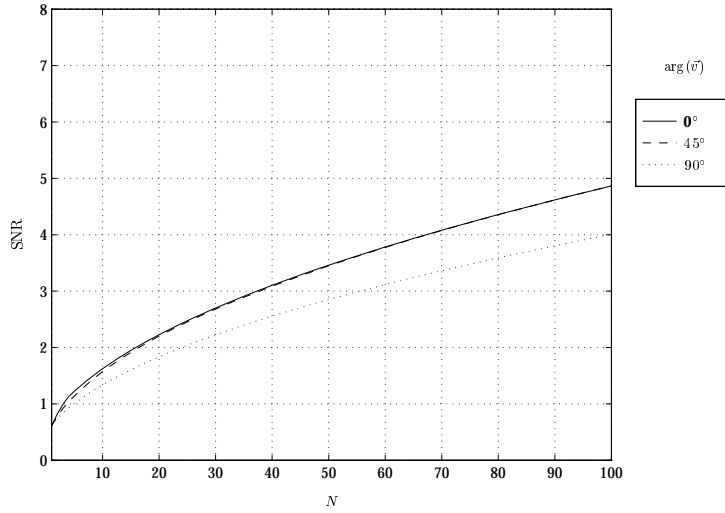


Figure D.100 Group E: Slope structure function estimator SNR vs. number of integration frames, N , for the DIMM geometry with a subaperture separation of $\vec{\rho} = (4.00D, 0.00^\circ)$, a turbulence power law of $\alpha = 3.6667$, a turbulence layer motion velocity magnitude $|\vec{v}| = 1.00D$, a ratio $L_0/D = \infty$, and a ratio of the slope measurement noise variance to the wavefront slope variance $\sigma_n^2/\Gamma_s(0) = 10\%$. The angle of the turbulence layer motion velocity, $\arg(\vec{v})$, is 0, 45, or 90 degrees.

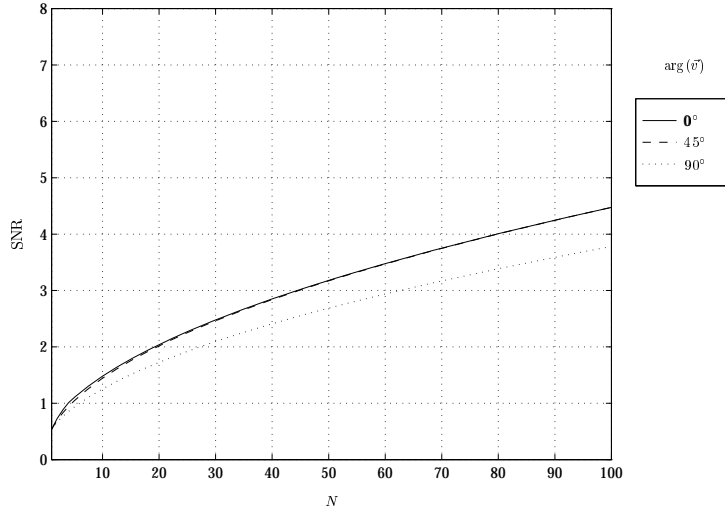


Figure D.101 Group E: Slope structure function estimator SNR vs. number of integration frames, N , for the DIMM geometry with a subaperture separation of $\vec{\rho} = (4.00D, 0.00^\circ)$, a turbulence power law of $\alpha = 3.6667$, a turbulence layer motion velocity magnitude $|\vec{v}| = 1.00D$, a ratio $L_0/D = \infty$, and a ratio of the slope measurement noise variance to the wavefront slope variance $\sigma_n^2/\Gamma_s(0) = 20\%$. The angle of the turbulence layer motion velocity, $\arg(\vec{v})$, is 0, 45, or 90 degrees.

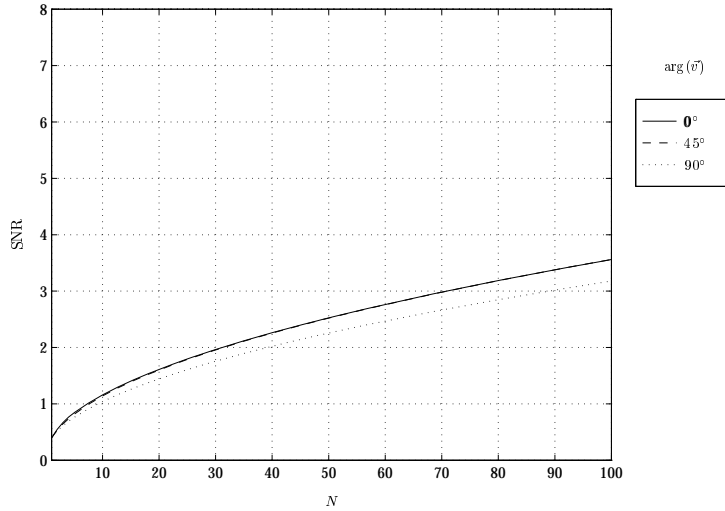


Figure D.102 Group E: Slope structure function estimator SNR vs. number of integration frames, N , for the DIMM geometry with a subaperture separation of $\vec{\rho} = (4.00D, 0.00^\circ)$, a turbulence power law of $\alpha = 3.6667$, a turbulence layer motion velocity magnitude $|\vec{v}| = 1.00D$, a ratio $L_0/D = \infty$, and a ratio of the slope measurement noise variance to the wavefront slope variance $\sigma_n^2/\Gamma_s(0) = 50\%$. The angle of the turbulence layer motion velocity, $\arg(\vec{v})$, is 0, 45, or 90 degrees.

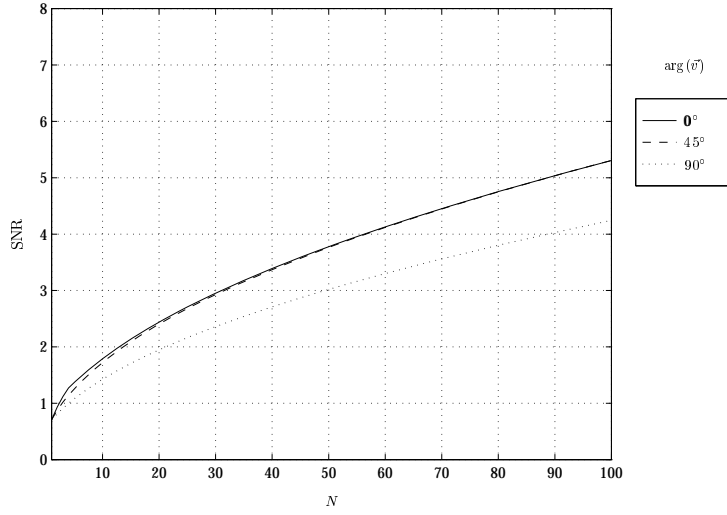


Figure D.103 Group E: Slope structure function estimator SNR vs. number of integration frames, N , for the DIMM geometry with a subaperture separation of $\vec{\rho} = (4.00D, 0.00^\circ)$, a turbulence power law of $\alpha = 3.6667$, a turbulence layer motion velocity magnitude $|\vec{v}| = 1.00D$, a ratio $L_0/D = \infty$, and a ratio of the slope measurement noise variance to the wavefront slope variance $\sigma_n^2/\Gamma_s(0) = 0\%$. The angle of the turbulence layer motion velocity, $\arg(\vec{v})$, is 0, 45, or 90 degrees.

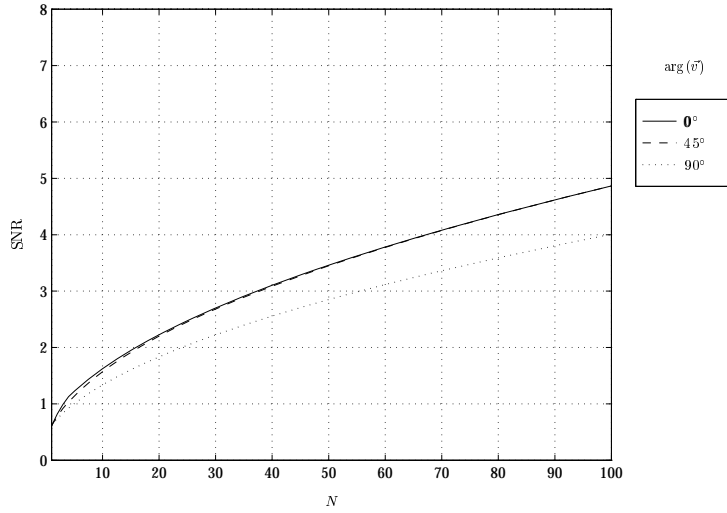


Figure D.104 Group E: Slope structure function estimator SNR vs. number of integration frames, N , for the DIMM geometry with a subaperture separation of $\vec{\rho} = (4.00D, 0.00^\circ)$, a turbulence power law of $\alpha = 3.6667$, a turbulence layer motion velocity magnitude $|\vec{v}| = 1.00D$, a ratio $L_0/D = \infty$, and a ratio of the slope measurement noise variance to the wavefront slope variance $\sigma_n^2/\Gamma_s(0) = 10\%$. The angle of the turbulence layer motion velocity, $\arg(\vec{v})$, is 0, 45, or 90 degrees.

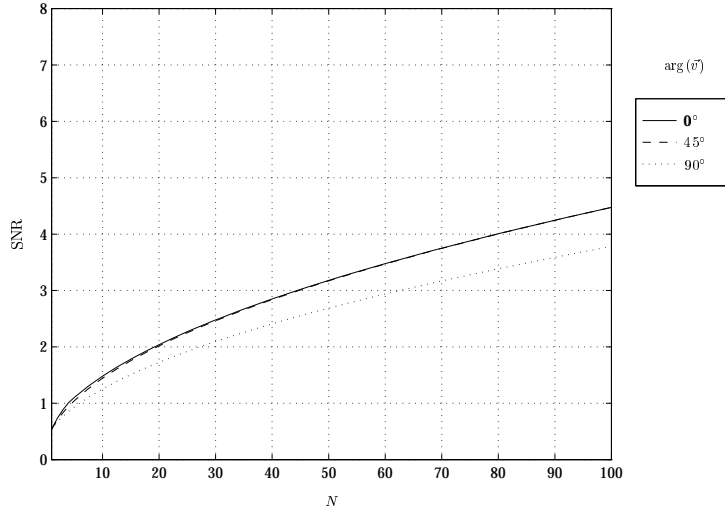


Figure D.105 Group E: Slope structure function estimator SNR vs. number of integration frames, N , for the DIMM geometry with a subaperture separation of $\vec{\rho} = (4.00D, 0.00^\circ)$, a turbulence power law of $\alpha = 3.6667$, a turbulence layer motion velocity magnitude $|\vec{v}| = 1.00D$, a ratio $L_0/D = \infty$, and a ratio of the slope measurement noise variance to the wavefront slope variance $\sigma_n^2/\Gamma_s(0) = 20\%$. The angle of the turbulence layer motion velocity, $\arg(\vec{v})$, is 0, 45, or 90 degrees.

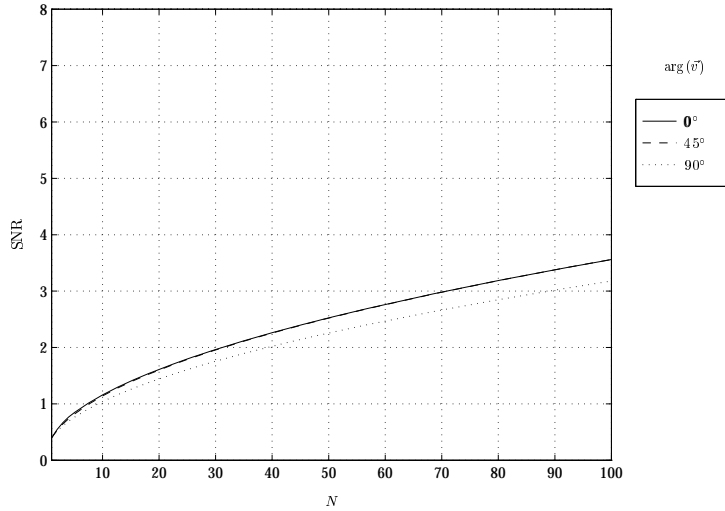


Figure D.106 Group E: Slope structure function estimator SNR vs. number of integration frames, N , for the DIMM geometry with a subaperture separation of $\vec{\rho} = (4.00D, 0.00^\circ)$, a turbulence power law of $\alpha = 3.6667$, a turbulence layer motion velocity magnitude $|\vec{v}| = 1.00D$, a ratio $L_0/D = \infty$, and a ratio of the slope measurement noise variance to the wavefront slope variance $\sigma_n^2/\Gamma_s(0) = 50\%$. The angle of the turbulence layer motion velocity, $\arg(\vec{v})$, is 0, 45, or 90 degrees.

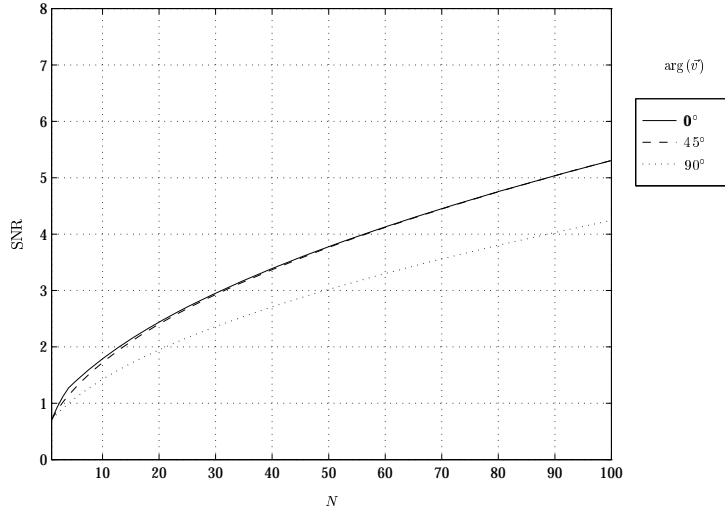


Figure D.107 Group E: Slope structure function estimator SNR vs. number of integration frames, N , for the DIMM geometry with a subaperture separation of $\vec{\rho} = (4.00D, 0.00^\circ)$, a turbulence power law of $\alpha = 3.6667$, a turbulence layer motion velocity magnitude $|\vec{v}| = 1.00D$, a ratio $L_0/D = \infty$, and a ratio of the slope measurement noise variance to the wavefront slope variance $\sigma_n^2/\Gamma_s(0) = 0\%$. The angle of the turbulence layer motion velocity, $\arg(\vec{v})$, is 0, 45, or 90 degrees.

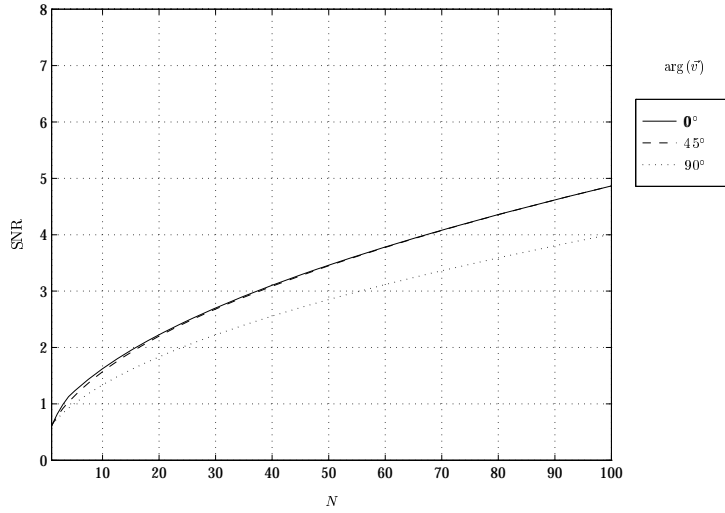


Figure D.108 Group E: Slope structure function estimator SNR vs. number of integration frames, N , for the DIMM geometry with a subaperture separation of $\vec{\rho} = (4.00D, 0.00^\circ)$, a turbulence power law of $\alpha = 3.6667$, a turbulence layer motion velocity magnitude $|\vec{v}| = 1.00D$, a ratio $L_0/D = \infty$, and a ratio of the slope measurement noise variance to the wavefront slope variance $\sigma_n^2/\Gamma_s(0) = 10\%$. The angle of the turbulence layer motion velocity, $\arg(\vec{v})$, is 0, 45, or 90 degrees.

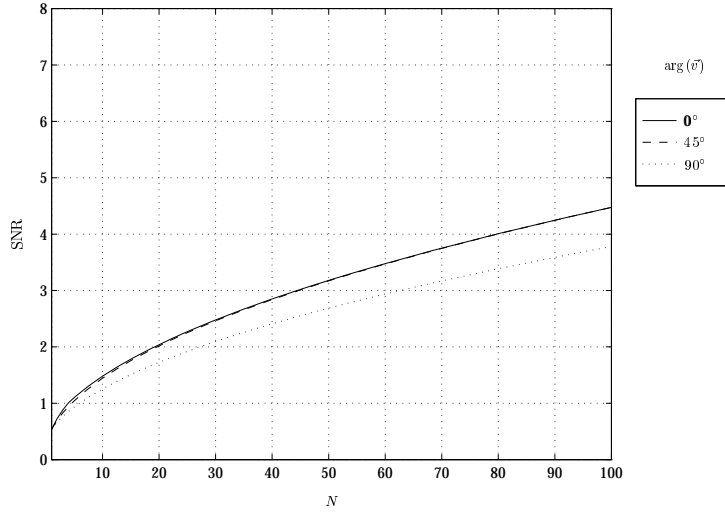


Figure D.109 Group E: Slope structure function estimator SNR vs. number of integration frames, N , for the DIMM geometry with a subaperture separation of $\vec{\rho} = (4.00D, 0.00^\circ)$, a turbulence power law of $\alpha = 3.6667$, a turbulence layer motion velocity magnitude $|\vec{v}| = 1.00D$, a ratio $L_0/D = \infty$, and a ratio of the slope measurement noise variance to the wavefront slope variance $\sigma_n^2/\Gamma_s(0) = 20\%$. The angle of the turbulence layer motion velocity, $\arg(\vec{v})$, is 0, 45, or 90 degrees.

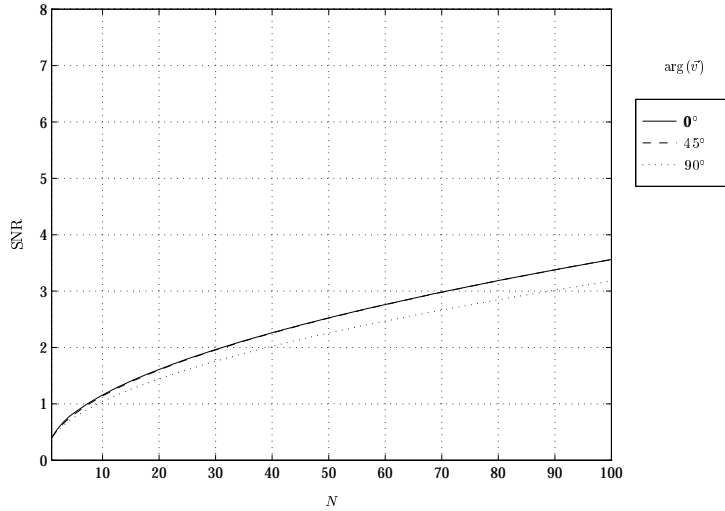


Figure D.110 Group E: Slope structure function estimator SNR vs. number of integration frames, N , for the DIMM geometry with a subaperture separation of $\vec{\rho} = (4.00D, 0.00^\circ)$, a turbulence power law of $\alpha = 3.6667$, a turbulence layer motion velocity magnitude $|\vec{v}| = 1.00D$, a ratio $L_0/D = \infty$, and a ratio of the slope measurement noise variance to the wavefront slope variance $\sigma_n^2/\Gamma_s(0) = 50\%$. The angle of the turbulence layer motion velocity, $\arg(\vec{v})$, is 0, 45, or 90 degrees.

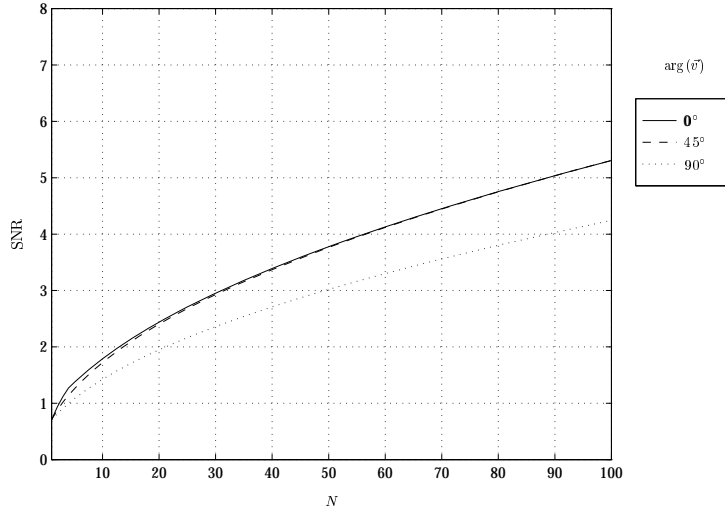


Figure D.111 Group E: Slope structure function estimator SNR vs. number of integration frames, N , for the DIMM geometry with a subaperture separation of $\vec{\rho} = (4.00D, 0.00^\circ)$, a turbulence power law of $\alpha = 3.6667$, a turbulence layer motion velocity magnitude $|\vec{v}| = 1.00D$, a ratio $L_0/D = \infty$, and a ratio of the slope measurement noise variance to the wavefront slope variance $\sigma_n^2/\Gamma_s(0) = 0\%$. The angle of the turbulence layer motion velocity, $\arg(\vec{v})$, is 0, 45, or 90 degrees.

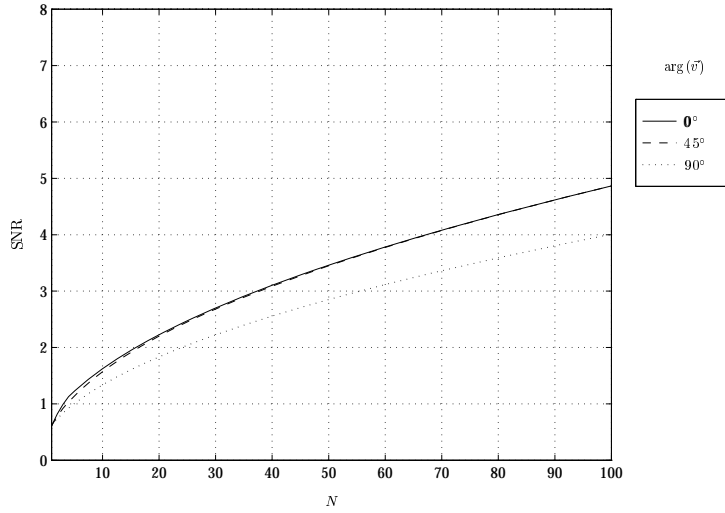


Figure D.112 Group E: Slope structure function estimator SNR vs. number of integration frames, N , for the DIMM geometry with a subaperture separation of $\vec{\rho} = (4.00D, 0.00^\circ)$, a turbulence power law of $\alpha = 3.6667$, a turbulence layer motion velocity magnitude $|\vec{v}| = 1.00D$, a ratio $L_0/D = \infty$, and a ratio of the slope measurement noise variance to the wavefront slope variance $\sigma_n^2/\Gamma_s(0) = 10\%$. The angle of the turbulence layer motion velocity, $\arg(\vec{v})$, is 0, 45, or 90 degrees.

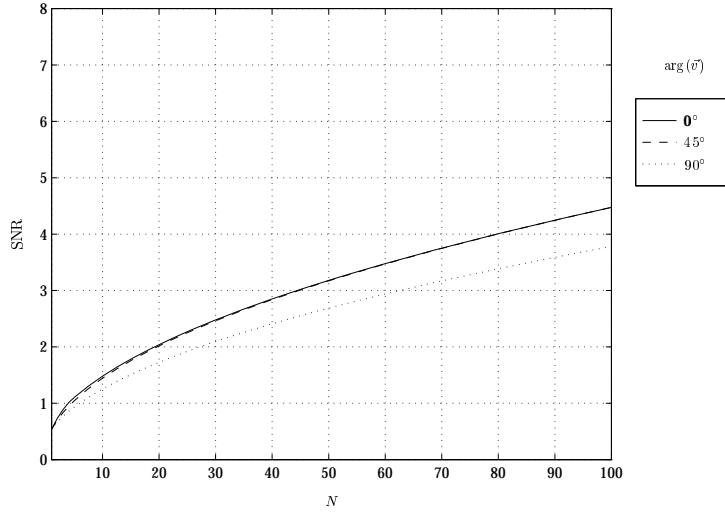


Figure D.113 Group E: Slope structure function estimator SNR vs. number of integration frames, N , for the DIMM geometry with a subaperture separation of $\vec{\rho} = (4.00D, 0.00^\circ)$, a turbulence power law of $\alpha = 3.6667$, a turbulence layer motion velocity magnitude $|\vec{v}| = 1.00D$, a ratio $L_0/D = \infty$, and a ratio of the slope measurement noise variance to the wavefront slope variance $\sigma_n^2/\Gamma_s(0) = 20\%$. The angle of the turbulence layer motion velocity, $\arg(\vec{v})$, is 0, 45, or 90 degrees.

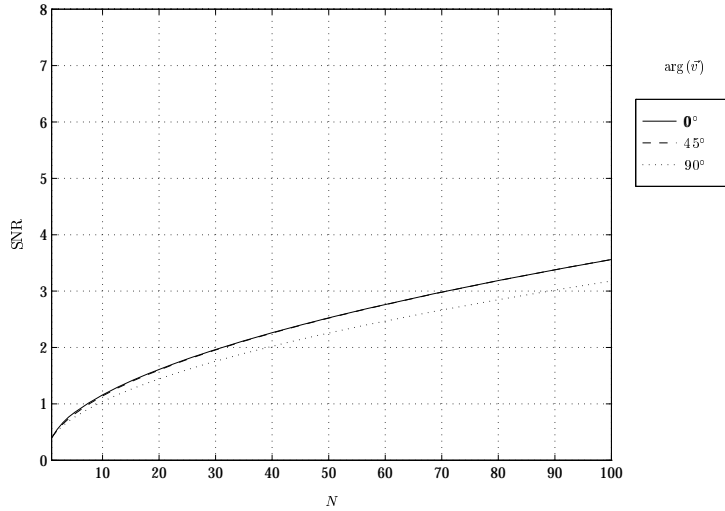


Figure D.114 Group E: Slope structure function estimator SNR vs. number of integration frames, N , for the DIMM geometry with a subaperture separation of $\vec{\rho} = (4.00D, 0.00^\circ)$, a turbulence power law of $\alpha = 3.6667$, a turbulence layer motion velocity magnitude $|\vec{v}| = 1.00D$, a ratio $L_0/D = \infty$, and a ratio of the slope measurement noise variance to the wavefront slope variance $\sigma_n^2/\Gamma_s(0) = 50\%$. The angle of the turbulence layer motion velocity, $\arg(\vec{v})$, is 0, 45, or 90 degrees.

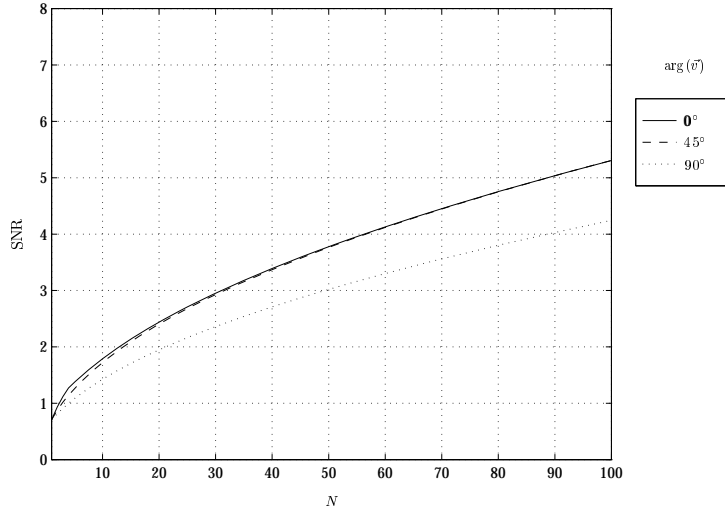


Figure D.115 Group E: Slope structure function estimator SNR vs. number of integration frames, N , for the DIMM geometry with a subaperture separation of $\vec{\rho} = (4.00D, 0.00^\circ)$, a turbulence power law of $\alpha = 3.6667$, a turbulence layer motion velocity magnitude $|\vec{v}| = 1.00D$, a ratio $L_0/D = \infty$, and a ratio of the slope measurement noise variance to the wavefront slope variance $\sigma_n^2/\Gamma_s(0) = 0\%$. The angle of the turbulence layer motion velocity, $\arg(\vec{v})$, is 0, 45, or 90 degrees.

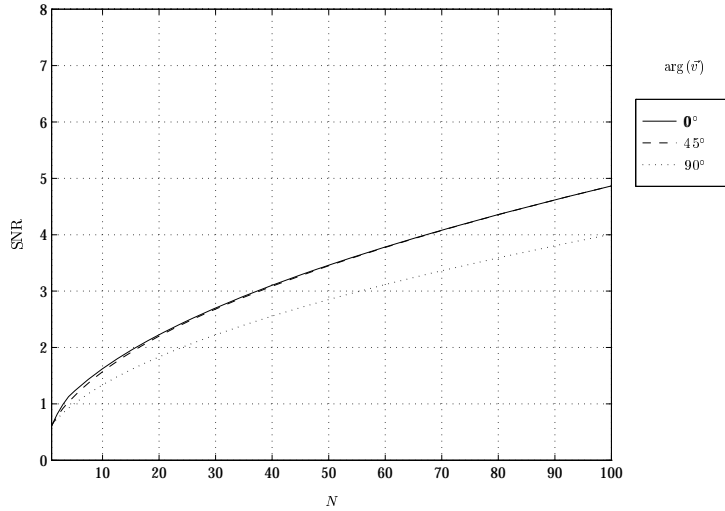


Figure D.116 Group E: Slope structure function estimator SNR vs. number of integration frames, N , for the DIMM geometry with a subaperture separation of $\vec{\rho} = (4.00D, 0.00^\circ)$, a turbulence power law of $\alpha = 3.6667$, a turbulence layer motion velocity magnitude $|\vec{v}| = 1.00D$, a ratio $L_0/D = \infty$, and a ratio of the slope measurement noise variance to the wavefront slope variance $\sigma_n^2/\Gamma_s(0) = 10\%$. The angle of the turbulence layer motion velocity, $\arg(\vec{v})$, is 0, 45, or 90 degrees.

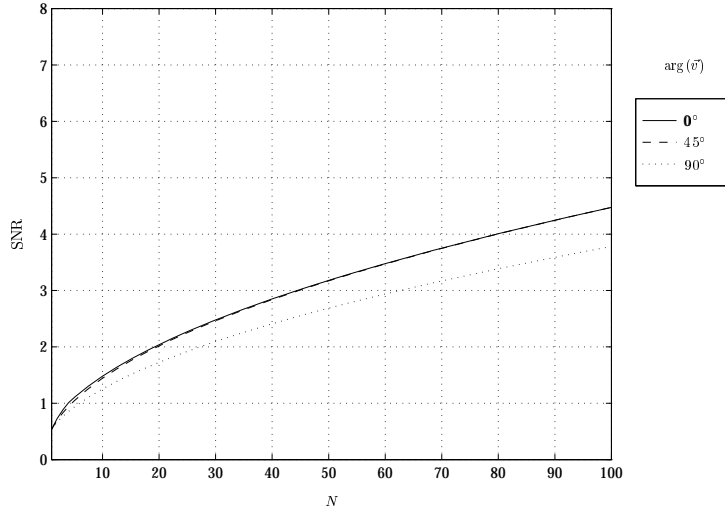


Figure D.117 Group E: Slope structure function estimator SNR vs. number of integration frames, N , for the DIMM geometry with a subaperture separation of $\vec{\rho} = (4.00D, 0.00^\circ)$, a turbulence power law of $\alpha = 3.6667$, a turbulence layer motion velocity magnitude $|\vec{v}| = 1.00D$, a ratio $L_0/D = \infty$, and a ratio of the slope measurement noise variance to the wavefront slope variance $\sigma_n^2/\Gamma_s(0) = 20\%$. The angle of the turbulence layer motion velocity, $\arg(\vec{v})$, is 0, 45, or 90 degrees.

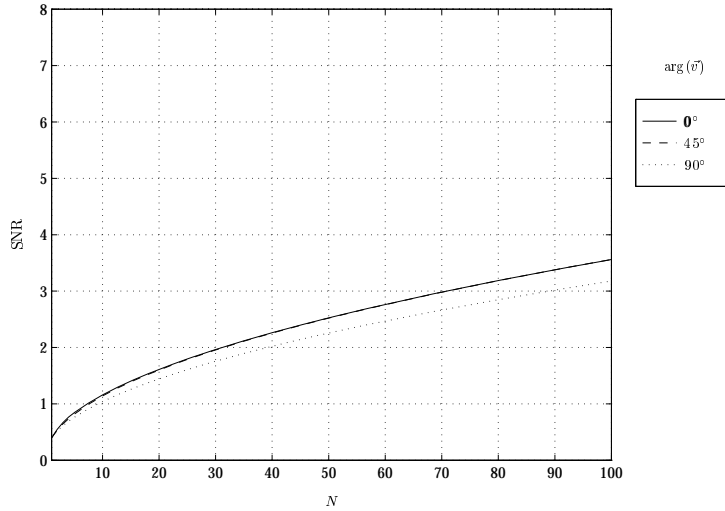


Figure D.118 Group E: Slope structure function estimator SNR vs. number of integration frames, N , for the DIMM geometry with a subaperture separation of $\vec{\rho} = (4.00D, 0.00^\circ)$, a turbulence power law of $\alpha = 3.6667$, a turbulence layer motion velocity magnitude $|\vec{v}| = 1.00D$, a ratio $L_0/D = \infty$, and a ratio of the slope measurement noise variance to the wavefront slope variance $\sigma_n^2/\Gamma_s(0) = 50\%$. The angle of the turbulence layer motion velocity, $\arg(\vec{v})$, is 0, 45, or 90 degrees.


Bibliography

1. Boreman, Glenn D. and Christopher Dainty. "Zernike expansions for non-Kolmogorov turbulence," *J. Opt. Soc. Am. A*, 13(3):517–522 (March 1996).
2. Eaton, Frank D., et al. "Comparison of two techniques for determining atmospheric seeing." *Optical, Infrared, and Millimeter Wave Propagation Engineering 926*. Optical, Infrared, and Millimeter Wave Propagation Engineering. SPIE, 1988.
3. Eaton, Frank D., et al. "Phase structure function measurements with multiple apertures." *Propagation Engineering 1115*. Propagation Engineering. SPIE, March 1989.
4. Fried, D. L. "Differential angle of arrival: Theory, evaluation, and measurement feasibility," *Radio Science*, 10(1):71–76 (January 1975).
5. Goodman, Joseph W. *Statistical Optics*. John Wiley & Sons, 1985.
6. Iye, M., et al. "Differential Dome-Seeing Monitor," *Publications of the Astronomical Society of the Pacific*, 104:760–767 (September 1992).
7. Nicholls, T.W., et al. "Use of Shack-Hartmann wavefront sensor to measure deviations from a Kolmogorov phase spectrum," *Applied Optics*, 20:2460–2463 (July 1995).
8. Noll, R. J. "Zernike polynomials and atmospheric turbulence," *J. Opt. Soc. Am.*, 66:207–211 (1976).
9. Primot, J., et al. "Deconvolution from wave-front sensing: a new technique for compensating turbulence-degraded images," *J. Opt. Soc. Am. A*, 7(9):1598–1608 (September 1991).
10. Roddier, F. "The effects of atmospheric turbulence in optical astronomy." *Progress in Optics 19*, edited by E. Wolf, 283–368, Amsterdam: North-Holland, 1981.
11. Roggemann, Michael C. and Byron M. Welsh. *Imaging through Turbulence*. CRC Press, Inc., 1996.
12. Sarazin, M. and F. Roddier. "The ESO differential image motion monitor," *Astron. Astrophys.*, 227:294–300 (1975).
13. Silbaugh, Eric E., et al. "Characterization of atmospheric turbulence phase statistics using wavefront slope measurements." Unpublished, 1996.
14. Stribling, Bruce Edward. *Laser Beam Propagation in Non-Kolmogorov Atmospheric Turbulence*. MS thesis, Air Force Institute of Technology, 1994.
15. Takato, Naruhisa and Ichirou Yamaguchi. "Spatial correlation of Zernike phase-expansion coefficients for atmospheric turbulence with finite outer scale," *J. Opt. Soc. Am. A*, 12(5):958–963 (May 1995).
16. ten Brummelaar, T.A. "The contribution of high order Zernike modes to wavefront tilt," *Optics Communication*, 115(April):417–424 (1995).
17. Vernin, Jean. "Measuring Astronomical Seeing: The DA/IAC DIMM," *Publications of the Astronomical Society of the Pacific*, 107:265–272 (March 1995).

18. Walters, D. L., et al. "Vertical path atmospheric MTF measurements," *J. Opt. Soc. Am.*, 69:828–837 (June 1979).
19. Welsh, Byron M. "Speckle imaging signal-to-noise ratio performance as a function of frame integration time," *J. Opt. Soc. Am.*, 12(6):1364–1374 (June 1995).
20. Wild, W. J. and R. Q. Fugate. "Untwinkling the stars—Part I," *Sky & Telescope*, 25–31 (June 1994).
21. Wild, W. J. and R. Q. Fugate. "Untwinkling the Stars—Part II," *Sky & Telescope*, 20–27 (June 1994).
22. Winker, D. M. "Effect of a finite outer scale on the Zernike decomposition of atmospheric optical turbulence," *J. Opt. Soc. Am. A*, 8(10):1568–1573 (October 1991).
23. Wolfram, Stephen. *Mathematica, The Student Book*. Addison-Wesley Publishing Company, 1994.
24. Ziad, A., et al. "Experimental estimation of the spatial-coherence outer scale from a wavefront statistical analysis," *Astronomy and Astrophysics*, 282(3):1021–1033 (1994).

Vita

Capt Toby D. Reeves received a Bachelor of Science degree in Electrical Engineering from the University of Alabama in July, 1990. Upon graduation he was commissioned as a second lieutenant in the United States Air Force, where he was assigned to the Follow-on Early Warning System Program Office as a Ground Communications Systems Manager. In January 1994, Capt Reeves became Project Manager of Infrared Space Experiments for the Space Based Infrared Systems Program Office. He is currently assigned to the Air Force Institute of Technology where he is conducting thesis research on Hartmann wave-front sensor performance when used in sensing atmospheric turbulence statistics. Upon graduation from AFIT he will be assigned to Rome Laboratory's Hanscom AFB facilities.

Permanent address: 

December 1996

Master's Thesis

PERFORMANCE ANALYSIS OF A HARTMANN WAVEFRONT SENSOR USED FOR SENSING ATMOSPHERIC TURBULENCE STATISTICS

Toby D. Reeves
Captain, USAF

Air Force Institute of Technology, WPAFB OH 45433-6583

AFIT/GEO/ENG/96D-17

Dr. Brent Ellerbroek, PL/LIG
3550 Aberdeen Ave S.E.
Phillips Lab / LIG
Kirtland AFB, NM 87117-5776

Approved for public release; Distribution Unlimited

Atmospheric turbulence parameters, such as Fried's coherence diameter, the outer scale of turbulence, and the turbulence power law, are related to the wavefront slope structure function (SSF). The SSF is defined as the second moment of the wavefront slope difference as a function of both time and position. Knowledge of the SSF allows turbulence parameters to be estimated. Hartmann wavefront sensor (H-WFS) slope measurements, composed of both signal and noise, allow the SSF to be estimated by computing a mean square difference of H-WFS slope measurements. The quality of the SSF estimate is quantified by the signal-to-noise ratio (SNR) of the estimator. This thesis develops a theoretical SNR expression for the SSF estimator. This SNR is a function of H-WFS geometry, the number of temporal frames included in the estimate, the outer scale, power law, and temporal properties of the turbulence. Spatial slope correlations are incorporated. Temporal slope correlations are incorporated using Taylor's frozen flow hypothesis. Results are presented for various H-WFS configurations and atmospheric turbulence properties.

Hartmann wavefront sensor, atmospheric turbulence sensing, signal-to-noise ratio,
slope structure function, slope structure function estimator, Zernike polynomials

227

UNCLASSIFIED

UNCLASSIFIED

UNCLASSIFIED

UL